
Quantification of the Impact of Space Radiation on the Human Brain in Preparation of a Human Exploration of Mars



Dissertation
in fulfilment of the requirements for the degree of
Doctor of Philosophy ("Dr. rer. nat.")
of the Faculty of Mathematics and Natural Sciences at Kiel
University

submitted by
Salman Khaksarighiri

Kiel, October 11, 2023

Salman Khaksarighiri

Quantification of the Impact of Space Radiation on the Human Brain in Preparation of a Human Exploration of Mars

Kiel, October 11, 2023

Approved by the Thesis Committee:

First examiner (Supervisor):	Prof. Dr. Robert F. Wimmer-Schweingruber
Second examiner:	Prof. Dr. Jan-Bernd Hövener
Date of the oral examination:	20.07.2023
Approved for publication:	20.07.2023

Signed:

Prof. Dr. Wolfgang J. Duschl

“Dedicated to my family”

“As I get older, I realise being wrong isn’t a bad thing like they teach you in school. It is an opportunity to learn something.”

Richard Feynman

Abstract

Humanity has always felt a primordial desire to explore the world we live in and what lies outside our planet. The curiosity to explore the unknown and push boundaries of what we already know can benefit society by driving technological advancements. It may also offer new perspectives on how future generations can adapt to the unique environmental conditions of space, enabling rapid adaptation beyond what normal evolution allows. Therefore, the ultimate frontier in the near-future space era will be a human mission returning to the Moon or venturing to Mars.

Missions to outer space represent a monumental scientific challenge associated with multidisciplinary issues from technology, medicine, physiology, psychology, and extreme radiation environmental conditions. These challenges have traditionally limited mission duration and destinations. Understanding the unique space environment and its biological effects is crucial for investigating the impact of space travel on astronauts, particularly as they venture beyond the International Space Station (**ISS**) in Low Earth Orbit (**LEO**) to destinations like the Moon and Mars. The high level of radiation in the space environment poses a significant challenge for human exploration of deep space and Mars. Unlike Earth, Mars lacks a protective magnetic field, exposing its surface to harmful high-energy space particles that can lead to genetic damage and increased health risks for astronauts.

The work presented in this thesis is an effort to model, understand and mitigate the potential risks of radiation that astronauts may be exposed to during a mission to outer space. In the first part of the thesis, we delve into a significant issue in space biology: the profound impact of deep-space radiation on the human brain. Our investigation encompasses two scenarios: first, we analyze the diverse effects of deep space radiation on various regions of the brain, and second, we conduct an evaluation of distinct thicknesses of shielding aimed at mitigating these adverse effects.

We cover the two most important sources of radiation in deep space: Galactic Cosmic Ray (**GCR**)s and Solar Energetic Particle (**SEP**)s. They represent the main high-energy ionizing radiation, potentially posing significant health risks for astronauts during space missions. Radiation mainly causes damage through ionization, making our primary focus

on ionizing radiation due to its significant biological effects. We have obtained some ready-to-use functions of dose deposit induced by particles, i.e., protons, helium ions, as well as heavier ions such as carbon, nitrogen, and iron impinging isotropically towards the human head. We also evaluate the radiation effects of neutrons as they can be generated in spacecraft, and their effects on biological tissues must be considered for assessing overall radiation risk during space missions. The most probable interactions of the primary particle with the brain structure and the generation of secondary particles, which may further interact with the head contributing to extra absorbed dose, have been included statistically in these functions. The influence of an extra shield between the particle source and the head has been considered using different thicknesses of aluminum, accounting for realistic thicknesses of protective shielding.

In the following study, to gain a comprehensive understanding of the radiation's directionality across a wide range of zenith angles (θ) on the Martian surface, we conducted three-dimensional GEANT4 simulations. Simulations allowed us to derive the θ -dependence of the dose rate on the surface of Mars. The simulation's results indicate that the downward radiation dose on the Martian surface exhibits a weak dependence on the zenith angle θ . Furthermore, we calculated the surface dose rates for various solar modulation potentials (Φ), which shows that weaker modulation results in a higher dose rate for each θ .

To validate our findings, we compared the simulated results with measurements obtained from the Radiation Assessment Detector (**RAD**) and found a reasonable agreement between the two. The **RAD** on board the Curiosity rover is part of the Mars Science Laboratory (**MSL**) mission, which provides insights into the composition, energy levels, and types of particles constituting the radiation environment on the Martian surface. Combining our model with the **RAD** sky view, we could calculate the expected dose rate contributed by particles arriving from the sky direction. Our analysis of dose rates under different sky-obstruction conditions and taking into account the zenith-angle dependence of radiation indicated that the flat-terrain albedo radiation on Mars contributes approximately $(19 \pm 1)\%$ to the total surface dose.

These findings are important for future human exploration of Mars, as they can help estimate the effectiveness of radiation shielding with different regolith geometries and optimize shielding designs for Martian habitats.

Zusammenfassung

Die Menschheit hat schon immer den Wunsch verspürt, die Welt und das Universum zu erforschen. Diese Neugier treibt nicht nur den technologischen Fortschritt voran, sondern eröffnet auch neue Perspektiven auf den Weltraum, unsere Existenz und unsere Zukunft. Besonders die Erforschung von Mond und Mars aufgrund ihrer räumlichen Nähe zur Erde, ihrer wissenschaftlichen Bedeutung und ihres Potenzials für zukünftige Raumfahrtmissionen von besonderem Interesse. Letzteres ist jedoch mit besonderen Herausforderungen verknüpft, wobei vor allem die Beantwortung von multidisziplinäre Fragestellungen in den Themengebieten Technologie, Medizin, Physiologie, Psychologie und die Auswirkung von Strahlung auf den Menschen eine entscheidende Rolle spielt. Die hohe Strahlungsbelastung im Weltraum, insbesondere aufgrund des fehlenden schützenden Magnetfelds auf dem Mars, erhöht das Risiko von gesundheitlichen Problemen bei Astronauten wie Krebs und genetischen Schäden. Die vorgestellte Arbeit versucht, die möglichen Strahlungsrisiken für Astronauten während einer Weltraummission zu modellieren, zu verstehen und zu reduzieren.

Der erste Teil der Arbeit befasst sich mit einem wichtigen Thema der Weltraumbiologie: Den tiefgreifenden Auswirkungen der Weltraumstrahlung auf das menschliche Gehirn. Diese Studie umfasst zwei Szenarien: Erstens werden die unterschiedlichen Auswirkungen der Weltraumstrahlung auf verschiedene Regionen des Gehirns analysiert und zweitens wird eine Bewertung verschiedener Abschirmungsdicken durchgeführt, um diese nachteiligen Auswirkungen zu mildern. Die wichtigsten Quellen der Strahlung im Weltraum sind dabei die galaktische kosmische Strahlung (galactic cosmic rays, **GCRs**) und solaren energiereichen Teilchen (solar energetic particles, **SEPs**). Beides ist hochenergetische ionisierende Strahlung, welche ein erhebliches Gesundheitsrisiko für Astronauten auf Weltraummissionen darstellen kann. Die vorliegende Arbeit entwickelt einige einsatzbereite Funktionen zur Dosisdeposition auf den menschlichen Kopf, die durch Teilchen - insbesondere Protonen, Heliumionen sowie schwerere Ionen wie Kohlenstoff, Stickstoff und Eisen - verursacht wird. Zusätzlich werden die Strahlungseffekte von Neutronen, welche als Sekundärteilchen in Raumfahrzeugen erzeugt werden können, und ihre Auswirkungen auf biologisches

Gewebe bei der Bewertung des Gesamtstrahlungsrisikos während längerer Weltraummissionen mit berücksichtigt. Die wahrscheinlichsten Wechselwirkungen der Primärteilchen mit der Gehirnstruktur und die Erzeugung von Sekundärteilchen, die ebenfalls mit dem Kopf interagieren und zu einer zusätzlichen absorbierten Dosis beitragen können, wurden statistisch in diese Funktionen einbezogen. Da Astronauten bei Weltraummissionen zusätzlich durch Raumfahrtanzüge geschützt sind, werden in den Analysen unterschiedliche Aluminiumdicken als realistische Schutzabschirmungen zwischen den Partikelquellen und dem Kopf berücksichtigt.

Im weiteren Verlauf wird eine dreidimensionale GEANT4- Monte-Carlo-Simulation durchgeführt, um ein umfassendes Verständnis der Richtungsabhängigkeit der Strahlung über einen breiten Bereich von Zenitwinkeln (θ) auf der Marsoberfläche zu gewinnen. Diese Simulation ermöglicht es zusätzlich, die θ -Abhängigkeit der Dosisleistung auf der Marsoberfläche abzuleiten. Die Ergebnisse der Simulation zeigen, dass die abwärts gerichtete Strahlungsdosis auf der Marsoberfläche eine schwache Abhängigkeit vom Zenitwinkel θ aufweist. Darüber hinaus wird die Oberflächendosisleistungen für verschiedene solare Modulationspotentiale (Φ) bestimmt, mit dem Ergebnis, dass eine schwächere Modulation zu einer höheren Dosisleistung für jedes θ führt. Die simulierten Ergebnisse werden zur Validierung mit den Messungen des **RAD** verglichen. Beide stellen eine sehr gute Übereinstimmung dar. Das **RAD** an Bord des Curiosity-Rovers ist Teil der **MSL**-Mission, und liefert Einblicke in die Strahlungsumgebung auf der Marsoberfläche in Bezug auf die Zusammensetzung, die Energieniveaus und die Arten von Teilchen. Durch die Kombination der entwickelten Modell mit Sichtfeld von **RAD**-Sicht auf den Himmel konnten wir die erwartete Dosisleistung berechnen, die von den vom Himmel eintreffenden Partikeln stammt.

Unsere Analyse der Dosisraten unter verschiedenen Bedingungen für die Abschirmung des Himmels und unter Berücksichtigung der Zenitwinkelabhängigkeit der Strahlung ergab, dass die Albedostrahlung des flachen Geländes auf dem Mars etwa $(19 \pm 1)\%$ zur gesamten Oberflächendosis beiträgt.

Diese Ergebnisse sind wichtig für Überlegungen zur zukünftigen Erkundung des Mars durch Menschen. Sie helfen bei der Abschätzung der potenziellen Wirksamkeit des Strahlenschutzes für eine bestimmte Regolith-Geometrie und bei der Optimierung des Designs des Strahlenschutzes für Marshabitats.

List of Relevant Peer-Reviewed Publications

The following is a list of peer-reviewed publications that are relevant in the context of this thesis and have been reprinted herein:

1. Publication 1: *Calculation of dose distribution in a realistic brain structure and the indication of space radiation influence on human brains*

Khaksarighiri, S., Guo, J., Wimmer-Schweingruber, R., Narici, L., Lohf, H. (2020). Life Sciences in Space Research, 27, 33-48. DOI:10.1016/j.lssr.2020.07.003

Own contribution: 80%

2. Publication 2: *An easy-to-use function to assess deep space radiation in human brains*

Khaksarighiri, S., Guo, J., Wimmer-Schweingruber, R., Narici, L. (2021). Scientific reports, 11(1), 11687. DOI:10.1038/s41598-021-90695-5

Own contribution: 80%

3. Publication 3: *The Zenith-Angle Dependence of the Downward Radiation Dose Rate on the Martian Surface: Modeling Versus MSL/RAD Measurement*

Khaksarighiri, S., Guo, J., Wimmer-Schweingruber, R. F., Löffler, S., Ehresmann, B., Matthiä, D., Donald M.Hassler, Cary Zeitlin, Berger, T. (2023). Journal of Geophysical Research: Planets, e2022JE007644. DOI:10.1029/2022JE007644

Own contribution: 80%

4. Publication 4: *Directionality of the Martian Surface Radiation and Derivation of the Upward Albedo Radiation*

Guo, J., **Khaksarighiri, S.,** Wimmer-Schweingruber, R. F., et.al. (2021). Geophysical Research Letters, 48(15), e2021GL093912. DOI:10.1029/2021GL093912

Own contribution: 50%

A comprehensive list of all publications I have contributed to can be found in Appendix D.

Contents

Abstract	iv
Zusammenfassung	vi
List of Figures	xi
List of Tables	xi
List of Acronyms and Initialisms	xii
1 Introduction	1
1.1 Humans in Space	1
1.2 Psychological problems	2
1.3 Physiological Problems	4
1.3.1 Micro-and Hyper-gravity	4
1.3.2 Radiation	6
1.4 Radiation Environment in Space	7
1.4.1 GCRs in Interplanetary Space	9
Energy Spectra of GCRs	11
Solar Modulation	12
1.4.2 SEPs in Interplanetary Space	13
1.5 Interaction between Radiation and Matter	14
1.5.1 Charged Particle Interactions	15
Ionization and Excitation	16
Stopping Power and the Bethe–Bloch Energy Loss Expression	17
Nuclear Interactions	19
1.5.2 Neutral Particle Interactions	20
1.6 Dosimetric Concepts	22
1.7 Dose Quantities	22
1.7.1 Absorbed Dose	23
1.7.2 Equivalent Dose and Relative Biological Effectiveness (RBE)	23
1.7.3 Effective Dose	24
1.7.4 Linear Energy Transfer (LET) and Quality Factor	25
2 Literature Review: In View of Humans in Space	27
2.1 Radiation Relevant for a Mars Mission	27

2.2	Radiation Exposure for Astronauts on a Mission to Mars	29
2.3	Spaceflight and Ground-based Models of Radiation Effects	32
2.3.1	Behavioral Effects of Charged Particles in Animal Models	36
2.4	Motivation	39
3	Dose Assessment : Instrument and Modelling	42
3.1	The MSL Radiation Assessment Detector Instrument	42
3.2	Geant4 Toolkit	46
3.2.1	Geant4-DICOM Package	47
3.3	3D Slicer	50
4	Publications	52
4.1	<i>Paper I: Modeling the Dose Distribution in the Human Brain</i>	54
4.2	<i>Paper II: Easy-to-Apply Approach to Forecast and Calculate the Radiation Effects of SEPs in Different Parts of the Brain Using Modeling Results</i>	72
4.3	<i>Paper III: Zenith-Angle Dependence of Downward Radiation Dose Rate on the Martian Surface</i>	85
4.4	<i>Paper IV: Modeling, Observations, and Albedo Radiation Analysis.</i>	100
5	Summary and Conclusions	112
6	Outlook	117
6.1	Space Radiation Environment and Ground-based Experiment Discrepancies	118
6.1.1	Radiation Environment Types	119
6.1.2	Irradiation Direction and Time	120
6.1.3	Human Phantoms	120
6.1.4	Shielding	122
	Bibliography	124
A	Convert NRRD files to PNG	158
B	Dose Resulting from GCRs and SEP Events	161
C	Calibration Curve	165
D	List of Peer-Reviewed Publications	167
	Acknowledgements	169
	Statutory Declaration	170

List of Figures

1.1	Biological features of spaceflight.	3
1.2	Spectra of oxygen ions in the near-Earth interplanetary space	9
1.3	Relative contribution of GCR nuclei	10
1.4	Differential flux of several GCR elemental species	12
1.5	The proton fluence spectra of 50 large SEP events	15
1.6	Total neutron cross sections of lead	20
1.7	Photon cross section as function of the energy in lead.	21
2.1	The radiation environment in deep space and on the Martian surface	29
2.2	Components of the space radiation environment	30
3.1	RAD recorded Martian surface dose rates	45
3.2	Schematic diagram of the RAD sensor head	46
3.3	Human brain segmented to different lobes using 3D-Slicer	51
6.1	Ground-based experiments and actual space radiation exposure discrepancies	119
B.1	Downward and upward GCR spectra dose rate in Frontal lobe.	164
B.2	The dose rates in the human head on the surface of Mars	164
C.1	CT number to mass density calibration curve	166

List of Tables

2.1	Brain regions mentioned in the thesis	39
2.2	Behavioural tests mentioned in this thesis.	41
B.1	Dose (cGy) from 51 SEP events in the human head	162
B.2	Dose (cGy) from 51 SEP events in different lobes of the human brain	163

List of Acronyms and Initialisms

ACE Advanced Composition Explorer

ACRs Anomalous Cosmic Rays

ALFMED Apollo Light Flash Moving Emulsion Detector

ARS Acute Radiation Sickness

AU Astronomical Unit

BON Badhwar-O'Neill

BREP Boundary REPresentation

BRF Brain Response Function

CIR Corotating Interaction Regions

CME Coronal Mass Ejection

CNS Central Nervous System

CRIS Cosmic Ray Isotope Spectrometer

CT Computed Tomography

DICOM Digital Imaging and Communications in Medicine

DNA Deoxyribonucleic Acid

ESA European Space Agency

ESP Energetic Storm Particle

FP Fokker–Planck

GCR Galactic Cosmic Ray

GOES Geostationary Operational Environmental Satellite

HEND High-Energy Neutron Detector

HU Hounsfield Unit

HZE High atomic number (Z) and Energy

ICRP International Commission on Radiological Protection

ICRU International Commission on Radiation Units and Measurements

IMF Interplanetary Magnetic Field

ISS International Space Station

LEO Low Earth Orbit

LET Linear Energy Transfer

LF Light Flash

LIS Local Interstellar Spectrum

LNT Linear-No-Threshold

LSAH Longitudinal Study of Astronaut Health

MARIE Mars Radiation Environment Experiment

MRI Magnetic Resonance Imaging

MSL Mars Science Laboratory

NASA National Aeronautics and Space Administration

NASCA NASA Study of Cataracts in Astronauts

NCRP National Council on Radiation Protection and Measurements

NRRD Nearly Raw Raster Data

NURBS Non-Uniform Rational B-Splines

PHA Pulse Height Analysis

RAD Radiation Assessment Detector

RBE Relative Biological Effectiveness

RSH RAD Sensor Head

RTG Radioisotope Thermoelectric Generator

SANS Spaceflight Associated Neuro-ocular Syndrome

SEP Solar Energetic Particle

SEPEM Solar Energetic Particle Environment Modelling

SMSP Shuttle-Mir Space Program

SOHO Solar and Heliospheric Observatory

SPEL Space-Permissible Exposure Limit

UNSCEAR United Nations Scientific Committee on the Effects of Atomic Radiation

Chapter 1

Introduction

1.1 Humans in Space

Throughout the course of human evolution, exploration has consistently been one of the imperative survival strategies. The journey into space officially began in 1957, when the first artificial satellite, Sputnik 1, was launched into space, and four years later, in 1961, Yuri Gagarin became the first human to voyage into space in Vostok 1 (Ji et al., 2021; Kuznetsov et al., 2015; Stuhlinger, 1999). Since then, developments in space technologies have provided opportunities for scientific, industrial, and even commercial missions to explore space outside our planet. Till now, over 600 astronauts have traveled to space, which include all who have flown to an altitude of 100 km or higher such as the [ISS](#) within [LEO](#) (Yazici et al., 2021). The pace is expected to accelerate as a market for private spaceflight missions with wealthy tourists takes shape.

But when venturing beyond Earth to interplanetary destinations like the Moon or Mars, space weather, which refers to the dynamic and ever-changing conditions in space, can impact various aspects of space missions and introduces a multitude of complexities and challenges for human exploration. Space weather encompasses conditions on the Sun, in the solar wind, magnetosphere, and ionosphere, which can influence the performance and reliability of both space-borne and ground-based technological systems, posing risks to human life and health (Schwenn, 2006; Wright Jr et al., 2010; Forstner et al., 2020). In light of these factors, ensuring the overall safety of astronauts and prioritizing their physical and mental well-being becomes critical for success of the mission.

Fortunately, humans have the advantage of adapting to their surroundings and adjusting themselves to extreme environments that often require challenging physical and mental exertions (Paulus et al., 2009; Ilardo and Nielsen, 2018). "Extreme environments" include prolonged and marked isolation experiences on Earth, such as the polar areas and submarine explorations, as well as beyond the boundaries of our planet, i.e. outer space.

The hazards that astronauts endure during spaceflight have significant effects on their physiological and mental well-being. These dangers arise from several factors, such as increased exposure to damaging radiation, altered gravity fields, prolonged periods of

isolation and confinement, living in an enclosed and potentially hostile environment, and the stress of being far from Earth (Gushin et al., 1993; Romero and Francisco, 2020; Afshinnekoo et al., 2020; Schorn and Roma, 2020; Williams, 2003; Beatty et al., 1999).

Figure 1.1 illustrates these factors, which collectively contribute to the challenging and demanding nature of space exploration.

In the following sections, we provide a brief overview of the physiological and psychological problems associated with space exploration. Among all the physiological and psychological challenges encountered in space missions, radiation is arguably the most significant concern due to its potential long-lasting effects even after the missions have concluded. We then shift our focus to the effects of radiation, which is the main topic of this study and a critical research priority in the field of space exploration. Understanding the biological consequences of radiation exposure is crucial for ensuring the well-being and safety of astronauts during their missions. We delve into the radiation environment in space, with a particular emphasis on **GCRs** and **SEPs** as the two main sources of radiation in deep space and on the surface of Mars, which are relevant to our study. Furthermore, we summarize key radiation-matter interaction processes for both charged and neutral particles in space. Finally, we provide an overview of dosimetric concepts in space, highlighting their significance in assessing radiation exposure during space missions.

1.2 Psychological problems

The most significant unknown with the potential to cause failure in space missions is the human factor, particularly psychological stressors, and effects on the astronaut's mind in a long-duration space environment. Behavioral health issues can lead to mistakes that jeopardize the mission or the lives of astronauts (Caddy, 2018). The deterioration of an astronaut's mental health during a 211-day mission on the Salyut 7 space station in 1982 highlights the need for more research into the psychological effects of space travel (Morris, 2014). While there have been significant advances in space exploration, understanding space psychology remains a challenge.

The confinement, heavy workloads, and sleep problems associated with long-duration space missions can lead to mood symptoms (Gushin et al., 1993; Tafforin et al., 2015), cognitive issues (Acharya et al., 2019; Cacao and Cucinotta, 2019; Moore et al., 2019), sleep disturbances (Barger et al., 2014), anxiety, depression, cumulative fatigue, asthenia, and neuroanatomical effects that may cause disturbed behavior in space (Morphew, 2001). According to a study, 78% of Space Shuttle crew members reported taking medications in space for motion sickness (30%), headaches (20%), insomnia (15%), or back pain (10%) (Jaffee, 2005; Pavy-Le Traon et al., 1997). There was also a use of new psychoactive medications on some flights, including olanzapine, risperidone, and SSRIs (Santy et al., 1988; Aleksandrovskiy and Novikov, 1996). Social conflicts are also expected from isolation and confinement during space missions due to multicultural factors such as differences in

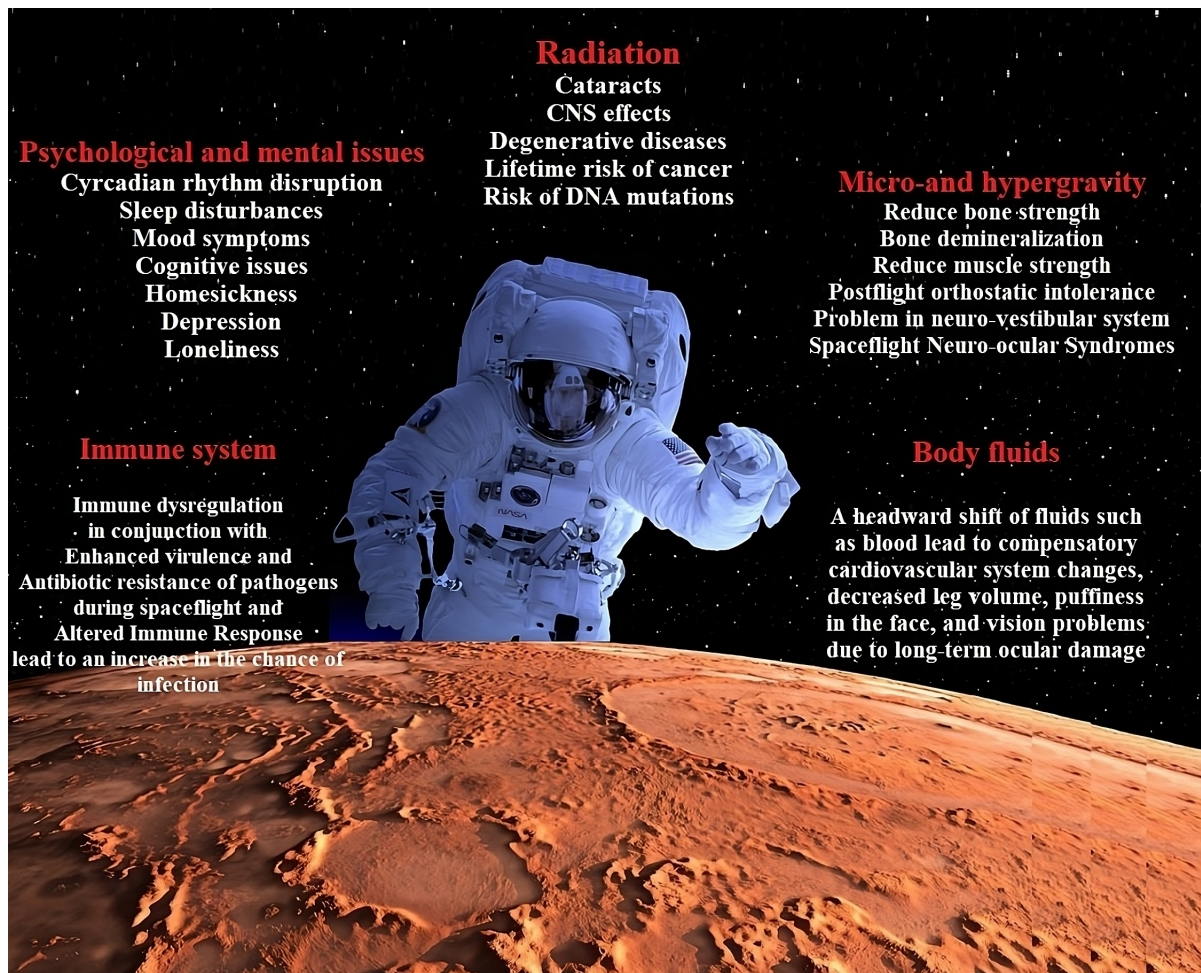


FIGURE 1.1: In space, microgravity, radiation, and confinement in a closed environment pose health risks and drive many physiological changes and psychological effects seen during spaceflight. The background image was captured and modified from Sofocleous (2019), and the astronauts image is taken from Pxhere (2017).

nationality, religion, social values, and political opinions. An international shuttle crew debriefing revealed that out of 42 incidents reported by nine US astronauts on **ISS** missions, five in-flight incidents were rated as having a high mission impact (Santy et al., 1993). Because of these studies and anecdotal evidence of the individual and interpersonal problems during the Shuttle-Mir Space Program (**SMSP**), and other long-duration Soviet missions (Palinkas, 2007; Kanas, 1998; Ellis, 2000), there has been a growing awareness that psychosocial issues are just as important to the success of long-duration missions in space as other dynamics related to crew health and safety. Although the psychological effects of long-duration space travel and living in outer space have not been thoroughly analyzed, similar studies exist on Earth. These studies have investigated similar environments such as polar areas and submarine explorations, which involve isolation, extreme conditions, and limited resources (Stuster, 2011). Besides, similar research has been conducted on astronauts in **LEO** on the **ISS** (Stuster, 2011; Kanas, 1990).

To address at least some of these psychological problems, scientists are using devices that prevent, minimize, or reverse deleterious effects during extended missions, such as actigraphy, which measures how much people move and the amount of ambient light around them to gauge sleep and alertness (Smith et al., 2018). The use of sleep-wake actigraphy and light exposure investigations is anticipated to provide valuable insights into defining light requirements, sleep-shifting protocols, and workload plans for future exploration missions. These studies may also help to determine if further countermeasures against sleep disruption need to be tested (Smith et al., 2018; Czeisler et al., 2009). While these psychiatric problems rarely reach clinical levels, they have resulted in instances of impaired performance capacity, significant conflict among crew members, and errors in performing operational tasks, and pose a challenge to the factors related to crew health and safety for the success of long-term missions in space (Kanas, 2015; Kanas and Manzey, 2008).

1.3 Physiological Problems

Apart from psychological barricades, a space voyage will also have to overcome the physiological issues intrinsic to the condition of the human body. Here, we outline some of these physiologic changes as an explicit consequence of long-term exposure to various gravity situations, cell damage from ionizing radiation, and potential permanent vision problems.

1.3.1 Micro-and Hyper-gravity

The human body has evolved to function best within the Earth's gravitational field, which is approximately 9.81 m/s^2 , along with the presence of a protective atmosphere. These factors contribute to the planet's habitability and enable optimal functioning of the human body. Our brain considers gravity as an essential factor during everyday activities to maintain balance and prevent falling. However, space travelers experience different gravitational forces, including microgravity during non-propulsive flight and on the surfaces of celestial bodies such as the Moon or Mars. They also experience intermediate periods of hypergravity during launch, ascent, descent, and landing. These varying gravitational conditions have distinct effects on the human body and must be considered when planning and conducting space missions (Barratt, 2019; Catling and Kasting, 2017).

Physiological systems that are particularly vulnerable to the effects of weightlessness include the sensory-motor and neuro-vestibular systems responsible for balance, as well as the cardiovascular system, musculoskeletal system, and bone strength, which can undergo demineralization in microgravity conditions (Bhaskaran et al., 2009; Zayzafoon et al., 2005; Williams, 2003). Skeletal muscle atrophy is also observed in these conditions (Androjna et al., 2012; Bhaskaran et al., 2009). These physiological changes are important to understand and address to mitigate their impact on astronauts during space missions.

The cardiovascular system, comprising the heart, veins, arteries, and capillaries, as well as the pulmonary system, represented by the lungs, nose, the trachea and the breathing

muscles (the diaphragm and the intercostal muscles), can adapt promptly to changes in gravity when blood and other body fluids shift from the lower extremities to the upper body parts. However, this leads to an enlarged heart in astronauts, as it tries to cope with the increased blood flow resulting from the accumulation of fluids in the upper body (Lau-nius, 1994). The body interprets this excess fluid as a flood and tries to eliminate it in a way that astronauts become less thirsty or their kidneys become more active (Antonutto et al., 2003; Morpew, 2001), which can cause post-flight orthostatic intolerance, lightheadedness, headaches, fatigue, altered vision, weakness, sweating, anxiety, heart palpitations, movement disorders, and the danger of bone fracture, among other symptoms, especially in the first days of one arrives at a place or return to Earth for the astronauts (Clément, 2011; Antonutto et al., 2003). Recovery from the effects of zero gravity can take over a year after a six-month mission, and astronauts can combat these symptoms by engaging in vigorous exercise or taking medications like Erythropoietin and Fludrocortisone (Buckey, 2006).

The neuro-vestibular system, responsible for the body's balance mechanisms, can be affected during space travel, leading to motion sickness symptoms such as disorientation, dizziness, decreased appetite, vomiting, extreme nausea, and sensory changes (Koizuka and Kato, 1999; Clément, 2011; Scherer et al., 2001). Weightlessness alters the functioning of the inner ear's otolith organs and semicircular canals, which detect motion, resulting in misinterpretation and inadequate responses by the brain (Iwase et al., 2020; Morpew, 2001). Considering astronauts' adaptation to weightlessness and their neuro-vestibular history is important in minimizing the impact of weightlessness on the system (Morpew, 2001; Scherer et al., 2001). Medications like lorazepam, meclizine, promethazine, and scopolamine have been used to treat severe motion sickness in space programs such as the Shuttle program and the ISS (Paule et al., 2004; Dornhoffer et al., 2004).

In a weightless environment, the skeletal muscles in the human body can go into hibernation mode and begin to atrophy, resulting in a loss of bone mass and decreased bone density (Morpew, 2001; Buckey, 2006). Astronauts can also experience changes in calcium balance, increased bone resorption, and increased urinary calcium excretion, an increase of bone resorption but little or no increase in bone formation, resulting in a loss of 1–1.5% of bone mass throughout a month (Stavrichuk et al., 2020). These effects can be mitigated through exercise and a balanced diet (Morpew, 2001; Paris, 2014).

Moreover, in the last decade of spaceflight, a syndrome called Spaceflight Associated Neuro-ocular Syndrome (**SANS**) has been gaining much attention due to its potential health implications on long-duration flights (Lee et al., 2018; Stenger et al., 2019). Although the human body is highly adaptive and can acclimatize to a change in the gravitational environment, physiological adaptations may have pathological consequences or lead to a reduction in fitness that challenges a space traveler's ability to conduct as usual upon return to Earth (Clément et al., 2020). It is important to understand how gravity affects human functions in space and to develop countermeasures against the physiological

effects of spaceflight that can result in undesired health and performance declines (Stenger et al., 2019).

1.3.2 Radiation

Radiation exposure is one of the most significant risks to human health during space missions. The effects of radiation on the human body depend on several factors, including the type and amount of radiation, the duration of exposure, and the shielding provided by spacecraft and spacesuits. Although the astronauts in **LEO** are more exposed to radiation than humans on the ground, they are still well protected due to the strong shielding against interplanetary radiation provided by the Earth's magnetic field, which attenuates the major effects of space radiation exposures for current **LEO** missions (Beatty et al., 1999). But future expeditions into interplanetary space, and in particular to the Moon and Mars, will introduce the spacecraft and its crew to an environment outside of this protective shield, which exposes astronauts to much higher levels of cosmic radiation compared to the current **LEO** missions. Astronauts orbiting in **LEO** are exposed to a radiation level of approximately 0.17 mGy/day, whereas the Apollo missions venturing beyond Earth's protective shield encountered a higher level of about 0.50 mGy/day. On Mars, data from the **RAD** instrument indicated an average daily radiation dose of approximately 0.21 mGy, while the lunar surface exhibited an average total absorbed dose rate of approximately 0.316 mGy/day (Zhang et al., 2020; Kasaboski and Hill, 2014; Guo et al., 2021b).

During the early times of human space explorations in the 1970s, an unusual visual phenomenon reported by Apollo astronauts raised attention to radiation effects on human brains and the Central Nervous System (**CNS**) system. They reported seeing flashes of light and experiencing painful cataracts. It was thought that these flashes were due to radiation of high charge and energy particles propagating through the retina and interacting with matter, which can trigger ionization Cerenkov light and depositing its energy directly into the eyes of the astronaut (Paris, 2014; Budinger et al., 1972). It is worth mentioning that the duration of the Apollo missions was relatively short compared to the anticipated future missions to Mars, which are expected to span two to three years. Such extended missions pose potential risks from radiation, including critical spacecraft damage, absorption of fatal radiation doses from large **SEPs**, and potential damage to Deoxyribonucleic Acid (**DNA**) at the cellular level, which may eventually increase the risk of cancer (Cucinotta, 2002; Meier et al., 2020).

There are several sources of radiation in space that can affect the human body. The primary source of space radiation are **GCRs**, which are high-energy particles that originate from outside our solar system (Axford, 1994; Parizot, 2014; Ahn et al., 2010; Arnould and Goriely, 2020). These particles can penetrate spacecraft and human tissue, potentially causing genetic damage and increasing the risk of cancer. Another source of space radiation are **SEPs**, which occur when the Sun releases bursts of energetic particles during solar

flares or coronal mass ejections. These particles can also penetrate the spacecraft and human tissue, and can cause acute radiation sickness in astronauts (Reames, 1995; Reames, 2013; Wijzen et al., 2019; Guo et al., 2021b). Extensive training and adherence to strict safety protocols are necessary to mitigate the risks of space radiation for astronauts. In addition, spacecraft and habitats can be specifically designed to offer adequate shielding against radiation exposure.

Continued research is essential to further our understanding of the effects of space radiation on various regions of the human body, including the brain. This knowledge is crucial to advance the development of innovative technologies, such as helmets that can effectively protect astronauts during extended-duration space missions. We need to deepen our understanding and invest in these advancements, to enhance the safety and well-being of astronauts as they embark on long-duration space exploration endeavors.

In the following sections, we will provide an overview of how humans would encounter these different types of radiation on a Mars voyage, followed by an analysis of how these radiation types would affect the human body.

1.4 Radiation Environment in Space

Particle populations in the heliosphere exhibit unique characteristics that depend on their origin, revealing important information about their source and acceleration mechanism into the interplanetary medium. According to Kallenrode, 2004, the general characteristics of the various heliospheric populations of oxygen ions, arranged according to their intensity versus energy, are illustrated in figure 1.2. By studying these characteristics, we can gain insights into the production and acceleration of these particles.

Within the heliosphere, particle populations include the solar wind, which is a continuous outflow of plasma containing protons, electrons, ionized helium, and all other elements with an energy range between ~ 0.4 to 10 keV/amu (Geiss, Gloeckler, and Von Steiger, 1995; Rouillard et al., 2021; Marov, 2015). It consists of both slow and fast components. The fast solar wind is associated with coronal holes, which are dark regions observed in X-ray images. The slow solar wind originates from regions near the Sun's equator. As the solar wind interacts with the Earth's magnetic field, it can lead to the energization and acceleration of ions and particles, such as oxygen ions, resulting in their presence in the near-Earth interplanetary space (Gosling, 2014; Schwenn, 2007). In addition to the particles carried by the solar wind, the interplanetary medium encompasses a significant constituent called cosmic rays. Although the Sun plays a crucial role as a source of particles within the heliosphere, it is important to recognize that cosmic rays also emanate from other sources, contributing to the overall population of these energetic particles.

- **GCs** refer to a specific type of highly energetic particles that originate isotropically from outside our solar system and are modulated as they traverse the turbulent

magnetic field embedded into the solar wind. These high-energy particles, predominantly protons, and atomic nuclei, travel vast distances through space before reaching our solar system. GCRs have diverse origins, including supernovae explosions, active galactic nuclei, and other cosmic events (Axford, 1994; Parizot, 2014; Arnould and Goriely, 2020).

- Anomalous Cosmic Rays (**ACRs**) are an intriguing phenomenon in the heliosphere, originating from neutral interstellar atoms that enter the heliosphere and undergo ionization. This ionization process can occur through either charge exchange with the solar wind or ionization induced by solar radiation. Following ionization, these particles are convected out to the heliopause as pickup ions, where they undergo acceleration to form the **ACRs** (Giacalone et al., 2022; Czechowski et al., 2001).
- **SEPs** are a type of energetic particles that originate from the Sun during solar events such as solar flares and Coronal Mass Ejection (**CME**)s. These events release immense amounts of energy and eject particles, including protons, electrons, and heavier ions, into space. **SEP** events can be impulsive or gradual, and the main difference between them lies in the timescale and characteristics of particle acceleration and release (Reames, 1995; Reames, 2013; Guo et al., 2021b).
- Corotating particles experience acceleration within Corotating Interaction Regions (**CIR**)s, which manifest as turbulent regions formed when a fast solar wind stream surpasses a slower solar wind stream. As a consequence of this interaction, the magnetic field becomes compressed, leading to the acceleration of particles confined within these regions. The resulting accelerated particles exhibit energy levels typically up to 10 MeV (Mullan, 1984; Heber, Sanderson, and Zhang, 1999; Wijsen et al., 2019; Pacheco Mateo, 2019).
- Energetic Storm Particle (**ESP**) events are characterized by enhancements in energetic ion and electron intensities that are observed during the passage of interplanetary shocks. These events are part of a broader category of **SEPs** observed both in interplanetary space and near Earth. The distinction between these different types of **SEP** events is based on the origin of the particles and the specific acceleration mechanisms they undergo. While impulsive and gradual **SEP** events have their defining characteristics, **ESP** events share most properties with other **SEPs**, except for variations in ion composition ratios, which depend on the origin of the particles and the particular acceleration process they experienced (Gosling, 1993; Pacheco Mateo, 2019; Malandraki and Crosby, 2018).

The various particle populations present in the heliosphere have significant implications for space exploration and the safety of astronauts. In our study, we focus on investigating the effects of **SEPs** and **GCRs** depicted in the blue region in figure 1.2 on astronauts, particularly their influence on the astronauts' brains. **GCRs** and **SEPs** are of greater interest when studying the effects of space radiation due to their abundance, high energy, and

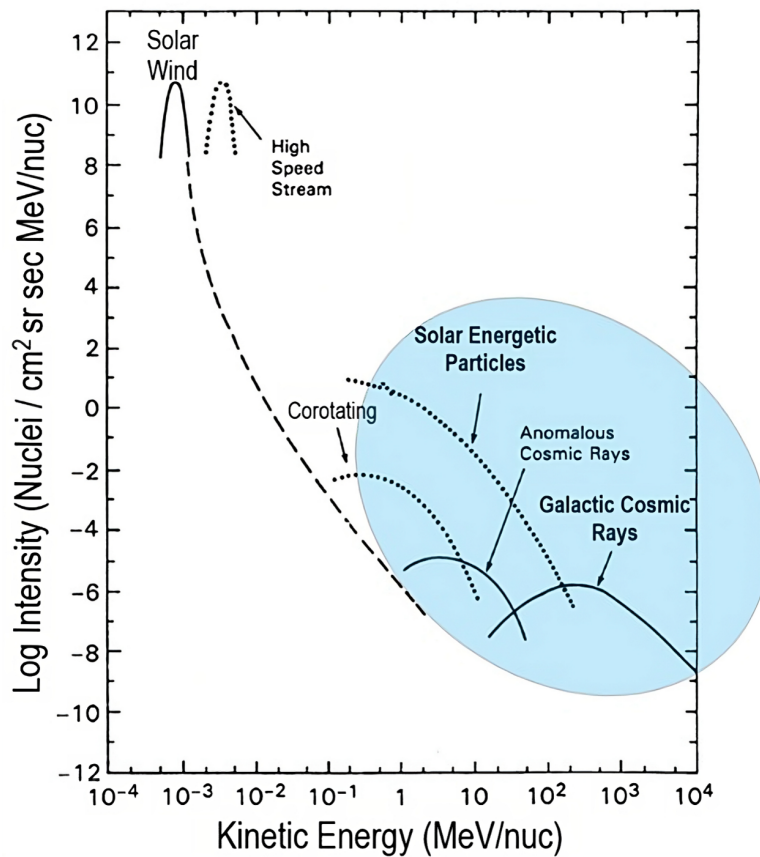


FIGURE 1.2: Spectra of oxygen ions in the near-Earth interplanetary space, showing the contributions of different populations (Stone et al., 1998; Mewaldt et al., 2001; Pacheco Mateo, 2019). In our study, we focus on investigating the effects of **SEPs** and **GCRs** highlighted in the blue region due to their potential hazards to astronauts during space missions, as these sources are of particular concern compared to others.

long exposure during extended space missions. These high-energy particles can penetrate deeply into the human body, posing significant health risks to astronauts.

1.4.1 GCRs in Interplanetary Space

The discovery of **GCRs** is credited to the work of physicist Victor Hess in the early 20th century (Friedlander, 2012; Grupen, 2021). Hess discovered a type of radiation originating from extra-terrestrial sources, which exhibited an increase in intensity at higher altitudes. He called it high-altitude radiation and was awarded the Nobel prize in physics for his pioneering work in the study of cosmic rays (Hess, 1912; Beckman, 2021; De Angelis, 2013). In the following decades, scientists continued to study cosmic rays using a variety of techniques, including balloon-borne detectors and ground-based instruments. In the 1960s and 1970s, the National Aeronautics and Space Administration (**NASA**) launched several spacecraft, including the Explorer and Interplanetary Monitoring Platform series, which were designed to study the properties of cosmic rays and their effects on spacecraft and

human health (Ness, 1996). **GCRs** are high-energy particles that originate from outside our solar system. They are thought to be created by a variety of astrophysical processes, such as supernova explosions, the acceleration of particles by black holes and pulsars, and other high-energy events in the galaxy and beyond (Ahn et al., 2010; Arnould and Goriely, 2020; Globus and Blandford, 2023; Butt, 2009). **GCRs** are composed of a variety of different particles, including protons, alpha particles, and heavier ions such as carbon, nitrogen, and oxygen. They have extremely high energies, often millions of times greater than the energies of particles in the solar wind. Figure 1.3 depicts the composition of **GCR** particles with energies ranging from 0.01-100 GeV/nuc. The graph shows the integrated total particle fluxes, absorbed dose rates, and dose equivalent rates. The values were obtained from computer simulations of an unshielded water phantom exposed to **GCR** at the **ISS** orbit in November 2009. The figure illustrates the substantial contribution of less abundant nuclei of High atomic number (Z) and Energy (**HZE**) ions to the overall **GCR** exposure, taking into account the absorbed dose and quality factor (Section 1.7.4). This contribution arises from the fact that the energy deposited by **HZE** ions in an individual cell is proportional to the square of the particle's charge, and their biological effectiveness is quantified by the dose equivalent rate, as elaborated in Section 1.7 (Benton and Benton, 2001; Reitz, 2008; Mrigakshi, 2013).

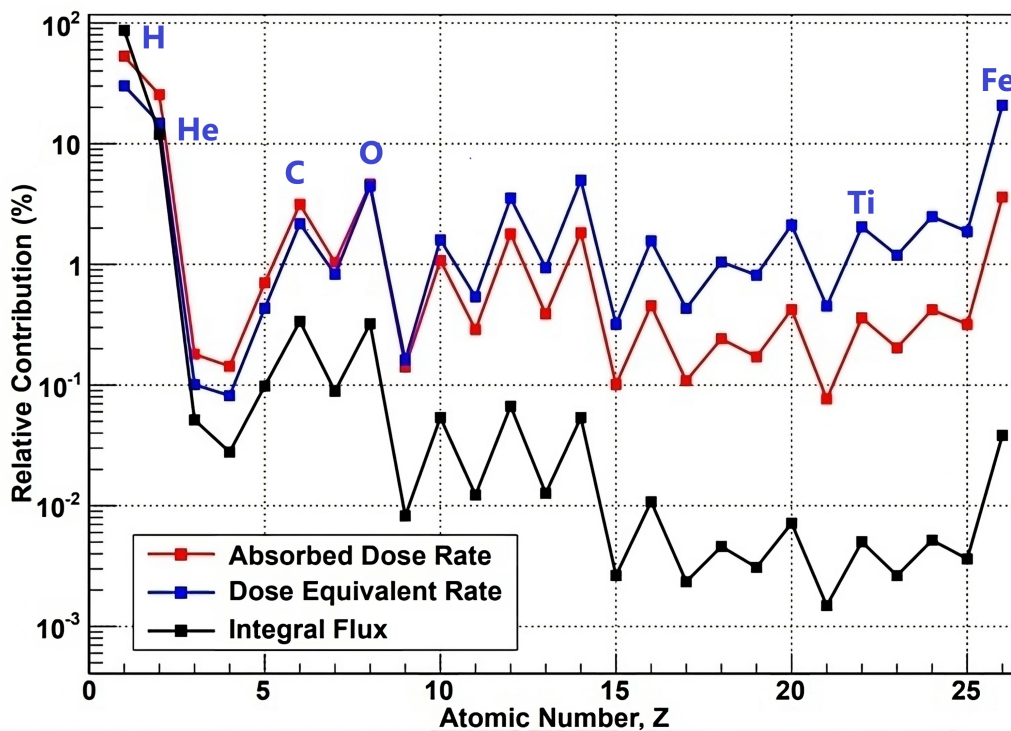


FIGURE 1.3: Relative contribution of GCR nuclei to total absorbed dose rate, dose equivalent rates, and flux integrated over energy (Benton and Benton, 2001; Reitz, 2008; Mrigakshi, 2013).

One of the primary concerns with **GCRs** is their potential to cause genetic damage and to increase the risk of cancer and other health problems in astronauts during long-duration

space missions. Unlike the solar wind, which can be shielded by the Earth's magnetic field, **GCRs** can penetrate deep into spacecraft and human tissue, making it difficult to protect astronauts from their harmful effects. Then, **GCRs** are an important part of the space environment that must be carefully considered when planning and executing human space exploration missions.

Energy Spectra of GCRs

The distribution of energies of particles in **GCRs** is referred to as their energy spectra. These high-energy particles have a wide range of energy levels, from a few million electron volts (MeV) to ultra-high-energy cosmic rays with over 10^{20} eV. Various methods such as ground-based detectors, balloon-borne detectors, and space-based instruments can be used to measure the energy spectra of **GCRs**. The energy spectrum of **GCRs** is expected to follow a power-law form for energies below the knee, where the knee denotes a deviation from the power-law distribution occurring at approximately 10^{15} eV (Hörandel, 2008; Amato, 2014). This transition marks a change in the power-law distribution behavior, and it is widely believed to signify a transition in the origin or acceleration mechanisms of cosmic rays. Specifically, it represents a shift from particles that are primarily accelerated by supernova remnants to those that are accelerated by alternative mechanisms. The energy spectra of **GCRs** exhibit another interesting feature known as the ankle, which is a bend in the power-law distribution that occurs at higher energies, around 10^{18} eV. The underlying cause of this phenomenon is not yet fully understood, but it is hypothesized to be related to the maximum energy that cosmic rays can achieve through their sources. Below the ankle energy, **GCRs** are believed to originate mostly from supernova explosions within the galaxy (Biermann and Sigl, 2001; Guo et al., 2021b). As **GCRs** travel towards the solar system, they encounter galactic magnetic fields which continuously deflect their path, resulting in a nearly isotropic flux in the solar system. While in the heliosphere, the intensity and composition of **GCRs** remain stable but are modulated by the varying heliospheric magnetic field during the solar cycle, as reported in studies such as (Cane et al., 1999; Guo et al., 2021b). **GCRs** within the inner heliosphere are comprised of around 2% of electrons, and 98% of atomic nuclei. **GCR** ions span from hydrogen to iron and beyond, encompassing a composition where approximately 87% are protons, 12% are helium nuclei, and the remaining 1% consists of heavier ions ($Z \geq 3$) (Simpson, 1983; Guo et al., 2021b).

In order to assess astronaut exposure associated with GCR exposure, models are used to describe relevant spectra of particles and energies appearing in deep space. These models are utilized to predict the GCR flux as a function of energy under different solar modulation conditions. The Badhwar-O'Neill (**BON**) model, which was used in our study was developed first in the 1990s (Badhwar and O'Neill, 1994; Badhwar and O'Neill, 1996; O'Neill, 2010). The **BON** model employs the spherically symmetric Fokker-Planck (**FP**) equation. The **FP** equation accounts for cosmic ray propagation in the heliosphere due to diffusion, convection, and adiabatic deceleration. The **BON** model provides the flux of **GCR** particles for a specific charge, Z , as a function of energy by solving the **FP** equation,

which is implemented in the **BON** model. The **BON** parameters are derived from measurements obtained through **NASA**'s Advanced Composition Explorer (**ACE**) and Cosmic Ray Isotope Spectrometer (**CRIS**) instruments. At ~ 100 Astronomical Unit (**AU**), **GCR** modulation is negligible and therefore a constant **GCR** field over space at that distance, referred to as the Local Interstellar Spectrum (**LIS**) is used as the boundary condition for the **BON** model. The **FP** equation then modifies the **LIS** to the desired radius from the Sun, assuming a steady-state heliosphere condition (O'Neill et al., 2015; Badhwar and O'Neill, 1996).

Figure 1.4 illustrates the differential **GCR** flux as a function of energy for protons, helium, oxygen, and iron ions as modeled by **BON** (Badhwar et al., 1994; O'Neill, 2010).

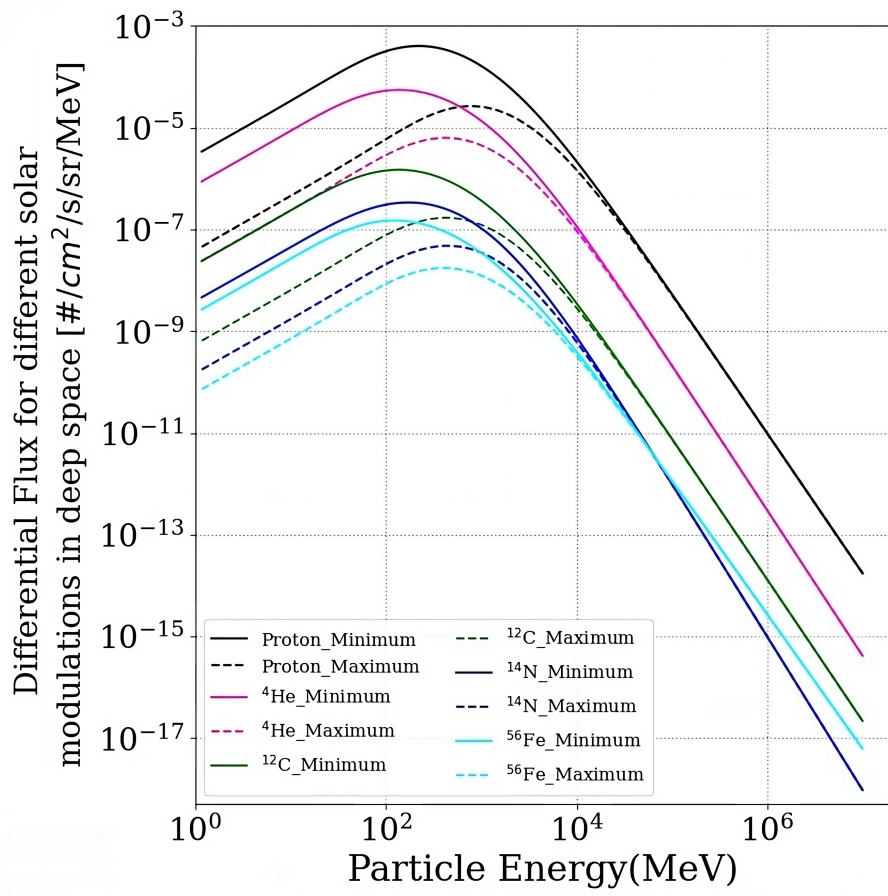


FIGURE 1.4: Differential flux of several **GCR** elemental species in the solar activity minimum and solar activity maximum conditions (Badhwar et al., 1994; Rojdev et al., 2015).

Solar Modulation

Solar modulation refers to the process through which the intensity and energy spectrum of cosmic rays are modified as they travel through space at nearly the speed of light and enter the solar system. The modulation of **GCRs** arise from several factors, including the influence of solar wind and the Interplanetary Magnetic Field (**IMF**) emitted by the Sun

(Usoskin et al., 2011; Shen et al., 2019; Badhwar and O'Neill, 1994). These elements change in accordance with the solar cycle, leading to fluctuations in the speed of particle transport mechanisms like diffusion, convection, adiabatic deceleration, and drifts. These solar influences cause changes in the properties of cosmic rays, including their intensity and distribution of energies (Potgieter, 2013; Gieseler, 2018). Solar modulation also refers to **GCR** variations with the ~ 11 year sunspot cycle and ~ 22 year solar magnetic cycle and is relevant to the space radiation environment and effects on Earth's atmosphere (Hale et al., 1919; Thomas et al., 2014; Ross and Chaplin, 2019). The solar modulation parameter (ϕ) also known as the solar modulation potential or the solar modulation index is a quantity that depends on several factors, including the Sun's magnetic field strength and polarity, the geometry of the heliospheric current sheet, and the solar wind speed and density (Usoskin et al., 2011; Bazilevskaya et al., 2014; Cholis et al., 2016). During periods of high solar activity, such as during the peak of the solar activity cycle, the Sun's magnetic field is stronger and more complex, which leads to a higher solar modulation parameter and a reduction in the flux of cosmic rays that reach the Earth's atmosphere. Conversely, during periods of low solar activity, such as during the solar activity minimum, the Sun's magnetic field is weaker and less structured, which leads to a lower solar modulation parameter and an increase in the flux of cosmic rays that reach the Earth's atmosphere (Bazilevskaya et al., 2014). Solar modulation is an important factor in the study of space weather and its effects on Earth's environment and technological systems (Gleeson and Axford, 1968; Rao, 1972). It is also important in astroparticle physics, as cosmic rays provide a unique window into the high-energy universe beyond the solar system.

1.4.2 SEPs in Interplanetary Space

The Sun stands as the source of **SEPs** within our solar system, encompassing a diverse range of particles such as electrons, protons, and ions with energies spanning from a few kilo-electron volts to several giga-electron volts. **SEPs** are high-energy particles that are accelerated by the strong electric and time-varying magnetic fields generated during solar eruptions, such as solar flares and **CMEs** (Pacheco Mateo, 2019; Guo et al., 2021b; Reames, 1995; Reames, 2013). Once **SEPs** are accelerated, they can travel through interplanetary space, and experience various physical processes that affect their properties. These include interactions with the solar wind plasma and magnetic field, scattering and diffusion, and acceleration by shocks and other plasma waves (Reames, 1995; Reames, 2013). One important aspect of **SEP** propagation in interplanetary space is their interaction with the **IMF**. The **IMF** is a complex and dynamic structure that is generated by the Sun's magnetic field and carried out with the solar wind. Flare- and shock-related mechanisms are prominent contenders for accelerating **SEPs** (Kouloumvakos et al., 2023). To observe **SEPs** in situ, their accelerated particles must reach spacecraft-linked magnetic field lines, regardless of the specific acceleration process (Rodriguez-Garcia et al., 2021; Vlahos et al., 2019). Rapid and expansive **CMEs** can generate potent shock waves in the corona and interplanetary

space, efficiently accelerating particles to high energies and dispersing them over vast distances from the eruption site. The diffusion of **SEPs** perpendicular to magnetic field lines or a combination of **CMEs**, shock waves, and **SEP** transport effects could contribute to the wide **SEP** distribution (Rodriguez-Garcia et al., 2021; Vlahos et al., 2019; Dalla et al., 2003; Kouloumvakos et al., 2023). The **SEPs** can then propagate more efficiently through interplanetary space and can reach the Earth's magnetosphere in a relatively short time (Guo et al., 2021b; Wijsen et al., 2019; Kahler, 1992). The properties of **SEPs** in interplanetary space can also be affected by the state of the solar activity cycle. When the Sun experiences high levels of solar activity, like during the peak of the solar activity cycle, can result in more efficient acceleration of **SEPs** and more intense **SEP** events. On the other hand, during periods of low solar activity, such as during the solar activity minimum, **SEPs** tend to occur less frequently and with lower intensity (Gopalswamy et al., 2020). In addition to their scientific interest, **SEPs** can also pose a significant hazard to astronauts and spacecraft in interplanetary space. The high-energy particles can cause radiation sickness, damage to electronics and other equipment, and even pose a risk to human life. Therefore, monitoring and forecasting of **SEPs** is an important aspect of space weather research and space mission planning. An **SEP** event can usually last between a few hours and a few days, and the flux of a **SEP** event can be orders of magnitude higher than **GCR** fluxes, especially at energies below a few hundreds of MeV.

Space-based observatories such as the Solar and Heliospheric Observatory (**SOHO**) (Domingo et al., 1995; Fleck, 2005) and the **ACE** (Stone et al., 1998), orbit the Sun-Earth interior libration point L1, while the Geostationary Operational Environmental Satellite (**GOES**) around the Earth are all located near 1 **AU** from the Sun. These observatories frequently provide simultaneous observations of **SEP** events, enabling valuable insights into the characteristics and behavior of these high-energy particles in different regions of the heliosphere. However, the information regarding the source of **SEP** events at the Sun is partially obscured due to the effects these particles experience during their journey through the inner heliosphere.

Figure 1.5 depicts the proton spectra integrated over each event duration of 50 **SEP** events reconstructed from measurements of **GOES** and **ACE** in the deep space environment near Earth from August 1997 to 2006 (Nymmik, 2015; Guo et al., 2021b; Khaksarighiri et al., 2021).

1.5 Interaction between Radiation and Matter

Radiation-matter interaction is a critical factor to consider for space missions, as space is filled with various forms of ionizing radiation that can pose risk to human health and the performance of electronic equipment. Radiation particles interact with matter as they move through it via electromagnetic and nuclear forces and create a wide range of secondary particles such as gamma radiation, electrons, muons, neutrons, pions and secondary protons, and heavy ions (Raphael et al., 2018; Messina et al., 1988). Neutrons and

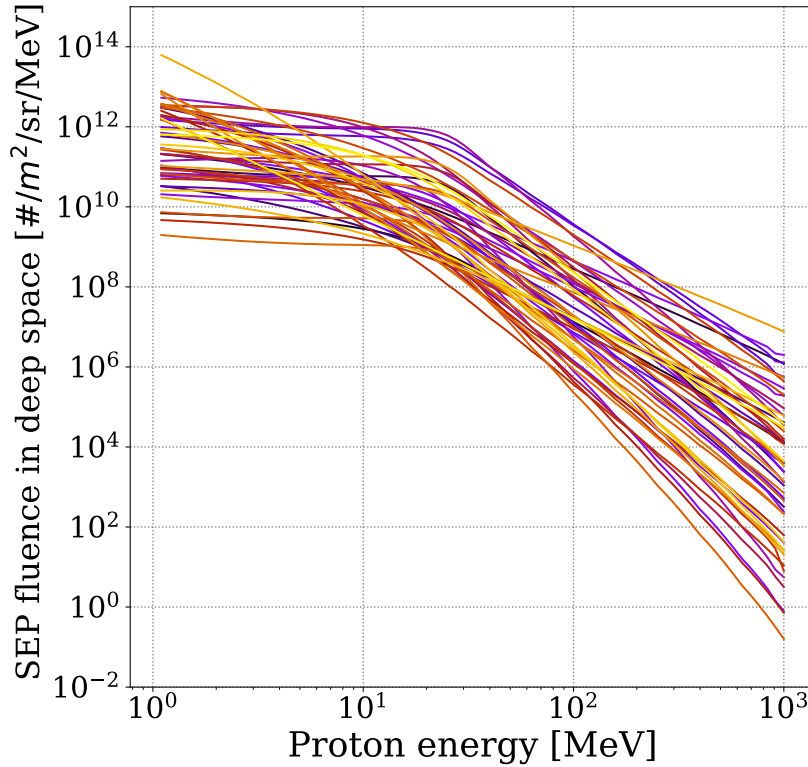


FIGURE 1.5: The proton fluence spectra of 50 large **SEP** events, integrated over each event duration, of events detected from August 1997 to 2006 near-Earth (Nymmik, 2015; Guo et al., 2021b; Khaksarighiri et al., 2021).

secondary ions hold particular significance in space applications due to their capacity to deposit substantial energy. Moreover, secondary neutrons, electrons, and photons play a crucial role in space radiation shielding, as they travel longer distances compared to heavier particles, resulting in energy deposition (Benton and Benton, 2001; Messina et al., 1988).

Here, we summarized some of the relevant radiation-matter interaction processes for space radiation for both charged particles and neutral particle interactions.

1.5.1 Charged Particle Interactions

For charged particles, whether they originate from the cosmic ray field, accelerators, or nuclear decays, the largest fraction of energy dissipated in matter is due to electromagnetic interactions between the Coulomb fields of the projectile and of the molecules, atoms, and solid-state bodies in the medium. As charged particles penetrate through matter, their own Coulomb field primarily interacts with the orbital electrons and then nuclei of any atoms they come across. In addition, strongly interacting particles like protons and alpha particles can also interact with nuclei through the short-range nuclear force (Lechner, 2018; Nikjoo et al., 2012). When charged particles interact with the orbital electrons of the absorber, they incur collision loss, leading to the loss of their energy, a significant portion

of which is transferred into ionization. Since the energy transfer from a charged particle to matter in each atomic interaction is generally minimal, the particle undergoes many interactions before expending its kinetic energy (Kamal, 2014; Sabol and Weng, 1995). The effects of these interactions, as described by the Bethe-Bloch equation (Section 1.5.1), vary depending on the properties of the particle and the target material. Understanding these variations is essential for accurately assessing the energy loss and ionization patterns of charged particles in different materials.

Ionization and Excitation

When high-energy particles such as cosmic rays and solar energetic particles interact with matter, they can lose energy primarily by ionizing and exciting atoms and molecules in the medium (Eidelman and Shwartz, 2021; Ahlen, 1980; Leroy and Rancoita, 2011). These processes occur when the high-energy particles transfer their energy to the atoms or molecules, leading to the ejection of electrons from the outer shell of an atom or molecule and resulting in the creation of secondary charged particles and photons, which can further interact with the medium and cause additional energy loss. The ionization process can occur in a variety of ways. High-energy particles collide with electrons in the target's outer shell, knocking them off and leaving behind a positively charged ion in one type of ionization process known as direct ionization (Ahlen, 1980; Leroy and Rancoita, 2011). In another type of ionization process, known as indirect ionization, high-energy particles first interact with molecules in the material, resulting in the formation of free radicals or other reactive species that can then go on to ionize other atoms or molecules. The degree of ionization depends on various factors, such as the energy and type of the incoming particles, and the density and composition of the matter (Ahlen, 1980; Grande and Schiwietz, 2004). In highly ionized environments, such as those found in space, the ionization process can have significant effects on the behavior of charged particles and electromagnetic fields. In the Earth's atmosphere, the ionization of the upper atmosphere by solar wind particles can lead to the creation of ionized plasma, which can interact with the Earth's magnetic field to create a variety of phenomena, such as auroras and magnetic storms (Richmond and Lu, 2000; Rees, 1995). The ionization process also plays a critical role in the operation of particle detectors used in space research, such as those used to detect cosmic rays and other high-energy particles. The ionization process plays a crucial role in the functionality of particle detectors utilized in space research. These detectors are designed to detect cosmic rays and other high-energy particles, including those detected by instruments like the **RAD**. Transferring energy to atoms and molecules in materials can cause the excitation of the electrons to higher energy states, which can result in the emission of secondary particles or photons and further interact with the material and cause additional energy loss. The excitation process is particularly relevant in space missions, where the exposure of spacecraft and their payloads to high-energy radiation is a significant concern (Stanev, 2004; Ahlen, 1980). The excitation of atoms and molecules in materials, such as electronic components, sensors, or detectors, can lead to the production of unwanted charge carriers

and for many instruments these kinds of interactions are an integral part of the measurement itself. Furthermore, the excitation process can cause radiation damage to biological tissue and the body of astronauts, making it a critical concern in the design and operation of space systems. The energy required for ionization can be calculated using the Bethe-Bloch equation, which relates the stopping power of the material to the energy and charge of the incoming particle (Ziegler, 1999; Leo, 1988; Leo, 2012).

Stopping Power and the Bethe–Bloch Energy Loss Expression

Stopping power is a crucial concept in radiation physics that describes the rate at which a charged particle loses energy while traversing a material. As introduced in the previous paragraph, this energy loss occurs as the charged particle interacts with the atoms or molecules in the material, transferring energy to the electrons through various interactions, including Coulomb scattering, ionization, and radiative losses (Lechner, 2018; Ahlen, 1980; Leroy and Rancoita, 2011).

The stopping power is determined by multiplying the probability per unit path length of a charged particle interacting with the material, often expressed in inverse length units as cm^{-1} , with the average energy loss per collision, typically expressed in units of energy, such as MeV. The resulting stopping power is usually measured in units of energy per length, such as MeV cm^{-1} (Sigmund, 1998; Busza and Goldhaber, 1984; Leroy and Rancoita, 2011). There are two main types of stopping power, namely collision stopping power and radiation stopping power (Saadi and Machrafi, 2020; Ahlen and Kinoshita, 1982). Collision stopping power, also known as electronic stopping power, refers to the energy loss that occurs due to interactions of charged particles with electrons in the material (Correa, 2018; Ahlen and Kinoshita, 1982). Radiation stopping power, on the other hand, occurs due to the emission of photons by the charged particle as it decelerates, a process known as Bremsstrahlung (Sigmund, 1998; Seltzer and Berger, 1982).

The total stopping power is the sum of the collision stopping power and radiation stopping power, and their relative contributions depend on various factors, including the energy and charge of the charged particle and the density and composition of the material (Busza and Goldhaber, 1984; Sigmund, 1998; Leroy and Rancoita, 2011).

The calculation of stopping power is vital in numerous applications, such as radiation dosimetry, radiation therapy, the design of radiation shielding, and the design of radiation detection instruments. The Bethe-Bloch equation is a theoretical model that relates the energy loss of charged particles to their velocity and the material properties they pass through and is often used to calculate stopping power (Leo, 1988; Leo, 2012; Morgan Jr and Eby, 1973). The Bethe-Bloch equation serves as an underlying principle not only in the operation of the **RAD** instrument but also in the functioning of any radiation detector for understanding the energy loss and ionization effects of charged particles.

$$-\frac{dE}{dx} = Kq^2 \frac{Z}{A} \frac{1}{\beta^2} \left[\frac{1}{2} \ln \frac{2m_e c^2 \beta^2 \gamma^2 T_{\max}}{I^2} - \beta^2 - \frac{\delta}{2} \right] \quad (1.1)$$

where,

$$K = 4\pi N_A r_e^2 m_e c^2$$

q : particle charge

Z : atomic number of material

A : atomic mass of material

N_A : Avogadro's number

m_e : electron mass

c : speed of light

r_e : classical electron radius

$$\beta = \frac{v}{c}$$

$$\gamma = \frac{1}{\sqrt{1 - \beta^2}}$$

T_{\max} : maximum energy transferable to an electron in a single collision

v : velocity of the particle

$$T_{\max} = \frac{2m_e c^2 \beta^2 \gamma^2}{1 + 2\gamma \frac{m_e}{m_0} + \left(\frac{m_e}{m_0}\right)^2}$$

I : mean excitation energy of material

m_0 : rest mass of the electron

δ : correction factor that depends on the velocity of the particle

The Bethe-Bloch equation relates the energy loss per unit distance of the particle to its velocity, the charge of the particle, and the properties of the material it is passing through. From the formula, it is clear that the stopping power is dependent on certain properties of the incident ion type, its energy, and also on the target material (Leo, 1988; Leo, 2012).

When particles have non-relativistic energy, their energy loss is dominated by the $1/\beta^2$ term in the equation. This term represents the Coulomb interactions between the charged particle and the electrons in the material, and it increases as the velocity and energy of the particle decrease. As a result, a characteristic maximum in the energy deposition with depth curve is observed at the end of their path in the medium, and this is known as the Bragg peak (Nahum, 2021; Swift and McNaney, 2009). The Bragg peak is an important feature of energy deposition patterns and has important applications in radiation therapy. It can be used to deliver radiation to a specific depth in tissue, while minimizing damage to surrounding healthy tissue. The location and sharpness of the Bragg peak depend on various factors, such as the energy and charge of the particle, the density and composition

of the material, and the width of the particle beam. Accurate modeling and measurement of the Bragg peak are important in the design and optimization of radiation treatment plans, as they can be used to deliver radiation to a specific depth in tissue while minimizing damage to surrounding healthy tissue (Byun et al., 2021; Zhang et al., 2021; Egami and Billinge, 2012). Experimental measurements of stopping power can also be carried out using various techniques such as transmission ionization chambers and solid-state detectors (Durrani and Bull, 2013; Powers, 1989).

Nuclear Interactions

Nuclear interactions between heavy ions and matter exhibit various forms, including elastic and inelastic scattering, fusion, and fragmentation. In the case of heavy ions with energies above 100 MeV/nucleon, inelastic nucleus-nucleus or nucleon-nucleus interactions become dominant due to the substantial momentum transfer involved (Hüfner, 1985). These interactions result in the formation of excited nuclear states or compound nuclei, which subsequently decay by emitting gamma rays, neutrons, and other particles (Hodgson, 1971; Tang, 1996). These processes are relevant in the case of the **RAD** and its operation on Mars, as high-energy particles, such as cosmic rays or solar energetic particles, interact with the Martian atmosphere and can undergo these interactions before reaching the detectors. The probability of inelastic interactions depends on factors such as the energy, nuclear charge, and mass of the projectile particles, as well as the nuclear structure of the target nucleus (Lechner, 2018; Scandale et al., 2010). The study of inelastic nucleus-nucleus or nucleon-nucleus interactions holds significance in comprehending nuclear properties and reactions under extreme conditions, including nuclear fusion and astrophysical environments. Additionally, it has practical applications in radiation therapy for cancer treatment, where heavy ion beams selectively damage tumor cells while minimizing harm to healthy tissue (Battistoni, 2016). In the context of space radiation, high-energy particles originating from cosmic rays and solar sources interact with matter through a range of processes. These include spallation, nuclear fragmentation, and nuclear reactions (Benton and Benton, 2001; Reedy and Arnold, 1972; Durante and Cucinotta, 2011). Understanding these processes is crucial for predicting the impact of space radiation on materials, electronic devices, and living organisms, as well as for developing radiation shielding and energy production technologies.

Spallation occurs when a high-energy particle collides with a nucleus, resulting in its fragmentation into smaller fragments and the release of energy and secondary particles such as neutrons and protons (Lechner, 2018; Goldhaber and Heckman, 1978) and all these processes are also relevant for particles that interacted with, for example, the Martian atmosphere, before they can reach the detector. Nuclear fragmentation, on the other hand, transpires when a high-energy nucleus collides with a target nucleus, causing it to break apart into multiple smaller fragments (Pietri et al., 2005).

1.5.2 Neutral Particle Interactions

A neutral particle, such as a neutron or photon, does not ionize materials through electromagnetic forces, unlike charged particles. Neutrons and photons can interact with atomic nuclei in several ways. Neutrons primarily engage with atomic nuclei through the strong nuclear force, while photons can indirectly ionize matter through various processes (Smith, 1988; Braibant, Giacomelli, et al., 2011; Park and Kang, 2011).

For neutrons, the most common interaction is elastic scattering, wherein the neutron transfers some of its kinetic energy to the nucleus, altering its direction. Inelastic scattering, on the other hand, occurs when the neutron is absorbed by the nucleus, exciting it to a higher energy state and resulting in the emission of gamma rays or other particles (Braibant, Giacomelli, et al., 2011; Park and Kang, 2011). Other possibilities include neutron capture, nonelastic reactions, and nuclear fission. The probability of these interactions depends on the energy of the incident neutron and the type of nuclide it interacts with. This probability, quantified by the cross-section, that measures a material's capability to capture neutrons of a specific energy, as illustrated in figure 1.6.

A cross-section is a measure of the effective area for a specific interaction to occur when particles collide. It quantifies the probability of a particular interaction taking place during particle collisions, providing a crucial parameter for understanding and predicting the outcomes of these interactions.

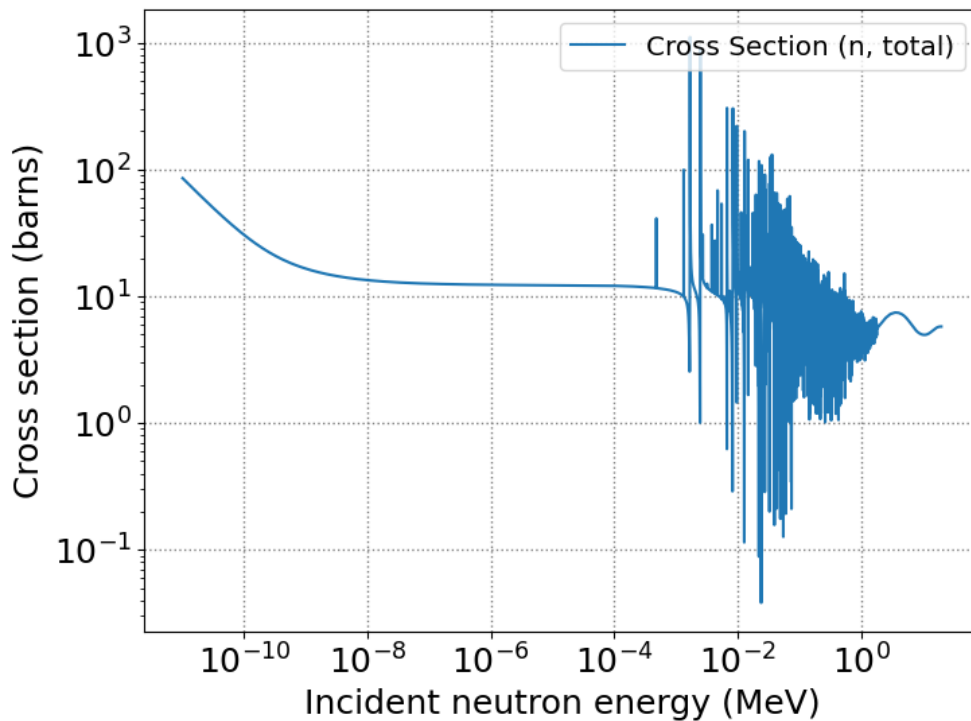


FIGURE 1.6: Total neutron cross sections of lead ($Z = 82$) at different neutron energies (Soppera et al., 2014).

For photons, the cross-section serves as a measure of the probability of interaction between incident photons and a material, involving processes such as photo-absorption or scattering, as depicted in figure 1.7. Among these interactions, Compton scattering is a prevalent occurrence where a photon collides with an electron, transferring a portion of its energy to the electron. This results in the electron recoiling, causing the photon to change direction (Podgorsak et al., 2003; Ragheb, 2011). Another significant interaction is the photoelectric effect, where a photon is entirely absorbed by an atom, leading to the ejection of an electron from its shell and subsequent ionization (Podgorsak et al., 2003; Ragheb, 2011). For high-energy photons, pair production becomes possible, where the photon transforms into an electron-positron pair in the presence of a nucleus. These produced particles can subsequently ionize the material or interact with other nuclei, potentially leading to the creation of secondary particles. The interactions of neutral particles with matter hold substantial significance across various fields, including nuclear physics, radiation protection, medical imaging, and space missions (Podgorsak et al., 2003; Ragheb, 2011).

Whereas photon cross-sections are proportional to the power of the atomic number of the target atom, neutron cross-sections vary between materials but do not have any clear identifiable rules.

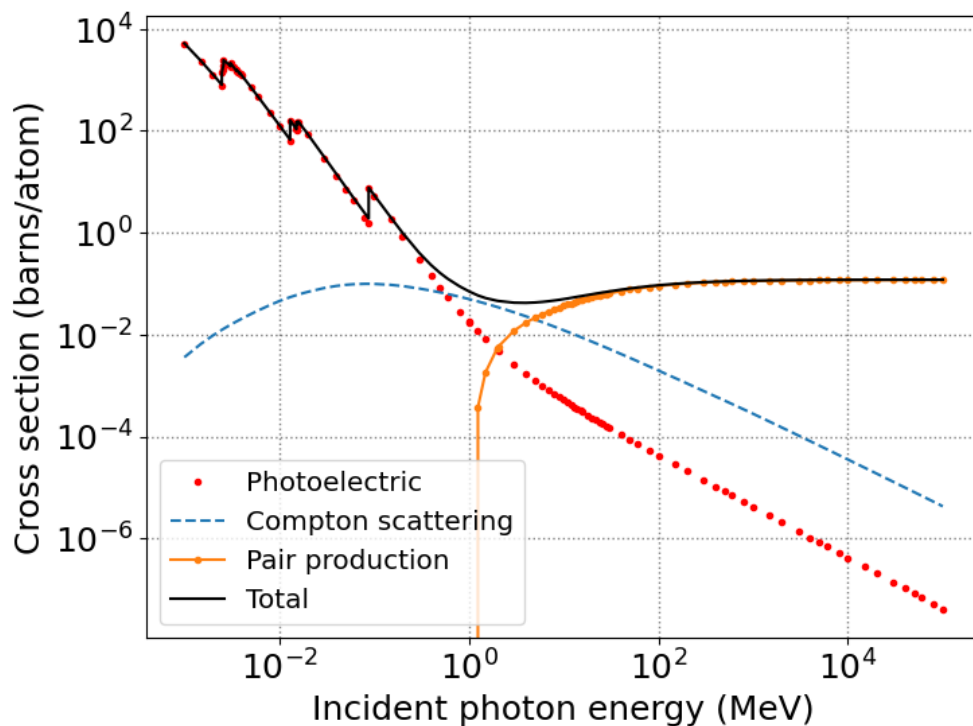


FIGURE 1.7: Photon cross section as function of the energy in lead ($Z = 82$) showing the contributions of the different processes (Berger, 1998).

1.6 Dosimetric Concepts

Dosimetric concepts in space are essential for investigating and quantifying radiation doses that astronauts receive during spaceflight. The significance of radiation exposure as a critical occupational hazard for astronauts arises from the diverse array of ionizing radiation sources they encounter during their space missions. Prominent among these sources are **GCRs** and **SEPs** (ICRU, 1962), both of which are substantial contributors to ionizing radiation in space. These varied radiation sources necessitate a comprehensive understanding of dosimetric concepts to ensure the safety and well-being of astronauts during their missions.

In order to protect individuals exposed to ionizing radiation, several advisory organizations were established in the 1920s, including the International Commission on Radiation Units and Measurements (**ICRU**) (Sinclair, 1981; Menzel, 2014), the International Commission on Radiological Protection (**ICRP**) worldwide (Sinclair, 1981; Harrison et al., 2021; Cousins et al., 2011), and the National Council on Radiation Protection and Measurements (**NCRP**) in the USA (Sinclair, 1981; Taylor, 1958; Kase, 2004). These organizations offer guidelines and recommendations for radiation protection and dose assessment, not only for space missions but also for other applications involving ionizing radiation (Taylor and Wyckoff, 1972; Hendee, 1993).

The **ICRP** and **ICRU** have set radiation exposure limits for astronauts and other space-flight crew members during missions. While the **ICRU** focuses on unit and measurement standards and provides guidance on how to calculate radiation doses for various forms of radiation in space, the **ICRP** addresses radiological protection. The **ICRP** sets specific dose limits for different groups, such as the 20 millisieverts per year limit for occupational exposure to ionizing radiation (McKenna-Lawlor et al., 2014; Walsh et al., 2019; Davies, 1993). Similarly, the **NCRP** provides recommendations on radiation protection and dose estimation for both general population and occupational exposure. The **NCRP** has published reports and recommendations on radiation protection for astronauts, including dose limits and exposure scenarios (Cucinotta et al., 2021). Other groups like **NASA** and the United Nations Scientific Committee on the Effects of Atomic Radiation (**UNSCEAR**) also provide instructions and recommendations for radiation protection and dose assessment for space missions (Boice Jr, 2017; Setlow, 1999). These agencies are essential for ensuring the safety of individuals exposed to ionizing radiation, including astronauts. Their recommendations and suggestions are based on extensive scientific research and aim to mitigate the dangers of ionizing radiation exposure in space and other environments.

1.7 Dose Quantities

Dose quantities refer to various measurements that are used to express the amount of radiation absorbed by an object or individual. In the following sections, we will discuss some of these quantities, drawing from the **ICRP** publications (Petoussi-Henss et al., 2020).

1.7.1 Absorbed Dose

Absorbed dose is a fundamental concept in radiation physics that measures the amount of energy deposited by ionizing radiation in a material per unit mass. Mathematically, absorbed dose, D , is defined as the ratio of the mean energy, $d\bar{\epsilon}$, imparted by ionizing radiation in a small volume element, to the mass, dm , of the matter within that volume (Carlsson, 1981; Cloutier, 1981; Petoussi-Henss et al., 2020; Breckow, 1993):

$$D = \frac{d\bar{\epsilon}}{dm} \quad (1.2)$$

The unit for absorbed dose is the gray (Gy), defined as the absorption of one joule of energy per kilogram of material. For the purpose of radiation protection, it is essential to determine the mean absorbed dose. This is defined as the total absorbed dose divided by the mass of the exposed tissue or organ. The mean absorbed dose, denoted by \bar{D} , is a crucial quantity for assessing the potential biological effects of radiation exposure. The magnitude of biological effects depends on the radiation's type, energy, dose rate, and sensitivity of the exposed tissue or organ. By measuring the mean absorbed dose, it is possible to estimate the risks associated with radiation exposure and take appropriate measures to protect against those risks (Harrison et al., 2021; Petoussi-Henss et al., 2020).

1.7.2 Equivalent Dose and Relative Biological Effectiveness (RBE)

The equivalent dose, H_T , in a specific organ or tissue T , is defined based on the average absorbed dose, $D_{T,R}$, resulting from radiation of type R in that volume. The radiation types R are determined by the type and energy of radiation, whether it is external radiation incident on the body or radiation emitted by radionuclides present within the body. Equivalent dose is an intermediate step in the calculation of effective dose. The definition of equivalent dose in an organ or tissue is given by the equation (Harrison et al., 2021; Petoussi-Henss et al., 2020; Cucinotta et al., 2003; Dietze and Menzel, 2004):

$$H_T = \sum_R w_R \times D_{T,R} \quad (1.3)$$

where w_R is the radiation weighting factor for radiation type R . The \sum is performed over all types of radiations involved. The unit of equivalent dose is the sievert (Sv), where, $1 \text{ Sv} = 1 \text{ J kg}^{-1}$ in the SI base units (Harrison et al., 2021; Petoussi-Henss et al., 2020).

The values of w_R account for the Relative Biological Effectiveness (RBE) of different types of radiation. These factors have been derived based on measurements of the RBE of various radiations for a range of biological endpoints associated with stochastic effects, which

are measures or observations of biological responses in living organisms that occur randomly with a probability that increases with radiation dose (Harrison et al., 2021; Petoussi-Henss et al., 2020). **RBE** is a radiobiology concept used to assess and compare the effectiveness of various radiation types in inducing biological damage. It measures the ability of a specific radiation type to produce a particular biological effect in relation to a standard radiation, typically X-rays or gamma rays. The **RBE** value is determined by comparing how much damage or destruction the reference radiation and the tested radiation cause to cells or tissues. **RBE** values can vary based on several parameters such as dose, dose rate, cell type, cell-cycle phase, sample volume, sample depth, and microenvironment (Paterson et al., 2022).

1.7.3 Effective Dose

Effective dose is a radiation protection quantity that takes into account the different types of radiation and their biological effectiveness in different tissues and organs of the human body. It is used to estimate the overall risk of radiation exposure to an individual and is expressed in Sv or rem.

To calculate the effective dose, first, the equivalent dose in each organ or tissue is determined by multiplying the absorbed dose in that organ or tissue by its radiation weighting factor (w_R), which accounts for the different biological effects of different types of radiation. The equivalent doses in all the organs and tissues are then summed together, weighted according to their respective tissue weighting factors (w_T), which reflect the relative importance of each organ or tissue in the overall health risk (Harrison et al., 2021; Petoussi-Henss et al., 2020; Hidajat et al., 1999; Guo et al., 2021b).

The effective dose (E) can be calculated using the following equation:

$$E = \sum_T w_T \times \sum_R w_R \times D_{T,R} = \sum_T w_T \times H_T \quad (1.4)$$

where w_T is the tissue weighting factor for tissue T and $\sum w_T$ concerning all tissues is equal to 1. D is absorbed dose, and H is equivalent dose. The process of averaging is applied to all organs and tissues in the human body for which specific radiation detriment values have been calculated, along with specified tissue weighting factors. Mathematically, the effective dose represents a weighted average of equivalent doses assigned to organs and tissues. The selection of w_T values aims to represent the contributions of individual organs and tissues towards the overall radiation detriment from stochastic effects, considering all ages and both sexes.

Effective dose is an important quantity for radiation protection because it allows for a comparison of the overall risk of different types of radiation exposure and dose constraints, reference levels, and limits concerning stochastic health effects are established in terms of

effective dose. It also helps to evaluate the effectiveness of radiation protection measures and in determining the risks associated with medical imaging procedures.

1.7.4 Linear Energy Transfer (LET) and Quality Factor

Linear Energy Transfer (**LET**) is a fundamental concept in radiation dosimetry that quantifies the amount of energy transferred by ionizing radiation to a material per unit length. It specifically refers to the average energy deposited by a charged particle along its track as it travels through the material. **LET** is commonly expressed in units of kiloelectronvolts per micrometer ($\text{keV}/\mu\text{m}$) (Harrison et al., 2021; Cucinotta et al., 2003; Dietze and Menzel, 2004; Guo et al., 2021b):

$$LET = \frac{dE}{dl} \quad (1.5)$$

LET is an essential factor in radiation protection, as it affects the biological effectiveness of ionizing radiation. High **LET** radiation is more effective at inducing biological damage than low **LET** radiation. The quality factor (Q) is a parameter used in radiation protection to account for the difference in biological effectiveness between different types of ionizing radiation.

The quality factor is a dimensionless factor that reflects the **RBE** of different types of ionizing radiation. The **RBE** is the ratio of the biological effect of a given dose of radiation to the biological effect of an equal dose of reference radiation (usually X-rays or gamma rays). Q is typically given by a function $Q(L)$, where L is the **LET** of the radiation in water, measured in units of $\text{keV}/\mu\text{m}$ (Valentin, 2003; Kerr, 1988).

At a point in tissue, the quality factor is given by the integral:

$$Q = \frac{1}{D} \int_0^{\infty} Q(L) D_L dL \quad (1.6)$$

where D represents the absorbed dose at that point, D_L is the distribution of absorbed dose in unrestricted **LET**, where "unrestricted **LET**" refers to the entire range of **LET** values for a given type of radiation at a specific point in tissue denoted by L , and $Q(L)$ is the quality factor as a function of L .

The integration is performed over D_L , which represents the dose contributed by charged particles (excluding their secondary electrons). $Q(L)$ is defined as a function of the unrestricted linear energy transfer, L_{∞} (often denoted as L or **LET**), of charged particles in water according to **ICRP** (ICRP, 1991; Wrixon, 2008):

$$Q(L) = \begin{cases} 1, & \text{if } L < 10 \text{ keV}/\mu\text{m} \\ 0.32L - 2.2, & \text{if } 10 \text{ keV}/\mu\text{m} \leq L \leq 100 \text{ keV}/\mu\text{m} \\ 300L^{-\frac{1}{2}}, & \text{if } L > 100 \text{ keV}/\mu\text{m} \end{cases} \quad (1.7)$$

Due to the unique and varied characteristics of the radiations present in space, particularly the significant high-**LET** component, a more accurate analytical expression for the quality factor, known as QF_{NASA} , has been developed specifically for space radiation. This factor has been incorporated into **NASA**'s risk projection model for estimating radiation-induced cancer mortality (Cucinotta et al., 2013; Goodhead, 2018; Cucinotta, 2015).

The quality factor employed by **NASA** encompasses more than just the **LET** of particles. It incorporates additional factors such as the atomic number (Z) and velocity (β) of the particles. These factors are combined using the track-structure parameter Z^2/β^2 (Cucinotta et al., 2013; Goodhead, 2018). In other words, **NASA**'s quality factor considers not only the energy deposited by the particles but also the influence of their atomic composition and speed. This comprehensive approach provides a more accurate assessment of the biological effects of radiation, acknowledging that different particles with varying properties can have distinct impacts on living tissues. **NASA** has also established limits on the dose equivalent for astronauts on space missions, and they take into account the different types of ionizing radiation encountered in space. For example, high-energy protons have a higher **LET** and therefore a higher **RBE** than low-energy protons or photons (Cucinotta et al., 2013; Goodhead, 2018; Papadopoulos et al., 2023; Cucinotta, 2015).

Chapter 2

Literature Review: In View of Humans in Space

This chapter presents a comprehensive literature review from the human space exploration perspective. First, we provide an overview of the types of radiation that astronauts can expect to encounter during deep space voyages and on the surface of Mars, with a specific focus on **GCRs** and **SEPs**, which constitute the main focal points of the thesis. Subsequently, the radiation exposure experienced by astronauts and the associated health risks during a mission to Mars is studied. Furthermore, the chapter delves into a detailed description of the potential effects induced by ionizing radiation on normal tissues, encompassing both acute and late effects. These findings are derived from data obtained from astronauts and spaceflight crews, as well as from ground-based experiments and simulation-based studies. Besides, we provide a thorough review of studies employing animal models to explore the behavioral effects induced by different charged particles.

2.1 Radiation Relevant for a Mars Mission

Radiation exposure poses a significant challenge to human missions to Mars, both during transit and on the planet's surface. During the transit phase, astronauts face exposure to **GCRs** and **SEPs**, which comprise highly energetic charged particles, mainly protons, and alpha particles, that originate from outside the solar system (Guo et al., 2021b; McGill et al., 2016; Cucinotta, 2015). As previously noted, **GCRs** have the ability to penetrate deeply into the human body, resulting in cellular and **DNA** damage. This damage is particularly pronounced during periods of solar minimum when the intensity of **GCRs** reaches its peak. Moreover, **SEPs**, elaborated upon in Section (1.4.2), can also cause a sudden increase in radiation exposure (Guo et al., 2021b; Hellweg et al., 2007; Cucinotta, 2015).

Radiation in deep space is nearly isotropic most of the time, i.e., it comes from the full 4π solid angle (Khaksarighiri et al., 2023; Zeitlin et al., 2019). Upon arrival on the Martian surface, additional radiation challenges arise due to Mars' lack of a global intrinsic magnetic field and only a thin atmosphere of about 2% of the columns depths on Earth (Guo et al., 2021b). The thin Martian atmosphere is not sufficient to stop a significant fraction of

GCRs, although it stops a large share of **SEPs** in typical events. Primary **GCRs** and **SEPs** can interact with the Martian atmosphere, producing secondaries that make the surface radiation field different from that in space. The planet itself provides excellent shielding against energetic particle radiation that would come from the bottom half of the full solid angle. There is, however, a small portion of the radiation that is directed upwards (Appel et al., 2018). The **GCRs** and **SEPs** interact with the atomic nuclei in the regolith (soil) on the Martian surface and produce secondary particles via spallation and fragmentation processes, which we refer to as secondary albedo. Guo, Khaksarighiri, et al. (2021) estimated that the albedo radiation, measured as an absorbed dose by **RAD**, on flat terrain is about 19% of the total surface dose. I.e., most of the radiation detected on the Martian surface is due to downward-directed particles. The secondary particles can be scattered back into space or reflected towards the planet and further interact with the Martian surface material during their propagation, which result in very complex spectra of both primary and secondary particle radiation (Guo et al., 2021b; Zhang et al., 2022; Guo, Khaksarighiri, et al., 2021). Secondary neutrons are of considerable concern because they do not undergo ionization directly due to their lack of an electric charge. As a result, they can easily penetrate through matter, especially in the "fast" energy range on the order of MeV, where their biological weighting factors are significant (Guo et al., 2021b; Zhang et al., 2022; Zeitlin, 2021). A comparison between the radiation in deep space and on the surface of Mars is shown in figure 2.1.

While the radiation in deep space is nearly isotropic, its angular distribution is modified as it travels through the Martian atmosphere to reach the surface. Particles coming through the atmosphere from the horizon need to pass through a much larger atmospheric column depth than particles coming from the vertical direction. The atmospheric column depth that a particle must traverse to reach the surface increases with zenith angle θ .

Several instruments with radiation detectors have been deployed in Mars orbit, while only **RAD** has been placed on Mars to assess its radiation environment. Mars Odyssey, launched in 2001, carried the Mars Radiation Environment Experiment (**MARIE**) and the High-Energy Neutron Detector (**HEND**) to measure radiation levels in Mars' orbit (Saunders et al., 2004; Desai and Knocke, 2007; Mase, 2005; Badhwar, 2004). The **RAD**, which is described in more detail in Section 3, is a scientific instrument designed to detect and analyze energetic particle radiation during the cruise to Mars and on the Martian surface. It was developed as part of the **MSL** and carried on board the Curiosity rover, which landed on Mars in 2012. **RAD**'s main scientific goals are to measure energetic particle spectra at the surface of Mars, determine dose and dose equivalent rates for human explorers on Mars, and validate Mars atmospheric transmission models and radiation transport codes (Hassler et al., 2012). The data collected by **RAD** is utilized to evaluate radiation risks for deep space and planetary missions, including future human exploration of Mars. The instrument has provided valuable data on the radiation environment on Mars, which can contribute to inform the design of future missions to the planet (Hassler et al., 2012; Guo et al., 2021b; Zeitlin et al., 2016). Till now, the **MSL** Curiosity rover has traveled more than

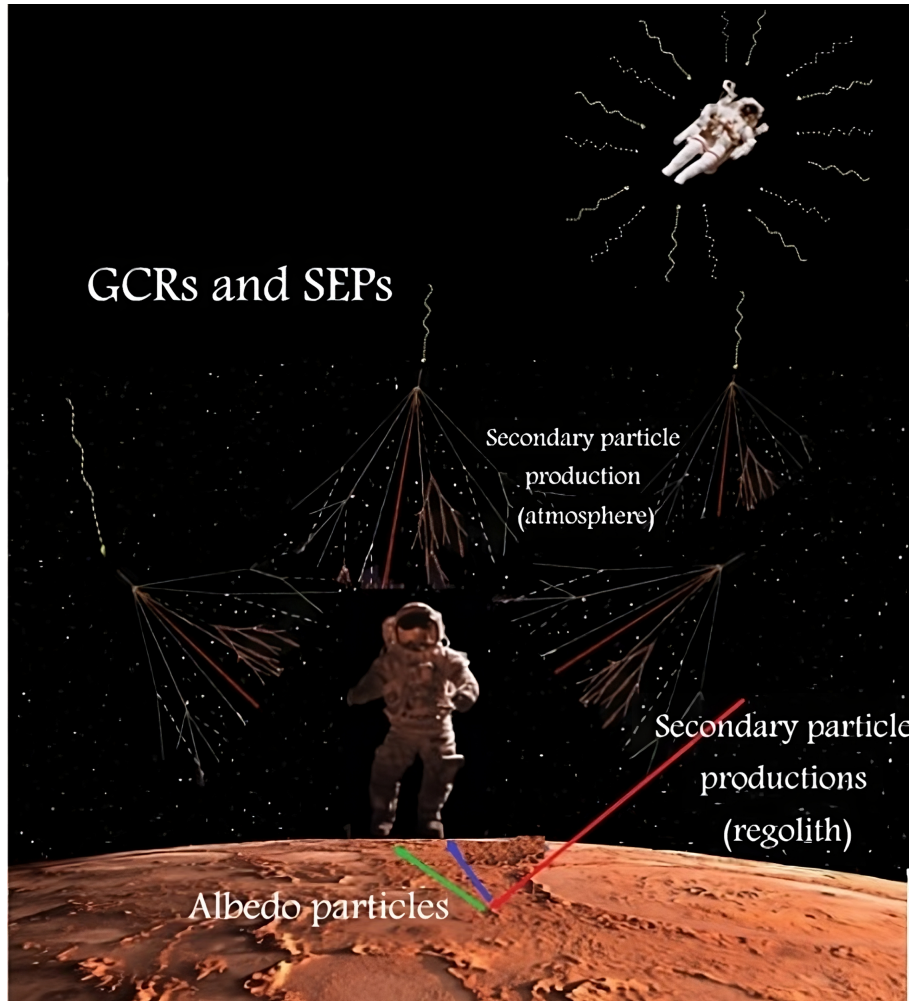


FIGURE 2.1: The radiation environment in deep space and Martian surface. The background image is captured and modified from Sofocleous (2019), the astronaut image is taken from gravity (2022), and cosmic rays from outer space is taken from Physicsisphun (2022).

29 kilometers on the surface of Mars. As Curiosity moves across the surface, its inclination with respect to the surface of an idealized, spherical Mars changes due to local topography. Wimmer-Schweingruber et al. (2015) used these variations to study the radiation shielding effect of the atmosphere and found that the radiation field is close to isotropic with a slight increase of shielding toward larger zenith angles. That study was limited to a maximum rover tilt angle of $\lesssim 15^\circ$. Figure 2.2 shows the components of GCR and SEP radiation effects on the surface of Mars.

2.2 Radiation Exposure for Astronauts on a Mission to Mars

Astronauts during space missions face significant health risks due to exposure to space radiation, including acute radiation syndromes, degenerative tissue risks, and the risk of

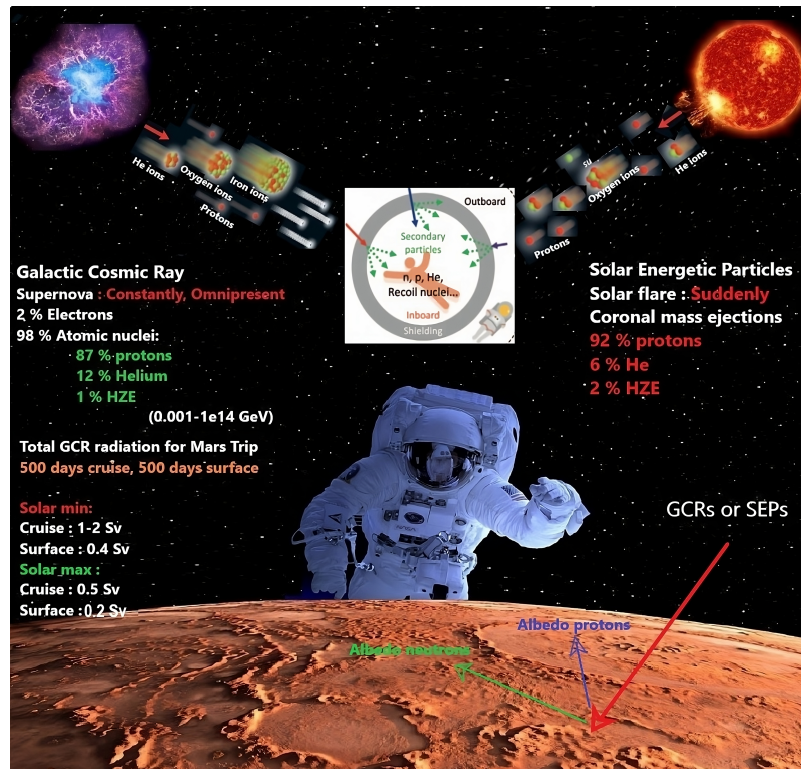


FIGURE 2.2: Components of the space radiation environment. The background image and astronaut image depicted were sourced from the same reference as figure 1.1.

radiation carcinogenesis. **NASA** has recognized these risks and developed an Integrated Research Plan to address them. To ensure the safety and well-being of astronauts, it is crucial to continue researching and developing effective mitigation strategies, particularly for long-duration space missions (Cucinotta and Durante, 2009; Cucinotta et al., 2009; Wu et al., 2009).

Space radiation exposure can immediately impact the success of a mission or result in late radiation effects for individual astronauts. Major **SEPs** typically contain high-energy particles, including **HZE** particles, and deliver highly variable doses to tissues. Radiation exposure during space missions can induce Acute Radiation Sickness (**ARS**), cutaneous injury, and other biological effects, depending on the dose, dose rate, radiation quality, and individual radiation sensitivity (Wu et al., 2009; Hu, Barzilla, et al., 2020). While avoidance of radiation risk is the best protective strategy, complete avoidance is nearly impossible, making countermeasures against adverse biological effects necessary for the success of long-term space missions (Hellweg et al., 2007; Kennedy, 2014). **ARS** is a complex of symptoms that occurs after a short and intense exposure to ionizing radiation, such as might occur during an **SEP** event. The severity of **ARS** depends on the radiation dose, the type of radiation, and the duration of exposure. The symptoms of **ARS** are typically divided into three stages: the prodromal stage, the latent stage, and the manifest illness stage. The prodromal stage occurs within hours to days after exposure and is characterized by nonspecific symptoms such as nausea, vomiting, and diarrhea. This stage is

followed by a latent stage, which can last for several days to weeks, during which time the individual may appear to have recovered. Finally, the manifest illness stage occurs, during which time the individual experiences more severe symptoms such as fever, dehydration, and damage to the immune system. If the radiation dose is high enough, death can occur within days to weeks after exposure (Heslet et al., 2012; Donnelly et al., 2010; Young, 1987). Late effects of ionizing radiation exposure in the space radiation environment are those that occur after a long period of continuous exposure to **GCRs**, as elaborated in Section (1.4.1). The risk of late effects from **GCR** exposure depends on a variety of factors, including the radiation dose, the type of radiation, the length of exposure, and the individual's age and overall health. In addition, the risk of exposure to **GCR** can vary depending on the **IMF**, as the **IMF** plays a crucial role in modulating the **GCR** flux, thus affecting the intensity and energy of cosmic rays reaching our solar system and Earth's atmosphere (Cucinotta et al., 2001; Boerma et al., 2015; Cucinotta et al., 2015).

NASA's primary focus lies in addressing the health risks associated with **GCRs** and **SEPs** radiation to astronauts because these types of radiation present significant challenges and potential hazards during space missions. **SEPs** have the potential to deliver tissue dose rates and doses ranging from 0 to 0.5 Gy/hour and 0 to 2 Gy, respectively, and skin doses greater than 5 Gy (Hu et al., 2009). Although the possibility of acute risks during internal vehicle operations is minimal, there exist scenarios during external vehicle activities such as lunar, trans-lunar, or Mars missions where **ARS** may occur (Kennedy, 2014). Proton radiation, the major type of radiation in an **SEP** event, may induce abnormalities in leukocytes, erythrocytes, and platelets, potentially compromising immune function in the microgravity environment of space (Kennedy, 2014; Hu et al., 2009).

Chronic exposure to the **GCR** radiation environment does not pose an immediate threat to astronauts' lives but increases the probability of long-term consequences, such as cancer development, cataracts, damage to the **CNS**, and hereditary effects. In addition, intense **SEP** events can contribute to deterministic effects, which manifest above a certain threshold and escalate with increasing exposure (Lobascio et al., 2018; Guo et al., 2021b). The **ICRP** divided radiation effects into stochastic effects and deterministic effects. For stochastic effects, limits are established to ensure that the risk of exposure-induced death from fatal cancer remains below 3% for career exposure (Cucinotta, 2010). The risk estimation is based on ground-based occupational experience. Deterministic effects, characterized by a direct cause-and-effect relationship between the level of radiation exposure and the severity of biological damage, become more pronounced as the radiation dose increases. These effects often have a threshold below which they do not occur (Kamiya et al., 2015).

Space radiation exposure has been shown to pose significant risks to the **CNS**, increasing the risk of developing Alzheimer's disease and attention deficits, among other risks (Cucinotta et al., 2014). Countermeasures for space radiation-induced adverse biological effects on the **CNS** include melatonin, lipoic acid, fruit extracts, and flavonoid glycosides from Ginkgo biloba (Kennedy, 2014; Manda, Ueno, and Anzai, 2007; Wotring and Wotring, 2012; Joseph et al., 1998).

It is clear that space radiation poses a significant risk to astronaut health, particularly in regards to the **CNS** and degenerative tissue risks such as cataracts. NASA has set a Space-Permissible Exposure Limit (**SPEL**) for short-term radiation exposure of **CNS** at 0.5 Gy in 30 days, but modeling has shown that some **SEP** events could exceed this limit inside the brain (Cucinotta, 2010). Radiation-induced cataracts are a long-term effect that may develop at a delayed stage, and exposure to large **SEP** events without sufficient protection could reach the proposed radiation cataract threshold of 0.5 Gy/year in a short time (Horneck et al., 2006; Guo et al., 2021b). Therefore, continued research and the implementation of effective mitigation strategies are of utmost importance to ensure the safety of astronauts during extended space missions.

Mitigation strategies encompass various measures such as the design of spacecraft and habitats with adequate shielding, appropriate limits on exposure time, and use of protective gear during extravehicular activities (Wilson et al., 2004; Horneck et al., 2003). Mathematical models have proven to be valuable tools for describing the correlation between radiation dosage and its biological effects in humans, in vitro cell cultures, and in vivo animal models. These models play a crucial role in predicting the clinical and subclinical outcomes of radiation exposure during space missions. However, there remains a notable gap in the field of space radiation effects studies and models, underscoring the need for measures to enhance their accuracy. To address this, these models should undergo validation by comparing their predictions with data from actual space missions and ground-based experiments capable of replicating space radiation exposure conditions. Within these experimental frameworks, the utilization of clinical diagnostic or radiotherapeutic devices can effectively reproduce the radiation type and dosage encountered in space, facilitating a comprehensive analysis of their impact on biological systems (Shibamoto et al., 2012; Ribba et al., 2006; Kim et al., 2015).

2.3 Spaceflight and Ground-based Models of Radiation Effects

Here, we describe various potential effects of ionizing radiation on normal tissues. These effects encompass both acute and late effects, based on data obtained from astronauts, ground-based experiments, and simulation-based studies.

After Aldrin reported flashes of light without real light on Apollo 11, several investigations were conducted on the measurements in space by astronauts on Skylab in 1974 (Pinsky et al., 1975) and on the Apollo-Soyuz Test Project (Page et al., 1977) and later on the Russian Mir space station, and the **ISS** (Narici, 2008). During the space measurements, a new detector called Apollo Light Flash Moving Emulsion Detector (**ALFMED**) was developed and deployed to link Light Flash (**LF**) perceptions with specific ions traveling through the eyes. The **ALFMED** detector provided the initial identification of two ions, which were

found to be heavier than oxygen, as the cause of **LF** perception (Pinsky et al., 1974; Osborne et al., 1975; Narici, 2008). To address this issue on the ground, a series of controlled experiments in accelerators were performed where subjects aligned their eyes or brains to the beamline and described their perceptions of the ions passing by. In 1972, experiments using high-energy nitrogen at Princeton-Penn Particle Accelerator and Lawrence Berkeley Laboratory (Budinger, 1972) revealed that energetic and charged particles passing through the occipital cortex or the retina cause light flashes in closed eyes. Initially, the source of these flashes was unclear, but it has been suggested that this phenomenon can have several causes. Some of these potential causes include Cherenkov radiation in the vitreous and direct excitation of the retina via ionization (Fazio et al., 1970; Osborne et al., 1975), indirect effects from protons released by neutrons or from alpha-particles generated by reactions with carbon, oxygen or nitrogen atoms, and scintillation in the eye lens (Fremlin, 1970; Budinger et al., 1971; McAulay, 1971; Avdeev et al., 2002). However, experiments involving helium and nitrogen beams have suggested that the effect is localized in the outer segments of rods and cones, possibly due to local energy deposition, as dark adaptation is required to observe the **LFs** (Budinger et al., 1972; Avdeev et al., 2002). Researchers have also suspected that secondary particles generated by the interaction of high-energy particles with metallic materials in the spacecraft, with a **LET** greater than $5\text{--}10\text{ keV}/\mu\text{m}$, have been linked to causing eye flashes (Budinger et al., 1972; Strigari et al., 2021). Researches conducted on the Mir space station has shown that the possibility of experiencing eye flashes increases with **LET**, reaching approximately 5% at around $50\text{ keV}/\mu\text{m}$ (Avdeev et al., 2002; Strigari et al., 2021).

Studies have also revealed that space radiation can cause genetic damage that alters the differentiation of lens epithelial cells, which can increase the possibility of developing cataracts (Cucinotta et al., 2001). These experiments did not observe any light sensations when the beams passed through the optical nerve or the visual cortex of the brain (Avdeev et al., 2002). Radiogenic cataracts were initially believed to be a deterministic effect with a threshold (Rehani et al., 2011). However, recent research has indicated that radiogenic cataracts are caused by genetic damage that leads to aberrant cellular differentiation of lens epithelial cells and may exhibit a linear dose-response relationship without a threshold (Strigari et al., 2021; Hamada and Sato, 2016). The first documented instances of radiogenic cataracts occurred in animal experiments in 1897 and a human radiation cataract in an x-ray laboratory worker (Chalupecky, 1897; Kleiman, 2012). The significance of shielding the lens against radiation exposure gained considerable recognition after the publication of two scientific papers in 1949, with the first study examining cataracts caused by atomic bomb (A-bomb) radiation, the second examining cataracts caused by cyclotron radiation; both studies involved neutron exposure (Cogan et al., 1949; Abelson and Kruger, 1949; Strigari et al., 2021). The Longitudinal Study of Astronaut Health (**LSAH**) and the NASA Study of Cataracts in Astronauts (**NASCA**) have investigated the incidence and progression of cataracts in astronauts. The **LSAH** data provide a historical record of cataract incidence in astronauts; however, they have been collected using a subjective method to record cataract severity and type. **LSAH** found a dose-effect threshold of about 8 mSv,

linking an increased risk of cataracts for astronauts with higher lens doses (≥ 8 mSv) of space radiation relative to other astronauts with lower lens doses (≤ 8 mSv) (Cucinotta et al., 2001). The **NASCA** study is a longitudinal investigation that spans over five years and aims to assess the impact of space radiation exposure on the severity, progression, and risk of lens opacity (Chylack Jr et al., 2009; Chylack Jr et al., 2012). According to the study's findings, there is evidence of a small yet detrimental effect of space radiation on cortical cataract lens opacities and, potentially, posterior subcapsular cataract lens opacities. After analyzing five years of data, with an average of 3.8 examinations per subject, preliminary results suggest no association between radiation exposure and progression rates for nuclear cataracts and posterior subcapsular cataracts. However, it is important to note that further investigation is necessary to gain a more comprehensive understanding of the risks associated with cataracts during space missions and to develop appropriate prevention and treatment strategies (Chylack Jr et al., 2009; Chylack Jr et al., 2012; Strigari et al., 2021).

During long-term missions to the moon or Mars, as well as the current **ISS** program, late effects of radiation, such as **CNS** effects, cataracts, and cancer are the most significant concerns (Strigari et al., 2021). The potential risks to the **CNS** could result in cognitive impairments such as behavioral changes, reduced motor function, and short-term memory loss (Cucinotta et al., 2014). Moreover, there are long-term risks to the **CNS**, including early aging, Alzheimer's disease, or other forms of dementia, which could be especially problematic during long-duration missions beyond low Earth orbit due to the absence of protection from Earth's magnetic field, and the long duration of the space mission (Sihver et al., 2015; Duda et al., 2021). It should be noted that the available data on radiation effects on the **CNS** in space are limited due to the relatively small number of humans who have ventured beyond the protective envelope of the Earth's magnetosphere. As part of the Apollo program, only 24 individuals, during 9 Apollo missions, have spent a maximum of approximately 12 days in deep space (Chancellor et al., 2014). Conducting realistic experiments to study radiation effects on human brains in space also presents significant ethical and technical challenges. Possible observation of **CNS** effects in astronauts participating in past **NASA** missions in **LEO** is also unlikely due to the protective effect of the Earth's magnetic field, the relatively short lengths of past missions as well as the small population size of astronauts (Cucinotta et al., 2014). Therefore, the potential risks to the **CNS** mentioned earlier can derive from either the ground experiments conducted on animal models or reports from the atomic bomb survivors (Brenner et al., 2020) and patients who were undergoing conventional cranial radiotherapy. Studies based on reports from patients undergoing conventional cranial radiotherapy and experiments in animals exhibited **CNS** behavioral changes such as chronic fatigue, long-term anxiety, and depression (Tofilon and Fike, 2000), as well as other negative effects on cognition, including disruptions in learning, memory, processing speed, attention, and cognitive flexibility (Andersen and Tewfik, 1985; Parihar et al., 2016; Parihar et al., 2015; Tang et al., 2012). Some intellectual disabilities have been observed among the children of the atomic-bomb survivors in Japan (OTAKE, 1998). In addition, the atomic bomb radiation exposure is associated with

elevated risks of major types of **CNS** tumors that appear to persist throughout life (Brenner et al., 2020). Investigation of the effects on the **CNS** using animal experiments reveals the enhanced degradation of **DNA** and changes in dopamine function (Rabin et al., 2000), which may cause accelerated striatal aging (Joseph et al., 1992). According to Britten et al. (2012), 1 GeV/u ^{56}Fe particles at doses as low as 20 cGy can significantly impair learning and memory in a rodent model, while proton radiation caused marked neurocognitive deficits at psychomotor vigilance tests at doses as low as 25 cGy (Hienz et al., 2010). The analysis of energy deposition in irradiated hippocampal neurons simulated with Geant4 as a 3D model of the rat's hippocampus suggests that a significant portion of the energy is accumulated by a dense population of granular cells in the dentate gyrus (Batmunkh et al., 2019; Strigari et al., 2021).

The radiobiology studies of **CNS** effects based on modeling of space radiation using experimental and empirical models suggest that space radiation risks during a long-term space mission to Mars may include damage to short-term memory, negative impacts on crew performance and decision-making, and Alzheimer's disease or other dementia as a late **CNS** effect (Cucinotta et al., 2014). Animal models using mice (Parihar et al., 2015; Parihar et al., 2016) exposed to doses of radiation equivalent to that of a cruise to Mars (Zeitlin et al., 2013) indicate that the corresponding space radiation may cause the reduction of dendritic complexity and the alteration in synaptic integrity and thus influence the cognitive performances over an extended period (Parihar et al., 2015; Parihar et al., 2016). In a study by Cacao et al. (2016), a predictive mathematical model was developed to assess the radiation-induced changes to neurogenesis resulting from acute or fractionated irradiation for various radiation types. This study also extended a mouse model of impaired neurogenesis in the hippocampal dentate gyrus after exposure to low-**LET** radiation to heavy ion irradiation. The results indicated that heavy-ion irradiation resulted in poor or no recovery from impaired neurogenesis, even at doses as low as 0.5 Gy in mice. Radiation exposure can result in changes in proteins associated with dopamine receptors and transporters in the brains of radiosensitive animals at mission-relevant doses and dose rates, indicating the importance of susceptibility in predicting radiation-induced **CNS** changes (Chancellor et al., 2014; Kiffer et al., 2019a; Strigari et al., 2021). Radiation exposure during space missions can cause cognitive impairments by changing neuron morphology and plasticity, and studies in mice indicate that radiation type and dose are crucial factors in this regard (Cherry et al., 2012).

Cancer risks for space missions are a concern due to the exposure of astronauts to ionizing radiation in space. These risks vary depending on several factors, such as the length of the mission, the type of radiation, and the shielding provided by the spacecraft. It assumes that even doses as low as 100 mGy may raise cancer risk, based on the Linear-No-Threshold (**LNT**) model of estimating cancer risk from exposure to ionizing radiation. While the actual risk remains uncertain, **NASA** has set radiation exposure limits based on the **LNT** model to help manage cancer and other health effects among astronauts. These limits are intended to keep cancer risks and other radiation-related health effects within

acceptable limits (Strigari et al., 2021; Valentin et al., 2007).

2.3.1 Behavioral Effects of Charged Particles in Animal Models

Despite the relatively low abundance of **HZE** ions within **GCRs**, they make a substantial contribution to the overall **GCR** exposure as shown in figure 1.3 which accounts for absorbed dose and quality factor contributions (explained in Section 1.7.4). This phenomenon arises from the fact that the energy deposition by **HZE** ions within individual cells is proportionate to the square of the particle's charge, underscoring their biological impact, as gauged by the dose equivalent rate, as discussed in Section 1.7 (Benton and Benton, 2001; Reitz, 2008; Mrigakshi, 2013).

It's noteworthy that despite the low relative abundance of ^{56}Fe in **GCRs**, estimated at approximately 0.003% (Mewaldt, 1994; Kiffer et al., 2019a), research into the effects of exposure to ^{56}Fe remains essential. This significance stems from its substantial contribution to overall **GCR** exposure when considering absorbed dose and the quality factor (as discussed in Section 1.7.4). This contribution arises from the fact that the energy deposited by **HZE** ions in an individual cell is proportional to the square of the particle's charge. Additionally, their biological impact is quantified through the dose equivalent rate, as elaborated in Section 1.7. Studies offer valuable insights into the broader risks associated with **HZE** particles and serve as a pivotal avenue for comprehending radiation impacts on the **CNS**, with ^{56}Fe being a pivotal particle used in in vivo research on radiation effects. Remarkably, doses as low as 20 cGy of ^{56}Fe have demonstrated the induction of deficits in thermoregulation and conditioned taste aversion, underscoring the significance of such research in understanding radiation's impact (Kandasamy et al., 1994; Kiffer et al., 2019a; Rabin et al., 2002). A dose of 10, 50, and 100 cGy of ^{56}Fe is shown to desensitize muscarinic striatal receptors and downstream signaling that refers to a series of molecular events that occur after a receptor on the cell surface is activated by a specific signal or stimulus in rats younger than 2 months (Kiffer et al., 2019a; Carrihill-Knoll et al., 2007; Joseph et al., 1993). Impairment of reversal learning, which refers to difficulty in adapting or altering a learned response when the rules or contingencies are reversed, can be caused by 1.5 Gy of whole-body or 3 Gy of cranial radiation in male rats and mice, respectively, but not by lower doses (10–50 cGy) (Haley et al., 2013; Kiffer et al., 2019a; Shukitt-Hale et al., 2000). Male rats exposed to 1.5 Gy of radiation showed sporadic deficits and increased oxidative stress in the prefrontal cortex one month after exposure (Denisova et al., 2002). Object memory is impaired 2 weeks after exposure to 10 and 40 cGy, and 3 months after exposure to 150 cGy in the novel object recognition test. Motor activity in an open field was reduced 3 months after exposure to 50 cGy (Impey et al., 2016; Allen et al., 2015). Radiation-induced attentional set deficits were observed in rats 3 months after exposure to 20 cGy (Lonart et al., 2012). In addition, 10-month-old rats displayed marked deficits in compound and simple discrimination (attentional set) after exposure to low doses (1–15 cGy) of 600 MeV/n ^{56}Fe (Jewell et al., 2018).

Doses as low as 5 cGy of ^{56}Fe can impair performance on the Barnes maze, with changes in the proteome indicating altered markers for memory performance, neurodegeneration, neuronal loss, neuroplasticity, and inflammation (Britten et al., 2017a; Britten et al., 2016). Transgenic knock-in models of mice that express human genes associated with Alzheimer's disease have shown evidence of amyloid accumulation and behavioral deficits after exposure to doses as low as 10 cGy of charged-particle radiation. Higher doses, such as 2 Gy, have been shown to affect motor behavior on the rotarod platform, as well as anxiety levels in the open field, and performance in the Morris water maze task (Cherry et al., 2012; Kiffer et al., 2019a; Higuchi et al., 2002).

Apart from ^{56}Fe , ^{48}Ti is another type of **HZE** particle that has been shown to induce behavioral deficits in various tests used in behavioral neuroscience and psychology. These tests are employed to investigate cognition, memory, and behavior impairments in animals due to the exposure to ^{48}Ti . Even low doses (500-1,000 MeV/n, 10-20 cGy) of ^{48}Ti significantly impacted compound discrimination and reversal after 3 months, but not simple discrimination (Hadley et al., 2016; Kiffer et al., 2019a). Spatial memory was also affected by doses as low as 5 cGy after 3 months. In addition, 5 cGy of ^{48}Ti negatively affected temporal order exploration and elevated plus maze anxiety, which is a common behavioral test used to assess anxiety in rodents after 3 and 6 months, but not in rats exposed to 1 or 10 cGy after 2 or 6 months. Dendritic remodeling was also observed in mice exposed to ^{48}Ti (Rabin et al., 2018; Kiffer et al., 2019a; Parihar et al., 2016; Parihar et al., 2015b; Britten et al., 2017b).

The most prevalent **HZE** particles in the **GCR** spectrum are ^{16}O and ^{12}C (Kiffer et al., 2019a; Mewaldt, 1994). **HZE** particles with $Z \geq 9$ contribute roughly 5-10% of the total radiation dosage on a mission to Mars. Moreover, NASA's permissible exposure limits for particles with $Z \geq 9$ are 10 cGy for a year and 25 cGy for a career (Nelson, Simonsen, and Huff, 2016). Male mice exposed to 10-25 cGy of ^{16}O radiation showed impaired short-term memory 2 weeks and 9 months after exposure in Y-maze tests, but not females exposed to 10-25 cGy. Surprisingly, doses of 0.4 and 0.8 Gy increased cued fear memory but had no effect on contextual fear memory a month post-exposure (Raber et al., 2015; Carr et al., 2018; Kiffer et al., 2019b).

Low doses (1-25 cGy) of ^{16}O radiation reduced operant conditioning (Rabin et al., 2014), and even 1 or 5 mGy induced anxiety in 15-month-old mice (Rabin et al., 2018). ^{16}O induced detrimental effects on the CNS, including altered immune activation and oxidative-stress responses, as well as dendritic remodeling changes in the hippocampus and pre-frontal cortex (Parihar et al., 2015b; Rabin et al., 2015; Kiffer et al., 2019b).

^{12}C has been found to cause an immediate loss of neurogenesis, proliferating neurons, neural precursors, and immature neurons in the **CNS**. These losses recover within 3 months but revert at 9 months after exposure to 1-3Gy in a dose-dependent manner (Rola et al., 2005; Zanni et al., 2018).

^4He is a crucial particle for studying the behavioral effects of space radiation due to its abundance in **GCRs** and **SEPs** as shown in figure 1.3, and its ability to induce acute hyperthermia in a dose-dependent manner. Although these effects can be reversed with cyclooxygenase inhibition (Kandasamy et al., 1994). Low doses of ^4He radiation (0.05, 0.1 cGy) increase protein expression of NOX-2 and pCREB, important transcription factors associated with free-radical production and long-term memory formation, respectively. Additionally, a dose of 0.1 Gy unexpectedly increases NRF2, a transcription factor involved in the expression of endogenous antioxidants (Rabin et al., 2019).

Studies have shown that exposure to 1 Gy of ^1H radiation has differential effects on morris water maze-dependent spatial memory, with mice spending less time in the target quadrant during the first probe trial 2 weeks after exposure (Impey et al., 2017). Reversal learning was also impaired in mice 6 months after receiving 10, 50, or 100 cGy, and spatial memory was compromised 3-6 months after exposure to 10-100 cGy (Bellone et al., 2015; Rudobeck et al., 2017). ^1H radiation has been shown to have destructive effects on brain cells, altering the dendritic length, complexity, and spine composition in the hippocampal DG, CA3, and CA1 even at low dosages of 50-200 cGy (Kiffer et al., 2018; Parihar et al., 2015a). Exposure to 50 cGy also significantly increased field excitatory postsynaptic potentials, reduced spontaneous oscillations, and decreased CB1-dependent tonic inhibition of GABA release in the CA1 (Bellone et al., 2015; Lee et al., 2017). Molecular changes due to ^1H radiation indicate altered expression of glutamatergic receptors and synaptic density markers in the hippocampus. It is also worth to mention that there may be differences in the way that different animal species respond to radiation exposure, particularly concerning **DNA** damage and repair mechanisms. It has been found by Romero-Weaver et al. (2013) that high-dose proton exposures in mice led to a temporary decrease in circulating white blood cells, but that these levels returned to normal within 30 days following exposure. However, in mini-pigs exposed to simulated **SEP** radiation, blood cell counts did not return to pre-irradiation levels, indicating that these animals may not be able to repair **DNA** damage caused by the radiation exposure as efficiently as mice (Romero-Weaver et al., 2013). These findings highlight the importance of considering the potential effects of radiation exposure in different animal species, and the need for further research to better understand the mechanisms of **DNA** damage and repair across different species. It's worth noting that animal models are an important tool for studying the effects of radiation exposure, but they may not always accurately reflect the responses of human cells or tissues. Therefore, it is of paramount importance to exercise utmost caution and meticulous consideration when extrapolating insights derived from animal studies to the complex and multifaceted realm of human responses. Table 2.1 presents the brain regions covered in the literature review of this thesis, while Table 2.2 offers a compilation of behavioral tests utilized to assess radiation effects in animal experiments.

TABLE 2.1: List of Brain regions mentioned in the literature review of this thesis

Brain region	Location	Functions
The prefrontal cortex (Preuss and Wise, 2022)	Anterionmost portion of the frontal lobe	Self-awareness Complex planning Problem solving Learning and Memory Decision making (Braver et al., 1997)
Hippocampus (Luo and Niki, 2003)	Embedded deep into temporal lobe	Major role in learning and memory (Opitz, 2014)
Hippocampal dentate gyrus (Sauer et al., 2020)	Part of the hippocampus in the temporal lobe	Pattern completion Novelty detection
The CA3 region	Subfield within the hippocampus	Contributes to the spatial working memory (Song et al., 2020), Pattern separation Pattern completion (Deuker et al., 2014)
The CA1 region	Within the hippocampus	Formation, consolidation, and retrieval of hippocampal dependant memories (Bartsch et al., 2011)
Muscarinic receptor	In the cortex, the striatum, and the hippocampus	Regulating various physiological functions (Kudlak et al., 2022).
Amygdala	Situated in the temporal lobe, near the brain's base and close to the hippocampus	Processing emotions, Memory consolidation (AbuHasan et al., 2019).

2.4 Motivation

In the first chapter of our thesis, we direct our attention toward the challenges faced by astronauts during space exploration, focusing particularly on understanding the biological impacts of radiation exposure. We delve into a comprehensive examination of the radiation environment in space, highlighting the significance of **GCRs** and **SEPs**. Furthermore, we provide an overview of key processes related to radiation-matter interaction and dosimetric concepts. The subsequent section entails an extensive review of relevant literature within the context of human space exploration. We discuss the various types of radiation encountered during deep space missions and on Mars, with a specific emphasis on **GCRs** and **SEPs**. Drawing upon data obtained from astronauts, spaceflight crews, ground-based experiments, and simulation-based studies, we summarize the radiation exposure levels and associated health risks faced by astronauts during missions to Mars. In addition, we review studies that have explored the behavioral effects of charged particles using animal models.

Despite the extensive research conducted on the effects of radiation on the human body, there still exists a significant knowledge gap in our comprehensive understanding of these effects. Specifically, there is a need to further investigate and accurately quantify the dose and energy of space radiation in specific regions of the brain, such as the lobes. These brain regions play critical roles in functionalities of the brain, such as decision-making, learning, memory, and so on, which are essential for the success of space missions. Bridging this knowledge gap is essential to effectively address the radiation risks faced by astronauts and ensure their well-being during space exploration endeavors. This research aims to address this gap by focusing on the initial part of the study, which involves calculating the energy deposition and dose distribution within the human head, with a particular focus on various regions of the human brain, including vital components such as the lobes and hippocampus region. Disruption of these brain regions caused by space radiation has the potential to impair cognitive functions, decision-making abilities, and overall brain performance, thereby presenting a significant concern for the success of future space missions. Our investigation encompasses two scenarios: first, we analyze the effects of deep space radiation on different regions of the brain, and second, we conduct an evaluation of different thicknesses of shielding of aluminum aimed at mitigating these adverse effects.

Moreover, the long-term presence of astronauts in space and on planetary surfaces, such as Mars, necessitates a thorough understanding of the radiation environment, and the development of appropriate countermeasures to ensure their safety and well-being. Previous research, such as the work conducted by Wimmer-Schweingruber et al. (2015), provided valuable insights into the zenith angle dependence of the particle fluxes reaching **RAD** and found that the radiation field on the Martian surface is nearly, but not entirely isotropic. However, the study was limited in terms of rover tilt angles and did not provide a comprehensive understanding of the zenith-angle dependence of the surface radiation field. To address this knowledge gap, our study aims to investigate the directionality of surface radiation over a wide range of zenith angles. By employing advanced three-dimensional Monte Carlo simulations using the Geant4 framework, we can model the complex interactions between **GCRs**, the Martian atmosphere, and the **RAD** detectors. This approach allows us to derive the zenith-angle dependence of the surface dose rate and gain valuable insights into the radiation exposure astronauts may experience during their exploration missions. The outcomes of this research will have significant implications for mission planning and astronaut safety. By understanding the distribution and characteristics of the surface radiation field, we can develop strategies to mitigate radiation risks, identify suitable landing sites with natural shielding features, and optimize the use of available resources to protect astronauts from the harsh radiation environment, particularly during solar energetic particle events.

TABLE 2.2: List of behavioural tests mentioned in the literature review of this thesis.

Behavioural tests	Summary of behavioural assays	Brain Region Targeted
Morris water maze	Involves animals navigating a water-filled pool to find hidden platforms using spatial cues, testing their spatial memory and cognitive flexibility.	Hippocampus Spatial memory
Y-maze test	The test assesses short-term spatial memory by observing mice in a Y-shaped maze over two trials on the same day, where the second trial involves exploring a novel arm with a different object. Mice tend to show more interest in novel objects.	Hippocampus
Attentional set-shifting	Animals learn to link a cue with a food reward in an arena with buried food, and changing the cue to assess digging preference tests their cognitive flexibility.	Prefrontal cortex
Barnes maze	Animals navigate a circular arena with multiple escape holes, identifying the correct one containing a shelter using spatial cues.	Hippocampus Prefrontal cortex
Elevated plus maze	The maze has open and closed arms, with animals usually favoring the closed arms due to height-induced anxiety, yet occasionally exploring the open arms.	Amygdala
Novel object recognition	After getting used to the environment, animals encounter two identical objects, and the next day, one object is replaced with a "novel object."	Hippocampus
Object in place	This test puts animals in a square arena with four objects. On the next day, when two object positions are switched, animals usually show greater interest in exploring these new locations compared to others.	Prefrontal cortex

Chapter 3

Dose Assessment : Instrument and Modelling

The quantification of dose quantities required for assessing radiation-related health risks involves either measurement techniques or numerical calculations employing computer simulations. The initial sections of this chapter offer an overview of the **RAD** instrument specifically designed to measure the radiation environment on Mars' surface. Subsequently, we introduce the utilization of Geant4 tools, widely employed for conducting simulations. Lastly, we delve into the discussion of tools employed for data analysis, enabling the evaluation of dose and energy distribution across various regions of the human brain.

3.1 The MSL Radiation Assessment Detector Instrument

The Radiation Assessment Detector (**RAD**), a scientific instrument aboard the Mars Science Laboratory (**MSL**), is designed to measure the radiation environment on the surface of Mars (Hassler et al., 2012; Grotzinger et al., 2012). It was developed in cooperation between the University of Kiel and Southwest Research Institute and is currently part of **NASA**'s Mars Science Laboratory mission, which includes the Curiosity rover. **RAD** is unique in the way that it provides the first-ever radiation measurements on the Martian surface. By detecting **GCRs**, **SEPs**, secondary neutrons, and other secondary particles created in the atmosphere and the Martian regolith, **RAD** enables scientists to investigate the radiation environment on Mars both past and present, with potential implications for habitability and the ability to sustain life. The instrument also addresses a significant concern for future human missions by measuring radiation exposure (Hassler et al., 2012). **RAD**'s capabilities are achieved through charged- and neutral-particle detection in a compact, low-mass, and low-power instrument that is highly configurable. The **RAD** is intended to measure both charged and neutral particles and compute the particle spectra along with dosimetric quantities such as the total ionizing dose rate and **LET** spectra. These objectives are aligned with its primary scientific goals, which entail characterizing the energetic

particle spectra present on the Martian surface, including **GCRs** and **SEPs**, as well as determining the radiation hazard for past or present life on Mars or for future human missions to the planet.

The RAD Sensor Head (**RSH**) shown in figure 3.2, composed of three silicon detectors each having the thickness of 300 μm for charged particle detection, a thallium-doped Cesium Iodide scintillator, plastic scintillators for neutron detection, anti-coincidence shielding, and front-end electronics. The **RAD** instrument is mounted just below the top deck of the rover with the charged particle telescope pointed in the zenith direction. The telescope geometry for charged-particle detection in the **RAD** is determined by the “A” and “B” detectors. The “A” detector is split into outer and inner areas, defining detectors “A1” and “A2” respectively, with “A2” consisting of the two innermost segments of the diode. The detection process involves two view cones, which are defined by the coincidence of hits in the “A” and “B” detectors. The first view cone is formed using the inner segment, specifically the “A2”-detector, which covers a half-angle of 18° . The second view cone utilizes the outer segment, the “A1”-detector, resulting in a larger cone with a half-angle of 32° . To detect charged particles, **RAD** requires an energy deposit in at least the “A” and “B” detectors, setting the lower limit for the particle’s kinetic energy to, for example, 6 MeV for protons. For higher energy charged particles, which penetrate the “B” detector and stop in “C”, “D”, or “E”, the total deposited energy (E) and the **LET** in one of the detectors are used to determine the particle’s charge and total kinetic energy. This technique is known as the dE/dx - E method and has been in use since the IMP-1 mission in the 1960s (McDonald and Ludwig, 1964). By using this technique, one can obtain important information about the charged particles present in the Martian radiation environment, including their energy, charge, and penetration depth (Hassler et al., 2012). Detectors “D”, “E”, and “F” are scintillation detectors (see figure 3.2). The CsI scintillator detector, “D”, in the shape of a truncated hexagonal pyramid, is situated directly below the charged particle telescope and aligned with the inner segment of detector “C”. Detector “D” is used to supply a measurement of the total particle energy for proton and alpha particles of up to 95 MeV/nuc. The “E” detector, a plastic scintillator, is located below the “D” detector and is mainly used for neutral particle detection. The “E” detector also stops a small percentage of charged particles. Being a CsI scintillator, detector “D” can detect secondary electrons generated by γ -rays effectively, while neutrons hitting the “E”-detector can interact with the hydrogen atoms in the plastic to produce recoil protons. By considering these interaction processes, an inversion method is employed to derive neutral particle spectra. This method takes into account the contributions from both gamma-ray interactions with the CsI scintillator and neutron interactions with the hydrogen atoms in the plastic material (Köhler et al., 2011).

Both “D” and “E” detectors are surrounded by another plastic scintillator (“F”) used as an anticoincidence shield to reject ions entering “D” or “E” detectors from the sides. **RAD** provides several direct data products, including dosimetry and Pulse Height Analysis (**PHA**) data.

Due to limited available telemetry for data transmission back to Earth, **RAD** selectively records a subset of measurable events in the form of **PHA** data, which contains essential information for thorough data analysis. Each event is assigned a **PHA** priority and stored based on available buffer sizes. While not all valid events can be transmitted due to storage and telemetry constraints, data from these events are stored in histograms. **PHAs**, primarily used to generate histograms for energy spectra visualization, have a broader utility encompassing identification of radiation energies, source intensity determination, material composition analysis, and radiation-matter interaction studies. Histograms, in turn, are one- or two-dimensional arrays where each element signifies the count of valid events in a specific energy bin, determined by the onboard data analysis algorithm employing nominal calibration factors (Hassler et al., 2012; Ehresmann et al., 2014). The **PHA** data collected by **RAD** consists of the energy spectrum of the charged particles detected by the detector. The energy spectrum refers to the distribution of high-energy particles or radiation, often associated with cosmic rays or high-energy astrophysical phenomena. This energy spectrum is a histogram that shows the number of particles detected at each energy level. By analyzing the energy spectrum, it is possible to identify the different types of particles present in the space radiation environment, such as protons, electrons, and heavy ions. To generate **PHA** data, different coincidence requirements are used, including a requirement for energy to be deposited in each detector from “A2” to “F”. This is particularly important for detecting penetrating particles, which can pass through multiple layers of material, as they can be identified by the energy they deposit in each detector (Hassler et al., 2012; Ehresmann et al., 2014).

Dosimetry data is essential for assessing the risks of radiation exposure to astronauts during long-term human exploration missions to Mars. The measurement of radiation doses on the Martian surface is achieved through the use of active dosimeters that employ two concurrent methods, namely the silicon detector “B” and the plastic scintillator “E” detector. For the dose measurement, these detectors are utilized omnidirectionally to measure the total deposited energy of any particle that passes through them without requiring any other coincidence requirements. The dose of ionizing radiation, including protons, neutrons, and other charged particles, present on the Martian surface can be measured using these two detectors. The silicon detector “B” is specifically designed to measure the dose of charged particles like protons and heavy ions. These particles deposit their energy in the silicon detector, resulting in a measurable signal that is used to determine the radiation dose. The plastic scintillator “E”, on the other hand, is designed to measure the dose of both charged particles and neutrons. The plastic scintillator has a composition similar to that of human tissue, making it more sensitive to neutrons than silicon detectors. When charged particles or neutrons enter the scintillator, they interact with the material, producing scintillation light, and the amount of light produced is proportional to the amount of energy deposited by the radiation, which enables the accurate measurement of the dose (Hassler et al., 2012; Guo et al., 2021b).

Figure 3.1 displays the time profile of the measured radiation dose rate by **RAD** from

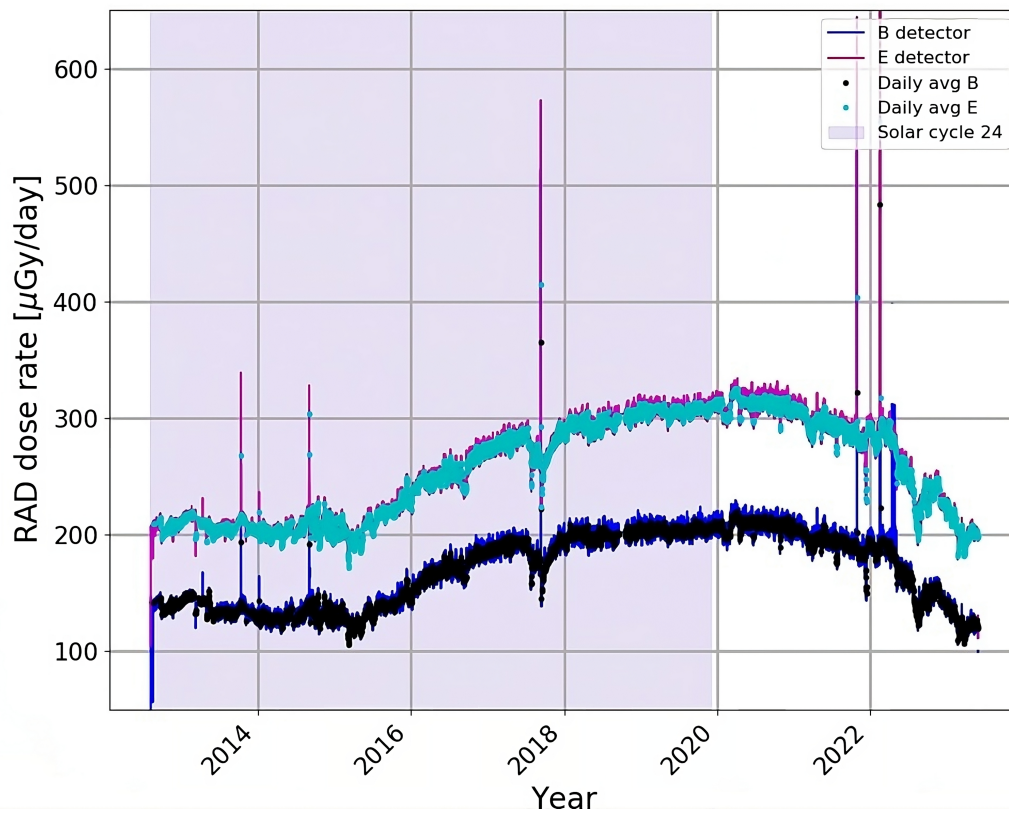


FIGURE 3.1: **RAD** recorded Martian surface dose rates in silicon detector B and plastic detector E since **MSL** landing until 2023 April. The silicon dose rate has been corrected for the background radiation contributed by the rover Radioisotope Thermoelectric Generator (**RTG**). The shaded region reported here begin before the maximum of solar cycle 24, continue through the solar maximum (2014–2015) and into the declining phase and the associated deep solar minimum.

the **MSL** landing until May 2023. The measurements were taken every 16 minutes, and the daily average data was obtained using a 1 day smoothing window. The peaks in the plot represent the **SEPs** seen by **RAD** on the surface of Mars. It's important to note that the absorbed dose in the plastic E detector is higher than that of the silicon B detector because the absorbed dose in the silicon B detector had its background contribution from the rover's **RTG** subtracted.

RAD's versatility and advanced technology make it a highly capable instrument, paving the way for future compact energetic particle detectors in space. Since the Curiosity rover's landing on August 6, 2012, **RAD** has been consistently measuring the radiation environment on the Martian surface and was also active during the majority of its 9-month flight to Mars, known as the cruise phase, to assess the radiation dose that astronauts would experience while traveling to Mars. The instrument has provided valuable information about the radiation environment on Mars, including the effects of solar storms and

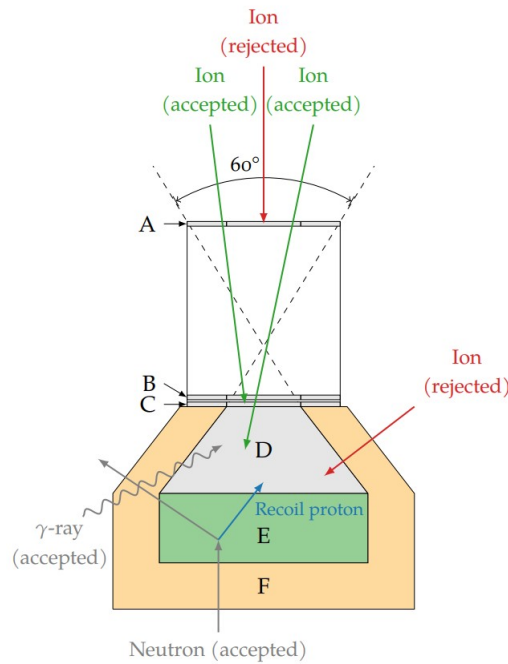


FIGURE 3.2: Schematic diagram of the **RAD** sensor head. Red, green, blue, and gray arrows show possible trajectories of charged and neutral particles through the detectors. Accepted particle trajectories are shown in green, and rejected trajectories are shown in red. Taken from Hassler et al., 2012.

the potential risks to human health during future manned missions to the planet (Guo et al., 2021b; Hassler et al., 2012).

3.2 Geant4 Toolkit

Geant4 (GEometry And Tracking, Agostinelli et al., 2003; Allison et al., 2016) is a widely used and well-established toolkit for simulating the passage of particles through matter. It is a three-dimensional tool that utilizes the object-oriented C++ programming language and employs the Monte Carlo method for simulating the behavior of particles as they interact with matter. It developed by the European Organization for Nuclear Research and is now widely used in various scientific fields, including high-energy physics, nuclear physics, space science, medical physics, and radiation protection. Geant4 provides a comprehensive set of tools for simulating the passage of particles through matter. It includes a geometry description package that allows users to define the physical and material properties of the target, as well as the placement and orientation of detectors. Geant4 also includes a tracking engine that simulates the motion of particles through matter, taking into account their interactions with the surrounding material and the electromagnetic and nuclear fields. One of the key features of Geant4 is its ability to simulate a wide range of particle interactions with matter. This includes electromagnetic interactions, such as ionization and bremsstrahlung, as well as hadronic interactions, such as nuclear scattering

and annihilation. Geant4 can also simulate optical photon interactions, such as scintillation and Cherenkov radiation.

Geant4 allows users to select physics models for particle interactions based on the specific radiation environment. This can be achieved through physics lists that combine models for different energy ranges (Geant4_Collaboration, 2017). The choice of physics list can affect the assessment of the radiation environment depending on factors like particle type, energy, and interacting materials (e.g., Guo et al., 2019). We utilized two different physics lists, "QGSP_BIC" and "QGSP_BERT", to examine their differences when applied to model the space radiation impact on human brains (Collaboration, 2020; Wright and Incerti, 2012; Geant4_Collaboration, 2017). Both lists incorporate the Quark-Gluon String model ("QGS") for high-energy particles ($> \sim 20$ GeV) (Apostolakis et al., 2009). The Precompound model (P) is also used to de-excite the remnant nucleus after the initial high-energy interaction (Yarba, 2012). Subsequently, the precompound model calls upon the Fermi breakup, multi-fragmentation, neutron evaporation, and photon evaporation models as required (Yarba, 2012; Geant4_Collaboration, 2017). For hadrons of energy ranges below ~ 10 GeV, the "QGSP_BIC" employs the Binary Cascade model, while "QGSP_BERT" uses the Bertini Cascade model within this energy range. In the case of neutrons, we also use the "HP" option in both lists, which switches on the high precision neutron elastic and inelastic scattering model for neutrons below 20 MeV (Adloff et al., 2014; Folger, Ivanchenko, and Wellisch, 2004; Heikkinen, Stepanov, and Wellisch, 2003). In modeling the Martian radiation environment, it has been found that different physics lists can affect the generation of secondary particles, especially those produced via spallation processes (Guo et al., 2019). However, the surface absorbed dose agrees within $\sim 5\%$ for different physics lists (Matthiä et al., 2016).

To accurately model the anatomy and physiology of patients, high-resolution computational models or phantoms are essential. These models must consider various factors, such as anatomy, tissue properties, computational efficiency, organ geometry and structures, and compatibility with simulation codes. Three types of human phantoms are discussed: stylized, voxel, and hybrid models. Stylized phantoms use primitive shapes to construct organs, while voxel phantoms assign labels based on anatomical regions and tissue characteristics to voxels in 3D. Hybrid phantoms combine voxel data with stylized modeling to create a phantom that benefits from the advantages of both voxel and stylized models. In our study, we used the Geant4-DICOM package (Giacometti et al., 2017) to build our model which is a voxelized model of the human head and will be explained in the next section (Akhavanallaf et al., 2022; Neufeld et al., 2018).

3.2.1 Geant4-DICOM Package

In order to investigate the impact of radiation on the human brain, the study described in 4.1, we utilized voxelized geometries in Geant4. These geometries were based on Computed Tomography (CT) scans of an actual head structure, encompassing the entire

brain. The Geant4-DICOM package was utilized for this purpose. Geant4-DICOM provides an interface with Digital Imaging and Communications in Medicine (**DICOM**) data, enabling the incorporation of realistic patient-specific information into the simulations to simulate radiation transport and interaction with matter in medical imaging and radiation therapy applications. The package is designed to enable the evaluation of the deposited dose in various materials and geometries and to simulate complex radiation sources, including photon, electron, and proton beams (Kim, 2012). The Geant4-**DICOM** package is a well-established simulation software provides a flexible and customizable simulation environment, which allows researchers and clinicians to simulate a wide range of medical imaging and radiation therapy modalities (Kimura et al., 2005; Kimura et al., 2004; Kim, 2012).

DICOM images are a standard format for storing and transmitting medical images and related data. **DICOM** images can contain a wide range of medical images, including X-rays, **CT** scans, Magnetic Resonance Imaging (**MRI**) scans, ultrasound images, and more. **DICOM** images consist of a header and image data. The header of a **DICOM** image contains a wealth of information about the image and the patient it represents. The header is a structured set of metadata that includes information such as patient demographics (e.g. name, age, sex), imaging modality (e.g. X-ray, **MRI**, **CT**), image orientation (e.g. which direction the image was taken from), and imaging parameters such as slice thickness, pixel size, which are important in using these images in Geant4 simulations. The header information is stored in a standardized format, which allows **DICOM** images to be easily exchanged and interpreted across different systems (Mildenberger et al., 2002). The Geant4-DICOM package includes tools for **DICOM** file manipulation and conversion, which facilitate the integration of **DICOM** data into the simulation environment. The procedure for reading **DICOM** images in the Gant4-DICOM package is as follows:

1. Load the **DICOM** files: To load **DICOM** files, the Geant4-**DICOM** package provides a class called *G4DICOM::G4DICOMReadImage*. This class takes the path to the **DICOM** file as an argument and returns a *G4DICOMImageInformation* object. The *G4DICOMImageInformation* object contains information about the image, such as its dimensions and pixel size, as well as the raw pixel data.
2. Read the header information: The header information contains metadata about the image. This metadata can be accessed using the *G4DICOMImageInformation* object returned by *G4DICOMReadImage*. Some of the important header fields that are typically used in simulations include:
 - PixelSpacing: The size of each pixel in millimeters
 - SliceThickness: The distance between adjacent slices in millimeters
 - ImagePositionPatient: The position of the image in the patient coordinate system
 - ImageOrientationPatient: The orientation of the image in the patient coordinate system

- Rows and Columns: The number of rows and columns in the image
3. Read the pixel data: The pixel data is the actual image data, stored as a two-dimensional array of pixel values. The raw pixel data can be accessed using the *G4DICOMImageInformation* object returned by *G4DICOMReadImage*. The pixel data is typically stored as a one-dimensional array of values, with each pixel value represented by a 16-bit or 32-bit integer. The order of the pixels in the array depends on the image orientation and can be determined using the *ImageOrientationPatient* header field.
 4. Convert Hounsfield Unit (HU) to density: The pixel data in a DICOM image can be treated as a two-dimensional array matrix. The value in each picture element, which is called a pixel, stands for the intensity in that pixel. For an image from CT scanning, the intensity stored in a pixel is the CT number in the HU. The definition of CT number in HU is:

$$HU = \left(\frac{\mu_m}{\mu_{water}} - 1 \right) \times 1000 \quad (3.1)$$

where μ_m is the linear attenuation coefficient of the CT X-ray in a voxel filled with a material marked as m , and μ_{water} is the linear attenuation coefficient of the CT X-ray in water. According to this definition, the HU of water and air are defined to be zero and -1000, respectively. Then, the HU for lung, soft tissues, and fat are negative, and the HUs for muscle and bone are positive (DenOtter and Schubert, 2022). The HUs, which also represents the radiodensity of the tissue, must be converted to mass density units before they can be piped into a Geant4 simulation. This conversion can be done using a calibration curve that relates HU values to densities. The calibration curve is typically obtained by measuring the HU values of a set of materials with known densities and fitting a curve to the data. More detail can be found in Appendix C.

5. Create a Geant4 volume: Once the pixel data has been loaded and converted to density units, a Geant4 volume can be created from the image data. This is typically done by creating a series of voxels with the appropriate dimensions and densities and then placing them in a logical volume. The dimensions of the voxels can be determined from the *PixelSpacing* and *SliceThickness* header fields.
6. Register the volume with Geant4: Finally, the volume must be registered with the Geant4 geometry manager so that it can be used in a simulation. This can be done using the *G4LogicalVolume* class, which takes the voxel data as an argument and creates a logical volume that can be placed in the simulation. Geant4-DICOM simulates the interaction of particles with the materials in the object being studied, and as a result, it calculates the total energy or dose deposited by particles in each voxel of the CT images.

3.3 3D Slicer

3D Slicer is a robust open-source software platform for medical image computing and visualization. Originally developed in the 1990s at the Surgical Planning Laboratory at Brigham and Women's Hospital in Boston, Massachusetts, it has since been continuously updated and improved by a community of researchers and developers. The primary aim of 3D Slicer is to make medical imaging data analysis, processing, and visualization more accessible, covering a variety of imaging modalities such as **MRI**, **CT**, PET, ultrasound, and microscopy. Medical imaging data is often provided in 2D slices, and 3D Slicer enables the reconstruction of these slices into interactive 3D models that can be explored and manipulated (Pieper et al., 2004; Kikinis et al., 2013).

One of the most significant strengths of 3D Slicer is its comprehensive toolkit for image processing and segmentation. Image processing involves manipulating image data to extract or enhance specific features of interest. Segmentation, on the other hand, involves dividing an image into distinct regions or objects based on their unique characteristics, such as texture or intensity.

In our study, we utilized the segmentation feature of 3D Slicer to segment the human brain into various lobes, creating a 3D matrix of this data. We then compared this output to the Geant4 energy deposit output in different voxels. Using this matrix method, we calculated the total dose deposited in various lobes of the human brain. 3D Slicer provides advanced tools for image processing and segmentation, such as filters for noise reduction and smoothing, algorithms for edge detection and feature extraction, and tools for region growing and contouring. These tools can be used to extract particular features of interest from medical images, such as tumors, blood vessels, or organs.

Due to the close density of different lobes, we manually segmented the different parts of the brain using the 3D Slicer. To do so, we loaded the image into the software and selected the "Segment Editor" module to create a new segment. We then chose a segmentation method such as "Threshold" or "Grow from Seeds" and adjusted the parameters until the desired regions were selected. We refined the segmentation using paint or erase tools and saved the segmented regions as individual segments or merged them into one segment. We repeated this process for each part we wanted to segment (Pieper et al., 2004; Velazquez et al., 2013). Once we segmented **CT** images, 3D Slicer enables it to be visualized in 3D space using several rendering techniques, including real-time volume rendering, surface rendering, and ray tracing. Real-time volume rendering allows the display of a 3D model of the image data that can be rotated and zoomed in real-time as shown in figure 3.3. Surface rendering creates a 3D model of the surface of an object in the image, which can be rendered with different materials and lighting conditions. Ray tracing is a more computationally intensive technique that allows for more realistic lighting and shadow effects. 3D Slicer can also provide information about each segmented part, such as mass, volume, surface area, and other quantitative measurements. These measurements can be obtained

using the "Segment Statistics" module in 3D Slicer, which allows for the calculation of various quantitative measurements for each segmented region (Pieper et al., 2004; Kikinis et al., 2013). After segmenting different parts of the Brain using our **CT** data in 3D Slicer, the results are saved in an Nearly Raw Raster Data (**NRRD**) file format used to store and share medical imaging data. **NRRD** files store both the image data and the metadata that describe the image data. The metadata include information such as the image's dimensions, the voxel size, the image orientation, and the data type of the image (e.g., integer or floating-point). **NRRD** files can store both 2D and 3D images, as well as multi-component images such as RGB color images, which have been used for different segments (Liu et al., 2010). The Python code in Appendix A has been used to convert the **NRRD** files to PNG and then read the data to build the matrix of the human brain categorized into different segments.

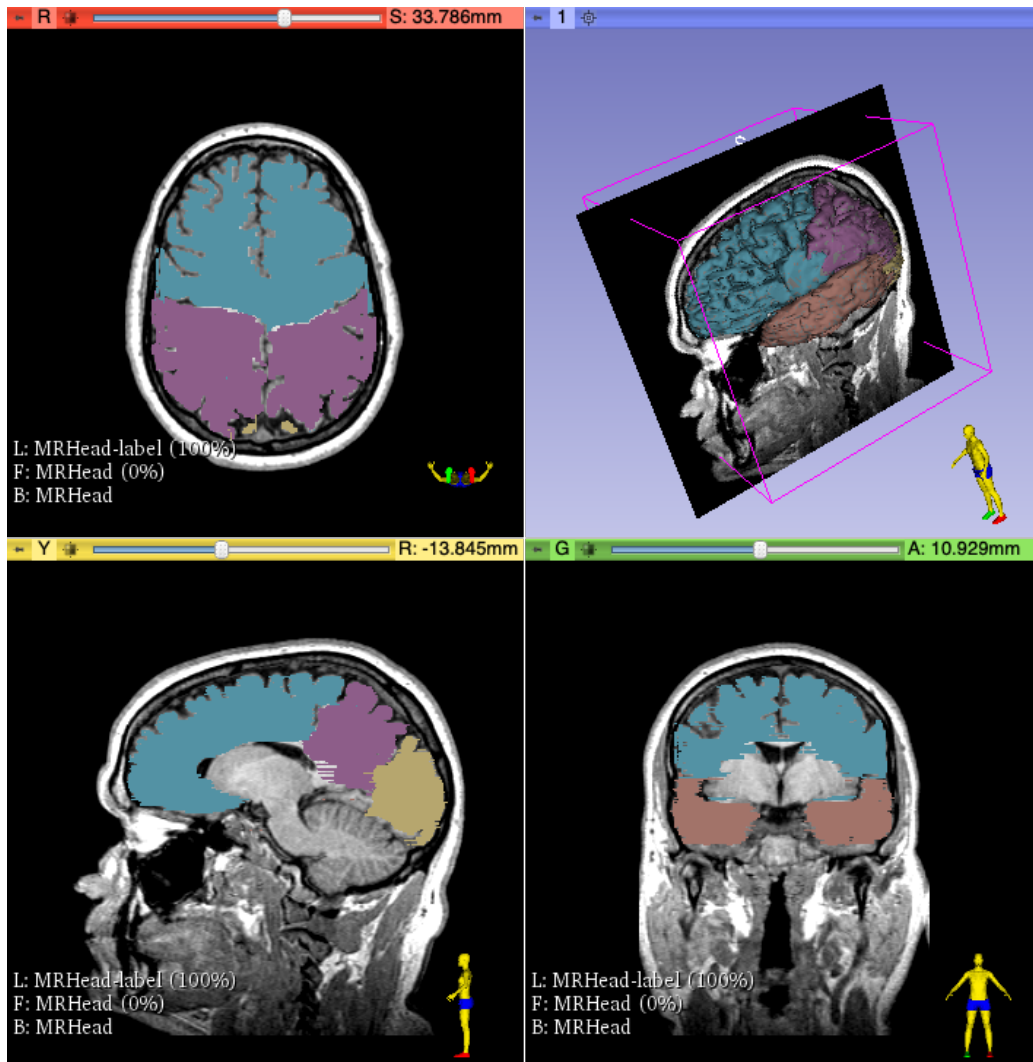


FIGURE 3.3: **DICOM** images segmented into four brain lobes of interest (blue for the frontal lobe, violet for the parietal lobe, brown for the temporal lobe, and yellow for the occipital lobe) viewed from different directions.

Chapter 4

Publications

During the initial phase of our research represented in papers [4.1](#) and [4.2](#), our primary focus was to provide insight into the advancement of human missions in deep space, with a specific emphasis on future endeavors to Mars. To achieve this goal, we developed a model of the human head using the Geant4 framework, while leveraging information provided by [CT](#) images. Our objective was to gain an understanding of the potential radiation risks that astronauts' brain may encounter during their journey. A critical aspect was to compute the energy and dose deposition within the human head and distinct regions of the human brain, encompassing the different lobes and the hippocampus region. Each part of the brain carries out specific functions, such as the frontal lobe's involvement in decision-making and the hippocampus's significant role in learning and memory. Space radiation has the potential to disrupt these components, which result in the impairment of cognitive functions, decision-making capabilities, and overall brain performance, making it a critical concern for the success of future space missions (Parihar et al., [2016](#); Britten, Wellman, and Sanford, [2021](#)). By utilizing [CT](#) images of the human head, we were able to create a detailed and accurate representation of the human brain within the Geant4 framework. It enabled us to simulate various scenarios and evaluate the radiation dose in different parts of the brain. Through this approach, we could provide valuable insights into the potential risks that astronauts may face in deep space. It can help researchers to develop strategies and countermeasures to effectively mitigate these risks by developing suitable helmets for astronauts.

By studying a significant number of historical events, we also derived empirical correlations from the statistical analysis of [SEPs](#) that allow us to establish a relationship between the properties of these [SEP](#) events and the resulting dose in different regions of the brain. By applying these empirical correlations, we can estimate the dose in the brain directly from the fluence of the initial [SEP](#)-event for a specific pivot energy, that represents the energy at which the dose deposit in the head has the best correlation with the original SEP fluence, without the need for extensive Monte Carlo simulations. This includes studying the effects of using various thicknesses of aluminum as shielding around the human head. This not only simplifies the prediction process but also saves computational resources, making it more efficient for near-real-time decisions.

Upon reaching the surface of Mars, the radiation environment differs from deep space, and the long-term presence of astronauts on planetary surfaces like Mars necessitates a thorough understanding of the radiation environment to ensure their safety and well-being. In deep space, radiation exhibits a near-isotropic distribution across the entire 4π solid angle. However, on the Martian surface, the planet itself acts as an effective shield against energetic particles from the lower half of the solid angle. Nevertheless, there is a small fraction of upward-directed radiation known as "albedo" particles, which is generated in the soil as by-products of the interaction between energetic particles and the Martian soil. Furthermore, as radiation traverses the Martian atmosphere en route to the surface, the angular distribution undergoes modifications. Particles entering the atmosphere from the horizon have to traverse a significantly larger atmospheric column compared to particles arriving from the vertical direction. In a following work published in paper 4.3 and paper 4.4, we focused on understanding the radiation risks on the Martian surface, which are primarily determined by GCRs with sufficient energy to penetrate the planet's atmosphere. Since the shielding provided by the Martian atmosphere increases with the zenith angle and leads to an increase in the creation of secondary particles, we used a Geant4 Monte Carlo simulation to derive the dependence of the surface dose rate on the zenith angle θ . Finally, combining this radiation model with the rover panoramic visibility map allowed us to predict a reduction in downward dose rate due to topographical obstructions (e.g., features such as buttes and valleys), which was larger than the data observed by RAD. We hypothesized that this difference can be attributed to albedo radiation coming from the butte and estimated the albedo radiation to be about $(19\pm1)\%$ of the total surface dose. The following sections present publications that contain many of the results from the investigations carried out during the research period. The publications are organized into separate sections and presented in a logical sequence that follows the evolution of the study.

Quantifying the Radiation Dose Rate of GCRs and SEPs on the Human Brain: Implications for the Impacts of Space Radiation in Deep Space

4.1 *Paper I: Modeling the Dose Distribution in the Human Brain*

It is crucial to model the potential risks of radiation exposure to the brain and cognitive function in order to pave the way for human space missions, such as crewed missions to the Moon or Mars. To achieve this, we conducted detailed Geant4 Monte Carlo simulations of particle interactions with a realistic brain structure extracted from actual CT scans. We studied the radiation distribution inside a human head and at different parts of the brain's lobes. The simulations were validated by comparing the results based on different human head structures and different physics lists in the particle transport code. Based on the validated models, we calculated Brain Response Function (BRF)s that represent the ready-to-use functions of energy/dose deposit induced by primary particles of protons, helium, neutron, and heavier ions such as carbon, nitrogen, and iron impinging isotropically towards the head. We used a matrix approach to obtain these BRFs, which describe the probabilistic description of the deposited energy of a primary particle with a defined type and energy in the brain. All possible interactions that may be triggered when the particle and its secondaries penetrate through the head are included in the BRF. These functions can be used to quickly convert a certain ambient GCR spectrum or SEPs into the absorbed energy/dose within the entire head and also at different lobes of the brain. Our simulations revealed that the absorbed dose for charged particles in the brain increase with incoming particle energy in the range below 100-150 MeV/nuc, after which they decrease slightly at higher energies. Alternatively, for primary neutrons, the contribution to the dose/energy increases with energy. We derived BRFs for dose deposit at different lobes, which only differ slightly at low energies (below ~ 100 MeV/nuc) due to the position and geometry of the lobes. Lobes with less external shielding by the cranium are more exposed to the radiation contribution by low-energy primary particles. We also discussed the influence of an extra shield between the particle source and the head, and the dose deposit in the brain depending on the shielding thickness. For charged particles, shielding effectively reduces the head/lobe dose contributed by low-energy particles, which is important during SEP events where most particles are below a few hundred MeV. However, the shielding of neutrons is non-trivial as the generation of secondaries by neutrons with energies $\gtrsim 200$ MeV becomes more effective with enhanced shielding depth. The study emphasizes the importance of using sufficient shielding protection against low-energy charged particles, which may have a substantial increase during SEP events. However, the shielding strategy against neutron-induced radiation is not as straightforward. The following article is reproduced from Khaksarighiri et al. (2020) with permission from Life Science in Space

Research journal:

Calculation of dose distribution in a realistic brain structure and the indication of space radiation influence on human brains

Khaksarighiri, S., Guo, J., Wimmer-Schweingruber, R., Narici, L., Lohf, H. (2020). Life Sciences in Space Research, 27, 33-48.

My contribution to this paper is 80% of the overall content and research efforts.



Contents lists available at ScienceDirect

Life Sciences in Space Research

journal homepage: www.elsevier.com/locate/lssr

Calculation of dose distribution in a realistic brain structure and the indication of space radiation influence on human brains

Salman Khaksarighiri^a, Jingnan Guo^{*,b,c,a}, Robert Wimmer-Schweingruber^a, Livio Narici^{d,e}, Henning Lohf^a

^a Institute of Experimental and Applied Physics, University of Kiel, Kiel, DE24118, Germany

^b School of Earth and Space Sciences, University of Science and Technology of China, Hefei, 230026, China

^c CAS Center for Excellence in Comparative Planetology, USTC, Hefei, China

^d Departments of Physics, the University of Rome 'Tor Vergata', Rome, Italy

^e INFN sect Tor Vergata, Rome, Italy

ARTICLE INFO

Keywords:

Space Exploration

Radiation Risk

Geant4

Brain simulation

ABSTRACT

One of the most important steps in the near-future space age will be a crew mission returning to the Moon and even a manned mission to Mars. Unfortunately, such a mission will expose astronauts to unavoidable cosmic radiation in deep space and on the Martian or lunar surface. Thus, a better understanding of the radiation environment for such a mission and the consequent biological impacts on humans, in particular the human brains, is critical. The need for this better understanding is strongly suggested by investigations on animal models and on human patients who were undergoing irradiation for cancer therapy in the head. These have revealed unexpected alterations in the central nervous system behavior and sensitivity of mature neurons in the brain to charged particles. However, such experiments shall not be carried out realistically in space using humans. Therefore, to investigate the impact of cosmic radiation on human brains and the potential influence on the brain functions, we model and study the cosmic particle-induced radiation dose in a realistic head structure. Specifically speaking, 134 slices of computed tomography (CT) images of an actual human head have been used as a 3D phantom in Geant4 (GEometry AND Tracking), which is a Monte Carlo tool for simulating energetic particles impinging into different parts of the brain and deliver radiation dose therein. As a first step, we compare the influence of different brain structures (e.g., with or without bones, with or without soft tissues) to the resulting dose therein to demonstrate the necessity of using a realistic brain structure for our investigation. Afterward, we calculate energy-dependent functions of dose distribution, for the most important (some of the most abundant and most biologically-relevant) particle types encountered during a deep space mission inside a spacecraft or habitat such as protons, helium ions, neutrons and some major heavier ions like carbon, nitrogen, and iron particles. Furthermore, two different scenarios have been modeled as a comparison: a human head without shielding protection and a human head with an aluminum shielding shell around (of varying thickness). These functions can then be used to fold with energetic cosmic-ray particle spectra of the ambient environment for obtaining the dose rate distribution at different lobes of the human brain. Our calculation of these functions can serve as a ready tool and a baseline for further evaluations of the radiation in the brain encountered during a space mission with different radiation fields, such as on the surface of the Moon or Mars.

1. Motivation and Introduction

In recent years, the development of space technology has provided opportunities for scientific, industrial, and even commercial missions to explore the space outside our planet. One of the most important steps in the near-future space age will be a crew mission returning to the Moon and even a manned mission to Mars. However, various issues may cause

health problems for astronauts in deep space and on the surface of other planets, such as physiological problems caused by microgravity or reduced gravity such as bone demineralization, skeletal muscle atrophy, and reductions in plasma volume or cell mass (Demontis et al., 2017; Hodkinson et al., 2017; Harris et al., 2015; Jandial et al., 2017). Psychological stresses may arise from isolation and living for months in a spacecraft with the high-pressure and high-risk environment (Sandal

* Corresponding author.

E-mail address: jnguo@ustc.edu.cn (J. Guo).

<https://doi.org/10.1016/j.lssr.2020.07.003>

Received 11 March 2020; Received in revised form 1 July 2020; Accepted 2 July 2020

Available online 15 July 2020

2214-5524/ © 2020 The Committee on Space Research (COSPAR). Published by Elsevier Ltd. All rights reserved.

et al., 2006; Kanas, 2014; 2010). In particular, risks induced by exposure to space radiation, have been classified as one of the key stoppers of such missions (Huff Janice. et al., 2016; Walsh et al., 2019; Cucinotta et al., 2017) and thus the assessment of such radiation and the evaluation of its biological consequences have been given one of the highest research priorities in the field of space exploration.

For long-term missions in space where high energetic particles are more abundant than those in normal daily life, ionizing radiation may induce cancer via particle interaction with Deoxyribonucleic acid (DNA) molecules, either through direct ionization process or by generating secondary particles and activating free radicals in the cell which further interact with the DNA chains. These interactions can damage the DNA structure and thus destruct the instructions encoded for cell reproduction (Cucinotta et al., 2001; Cucinotta and Durante, 2006; Cucinotta et al., 2013; Barcellos-Hoff et al., 2015; Huff Janice. et al., 2016). Additionally, radiation can also interfere with the central nervous system and induce degenerative effects, including cataracts (Cucinotta et al., 2014; Kennedy, 2014). Some researchers suggest that heart diseases may also occur (Boerma et al., 2015; Delp et al., 2016; Reynolds and Day, 2017), while some others argue there is no evidence for an increase in circulatory disease mortality in astronauts (Cucinotta et al., 2016).

1.1. Radiation environment for a deep-space mission

The main radiation exposure for astronauts during a deep space mission outside Earth's magnetosphere and radiation belts includes the omnipresent Galactic Cosmic Ray (GCR) background, and the sporadic Solar Energetic Particles (SEP) generated during solar eruptions.

GCRs constitute a continuous, relatively low flux of very high energy particles, made up of roughly 87% protons, 12% helium ions, and only about 1% heavier nuclei (Simpson, 1983). They originate from outside the solar system and are modulated by heliospheric magnetic fields, which evolve dynamically as solar activity varies in time and space, with a quasi-periodical 11-year cycle (Parker, 1965, e.g.). GCR flux may be one order of magnitude higher (at low energies below a few GeV/nuc) during solar minimum years than during Solar maximum conditions due to modulated particle diffusion by heliospheric magnetic fields. This would correspond to a small, but still significant, difference in the total dose.

In contrast to GCRs, SEPs – mainly protons and electrons – are accelerated and released into interplanetary space during sporadic solar eruptions such as flares and Coronal Mass Ejection (CME) associated shocks (Lario, 2005, e.g.). Therefore SEP events are more likely to occur during solar maximum and can consist of various particle species which are accelerated in a wide energy range from suprathermal (few keV) up to relativistic (few GeV) energies (Desai and Giacalone, 2016).

Extra shielding material interposing between space GCRs/SEPs and the astronauts will change the radiation field and thus the exposure to the astronauts. The shielding material modulates the primary radiation. This shield could be space vessels, planetary habitats, space suits, or planetary atmosphere or even regolith. Most importantly, this process will produce neutrons that are quite biologically-relevant for humans.

1.2. Radiation effects on human/animal brains

As known, our brain regulates the functions of our body and interprets information from the outside world. During a deep space mission such as a journey to Mars, astronauts ought to accommodate to a completely different environment which requires the flexibility and adaptivity of the brain. This means assessing the potential influence of radiation on a human brain is critical for mission success.

Following the Apollo 11 mission report of Aldrin about flashes of light perceived without real light, several investigations were carried out to study the problem on the ground and in orbit. In 1972, experiments using high energy nitrogen at Princeton-Penn Particle

Accelerator and Lawrence Berkeley Laboratory (Budinger et al., 1972) revealed that energetic and charged particles passing through the occipital cortex or the retina cause light flashes in closed eyes. This phenomenon has also been reported by astronauts during other Apollo missions (Pinsky et al., 1974) and later on the Russian Mir space station as well as on the International Space Station (ISS) where dedicated investigations have also been considered (for an overview and a complete list of all these ground and space studies see Narici (2008)).

Investigations on the acute electrophysiological behavior of mice during eye/brain irradiation with very short carbon ion pulses (2 ms, 10^3 ions per pulse) showed for the first time the existence of electrophysiological responses to particles and their similarity to those produced by light (Sannita et al., 2007). Furthermore, it was shown that the relevant interaction was probably not only in the retina but possibly also in the optic nerve / visual cortex (Carozzo et al., 2015). Similar results have been shown in astronauts flying in the ISS (Narici, 2008). These studies, aimed at investigating the origin of the light flashes mentioned above, were completed by a biochemical investigation of the possible mechanisms involving the retina (Narici et al., 2012; 2013).

Studies based on reports by patients who were undergoing conventional cranial radiotherapy pointed out that central nervous system (CNS) behavioral changes may occur, such as chronic fatigue, long-term anxiety, and depression (Tofilon and Fike, 2000). Other progressive and adverse effects on cognition, including disturbances in learning, memory, processing speed, attention, and cognitive flexibility, have been reported following conventional radiotherapy and in experiments with animal models (Andersen and Tewfik, 1985; Parihar et al., 2016; 2015; Tang et al., 2012). Most recently it has been shown studying proton-therapy patients that these illusions can affect other senses as well, requiring, therefore, a more general, still unknown, interaction mechanism (Narici et al., 2020). Some children of the atomic-bomb survivors in Japan had even become children with intellectual disabilities (OTAKE, 1998). Investigation of the CNS effects using animal models reveals the enhanced degradation of DNA and changes of dopamine function (Rabin et al., 2000), which may cause accelerated striatal aging (Joseph et al., 1992).

Radiobiology studies of CNS effects based on modeling of space radiation using experimental and empirical models assessed their possible effects expected during a long-term space mission to Mars (Cucinotta et al., 2014). These studies also suggest that space radiation risks include possible damage in short-term memory as well as negative effects on the crew's performance and decisions. Additionally, Alzheimer's diseases or other dementia could also be detected as a late CNS effect.

Research using mice exposed to doses of radiation equivalent to that of a cruise to Mars (Zeitlin et al., 2013) indicates that the corresponding space radiation may cause the reduction of dendritic complexity and the alteration in synaptic integrity and thus influence the cognitive performances over an extended period (Parihar et al., 2015; 2016). These medical and experiment models can be further used to evaluate carcinogenesis risks in astronauts due to exposure to space radiation.

The above studies suggest that the cosmic radiation may interfere with normal brain functions, in acute and/or chronic ways. In this paper, we will simulate the physical parameters (fluence, dose) and leave their connection to risk assessment to a following work.

1.3. Structure of a human brain

Realistic experiments for radiation effects on human brains in space are ethically and technically challenging. Therefore, we model the impact of cosmic radiation on human brains and investigate the related risks. In particular, this involves the ionizing radiation-induced secondary radiation in different parts of a real human brain structure.

As known, human heads have a complex shape and structure compared to some other body organs and consists of various substances, including bones, water, soft tissues, and harder tissues.

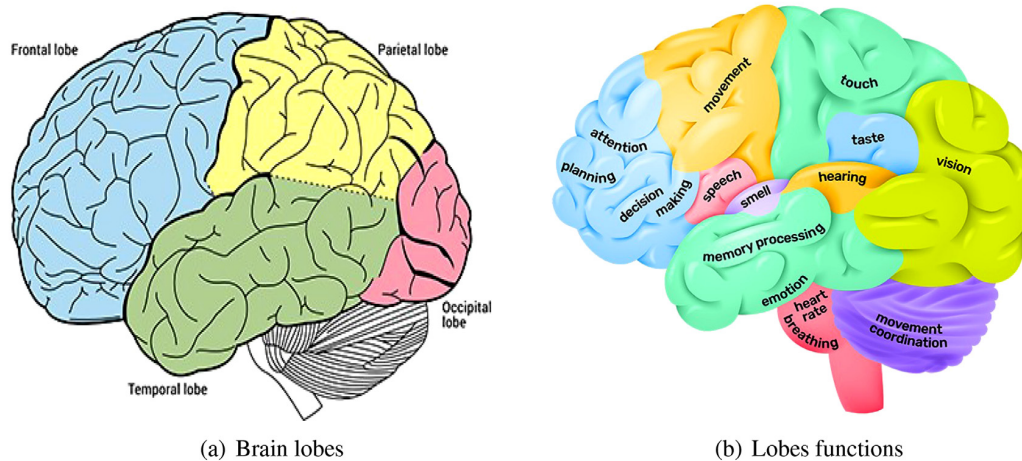


Fig. 1. Structures and functions of a human brain. (a) Different lobes of a human brain. (b) Main functions of different parts of the brain. (Institute, 2018)

In a human head, the CNS composes of the brain and spinal cord. The uppermost region of the CNS is called the cerebrum, which is the largest part of the brain containing the cerebral cortex and some sub-cortical structures. The cerebral cortex is the exterior layer that gives the brain its characteristic wrinkly appearance. The cerebral cortex contains two cerebral hemispheres joined by the corpus callosum. Each hemisphere is divided into frontal, parietal, temporal, and occipital lobes, as shown in Fig. 1 (a). Although most brain functions rely on several different regions across the entire brain working in conjunction, each lobe is mainly responsible for certain cognitive functions (Zhang, 2019b; 2019a), as indicated in Fig. 1 (b). The main functions of each lobe can be briefly summarized as:

- **Frontal lobe:** This region of the brain occupies the front part of the skull and lies behind the forehead. It is associated with planning, decision making, voluntary muscle movement, processing speech, smell, and emotions.
- **Parietal lobe:** This part of the brain processes sensory information and is responsible for determining spatial awareness, navigation, and positioning. It is also involved in processing information related to taste, temperature, and touch.
- **Temporal lobe:** This lobe is associated with processing visual and auditory information and controls some aspects of language perception, memory, and emotion.
- **Occipital lobe:** This is the visual processing center of the brain and contains the largest proportion of the visual cortex region.

Therefore, it is critical to access the amount of energy deposited in each lobe in the cosmic radiation environment for crewed space missions and consequently improve the evaluation of potential effects on astronauts' cognitive performance.

2. Model Description and Implementation

Geant4 (Agostinelli et al., 2003; Allison et al., 2016, GEometry And Tracking,) is a well-established, and three-dimensional Monte Carlo particle transport tool that uses object-oriented C++ programming language and the version of 10.4 has been used in the current study. GEANT4 has been successfully utilized for different applications and purposes, varying from simulations of large complex high-energy experiments to medical cancer radiotherapy to microdosimetry in space radiation and so on.

2.1. Head geometry for the simulation based on CT images

Impacts of space radiation on human torso and organs therein have been considered in various previous works such as, by the recent ESA/PERSEO (PERsonal Radiation Shielding for interplanetary missiOns) project (Vuolo et al., 2017; Baiocco et al., 2018) using the GEANT4/GRAS toolkit. As a complementary study, only the head structure is included in our study, while the human body and its exposure to radiation, are not discussed here. We do note that the body mass could act as a shield partially protecting the brain from below, and modify some of the upward radiation towards the head. Therefore, the model used here with an isotropic spherical source surrounding the head might result in an over-estimation of the corresponding dose in the brain. More precise estimations of the upward radiation would require further modeling with an additional body phantom to which the head is attached.

In this study, we use voxelized geometries in GEANT4 based on CT scans of a real head structure, which contains the whole brain structure shown in Fig. 1. Specifically speaking, there are 134 slices of CT images, each with 1.01 mm thickness, originally in Digital Imaging and Communications in Medicine (DICOM) format (Varma, 2012). The slices are parallel to the ground in the frame of a standing person. They are taken from the top of the head to the part of the lower jaw and some parts of the neck, covering the whole brain structure. An example of a re-constructed head based on the CT images can be found in Fig. 12 of Appendix A.

Each DICOM file consists of a Metadata header followed by binary data for each pixel. Metadata describes the image matrix dimensions, the depth of the slice layer, the patient information, and so on. The pixel data contain numerical values with so-called Hounsfield units (HU), which are dimensionless units describing the density (also called radiodensity) of each voxel (Bushberg et al., 2012; Kalender, 2011). One HU can be mathematically defined as:

$$1 \text{ HU} = 1000 \times \frac{\mu - \mu_{\text{water}}}{\mu_{\text{water}} - \mu_{\text{air}}}, \quad (1)$$

where μ_{water} and μ_{air} are the linear attenuation coefficients of water and air, respectively. In CT images, the linear attenuation coefficient (μ) is a constant for certain material that describes the fraction of attenuated incident photons in a monoenergetic beam per unit thickness of the target material. It includes the most relevant interactions, including coherent scatter, Compton scatter, and photoelectric effect. Equation 1 sets the radiodensity of water to 0 and the radiodensity of air to -1000 HU. Materials with densities between water and air would have HU values in between, and materials with densities larger than water (e.g.,

bones) would have positive HU values.

Based on the 3D matrix in these CT images containing values in HU, we set up the head geometry in GEANT4 for the following particle transport simulations. To do so, the HU value of each voxel is converted to the material composition and density. Using the Jiang and Paganetti procedure (Jiang et al., 2007), HU values between -1000 to 5000 are divided into several intervals representing different parts of the brain (e.g., water, soft tissue, bone, etc.) with different densities.

2.2. Particle source setup and method of the simulation

Particle Source Setups: Our system comprises a particle source, which induces primary and secondary particle interactions with the brain, and a human brain, which is modeled with different levels of detail. We first show (in Sec. 3.1) that it is important to have maximum brain details based on the head geometry imported from CT images as described above in Sec. 2.1. The particle source is set up tightly around the human head. Primary particles with a specific type, energy, and direction, are generated in the inner part of the sphere. Protons, Helium ions, neutrons, and heavier ions such as carbon, nitrogen, and iron particles have been considered in the current study as they are the most abundant and biologically-relevant particles in the environment of a deep space mission. GCR protons and helium ions make up 99% of the GCR flux (Sec. 1.1) and neutrons, as secondaries generated through *in-situ* shielding, contribute to an additional important component such as on the surface of Mars (Köhler et al., 2014) or within a spacecraft in deep space (Köhler et al., 2015). Heavy ions, such as carbon and nitrogen in deep space, are also considered due to their high biological relevance. Irons, have also been studied here because they are currently thought to be a significant contribution to CNS risks in ground-based experiments (Rivera et al., 2013; Liu et al., 2019). However, they fragment more easily, and their contributions to the radiation behind a shield, can be significantly reduced as measured within a spacecraft (Ehresmann et al., 2016) or on the surface of Mars (Ehresmann et al., 2014).

The number of particles, their energy range and distribution, as well as the size of the source spheres, are shown in Table 1 for different simulation setups. Apart from the model setup for scenario 1, which is a test scenario, all simulations have considered an isotropic source of particles around the human head. Particles are generated in a Monte Carlo manner in GEANT4, each with an initial energy and direction following the required initial distribution. As they pass through the head structure, they may lose their energy via ionization energy loss or interact with the head materials and generate secondaries, which further contribute to the dose deposit in the brain. We can obtain the dose accumulated inside the entire brain and also at different parts of the brain.

Extra shield around the head: We also implement a “shield” between the source and the brain in a few simulation setups shown in Sec. 3.4. This shield may mimic several different kinds of shielding: the vessel hull plus instrumentation, the walls of a Mars base, extra “personal” shield worn by the astronaut around the head, etc. In the case of extra-vehicle activities (EVA), this shield will be provided just by the suit

helmet. The shield is modeled in aluminum equivalent, which is a simplified and conventional choice used in the community. The used thicknesses are 0.2 cm, 0.5 cm, 2 cm, 5 cm, and 10 cm, with the first being compatible with a suit helmet thickness and the rest for different possible shielding depths within a habitat. Some previous work based on ALTEA measurements (Tessa et al., 2009; Narici et al., 2012) has provided estimations of Al-equivalent shielding depths in different directions of the ISS ranging from 5 cm to 16 cm, with the 16 cm (more than 40 g/cm²) case corresponding to the shielding in the direction where most of the moduli/nodes of the station are aligned and is an unlikely situation for a vessel for deep space. The results of the dose distribution inside the brain are then compared with the “no shield” results.

Brain Response Functions: Normally one can use a known particle spectrum (either generated from models or obtained from direct measurement) as initial (primary) particles to simulate the particle interactions with the brain. However, to enhance the flexibility of our modeled results making it possible to quickly obtain the dose (and dose distribution) for different incoming particle spectra, we use a matrix approach following (Guo et al., 2018; 2019b) to obtain the “brain response functions” (BRF) of the dose dependence on primary particle energy. A BRF function is a probability description of all possible interactions of a particle with a defined type and energy entering the human head depositing energy at a certain part of the brain. The function has a unit of dose per fluence of primary particles (protons, 4He, neutrons, or carbon, nitrogen, and iron ions) and can be used to fold (i.e., multiply per energy bin and then integrate) with a given primary particle spectrum for obtaining the radiation dose inside the brain, similar to the approach in Guo et al. (2019b).

Different Simulation Scenarios: Table 1 also shows four different scenarios with different simulation setups: the first two are aimed at model validation and investigation of its potential limitations and uncertainties while the last two scenarios are the main outputs of our research. The main purpose and setup for each simulation scenario are listed below.

- **scenario 1:** To evaluate the necessity/difference of using a head structure with realistic brain densities in contrast to using a simplified water-equivalent head, we compare simulation results based on a head geometry with different contents (different material and densities).
- **scenario 2:** We compare the calculated BRFs using two different physics lists of GEANT4 in order to explore the influence of different particle interaction models on the results.
- **scenario 3:** The energy and dose BRFs of incoming protons, neutrons, Helium ions and some heavier ions such as Carbon, Nitrogen and Iron particles for different lobes of the brain are calculated.
- **scenario 4:** The energy and dose BRFs of the same particles as in scenario 3 are calculated, with an additional layer of aluminum shielding between the head and the particle source sphere.

In the next section, we will go through each of these four scenarios

Table 1
GEANT4 Model setup for different simulation scenarios. More descriptions can be found in the text of section 3.

Various scenarios	Physics list	Particle Number	Energy distribution	Energy (range)/MeV	Source shape & distribution
Scenario 1 (Sec. 3.1): Different head structures	QGSP_BIC	10 ⁷	Mono	100	Sphere r=20 cm
Scenario 2 (Sec. 3.2): Different physics lists	3 head structures: (a) water, (b) water & bone, (c) actual head CT scan QGSP_BIC QGSP_BERT	10 ⁶ per bin	100 log bins	1-10 ⁴	Sphere r=20 cm
Scenario 3 (Sec. 3.3): Dose distribution in lobes	QGSP_BIC	10 ⁶ per bin	100 log bins	1-10 ⁴	Sphere r=20 cm
Scenario 4 (Sec. 3.4): Head with shielding	4 lobes: frontal, parietal, temporal and occipital lobe QGSP_BIC	10 ⁶ per bin	100 log bins	1-10 ⁴	Sphere r=20 cm
	4 lobes and 5 shielding depths (2mm, 2cm, 5mm, 5cm and 10cm of Al)				

and discuss the main simulation results of each scenario.

3. Simulation Results and Discussions

3.1. Scenario 1: comparison of three different head structures

An approximate spherical shape, with an average size of human heads, filled with water, has been often used by previous studies for assessing the radiation therein (Solovev.A.N, 2015; Diaz Merchan and Torres, 2016; Zhang.Rui, 2010). However, we would like to evaluate the difference and possible advantage of using a realistic head structure in comparison to using a water-filled head structure concerning the dose distribution inside the brain. As shown in Fig. 2, we consider three different head structures: (a) a head filled with only water by setting all HU values into zero within the head of the CT images, (b) a head structure containing water, a hollow part (the nose) and all other hard tissues with a fixed density of bones, and (c) the actual complex head with densities in each voxel obtained using the procedure of Jiang et al. (2007) as described in Sec. 2.1.

To highlight the contrast of the comparison, we use mono-energetic protons with an energy of 100 MeV, which should have the ionizing stopping depth in water (≈ 7 cm) within the size of a human head. Particles with lower energies may not reach the innermost part of the brain to reflect possible differences of the deposited energy among different setups. Particles with higher relativistic energies would likely pass through the brain depositing the minimum energy loss, and can not easily show the dose distribution differences in three setups. As noted in Table 1, a total of 10^7 particles, have been simulated with their initial position uniformly distributed on a sphere of 20 cm radius surrounding the head. In the current scenario, the initial direction of particles from the source sphere is set to be perpendicular to the sphere. In other words, all particles are directed approximately towards the center of the brain. In comparison to the isotropic initial direction used in other scenarios, this setup can maximize the simulation efficiency (i.e., all particles will pass the brain with approximately maximum interaction length) and also better show the stopping depth of the particles which reflects the position of the maximum dose deposit in the brain.

The upper panels of Fig. 3 plot the dose distribution in the three different head structures shown at the same CT slice as in Fig. 2. The 2D images contain dose values at this slice resulting from 10^7 particles of 100 MeV initial energy. Since the number of particles (or the primary radiation flux) is adjustable in simulations, the shown absolute values of the dose in the color bar, should not be taken as a realistic demonstration of dose deposit. In case (a) where the head contains only water, the maximum dose is detected near the center of the brain, which

corresponds to the approximate stopping depth of 100 MeV protons in water. In case (b) where the bone and hollow parts are also considered, the dose distribution shows more patterns following the structure of the head. In case (c) where the real head densities are used in the simulation, the maximum dose, in the center of the head, as shown in cases (a), and (b) is less visible. This is because protons in case (c) lose more energy passing through the bone and tissue structure at the outer part of the brain and consequently result in less energy deposit at the innermost part of the head.

The lower panels of Fig. 3 show the differences of the 2D images when comparing cases (a), (b), and (c). A difference as large as 0.6–0.7 μGy , which is more than half of the maximum dose deposited in the brain shown in the upper panels, can be visible at the frontal central part of the head when comparing case (a) and (b) or case (a) and (c). While this is the maximum difference found at individual pixels of the selected slice, we also compared the difference of the dose recorded in each lobe. For the frontal lobe, the overall difference between (a) water and (b) water-bone is 12.7%, between (a) water and (c) head, reaches 15.3%, and between (b) water-bone and (c) head is lower: 2.6%. For the parietal lobe, the dose difference between (a) and (b) is 16.6%, between (a) and (c), is as large as 26.9% and between (b) and (c) is 9.5%. For the temporal lobe, the difference between (a) and (b) is 6.6%, between (a) and (c), reaches 12.5%, and between (b) and (c) is 5.8%. Finally, for the occipital lobe, the difference between (a) and (b) is 12%, between (a) and (c), is 8.9% and between (b) and (c) is only about 3%.

Therefore, for incoming particles with the energy around 100 MeV, the difference of the calculated dose deposit in each lobe among three different head structures depends on the geometry and the location of the lobes. Since we are interested in the dose deposit in each lobe for the evaluation of the radiation effects on brain functions, in this study, we adopt the realistic head structure, as shown in Fig. 2 (c). We do note that in the case of GCR radiation, which contains a large amount of high-energy particles, the difference between different geometries could be much smaller. However, within a heavily shielded habitat where low-energy secondaries are more abundant or during an SEP event where most particles are below hundreds of MeV, this consideration would become important.

3.2. Scenario 2: comparison between different physics lists

To maximize its flexibility, GEANT4 allows users to select physics models of particle interactions relevant to the considered radiation environment via defining a specific 'physics list' which, is named based on the combination of various models in different energy ranges (Geant4_Collaboration, 2017). Depending on the incoming particle type, energy, and the material that particles interact with, different

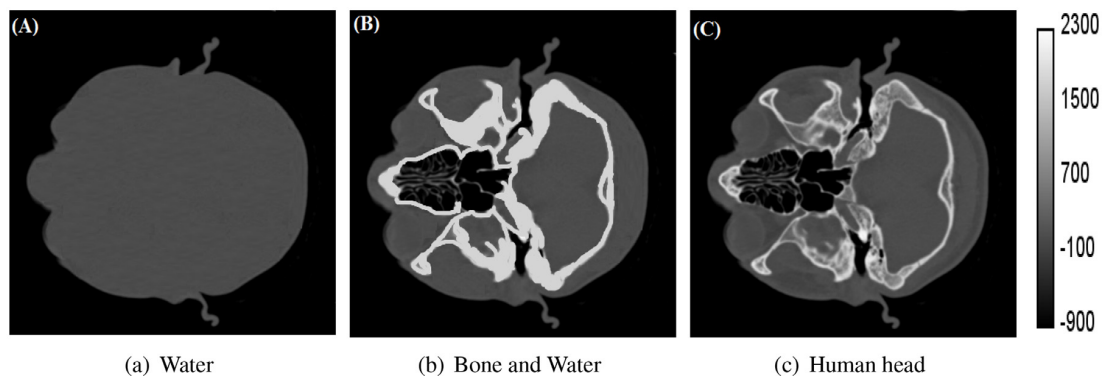


Fig. 2. Different head structures/contents as three different setup geometries for the GEANT4 simulations. Each panel displays the HU values (shown in the color bar) of a CT slice as a cross-section of the head viewed from above (the person is facing the left side of the image). The slice at a depth of 11 cm, near the nose, is chosen out of 134 slices for displays here. The image in (a) shows a head filled with only water by setting all HU values to zero within the head; the head in (b) contains water, bone and a hollow part (the nose); the head in (c) is the original CT scan of the head containing different structures: water, bones, hard and soft tissues.

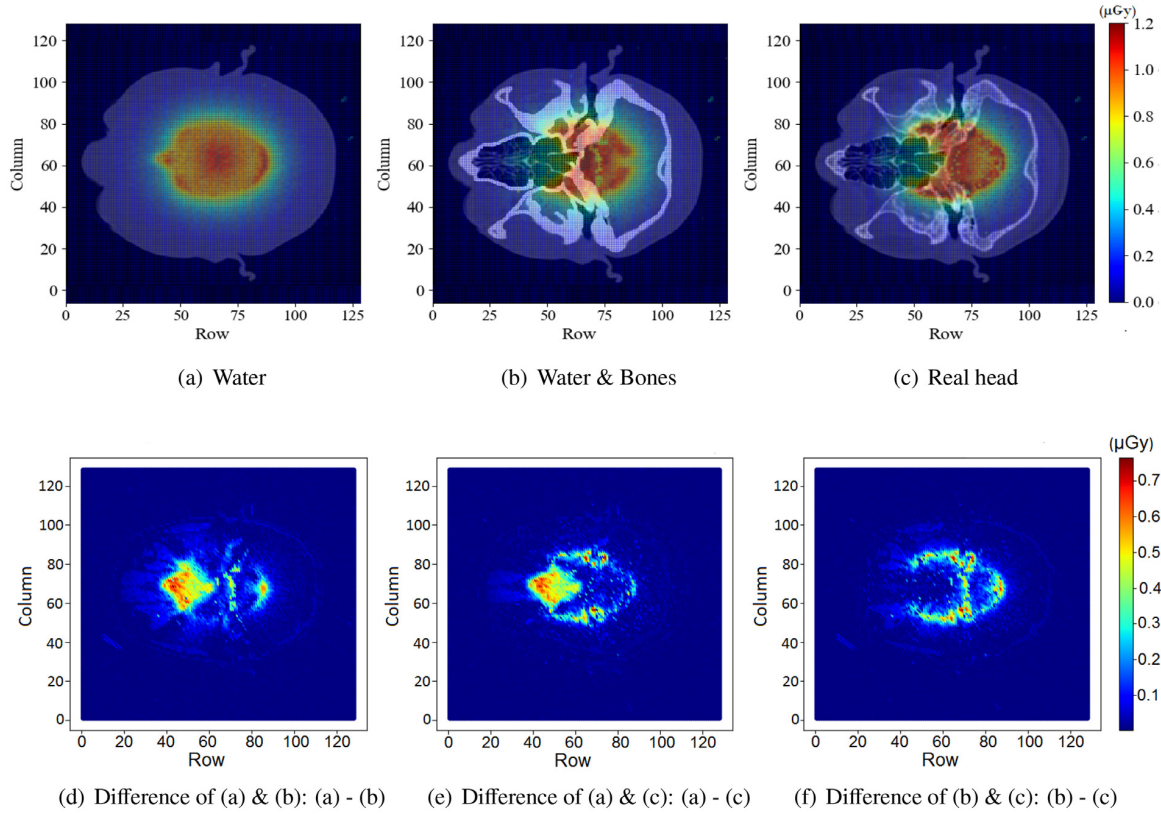


Fig. 3. Upper panels: Dose distribution of 10^7 protons with an initial energy of 100 MeV impinging towards the approximate center of the brain based on three different structures of a head: (a) filled with water, (b) containing water, bones and a hollow part, and (c) with actual densities extracted from the CT scan. A transparent layer showing the structure of the head, as in Fig. 2 is also superposed in each panel. Lower panels: Image difference (subtraction of the values at the same pixel position from two images) between case (a) and (b), case (a) and (c) as well as case (b) and (c).

physics lists might result in a different assessment of the radiation environment (Guo et al., 2019a, e.g.).

To better estimate the uncertainty of our modeling approach, we employ two different physics lists, "QGSP_BIC" and "QGSP_BERT", to examine their differences when applied to model the space radiation impact on human brains. Both lists include "QGS" which stands for the Quark-Gluon String model for high energy particles ($> \sim 20$ GeV). "P" stands for the Precompound model used for the de-excitation process for nucleon-induced reactions below 1–2 MeV. BIC uses the Binary Cascade Model for particles $< \sim 10$ GeV. However, BERT uses the Bertini Cascade Model in this energy range. In the case of examining neutrons, we also use, in both lists, the "HP" option, which switches on the high precision neutron elastic and inelastic scattering model for neutrons below 20 MeV.

Initial particles uniformly distributed on a sphere with a 20 cm radius (Table 1) have impinged isotropically inward towards the head. The particle energies are distributed from 1 MeV to 10 GeV uniformly in 100 bins with the bin width growing logarithmically with energy. A total of 10^8 particles have been simulated with 10^6 particles in each bin. In other words, the simulated particles have a power-law distribution with a power-law index of $\alpha = -1$. Based on above-described setup of particle source geometry and energy distribution, a total of six simulations have been carried out in scenario 2: primary protons or helium ions simulated using the QGSP_BERT physics list, primary protons or helium ions with QGSP_BIC, primary neutrons with QGSP_BERT_HP, and finally primary neutrons with QGSP_BIC_HP.

Fig. 4 plots the comparison of the calculated dose between two GEANT4 physics lists. The x-axis of the figure shows the initial energy of the incident particles. The y-axis shows the total deposited dose in

the brain, as a function of incoming particle energy and it is, normalized to the fluence used in the simulation which is the number of particles in each bin (10^6) scaled by πA with π being the integrated solid angle of the source, A being the area of the source sphere, i.e., $A = 4\pi r^2$ ($r = 20$ cm). Since the difference of BRFs from different physics lists are hardly seen in the figure, we plot the ratio of the BRF between two physics lists in the lower panel of the figure. The differences are within 2.5%, 3.8 %, and 6.8 % for protons, neutrons, and helium ions, respectively, which suggests that the choice between these two lists hardly affects the assessment of the resulting dose deposit for concerned particle energy range and head materials. Therefore, in the following simulation scenarios, we use only the QGSP_BIC (or QGSP_BIC_HP for neutrons) list for simulating the dose deposit inside the head as well as the brain therein.

3.3. Scenario 3: Energy and dose functions for different lobes of the brain

In this scenario, we simulate the dose distribution within different parts of the human brain using actual head densities extracted from the CT images. Protons, neutrons, Helium, and heavier ions such as Carbon, Nitrogen, and Iron particles, have been considered as source particles, and their number, energy distribution, and the initial velocity distribution are set up, in the same way as in scenario 2 (Sec. 3.2). In order to extract the total energy and dose deposit in each part (lobe) of the brain, we use a 3D-Slicer tool to differentiate each voxel into different lobes of the brain structure: frontal, parietal, temporal and occipital lobes as described in Sec. 1.3. More descriptions of the 3D-Slicer tool can be found in Appendix A. There are two ways to calculate the total dose deposit in each lobe. First, after reading out the energy deposit in

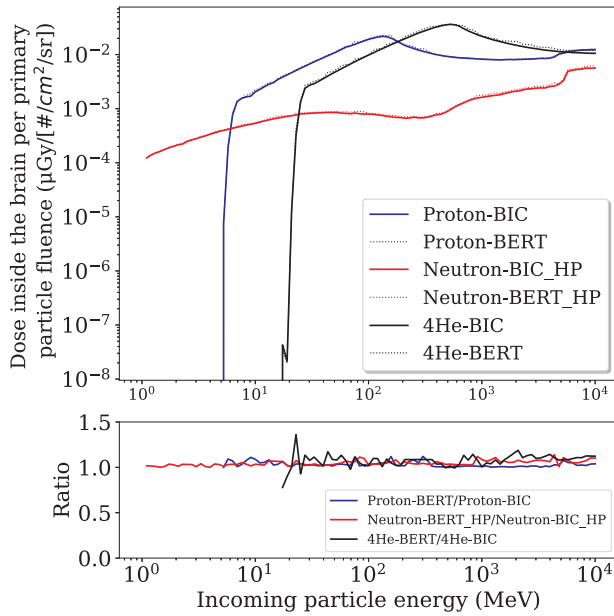


Fig. 4. Upper panel: Normalized dose functions versus incident particle energy (either protons, neutrons or ^4He ions) based on simulation results using different physics lists of GEANT4: QGSP_BIC (blue solid) and QGSP_BERT (blue dotted) for protons, QGSP_BIC_HP (red solid) and QGSP_BERT_HP (red dotted) for neutrons, as well as QGSP_BIC (black solid) and QGSP_BERT (black dotted) for ^4He ions. Lower panel: The ratio of the functions between two physics lists for protons (blue) and neutrons (red) and ^4He ions (black), respectively. The simulation setup is described in Sec. 3.2.

each voxel from the original GEANT4 simulations, we sum up the energy from voxels belonging to the same lobe, which is then converted into dose by dividing the total mass of that lobe. Second, we average the dose of all voxels belonging to the same lobe to be the dose in that lobe. The results obtained from the two methods are hardly distinguishable, and here we show the dose functions based on the first method.

Figs. 5, 6, and 7 show the response functions of the deposited energy and dose versus incident particle energy (from 1 MeV to 100 GeV for Iron and from 1 MeV to 10 GeV for other species) within each of the 4 major lobes of the brain. The figure reveals that the deposited energy and dose for protons in the human brain increase with incident energy for particles below ~ 100 – 150 MeV where the peak of the BRF is detected. This is because the head has an approximate size (radius), which is equivalent to the stopping depth of protons with ~ 100 – 150 MeV energies. The same pattern can be seen for helium ions in the energy range of about 400–500 MeV (~ 100 – 150 MeV/nuc) as well as for heavier ions such as carbon, nitrogen, and iron particles in the energy ranges 1200–1500 MeV, 1450–1900 MeV, and 6500–8800 MeV respectively. Above this energy, charged particles start penetrating through the head more easily, thus depositing slightly less dose/energy inside the brain. Meantime, particles with higher energies and charges are also more likely to generate secondary particles, which can also contribute to the dose. That is why the BRF does not decline significantly, and in fact, rises up slightly at high energies above a few GeV/nuc, as shown in Fig. 5.

However, in contrast to charged particles, neutrons present a different trend, as shown in Fig. 8: the contribution to the dose/energy increases with neutron energy. This is because neutrons, with zero charge, can induce cascaded generation of secondary particles by successively triggering complex nuclear reactions in the human body, such as via elastic interactions producing recoil protons, which would further deposit dose through ionization processes. The efficiency of this process grows with the energy of incoming neutrons.

The upper panels of Figs. 5, 6, and 7 plot the total energy, normalized by primary particle fluence in each bin, deposited in each brain lobe. It clearly shows that energy deposited in the frontal lobe is largest for all incident particle types at different energies. This is followed by the parietal lobe, temporal lobe, and the occipital lobe. This difference is mainly due to the size/mass differences of the four lobes (see Fig. 1) as the total radiation energy is proportional to the material mass.

On the other hand, dose, as shown in the lower panels of the figures, differs little between different lobes, especially for incident particles with high energies. This is because the dose is scaled to the mass of the target material (see its definition in Sec. 1.1). However, at low energies (charged particles below about 100 MeV/nuc), there are some differences in the dose BRF between different lobes. This is mainly due to the position and geometry of the lobes within the head. For lobes that have a larger outer part, charged particles with low energies are more likely to reach and stop therein. For the inner part of the lobes, particles without sufficient energy may not reach there. Also, the head structure plays a role. As shown in Fig. 2, there are less bone and hard tissues at the front side of the head, thus leaving the frontal lobe more exposed to low-energy particles.

However, for neutrons, there is no real differentiation of the dose BRF between different lobes as neutrons are free-of-charge and do not follow the basic procedure of ionization energy loss. They generate secondaries (both charged and neutral particles), which further penetrate through the head, and interact with materials therein and, thus, their contribution to dose grows with energy. Since neutrons rarely exist in deep space and are generated mostly as secondaries in a shielded environment, this makes it particularly important to assess the full neutron spectra in such an environment, e.g., within a spacecraft or on/below the planet's surface.

3.4. Scenario 4: Evaluation of the shielding effect on brain response functions

To evaluate the efficiency of the extra shield against space radiation, the optimal shielding depth, and the effects on different lobes, we set up an additional simulation scenario with a spherical shell of aluminum between the head and the particle source sphere. Some simulations and experimental works recommend that hydrogenous materials could be more effective than aluminum for radiation shielding in space missions (Zeitlin, 2019). However, we use aluminum in our model, which is the most conventional approximation for shielding calculations, and different shielding depths can be directly taken as aluminum-equivalent shielding.

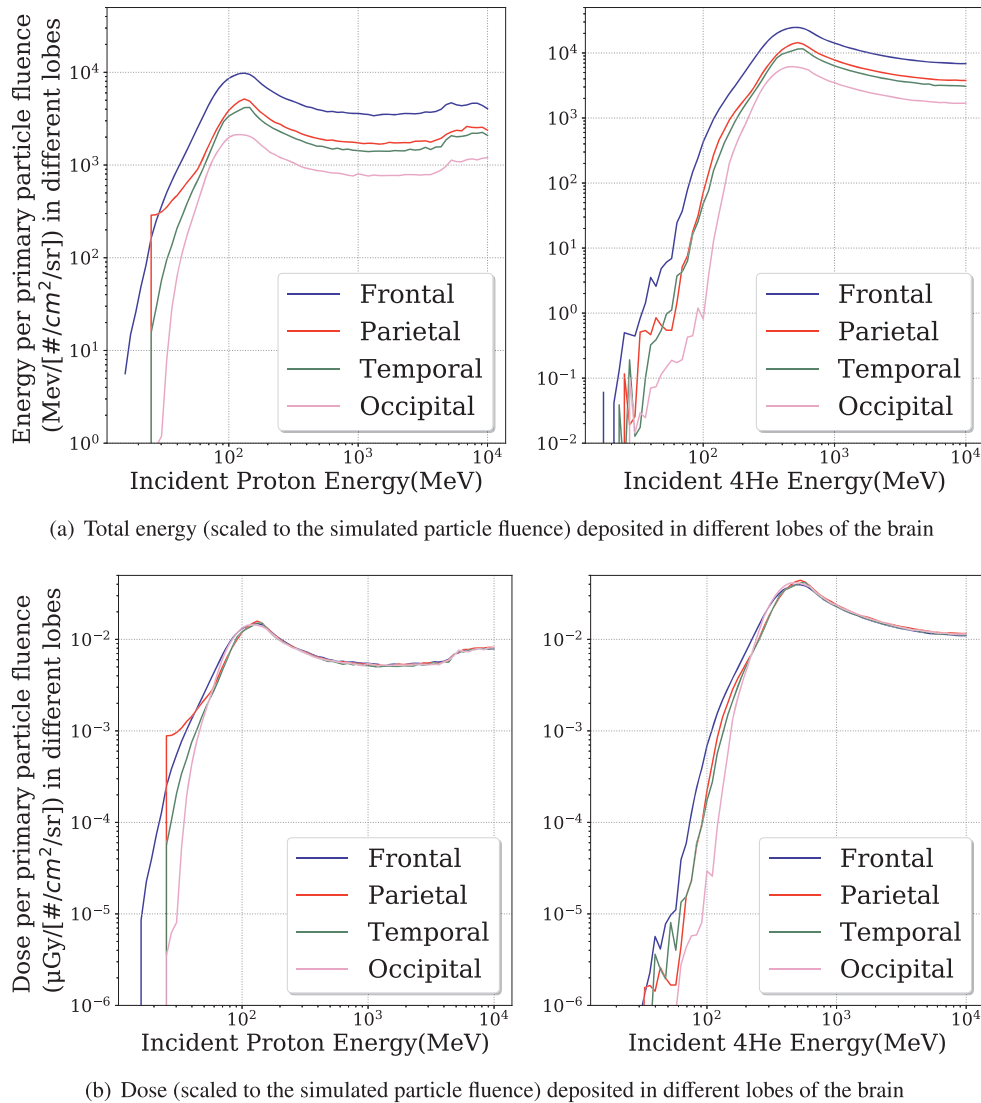
For deep space EVA and planetary surface missions, shielding around astronauts' heads would be provided just by a helmet, and we use a spherical shell of 2 mm (corresponding to a weight of ~ 3 kg) and of 5 mm (~ 7 kg) between the head and the particle source, to approximate the astronaut's helmet. For a space vessel or a planetary base, a thicker shield, can be expected, and we use 2 cm, 5 cm, and 10 cm as three cases of shielding thickness, corresponding to different aluminum equivalent thicknesses measured within the ISS (Tessa et al., 2009; Narici et al., 2012) (also see Section 2.2).

Protons, neutrons, helium, and heavier ions such as carbon, nitrogen, and iron particles have been considered, as source particles and their number, energy distribution, and the initial velocity distribution are set up, in the same way as in scenario 2, 3 (Sections 3.2, and 3.3). We note that when calculating these source particles through the shield reaching the head, all secondaries generated by the shield materials are considered as well in contributing to the final dose deposit in the brain.

3.4.1. Shielding effects on the BRF of the entire head

The results of the BRF of dose distribution within the whole head are shown in Fig. 9 for protons, neutrons, and heavy ions.

Charged Particles: For charged particles, it is clearly shown that even just a 2-mm shielding, can already drastically reduce the dose



(a) Total energy (scaled to the simulated particle fluence) deposited in different lobes of the brain

(b) Dose (scaled to the simulated particle fluence) deposited in different lobes of the brain

Fig. 5. Normalized energy (upper panels) and dose (lower panels) functions versus incident particle energy for protons (left panels) and ^4He (right panels) ions in different lobes of a human brain. The simulation setup is described in the text of Sec. 3.3.

contributed by particles below ~ 20 MeV/nuc, by 3–4 orders of magnitude. This, as known, would be an outstanding improvement during SEP events, which normally contain a high flux of low-energy protons. The approximate cutoff energy for thicker shields are about 30 MeV/nuc, 70 MeV/nuc, 120 MeV/nuc and 200 MeV/nuc for 5 mm, 2 cm, 5 cm, and 10 cm shielding thicknesses, respectively. However, it is also noticeable that the contribution to dose at higher energies above about 500 MeV/nuc starts to increase slightly with shielding depth, as clearly shown in the case of protons. This is mainly because higher energy particles are more likely interacting with the shielding material, generating lower-energy secondaries, which can further deposit energy in the brain.

Neutrons: Alternatively, the “shielding” effect on neutrons is more complex. At low energies below about 50 MeV, shielding can indeed reduce the dose contribution by about 30%. However, above ~ 100 –200 MeV, there is an opposite trend showing that more shielding, ≥ 5 -mm thickness, is efficiently enhancing the dose deposited by neutrons in the brain. The reason is due to the effective generation of secondaries by neutrons with the shielding material, which further contributes to the dose deposit in the brain. Nevertheless, it seems that 2-mm

shielding depth, when compared to no shielding, is visibly reducing dose in the head for both low and high energy neutrons, by about 15% averaged over the entire energy range.

The different effect of shielding on charged particles and high-energy neutrons highlights the importance of a thorough understanding of the energy-dependent radiation field before applying the most-appropriate shielding protection. For instance, during an EVA case, when most abundant primary radiation comes from charged particles, shielding would be very important. However, on the surface of a planet with an atmosphere, such as Mars, the radiation field may contain abundant neutrons generated by the planetary atmosphere/soil. With the existence of neutrons above ~ 100 MeV, extra shielding might even be counterproductive. A careful study of the charged and neutron spectra across all energies becomes crucial for evaluating if the extra shielding would have positive or negative effects on the brain functions of astronauts.

3.4.2. Shielding effects on the BRF of different lobes of the brain

The effect of the extra shield has also been evaluated for different lobes of the brain, as shown in Fig. 10 for incident protons, ^{12}C ions and

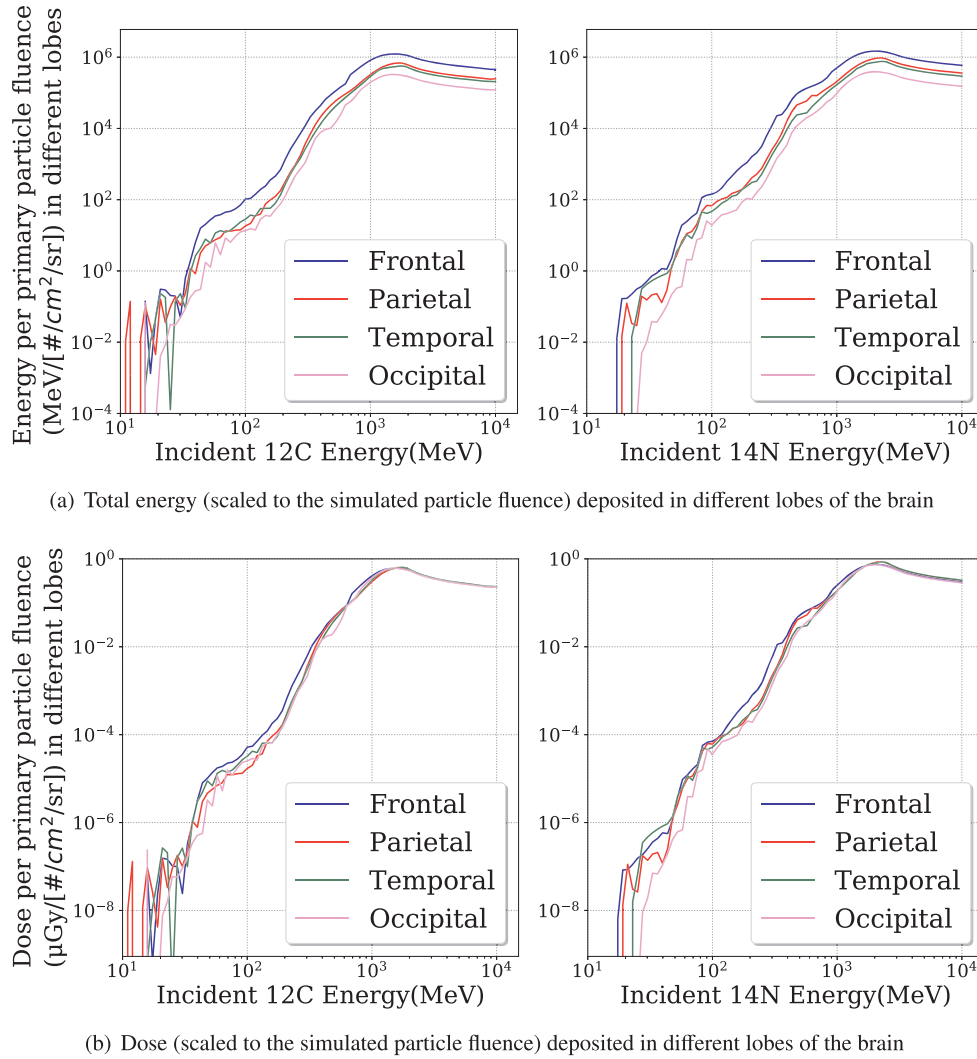


Fig. 6. Normalized energy (upper panels) and dose (lower panels) functions versus incident particle energy for ¹²C (left panels) and ¹⁴N (right panels) ions in different lobes of a human brain. The simulation setup is described in the text of Sec. 3.3.

neutrons. We have not plotted the results from Helium ions, ¹⁴N, or ⁵⁶Fe ions since they show rather similar properties as protons and ¹²C ions for the same energy (MeV/nuc). Furthermore, as shown in Fig. 9, the results relative to 2-mm and 5-mm shielding are almost the same for neutrons, so we omit to discuss the 5-mm results in this subsection.

As previously shown in Fig. 5(b), in the case of no aluminum shielding, the BRF for different lobes can be distinguished for low-energy protons (and also helium ions). However, Fig. 10 shows that curves with the same style (of a given shielding) but different colors (representing different lobes) are hardly distinguishable from each other. In other words, there is little difference between BRFs for different lobes when an extra aluminum shell is added around the head. This is because of the differences in functions for various lobes, as shown in Fig. 5(b) were mainly due to the low-energy particles reaching the outer part of the lobes and depositing energy therein. With the additional shielding, most primary low-energy particles can already be efficiently stopped before reaching the head and the brain therein, as shown in Fig. 9(a). Consequently, there are less visible differences in the dose functions at different lobes as they are now more embedded and protected from the external radiation. For protons (and charged particles), the effect of the shielding is still visible, as better shown in the top right panel of Fig. 10(a) for particles below about 200 MeV/nuc. However,

with the 2-mm shielding thickness, the effect is rather insignificant in contrast to what is shown in Fig. 9(a). The reason is that Fig. 9(a) shows the dose deposited in the entire head, including the internal brain as well as the external skull, while Fig. 10(a) only considers the dose deposited inside the brain lobes. The shielding due to the 2-mm helmet in Fig. 9(a)-(e) is effectively stopping most charged particles below about 20 MeV/nuc which can reach the head, but can hardly go through the head skull to reach the internal brain lobes. Therefore when considering dose deposit in the brain lobes by primary charged particles, the 2-mm helmet is not an effective improvement from the existing head skull.

The BRFs of different lobes induced by neutrons as shown in Fig. 10(c) have rather similar trends as in Fig. 9(f) considering the function versus different incoming neutron energies. There are no significant differences between different lobes for a given shielding depth (curves with different colors and the same line style), similar to the result in Fig. 5. The shielding effect by an extra shield around the head is visible for neutrons below about 100-150 MeV, with however rather small improvements when the shielding thickness increases. For neutrons above the energy of about 300 MeV, the extra shielding is counterproductive due to the enhanced interaction of neutrons with the shielding material. For instance, 5-cm extra shielding can increase the dose resulting from 5 GeV neutrons by about 100% in comparison to

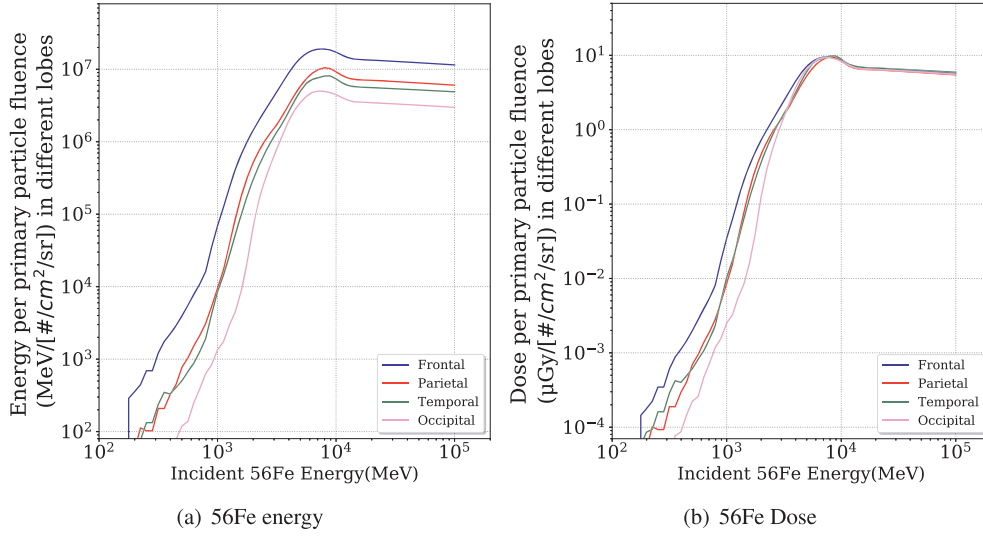


Fig. 7. Normalized energy and dose functions for ^{56}Fe versus incident particle energy in different lobes of a human brain. The simulation setup is described in the text of Sec. 3.3.

the case of no shielding, as better shown in the magnified panel on the right of Fig. 10(c).

3.5. Application of the simulated results - Estimating the radiation in the astronaut's brain in deep space

In this section, we present an example of how to apply our ready functions for calculating the resulted radiation inside the astronaut's brain. In Fig. 11, we show an example of the possible application of these ready functions for GCRs in deep space. The proton-induced BRF in different lobes of the brain is plotted in Fig. 11 (a). The GCR energy spectra under different solar modulations predicted by the Badhwar O'Neill model (O'Neill, 2010) are plotted in panel (b) with larger solar modulation potential corresponding to stronger modulation and decreased GCR fluxes. Taking the function for the frontal lobe as an example, we multiply it with the differential flux of GCRs in deep space bin by bin and obtain the dose contribution from each energy bin of primary protons as shown, in Fig. 11 (c). The summed dose from all

energy bins corresponds to the dose deposit inside the frontal lobe as contributed by all GCR protons under a certain modulation condition. It is between 45 and 266 $\mu\text{Gy/day}$ with the lower and upper values representing solar maximum and minimum conditions, respectively.

The same procedure has been done, for the potential human mission, on the surface of Mars in light of the novel results of the Martian surface radiation field measured by the Radiation Assessment Detector (Hassler et al., 2014, RAD). In this case, we also need to consider the primary GCRs interacting with the Martian atmosphere and regolith and generate a surface radiation field that is different from that in deep space. These surface particles including protons, Helium ions, and neutrons are then, used to further assess the dose deposit inside the brain. The particle spectra and radiation dose measured by RAD have been recently used to validate predictions by particle transport models (Daniel et al., 2016; Guo et al., 2019a). Since the modeled surface spectra have a more complete energy range than the measured ones, we use the modeled surface particle spectra (Guo et al., 2019a) to multiply with the calculated brain dose functions for obtaining the dose deposit

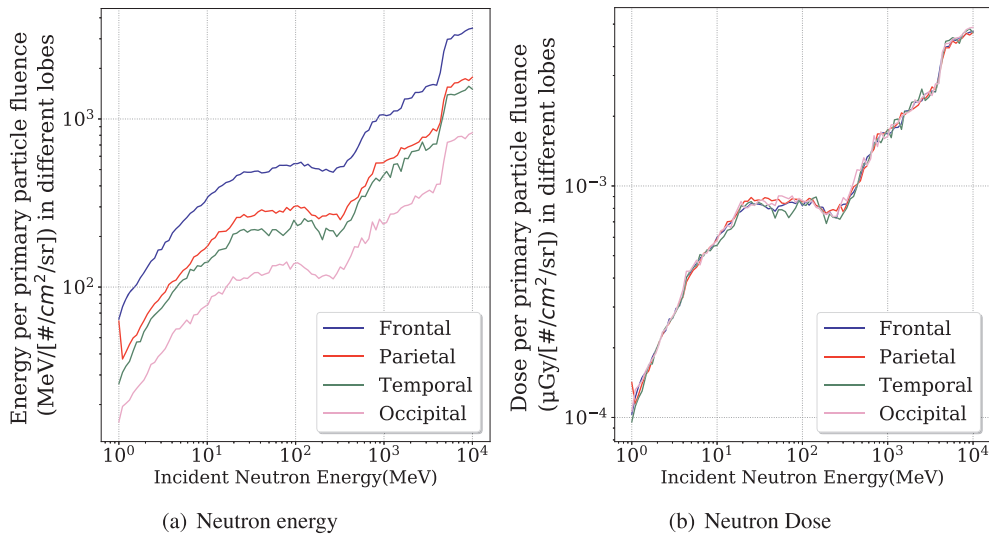


Fig. 8. Normalized energy and dose functions for Neutron versus incident particle energy in different lobes of a human brain. The simulation setup is described in the text of Sec. 3.3.

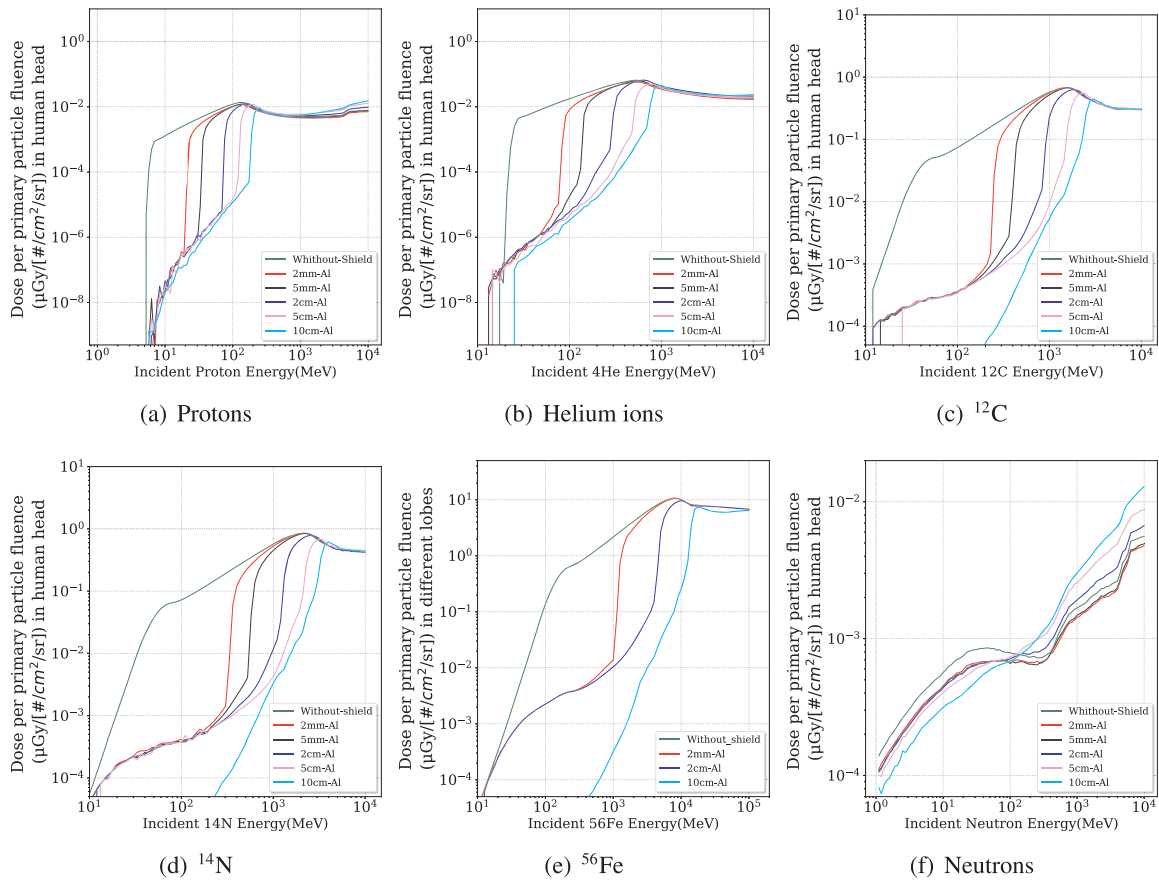


Fig. 9. Brain response function of dose deposit (normalized to the simulated particle fluence) within the entire head versus incident particle energy for (a) protons, (b) helium ions, (c) ^{12}C ions, (d) ^{14}N ions, (e) ^{56}Fe ions and (f) neutrons respectively. An aluminum shell with different thickness (2 mm, 5 mm, 2 cm, 5 cm, and 10 cm indicated by differently-colored curves), has been added between the head and the source sphere as a proxy of an extra shield as described in Sec. 3.4.

in the brain of an astronaut on the surface of Mars. Considering primary proton and Helium particles in deep space and arriving at Mars, we obtain the summed dose rate in the entire human head ranging from about 80 to 295 $\mu\text{Gy}/\text{day}$ on the surface of Mars with the lower and upper values representing solar maximum and minimum conditions, respectively. These values for Mars surface are slightly smaller than the measured tissue-equivalent dose rate by RAD for the mars surface under different solar activities on Mars (Guo et al., 2015) since there are other particle types included in the actual measurement.

In our follow-up work, we will study the dose deposit and distribution inside the brain under different circumstances, such as during solar particle events, inside a spacecraft, or on the surface of the Moon in more detail and discuss the implications of the results for future space missions.

4. Summary and Conclusion

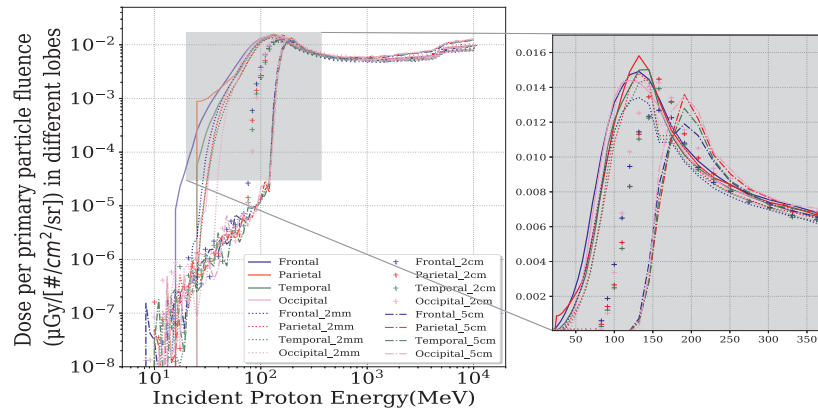
To prepare for future manned missions exploring space, such as a crewed mission to the Moon or Mars, it is of utmost importance to model and understand the potential risks of radiation that astronauts may be exposed to. In particular, our brains, and the central nervous systems are essential in driving us to make cognitive decisions and responsible performances which might be disrupted by elevated radiation in space both in the short term and in the long term (Sec. 1.2).

As known, our brain has a complex shape and structure containing several lobes with each mainly responsible for specific cognitive functions (Sec. 1.3). It is, therefore, important to assess the impact of ambient cosmic radiation on the brain and also in each lobe to better

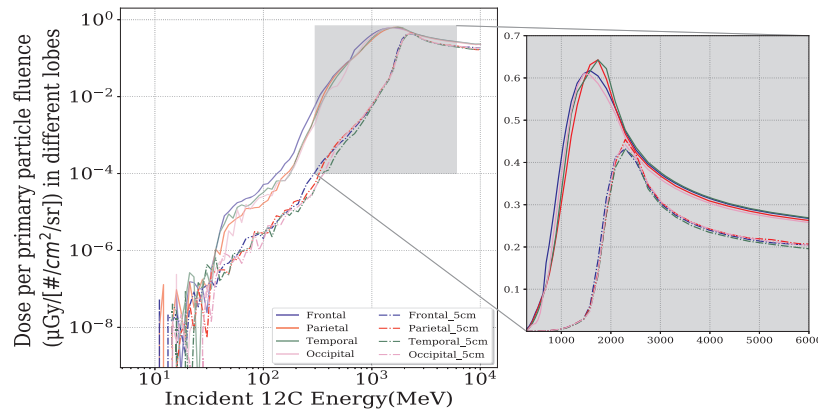
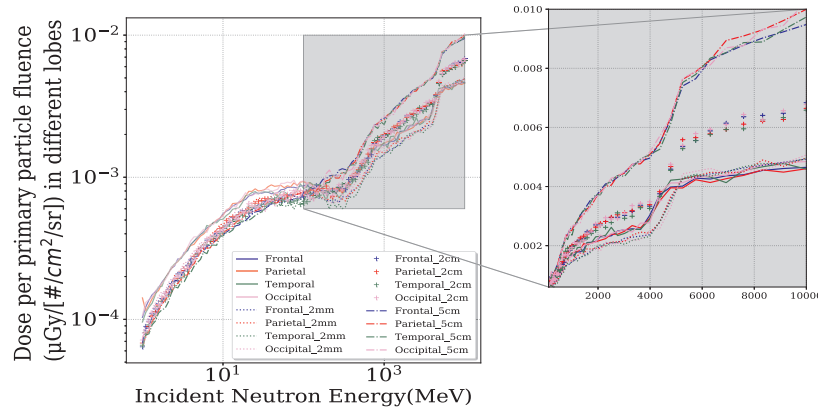
evaluate potential effects on astronauts' brain functions and consequent cognitive performances during space missions. With the above motivation, we have carried out detailed GEANT4 Monte Carlo simulations of particle interactions with a realistic brain structure, which is extracted from actual CT scans to study the radiation distribution inside a human head and at different parts of the brain lobes.

As a model validation, we first compared the calculation results based on different human head structures (Sec. 3.1): a head filled with water, a head composed of water and a skull, and finally the actual head structure with densities derived from CT images. We found that using an actual head structure in the model is important for primary protons with the energy around 100s of MeV, especially when considering dose distributions at different parts of the brain. Additionally, we have also compared the results from the choice of two different physics lists (QGSP_BIC and QGSP_BERT) in the particle transport code (Sec. 3.2) and found that they are very similar concerning the dose deposition.

Based on such validated models, we have then calculated and obtained some ready-to-go functions of energy/dose deposit induced by primary particles of protons, helium, neutron as well as heavier ions such as Carbon, and Nitrogen impinging isotropically towards the head (Sec. 3.3). The most probable interactions of the primary particle with the brain structure and the generation of secondary particles, which may further interact with the head contributing to extra absorbed dose, have been included statistically in these functions. In other words, these are brain response functions (BRF) transforming the fluence of incoming particles with a given type and initial energy into the deposited energy or dose at different parts of the head. These ready functions can be used to quickly convert a certain ambient cosmic-ray spectrum (e.g.,



(a) Primary proton induced dose functions for different lobes under various shielding depths

(b) Primary ¹²C ion induced dose functions for different lobes under various shielding depths

(c) Primary neutron induced dose functions for different lobes under various shielding depths

Fig. 10. Dose functions (normalized to the simulated particle fluence per bin) versus incident particle energy, are shown for (a) protons, (b) ¹²C ions, and (c) neutrons respectively. Functions from simulations with aluminum shielding shells added around the head are shown, with differently-styled curves for different shell thicknesses. In each shielding case, functions for four different lobes (frontal, parietal, temporal, and occipital lobes), are shown by differently-colored curves. The gray parts of the left panels are magnified and shown in linear scales in the right panels.

in deep space, on planetary surfaces, or within habitats of a spacecraft) into the absorbed energy/dose within the entire head and also at different lobes of the brain. We show an example of such an application in [Section 3.5](#).

We found the deposited energy and dose for charged particles in the brain grow with incoming particle energy in the range below 100–150 MeV/nuc and then decrease slightly at higher energies. The peak

energy deposit is the approximate maximum stopping energy of charged particles passing through the size of a head. Alternatively, for primary neutrons, the contribution to the dose/energy increases with energy. The BRFs derived for dose deposit at different lobes only differ slightly at low energies (below ~ 100 MeV/nuc) due to the position and geometry of the lobes: lobes with less external shielding by the skull are more exposed to the radiation contribution by low-energy

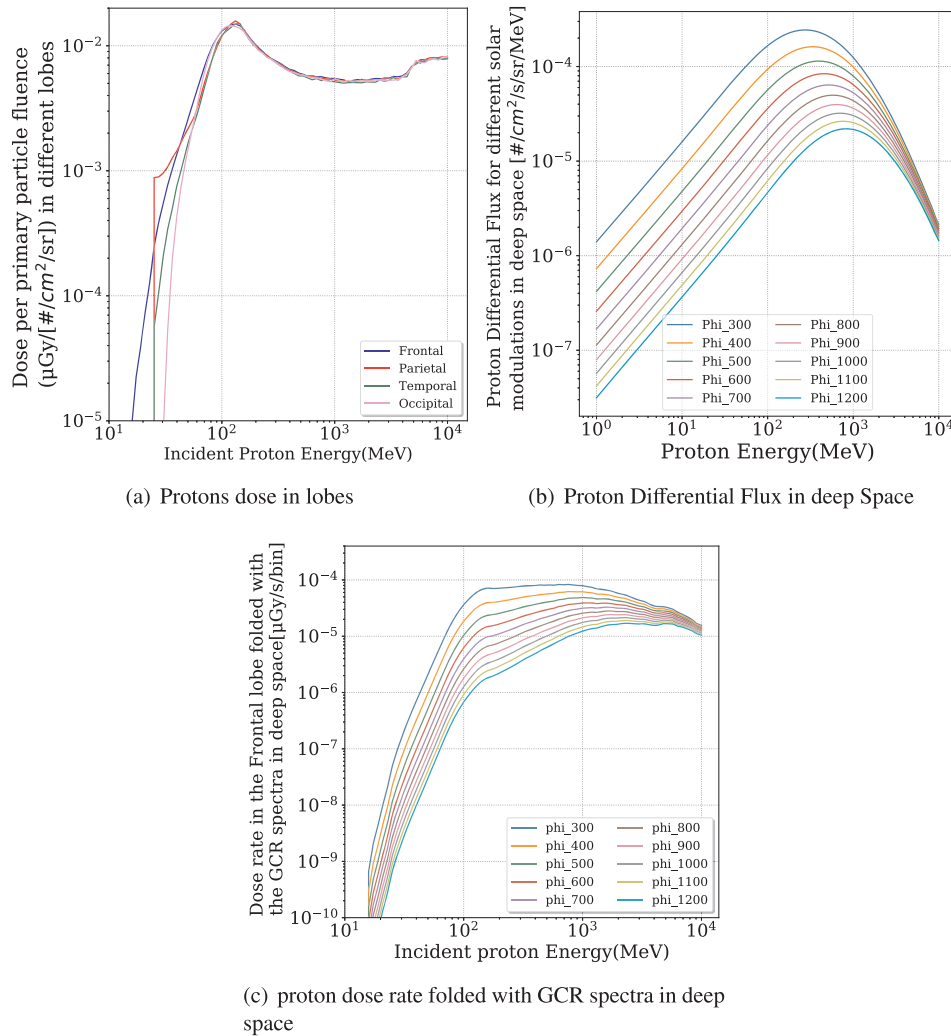


Fig. 11. An example of how to use the ready brain response functions for calculating the radiation dose rate inside different lobes of the brain in deep space as described in Sec. 3.5. (a) shows the BRF functions without shielding as calculated in Sec. 3.3. (b) shows the differential flux of GCRs in deep space as obtained from the Badwar O'Neil model (O'Neill, 2010) with larger modulation potential showing decreased GCR fluxes. (c) shows the folded results using the frontal lobe function in (a) and the GCR spectra in (b). More details of the folding procedure can be found in Sec. 3.5.

primary particles.

Moreover, We have also considered the influence of an extra shield between the particle source and the head, and its effect on the brain depending on the shielding thickness (Sec. 3.4). For charged particles, shielding is effectively reducing the head/lobe dose contributed by low-energy particles, which should be concerned as an important mitigation approach during SEP events where most particles are below a few hundred MeV. However, the shielding of neutrons is non-trivial as the generation of secondaries by neutrons with energies $\gtrsim 200$ MeV becomes more effective with enhanced shielding depth. The BRFs obtained for different lobes when an extra shielding shell is provided seem indistinguishable from each other. This is due to the effective shielding of the shield against low-energy primary particles, which could have caused some function difference via reaching the outer part of the lobes. In other words, without any shielding protection, the frontal lobe, which has a larger part less protected by the skull, would have been more exposed to low-energy particles (protons below ~ 20 MeV as shown in Fig. 5(a)). As the frontal lobe is closely related to logical thinking, decision making, and muscle movement, possible exposure to a large amount of low-energy charged particles without any shielding protection may become mission-critical. However, with an extra

protection of about 2-cm aluminum, most protons below about 70 MeV could hardly reach the head, as shown in Fig. 10 and the BRFs for different lobes are rather similar. Our result emphasizes the importance of using sufficient shielding protection against low-energy charged particles, which may have an alarming increase during SEP events.

On the other hand, shielding strategy against neutron-induced radiation is not as simple. Although an extra aluminum shell could reduce the dose contributed by neutrons below about 200 MeV by some 30%, increased shielding against higher energy neutrons might become counterproductive due to the enhanced generation of secondaries by such neutrons. Therefore, for a radiation field where neutrons might be abundant as they are generated by primary GCRs interacting with the local environment, such as on the surface of Mars or within a spacecraft (Köhler et al., 2014; Köhler et al., 2015; Guo et al., 2017), the correct evaluation of both the charged and neutron flux over the entire energy range becomes very important for assessing the proper shielding depth. This will be more carefully investigated in our future work.

Declaration of Competing Interest

None.

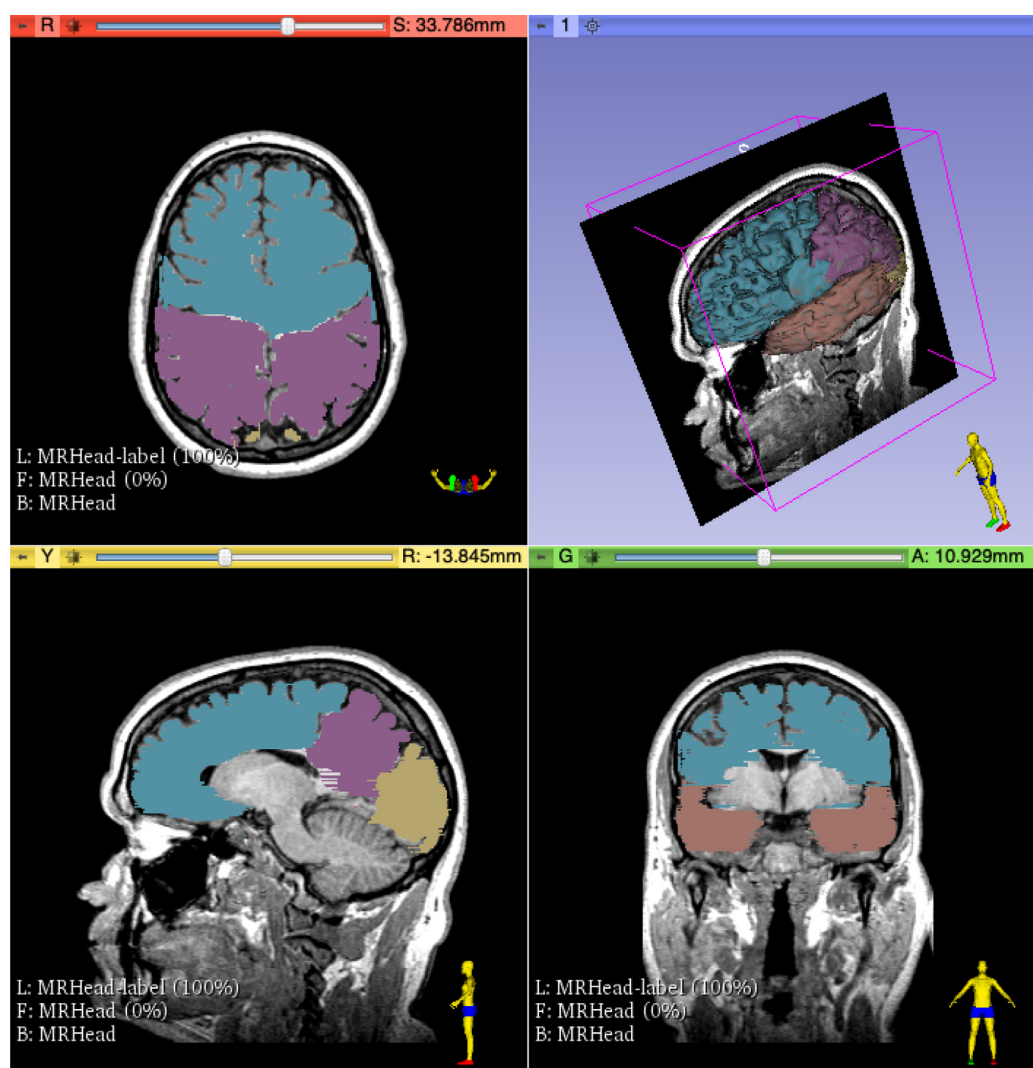


Fig. 12. Digital Imaging and Communications in Medicine (DICOM) images segmented into four brain lobes of interest (blue for frontal lobe, violet for parietal lobe, brown for temporal lobe and yellow for occipital lobe) viewed from different directions.

Acknowledgments

J.G. is supported by the Strategic Priority Program of the Chinese Academy of Sciences (Grant No. XDB41000000 and XDA15017300), the Key Research Program of the Chinese Academy of Sciences (Grant No. QYZDB-SSW-DQC015), and the CNSA pre-research Project on Civil Aerospace Technologies (Grant No. D020104). S.K. and R.F.W.S. are supported by DLR and DLR's Space Administration grant numbers 50QM0501, 50QM1201, and 50QM1701 to the Christian Albrechts University, Kiel. L.N. acknowledges ASI support under agreement ALTEA-BrainRad, 2016-28-H.O. We thank Jan Christoph Terasa (from University of Kiel) and Yidong Yang (from University of Science and Technology of China) for useful discussions on GEANT4 simulation setups.

Appendix A. Segmentation of the brain structure using the 3D-Slicer tool

3D-Slicer is a commonly used open-source platform and medical software that can be used for scientific visualization, image processing, data analysis, and identification of anatomical structures (Domínguez et al., 2015; Ratib et al., 2011; Caban et al., 2007). It was built through

support from the National Institutes of Health and a global developer community for handling DICOM images and a variety of other formats. It brings free and powerful cross-platform processing tools to a variety of applications for physicians and researchers.

In this study, the 3D-Slicer tool has been used to create a three-dimensional visualization of the human head, and segment different parts of the human brain, based on CT images with DICOM formats, as explained in Sec. 2.1. Specifically speaking, to segment the brain shown in CT images into different lobes, we use 3D-Slicer to load the DICOM data, and a 3D brain topology is reconstructed connecting 134 slices of CT images, as shown in Fig. 12. We then manually select the pixels (or voxels in 3D) which belong to the same lobe into a separate volume. The figure also shows the four segmented lobes with different colors as viewed from different directions. The segmentation results have been compared to the e-Anatomy the interactive atlas of human anatomy (e Anatomy, 2010), and both are very comparable.

Note that there is no efficient or precise way to do this automatically, mostly due to the complexity of the brain and the individual differences between different CT images. In fact, we have tried to develop an algorithm for the segmentation by calculating the density differential for identifying boundaries. However, as voxels from different lobes have very similar densities, this method is sub-optimal.

Moreover, the size of each voxel, as well as the total number of voxels for each lobe section can be obtained from 3D-Slicer. This information is further used to determine the total volume and mass of each lobe. The volume of the frontal, temporal, parietal, and occipital lobes are 63.72, 58.26, 38.31, and 23.71 cm^3 , respectively.

References

- Agostinelli, S., et al., 2003. GEANT4: A Simulation toolkit. *Nucl. Instrum. Meth. A* 506, 250–303. [https://doi.org/10.1016/S0168-9002\(03\)01368-8](https://doi.org/10.1016/S0168-9002(03)01368-8).
- Allison, J., et al., 2016. Recent developments in Geant4. *Nucl. Instrum. Meth. A* 835, 186–225. <https://doi.org/10.1016/j.nima.2016.06.125>.
- e Anatomy, 2010. e-anatomy the interactive atlas of human anatomy. 10.37019/e-anatomy.
- Andersen, B.L., Tewfik, H.H., 1985. Psychological Reactions to Radiation Therapy: Reconsideration of the Adaptive Aspects of Anxiety. *J Pers Soc Psychol* 48, 1024–1032. <https://doi.org/10.1037/0022-3514.48.4.1024>.
- Baiocco, G., Bocchini, L., Giraudo, M., Barbieri, S., Narici, L., Lobascio, C., Ottolenghi, A., collaboration, P., 2018. Innovative Solutions for Personal Radiation Shielding in Space. *Radiation Protection Dosimetry* 183 (1–2), 228–232. <https://doi.org/10.1093/rpd/ncy216>.
- Barcellos-Hoff, M.H., Blakely, E.A., Burma, S.e., Fornace, A.J., Gerson, S., Hlatky, L., Kirsch, D.G., Luderer, U., Shay, J., Wang, Y., Weil, M.M., 2015. Concepts and challenges in cancer risk prediction for the space radiation environment. *Life Sciences and Space Research* 6, 92–103. <https://doi.org/10.1016/j.lssr.2015.07.006>.
- Boerma, M., Nelson, G.A., Sridharan, V., Mao, X.-W., Koturbash, I., Hauer-Jensen, M., 2015. Space radiation and cardiovascular disease risk. *World J Cardiol* 7, 882–888. <https://doi.org/10.4330/wjcv.v7.i12.882>.
- Budinger, T.F., Lyman, J.T., Tobias, C.A., 1972. Visual Perception of Accelerated Nitrogen Nuclei interacting with the Human Retina. *Nature* 239 (5369), 209–211. <https://doi.org/10.1038/239209a0>.
- Bushberg, J.T., Seibert, J.A., Leidholdt, E.M., Boone, J.M., 2012. The essential physics of medical imaging. 3. Lippincott Williams and Wilkins.
- Caban, J.J., Joshi, A., Nagy, P., 2007. Rapid Development of Medical Imaging Tools with Open-Source Libraries. *J Digit Imaging* 20, 83–93. <https://doi.org/10.1007/s10278-007-9062-3>.
- Carozzo, S., Ball, S.L., Narici, L., Schardt, D., Sannita, W.G., 2015. Interaction of 12c ions with the mouse retinal response to light. *Neuroscience letters* 598, 36–40.
- Cucinotta, F.A., Alp, M., Sulzman, F.M., Wang, M., 2014. Space radiation risks to the central nervous system. *Life Sciences and Space Research* 2, 54–69. <https://doi.org/10.1016/j.lssr.2014.06.003>.
- Cucinotta, F.A., Durante, M., 2006. Cancer risk from exposure to galactic cosmic rays: implications for space exploration by human beings. *Lancet Oncol* 7 (431–436), 682–688. [https://doi.org/10.1016/S1470-2045\(06\)70695-7](https://doi.org/10.1016/S1470-2045(06)70695-7).
- Cucinotta, F.A., Hamada, N., Little, M.P., 2016. No evidence for an increase in circulatory disease mortality in astronauts following space radiation exposures. *Life Sciences and Space Research* 10, 53–56. <https://doi.org/10.1016/j.lssr.2016.08.002>.
- Cucinotta, F. A., Kim, M., Chappell, L., 2013. Space radiation cancer risk projections and uncertainties.
- Cucinotta, F.A., Schimmerling, W., Wilson, J.W., Peterson, L.E., Badhwar, G.D., Saganti, P.B., Dicello, J.F., 2001. Space Radiation Cancer Risks and Uncertainties for Mars Missions. *Radiation Research* 156 (5), 682–688. [https://doi.org/10.1667/0033-7587\(2001\)156\[0682:SRCRAU\]2.0.CO;2](https://doi.org/10.1667/0033-7587(2001)156[0682:SRCRAU]2.0.CO;2).
- Cucinotta, F.A., To, K., Cacao, E., 2017. Predictions of space radiation fatality risk for exploration missions. *Life Sciences and Space Research* 13, 1–11. <https://doi.org/10.1016/j.lssr.2017.01.005>.
- Delp, M.D., Charvat, J.M., Limoli, C.L., Globus, R.K., Ghosh, P., 2016. Apollo Lunar Astronauts Show Higher Cardiovascular Disease Mortality: Possible Deep Space Radiation Effects on the Vascular Endothelium. *Scientific Reports* 6, 29901. <https://doi.org/10.1038/srep29901>.
- Demontis, G.C., Germani, M.M., Caiani, E.G., Barravecchia, I., Passino, C., Angeloni, D., 2017. Human Pathophysiological Adaptations to the Space Environment. *Frontiers in Physiology* 8, 547. <https://doi.org/10.3389/fphys.2017.00547>.
- Desai, M., Gialalone, J., 2016. Large gradual solar energetic particle events. *Living Reviews in Solar Physics* 13 (1), 3. <https://doi.org/10.1007/s41116-016-0002-5>.
- Diaz Merchan, J., Torres, D., 2016. A geant4 simulation of the depth dose percentage in brain tumors treatments using protons and carbon ions. 1753. pp. 080019. <https://doi.org/10.1063/1.4955389>.
- Domínguez, M.G., Hernández, C., Ruisoto, P., Juanes, J.A., Prats, A., Hernández, T., 2015. Application of the 3d slicer software in the study of the brain's ventricular system. *Proceedings of the 3rd International Conference on Technological Ecosystems for Enhancing Multiculturality*. ACM, New York, NY, USA, pp. 31–37. <https://doi.org/10.1145/2808580.2808586>.
- Ehresmann, B., Hassler, D.M., Zeitlin, C., Guo, J., Köhler, J., Wimmer-Schweingruber, R.F., Appel, J.K., Brinza, D.E., Rafkin, S.C., Böttcher, S.I., et al., 2016. Charged particle spectra measured during the transit to mars with the mars science laboratory radiation assessment detector (msl/rad). *Life Sciences in Space Research* 10, 29–37.
- Ehresmann, B., Zeitlin, C., Hassler, D.M., Wimmer-Schweingruber, R.F., Böhm, E., Böttcher, S., Brinza, D.E., Burmeister, S., Guo, J., Köhler, J., Martin, C., Posner, A., Rafkin, S., Reitz, G., 2014. Charged particle spectra obtained with the Mars Science Laboratory Radiation Assessment Detector (MSL/RAD) on the surface of Mars. *Journal of Geophysical Research (Planets)* 119 (3), 468–479. <https://doi.org/10.1002/2013JE004547>.
- Geant4.Collaboration, 2017. Geant4 physics reference manual 10.4. Accessible from the GEANT4 web page.
- Guo, J., Saša, B., Röstel, L., Terasa, J.C., Herbst, K., Heber, B., Wimmer-Schweingruber, R.F., 2019. Implementation and validation of the geant4/atris code to model the radiation environment at mars. *Journal of Space Weather and Space Climate* 9 (A2). <https://doi.org/10.1051/swsc/2018051>.
- Guo, J., Wimmer-Schweingruber, R.F., Grande, M., Lee-Payne, Z.H., Matthiä, D., 2019. Ready functions for calculating the martian radiation environment. *Journal of Space Weather and Space Climate* 9 (A7). <https://doi.org/10.1051/swsc/2019004>.
- Guo, J., Zeitlin, C., Wimmer-Schweingruber, R., Hassler, D.M., Köhler, J., Ehresmann, B., Böttcher, S., Böhm, E., Brinza, D.E., 2017. Measurements of the neutral particle spectra on Mars by MSL/RAD from 2015-11-15 to 2016-01-15. *Life Sciences and Space Research* 14, 12–17. <https://doi.org/10.1016/j.lssr.2017.06.001>.
- Guo, J., Zeitlin, C., Wimmer-Schweingruber, R.F., McDole, T., Köhl, P., Appel, J.C., Matthiä, D., Krauss, J., Köhler, J., 2018. A generalized approach to model the spectra and radiation dose rate of solar particle events on the surface of mars. *The Astronomical Journal* 155 (1), 49. <https://doi.org/10.3847/1538-3881/aaa085>.
- Guo, J., Zeitlin, C., Wimmer-Schweingruber, R.F., Rafkin, S., Hassler, D.M., Posner, A., Heber, B., Köhler, J., Ehresmann, B., Appel, J.K., et al., 2015. Modeling the variations of dose rate measured by rad during the first msl martian year: 2012–2014. *The Astrophysical Journal* 810 (1), 24.
- Harris, L.R., Jenkin, M., Jenkin, H., Zacher, J.E., Dyde, R.T., 2015. The effect of long-term exposure to microgravity on the perception of upright. *npj Microgravity* 3, 3. <https://doi.org/10.1038/s41526-016-0005-5>.
- Hassler, D.M., Zeitlin, C., Wimmer-Schweingruber, R.F., Ehresmann, B., Rafkin, S., Eigenbrode, J.L., Brinza, D.E., Weigle, G., Böttcher, S., Böhm, E., Burmeister, S., Guo, J., 2014. Mars' Surface Radiation Environment Measured with the Mars Science Laboratory's Curiosity Rover. *Science* 343 (6169), 1244797. <https://doi.org/10.1126/science.1244797>.
- Hodkinson, P., Anderton, R., Posselt, B., Fong, K., 2017. An overview of space medicine. *British Journal of Anaesthesia* 119 (S1), i143–i153. <https://doi.org/10.1093/bja/aex336>.
- Huff Janice, J., Lisa, C., Steve, B., Lori, C., Kerry, G., Sarah, L., Lisa, S., Tony, S., Charles, W., 2016. Risk of radiation carcinogenesis: Human research program space radiation element.
- Institute, Q. B., 2018. Lobes of the brain.
- Jandial, R., Hoshide, R., Waters, J.D., Limoli, C.L., 2017. Space-brain: The negative effects of space exposure on the central nervous system. *SNI: Neuroanatomy and Neurophysiology*. <https://doi.org/10.4103/sni.sni.250.17>.
- Jiang, H., Seco, J., Paganetti, H., 2007. Effects of Hounsfield number conversion on CT based proton Monte Carlo dose calculations. *Med Phys* 34, 1439–1449. <https://doi.org/10.1118/1.2715481>.
- Joseph, J.A., Hunt, W.A., Rabin, B.M., Dalton, T.K., 1992. Possible Accelerated Striatal Aging Induced by 56 Fe Heavy-Particle Irradiation: Implications for Manned Space Flights. *Radiation Research* 130 (1), 88. <https://doi.org/10.2307/3578484>.
- Kalender, W.A., 2011. Computed tomography: fundamentals, system technology, image quality, applications.3. Publicis Publishing.
- Kanas, N., 2010. From Earth's orbit to the outer planets and beyond: Psychological issues in space. *Acta Astronautica* 68, 576–581. <https://doi.org/10.1016/j.actaastro.2010.04.012>.
- Kanas, N., 2014. Psychosocial issues during an expedition to Mars. *Acta Astronautica* 103, 73–80. <https://doi.org/10.1016/j.actaastro.2014.06.026>.
- Kennedy, A.R., 2014. Biological effects of space radiation and development of effective countermeasures. *Life sciences in space research (Amst)* 1, 10–43. <https://doi.org/10.1016/j.lssr.2014.02.004>.
- Köhler, J., Zeitlin, C., Ehresmann, B., Wimmer-Schweingruber, R., Hassler, D., Reitz, G., Brinza, D., Weigle, G., Appel, J., Böttcher, S., et al., 2014. Measurements of the neutron spectrum on the martian surface with msl/rad. *Journal of Geophysical Research: Planets* 119 (3), 594–603. <https://doi.org/10.1002/2013JE004539>.
- Köhler, J., Ehresmann, B., Zeitlin, C., Wimmer-Schweingruber, R., Hassler, D., Reitz, G., Brinza, D., Appel, J., Böttcher, S., Böhm, E., Burmeister, S., Guo, J., Lohf, H., Martin, C., Posner, A., Rafkin, S., 2015. Measurements of the neutron spectrum in transit to mars on the mars science laboratory. *Life Sciences in Space Research* 5, 6–12. <https://doi.org/10.1016/j.lssr.2015.03.001>.
- Lario, D., 2005. Advances in modeling gradual solar energetic particle events. *Advances in Space Research* 36 (12), 2279–2288. <https://doi.org/10.1016/j.asr.2005.07.081>.
- Liu, B., Hinshaw, R.G., Le, K.X., Park, M.-A., Wang, S., Belanger, A.P., Dubey, S., Frost, J.L., Shi, Q., Holton, P., Trojanczyk, L., Reiser, V., Jones, P.A., Trigg, W., Di Carli, M.F., Lorello, P., Caldaron, B.J., Williams, J.P., O'Banion, M.K., Lemere, C.A., 2019. Space-like 56fe irradiation manifests mild, early sex-specific behavioral and neuropathological changes in wildtype and alzheimer's-like transgenic mice. *Scientific reports* 9 (1), 12118. <https://doi.org/10.1038/s41598-019-48615-1>.
- Daniel, M., Bent, E., Henning, L., Jan, K., Cary, Z., Jan, A., Tatsuhiko, S., Tony, S., Cesar, M., Thomas, B., Eckart, B., Stephan, B., David, E.B., Soenke, B., Jingnan, G., Donald, M.H., Arik, P., Scot, C.R.R., Günther, R., John, W.W., Robert, F.W.-S., 2016. The martian surface radiation environment - a comparison of models and msl/rad measurements. *J. Space Weather Space Clim.* 6, A13. <https://doi.org/10.1051/swsc/2016008>.
- Narici, L., 2008. Heavy ions light flashes and brain functions: recent observations at accelerators and in spaceflight. *New Journal of Physics* 10 (7), 075010. <https://doi.org/10.1088/1367-2630/10/7/075010>.
- Narici, L., Casolino, M., Di Fino, L., Larosa, M., Larsson, O., Piccozza, P., Zacone, V., 2012. Iron flux inside the International Space Station is measured to be lower than predicted. *Radiation Measurements* 47 (10), 1030–1034. <https://doi.org/10.1016/j.radmeas.2012.07.006>.

- Narici, L., Paci, M., Brunetti, V., Rinaldi, A., Sannita, W., De Martino, A., 2012. Bovine rod rhodopsin. 1. bleaching by luminescence in vitro by recombination of radicals from polyunsaturated fatty acids. *Free Radical Biology and Medicine* 53 (3), 482–487.
- Narici, L., Paci, M., Brunetti, V., Rinaldi, A., Sannita, W.G., Carozzo, S., DeMartino, A., 2013. Bovine rod rhodopsin: 2. bleaching in vitro upon 12c ions irradiation as source of effects as light flash for patients and for humans in space. *International journal of radiation biology* 89 (10), 765–769.
- Narici, L., Titova, E., Obenaus, A., Wroe, A., Loreda, L., Schulte, R., Slater, J.D., Nelson, G.A., 2020. Multiple sensory illusions are evoked during the course of proton therapy. *Life Sciences in Space Research*.
- O'Neill, P.M., 2010. Badhwar-o'Neill 2010 galactic cosmic ray flux model-revised. *IEEE Transactions on Nuclear Science* 6 (57), 3148–3153. <https://doi.org/10.1109/TNS.2010.2083688>.
- OTAKE, M., 1998. Review: Radiation-related brain damage and growth retardation among the prenatally exposed atomic bomb survivors. *International Journal of Radiation Biology* 74 (2), 159–171. <https://doi.org/10.1080/095530098141555>.
- Parihar, V.K., Allen, B., Tran, K.K., Macaraeg, T.G., Chu, E.M., Kwok, S.F., Chmielewski, N.N., Craver, B.M., Baulch, J.E., Acharya, M.M., Cucinotta, F.A., Limoli, C.L., 2015. What happens to your brain on the way to Mars. *Science Advances* 1 (4). <https://doi.org/10.1126/sciadv.1400256>. e1400256–e1400256
- Parihar, V.K., Allen, B.D., Caressi, C., Kwok, S., Chu, E., Tran, K.K., Chmielewski, N.N., Giedzinski, E., Acharya, M.M., Britten, R.A., Baulch, J.E., Limoli, C.L., 2016. Cosmic radiation exposure and persistent cognitive dysfunction. *Scientific Reports* 6, 34774. <https://doi.org/10.1038/srep34774>.
- Parker, E.N., 1965. The passage of energetic charged particles through interplanetary space. *Planetary and Space Science* 13, 9–49. [https://doi.org/10.1016/0032-0633\(65\)90131-5](https://doi.org/10.1016/0032-0633(65)90131-5).
- Pinsky, L.S., Osborne, W.Z., Bailey, J.V., Benson, R.E., Thompson, L.F., 1974. Light Flashes Observed by Astronauts on Apollo 11 through Apollo 17. *Science* 183 (4128), 957–959. <https://doi.org/10.1126/science.183.4128.957>.
- Rabin, B.M., Joseph, J.A., Shukitt-Hale, B., McEwen, J., 2000. Effects of Exposure to Heavy Particles on a Behavior Mediated by the Dopaminergic System. *Advances in Space Research* 25 (10), 2065–2074. [https://doi.org/10.1016/S0273-1177\(99\)01014-5](https://doi.org/10.1016/S0273-1177(99)01014-5).
- Ratib, O., Rosset, A., Heuberger, J., 2011. Open Source software and social networks: Disruptive alternatives for medical imaging. *European Journal of Radiology* 78, 259–265. <https://doi.org/10.1016/j.ejrad.2010.05.004>.
- Reynolds, R.J., Day, S.M., 2017. Mortality due to cardiovascular disease among apollo lunar astronauts. *Aerospace medicine and human performance* 88 (5), 492–496.
- Rivera, P.D., Shih, H.-Y., Leblanc, J.A., Cole, M.G., Amaral, W.Z., Mukherjee, S., Zhang, S., Lucero, M.J., Decarolis, N.A., Chen, B.P.C., Eisch, A.J., 2013. Acute and fractionated exposure to high-let (56)fe hze-particle radiation both result in similar long-term deficits in adult hippocampal neurogenesis. *Radiation research* 180 (6), 658–667. <https://doi.org/10.1667/rr13480.1>.
- Sandal, G., Leon, G.R., Palinkas, L., 2006. Human challenges in polar and space environments. *Rev Environ Sci Biotechnol* 5, 281–296. <https://doi.org/10.1007/s11157-006-9000-8>.
- Sannita, W.G., Peachey, N.S., Strettoi, E., Ball, S.L., Belli, F., Bidoli, V., Carozzo, S., Casolino, M., Di Fino, L., Picozza, P., et al., 2007. Electrophysiological responses of the mouse retina to 12c ions. *Neuroscience Letters* 416 (3), 231–235.
- Simpson, J., 1983. Elemental and isotopic composition of the galactic cosmic rays. *Annual Review of Nuclear and Particle Science* 33 (1), 323–382. <https://doi.org/10.1146/annurev.ns.33.120183.001543>.
- Solovev, K.S., Fedorov, V.V., 2015. Comparative analysis of mcnp and geant4 codes for fast-neutron radiation treatment planning. *Nuclear Energy and Technology* 1, 14–19. <https://doi.org/10.1016/j.nucet.2015.11.004>.
- Tang, Y., Luo, D., Rong, X., Shi, X., Peng, Y., 2012. Psychological Disorders, Cognitive Dysfunction and Quality of Life in Nasopharyngeal Carcinoma Patients with Radiation-Induced Brain Injury. *PLoS ONE* 7 (6), e36529. <https://doi.org/10.1371/journal.pone.0036529>.
- Tessa, C.L., Fino, L.D., Larosa, M., Narici, L., Picozza, P., Zacont, V., 2009. Estimate of the space station shielding thickness at a uslab site using altea measurements and fragmentation cross sections. *Nuclear Instruments and Methods in Physics Research Section B: Beam Interactions with Materials and Atoms* 267 (19), 3383–3387. <https://doi.org/10.1016/j.nimb.2009.06.107>.
- Tofilon, P.J., Fike, J.R., 2000. The Radioresponse of the Central Nervous System: A Dynamic Process. *Radiation Research* 153 (4), 357–370. [https://doi.org/10.1667/0033-7587\(2000\)153\[0357:TROTCN\]2.0.CO;2](https://doi.org/10.1667/0033-7587(2000)153[0357:TROTCN]2.0.CO;2).
- Varma, D.R., 2012. Managing DICOM images: Tips and tricks for the radiologist. *Indian J Radiol Imaging* 22, 4–13. <https://doi.org/10.4103/0971-3026.95396>.
- Vuolo, M., Baiocco, G., Barbieri, S., Bocchini, L., Giraudo, M., Gheysens, T., Lobascio, C., Ottolenghi, A., 2017. Exploring innovative radiation shielding approaches in space: a material and design study for a wearable radiation protection spacesuit. *Life Sciences in space research* 15, 69–78.
- Walsh, L., Schneider, U., Fogtman, A., Kausch, C., McKenna-Lawlor, S., Narici, L., Ngo-Anh, J., Reitz, G., Sabatier, L., Santin, G., Sihver, L., Straube, U., Weber, U., Durante, M., 2019. Research plans in Europe for radiation health hazard assessment in exploratory space missions. *Life Sciences in Space Research* 21, 73–82. <https://doi.org/10.1016/J.LSSR.2019.04.002>.
- Zeitlin, C., 2019. *Space Radiation Shielding*. Springer International Publishing, Cham, pp. 1–17.
- Zeitlin, C., Hassler, D.M., Cucinotta, F.A., Ehresmann, B., Wimmer-Schweingruber, R.F., Brinza, D.E., Kang, S., Weigle, G., Böttcher, S., Böhm, E., Burmeister, S., Guo, J., Köhler, J., Martin, C., Posner, A., Rafkin, S., Reitz, G., 2013. Measurements of Energetic Particle Radiation in Transit to Mars on the Mars Science Laboratory. *Science* 340 (6136), 1080–1084. <https://doi.org/10.1126/science.1235989>.
- Zhang, J., 2019. Cognitive functions of the brain: Perception, attention and memory. *CoRR abs/1907.02863*.
- Zhang, J., 2019. Secrets of the brain: An introduction to the brain anatomical structure and biological function. *CoRR abs/1906.03314*.
- Zhang, R., F.N., Taddei, P., 2010. Water equivalent thickness values of materials used in beams of protons, helium, carbon and iron ions. *Phys Med Biol* 1, 14–19. <https://doi.org/10.1088/0031-9155/55/9/004>.

4.2 *Paper II: Easy-to-Apply Approach to Forecast and Calculate the Radiation Effects of SEPs in Different Parts of the Brain Using Modeling Results*

Space missions require an easy-to-apply approach to forecast and calculate the radiation effects of **SEPs**, which can cause severe acute syndromes in astronauts. In Paper 4.1, we used Geant4 Monte Carlo simulations to analyze how highly energetic particles interact with the human head's structure, generating statistical functions summarizing the dose deposit in various lobes of the human brain, and under different shielding scenarios. In this paper, we applied these functions to examine the **GCR** and **SEP** environment that astronauts could potentially encounter in deep space. We used Badhwar O'Neil input **GCR** spectra and 50+ historical **SEP** events to calculate dose rates in different brain lobes. In our evaluation of the shielding effects around the human head, we observed that thicker shielding materials yielded a significant reduction in the dose rate experienced by the brain. This effect was particularly pronounced in mitigating the impact of **SEP**. For instance, we found that a 2 cm aluminum shield could potentially decrease the dose from **SEPs** by as much as 90%. Such a dose reduction is deemed sufficient to safeguard astronauts from the development of acute radiation syndromes. We also conducted a statistical analysis of the dose versus the properties of incoming **SEP** spectra. By examining 50+ historical **SEP** events, we have developed a set of empirical correlations that can predict the dose of radiation that the brain will receive from an incoming **SEP** event. These correlations are highly effective in simplifying the forecasting process, while maintaining a high degree of accuracy comparable to that of a full Monte Carlo simulation. Furthermore, our approach offers significant computational advantages by reducing the computational power required and simplifying the prediction process.

To develop our empirical correlations, we analyzed the **SEP** spectral data from historical events and identified simple functions that can calculate the dose from an **SEP** event at a specific part of the brain or human head, taking into account different thicknesses of shielding. Our approach only requires the intensity of the **SEP** at the pivot energy, making it very user-friendly. Our simplified approach allows for quick and accurate predictions of the consequences of an SEP event, enabling us to develop effective strategies to mitigate the potential harm it may cause. The following article is reproduced from Khaksarighiri et al. (2021) with permission from "Scientific Reports" journal:

An easy-to-use function to assess deep space radiation in human brains

Khaksarighiri, S., Guo, J., Wimmer-Schweingruber, R., Narici, L. (2021). Scientific Reports, 11(1), 11687.

My contribution to this paper is 80% of the overall content and research efforts.



OPEN

An easy-to-use function to assess deep space radiation in human brains

Salman Khaksarighiri¹, Jingnan Guo^{1,2,3✉}, Robert Wimmer-Schweingruber¹ & Livio Narici^{4,5}

Health risks from radiation exposure in space are an important factor for astronauts' safety as they venture on long-duration missions to the Moon or Mars. It is important to assess the radiation level inside the human brain to evaluate the possible hazardous effects on the central nervous system especially during solar energetic particle (SEP) events. We use a realistic model of the head/brain structure and calculate the radiation deposit therein by realistic SEP events, also under various shielding scenarios. We then determine the relation between the radiation dose deposited in different parts of the brain and the properties of the SEP events and obtain some simple and ready-to-use functions which can be used to quickly and reliably forecast the event dose in the brain. Such a novel tool can be used from fast nowcasting of the consequences of SEP events to optimization of shielding systems and other mitigation strategies of astronauts in space.

Among various issues that may cause health problems for astronauts, the hazard from radiation on interplanetary flights is currently one of the major obstacles, especially for long-duration missions to outer space, e.g., a manned mission to Mars^{1,2}. While space radiation research has grown swiftly in recent years, substantial uncertainties remain in predicting and extrapolating the responses of humans to radiation exposure. One of the reasons may be because only 24 human beings have ventured beyond the protective envelope of the Earth's magnetosphere for a maximum of approximately 12 days (Apollo 17)³.

Exposure to charged particles during long-term missions in space, where high-energy particles are more abundant than in Earth orbit, can lead to substantial biomedical or health risks for astronauts^{3,4}. Space radiation risks include carcinogenesis, degenerative tissue effects, central nervous system (CNS) decrements^{5,6}, heart diseases^{7,8} and acute radiation syndrome^{9–12}. Acute effects are possible when astronauts are exposed to large SEP events, which produce a high radiation dose^{13,14}. On the other hand, a major concern of space radiation is the long-term effect on astronauts, which can include cataracts, an increased chance of cancer, and some health effects are even thought to be passed on to the next generations by mutated genes^{1,5,9,15}.

Radiation environment in deep space. The deep-space radiation environment is determined by two major sources of ionizing radiation, with Galactic Cosmic Rays (GCRs) and Solar Energetic Particle (SEP) events. Protons and helium ions comprise about 87% and 12% of GCRs, respectively¹⁶, with additional contributions by heavier nuclei such as carbon, nitrogen, oxygen, and iron. Despite their small abundance of about 1%, these heavy ions are of particular concern for manned space missions because of their relatively high Linear Energy Transfer, and the uncertainties of their biological effects. Once they have entered the solar system, the GCRs are modulated by the heliospheric magnetic field, which changes with the 11-year solar activity cycle [e.g.¹⁷]. The flux of GCR protons may be two orders of magnitude higher during solar minimum than during solar maximum years at energies below about 100 MeV as shown in Fig. 2b (as obtained from a GCR model that will be explained in detail in "Calculation method and setups"). The flux of GCRs is low, but their influence integrated over a typical duration of a Mars mission of 3 years can be substantial. A risk assessment study of exposure to space travelers¹⁸ estimates that 20 million out of 43 million hippocampus cell nuclei will be directly hit by one or more particles, with charge $Z > 15$ assuming the 1972 GCR spectrum after the peak year of solar cycle 20.

On the other hand, SEP events are dominated by protons and electrons, which are accelerated in sporadic solar eruptions such as flares or shocks driven by Coronal Mass Ejection (CME) (e.g.¹⁹). Small and flare-associated

¹Institute of Experimental and Applied Physics, University of Kiel, 24118 Kiel, Germany. ²School of Earth and Space Sciences, University of Science and Technology of China, Hefei 230026, China. ³CAS Center for Excellence in Comparative Planetology, USTC, Hefei, China. ⁴Departments of Physics, The University of Rome 'Tor Vergata', Rome, Italy. ⁵INFN Roma Tor Vergata, Rome, Italy. ✉email: jnguo@ustc.edu.cn

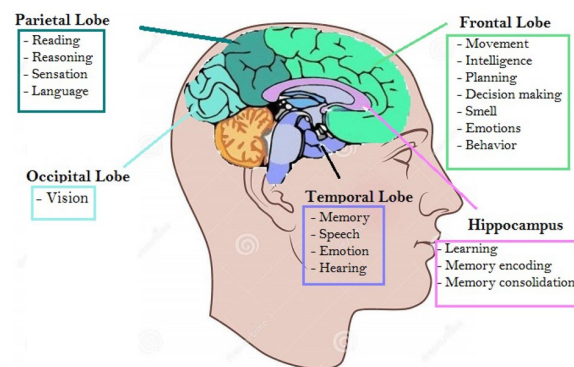


Figure 1. Structures of a human brain including different lobes and hippocampus with their corresponding major functions adapted from²⁷. The position might appear different due to the selected 2D cut of the 3D structure. More descriptions can be found in “[Radiation effects on human brains](#)”.

SEP events can occur at any time during the solar cycle, whereas larger SEP events tend to occur during periods of high solar activity. They can lead to high radiation doses in short time intervals²⁰.

Radiation effects on human brains. Our brain is the command center for the human nervous system, which interprets information from the outside world and directs our body’s internal functions. The cerebrum is the largest portion of the brain containing the cerebral cortex, which is responsible for most of the actual information processing in the brain. The cerebral cortex is divided into four cortex lobes: the frontal lobe, temporal lobe, parietal lobe, and occipital lobe. These lobes are responsible for various functions in the body that include everything from sensory perception to decision-making and problem-solving²¹, as indicated in Fig. 1. We also consider the hippocampus region in our study, which is a structure within the medial aspect of the temporal lobe that can be identified as a layer of densely packed neurons and plays a vital role in regulating learning, memory encoding, memory consolidation, and spatial navigation²².

The brain ventricular is a highly conserved aspect of brain structure, a series of connected cavities lying deep within the brain, filled with cerebrospinal fluid (CSF). These structures are responsible for the production, transport, and removal of CSF. The brain ventricles can enlarge during spaceflight^{23–26}. While this is a real change in the structure of the brain, its relevance in these studies is uncertain, and there is no model for it under zero gravity conditions. Therefore, we did not include this effect in our simulations of a realistic brain structure.

Different radiation effects have been reported from patients experiencing conventional cranium radiotherapy or treatments for glioma brain tumor such as, adverse effects and behavioral changes in CNS, long-term anxiety, depression, disturbances in learning, memory, processing speed, attention, and cognitive flexibility^{28–32}. Acute or short-term radiation effects may occur during or immediately after the course of radiation, such as fatigue or hair loss. Late or long-term effects include white matter changes, radionecrosis, neuropsychological and endocrine changes (hormonal)^{32–35}.

Animal models and experimental studies of exposing mice to doses of radiation corresponding to that of a cruise to Mars³⁶ suggest that the radiation exposure may impair cellular signaling in the hippocampus, a brain region bound to learning and memory³⁷, and may also cause damage in short-term memory as well as disturb the crew’s performance and decision making procedure³⁸. It also reveals the capability of radiation to significantly decrease the structural complexity and synaptic integrity of neurons throughout different regions of the brain, inducing compromised cognitive performance of mice²⁹.

To better assess the space radiation effect on the brain, we study the GCRs and SEP events induced dose deposit in different lobes and in the hippocampus region of the brain by calculating the dose distribution inside an actual three-dimensional head structure extracted from computed tomography (CT) images. Thus this paper consists of three parts. First, we introduce and describe the method for calculating radiation doses inside the brain. Second, we estimate the GCR radiation dose deposit inside different lobes and in the hippocampus region of the brain, with various depths of shielding around the head. Third, we consider the consequence of SEP events using SEP spectral data of 50 historical events and find some easy-to-use functions, which can quickly convert the SEP event intensity at a certain pivot energy to the final dose deposit in the brain, following a method developed by³⁹. Finally, we evaluate the implications of our calculations in the context of astronauts performing interplanetary space missions.

One important output of this work is to provide a quantitative assessment that could help to produce a possible ‘alarm’ for the SEPs. Our results would be used to predict the importance of the coming radiation event and, together with the knowledge from radiation treatments for cancer, and the growing understanding of the influence of radiation on cognitive functions⁴⁰, to forecast the level of radiation effects and the subsequent risks, providing grounds for the related alarm.

Calculation method and setups

Previous studies of radiation effects on CNS have most commonly reported measurements or calculations of Dose (Gy) to characterize the radiation risk. Alternatively, in some works, it has been suggested that particle fluence or the measure of the number of electrons emitted per unit track length are better predictors for the effectiveness of different particles for neurobehavioral dysfunction⁴⁰. In the current study, we stay with the basic physical unit of the radiation dose, i.e., energy deposit per unit mass, as the results can be more easily related to the biological radiation experiments.

In a previous study⁴¹, we calculated the dose distribution in different parts of the human brain using actual head densities extracted from CT images. The particle transport simulations have been carried out using version 10.4 of Geant4 toolkit [GEometry And Tracking^{42,43}], a well-established and three-dimensional Monte Carlo particle transport tool.

We used a matrix approach following^{44,45} to obtain “brain response functions” (BRFs) of the dose dependence on the primary particle type and energy. A BRF is a probabilistic description of the deposited energy of a primary particle, with a defined type and energy, in the brain. All possible interactions, which may be triggered when the primary particle and its secondaries penetrate through the head, are included in the BRF. Primary particles of protons and helium ions, as well as carbon, nitrogen, and iron, are considered to construct these BRFs⁴¹. The BRF has a unit of dose per fluence of primary particles and can be used to fold (i.e., multiply per energy bin and then integrate) with a given primary particle spectrum for obtaining the radiation dose inside the brain, similar to the approach in⁴⁶.

Extra shield around the head: As humans in space would always have a certain kind of shielding protection, we simulated various depth of aluminum shielding (0.2 cm, 0.5 cm, 2 cm, 5 cm, and 10 cm) between the radiation source and the brain. Aluminum (Al) was used because it is a conventional choice used in the community, so that our result can be more easily compared to previous works^{47,48}. The thickness chosen here can be approximating a helmet, spacesuit, and other possible shielding depths of a habitat⁴¹. It is important to note that primary GCRs and SEP events passing through shielding materials may undergo inelastic interactions with the ambient atomic nuclei losing some or all their energy and also creating secondary particles via spallation and fragmentation processes, resulting in a radiation field including both primary and secondary particle radiation inside the space vehicle (e.g.⁴⁹). These secondaries including neutrons which are highly relevant for their biological effects are modeled and propagated further in our models and they may also contribute to the dose in the brain within the shielding.

GCRs in deep space: In “Deep-space radiation from GCRs” we fold the BRFs with deep space GCR spectra under different solar modulations as predicted by the Badhwar O’Neil model⁵⁰ and shown in Fig. 2b. We show results for solar modulation potentials (Φ) between 300 MV and 1200 MV. A large Φ value corresponds to a strong solar modulation with enhanced interplanetary magnetic fields that depress the GCR flux around the solar maximum; a smaller Φ instead represents weaker solar activities with less-modulated and thus higher GCR flux. Dose deposits in different lobes of the brain and in the hippocampus region are then calculated based on various solar modulation conditions and different Al-shielding depths.

SEP events in deep space: In the second part of this work, we use BRFs to fold with a variety of SEP events shown in Fig. 2b. The SEP spectra represent some historical large events from August 1997 to 2006, reconstructed from measurements of the Geostationary Operational Environmental Satellite (GOES) and the Advanced Composition Explorer (ACE) satellite at the deep space environment near Earth⁵¹. Such events show different spectral properties (intensities and shapes), which complicate the assessment of the radiation dose experienced by astronauts. We, therefore, carry out a statistical study of the correlation between the dose deposit in the brain by each event and the SEP spectral parameters and obtain some easy-to-use functions. These functions rely on the so-called pivot energy of the original SEP spectra at which the spectral index does not influence the final dose deposit³⁹.

Simulation results and discussion

Application of the simulated results—the procedure to apply our ready functions for calculating the resulted radiation inside a brain.

In this section, we demonstrate how to apply readily-calculated BRFs to obtain the radiation dose rate inside the four main lobes, and in the hippocampus region of an astronaut’s brain. The procedure of the application and the results for deep-space exposure to GCRs are shown in Fig. 2.

The BRFs for protons in the different lobes, and in the hippocampus region of the brain are plotted in Fig. 2a. After folding them with the various possible input spectra, shown in panel (b) of Fig. 2, i.e., multiplying the values of BRF with the spectra flux in each corresponding energy-bin, one obtains the dose rate in the different lobes as a function of energy as shown in panel (c). The integration of the total dose rate over all energies gives the radiation deposit by the primary GCR protons in the brain (or at a certain part of the brain). Mathematically, the procedure described above can be summarized as given in Eq. (1).

$$\dot{D} = \left\{ \frac{D}{f} \right\} \times F, \quad (1)$$

where $D(\mu\text{Gy})$ is the dose deposit in each lobe resulted from simulation, f is the fluence of the source used in the simulation in units of particles $\text{cm}^{-2} \text{sr}^{-1} \text{MeV}^{-1}$, F represents the double-differential (both energy- and time-differential) flux of GCRs in units of particles $\text{cm}^{-2} \text{sr}^{-1} \text{MeV}^{-1} \text{s}^{-1}$, finally, \dot{D} is the GCR-induced dose rate in each lobe given in $\mu\text{Gy/s}$. We note that when applying the above method to SEP events, F is integrated over the respective time duration for each event so that the obtained dose is not time-differential and has the unit of μGy .

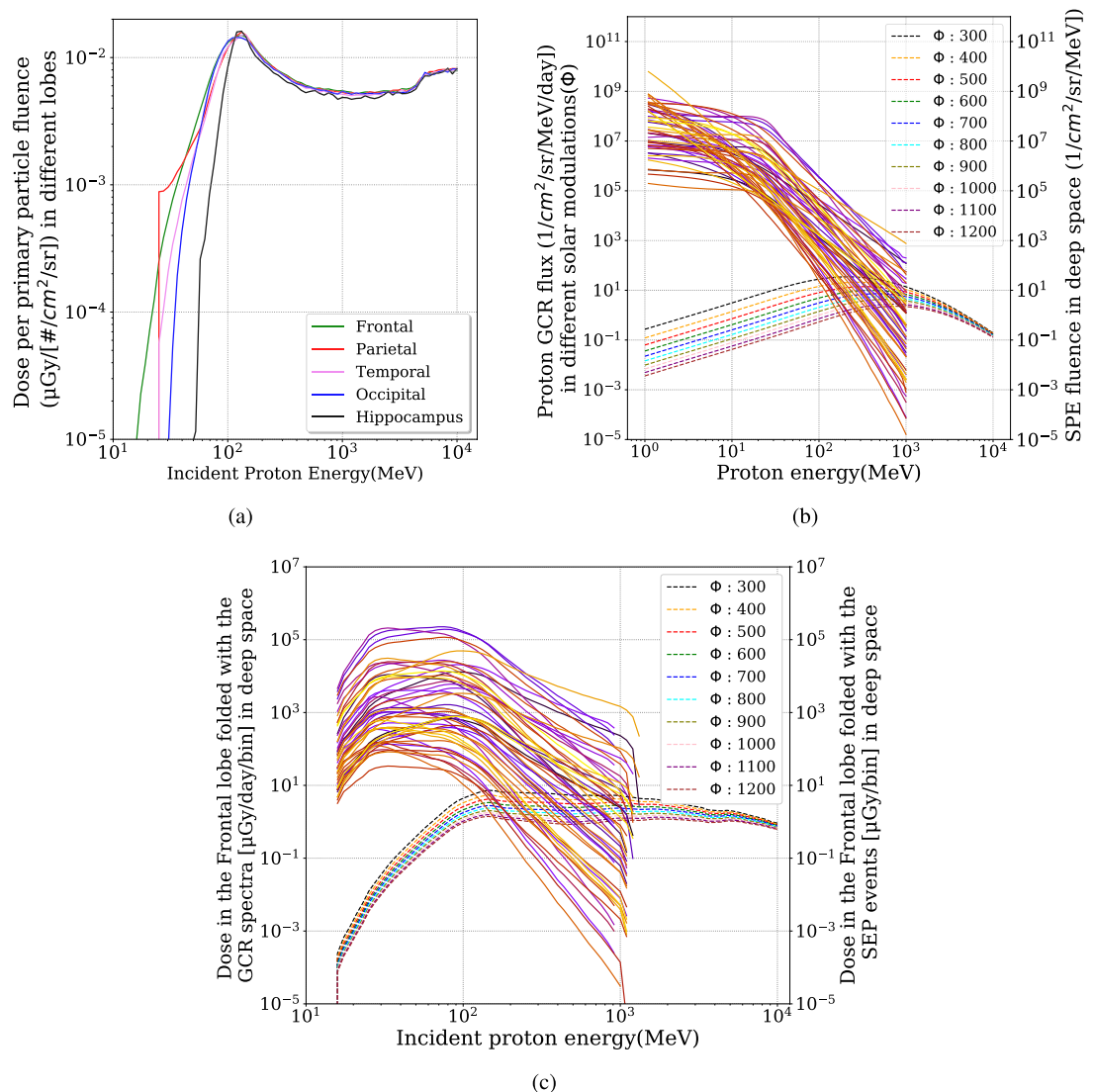
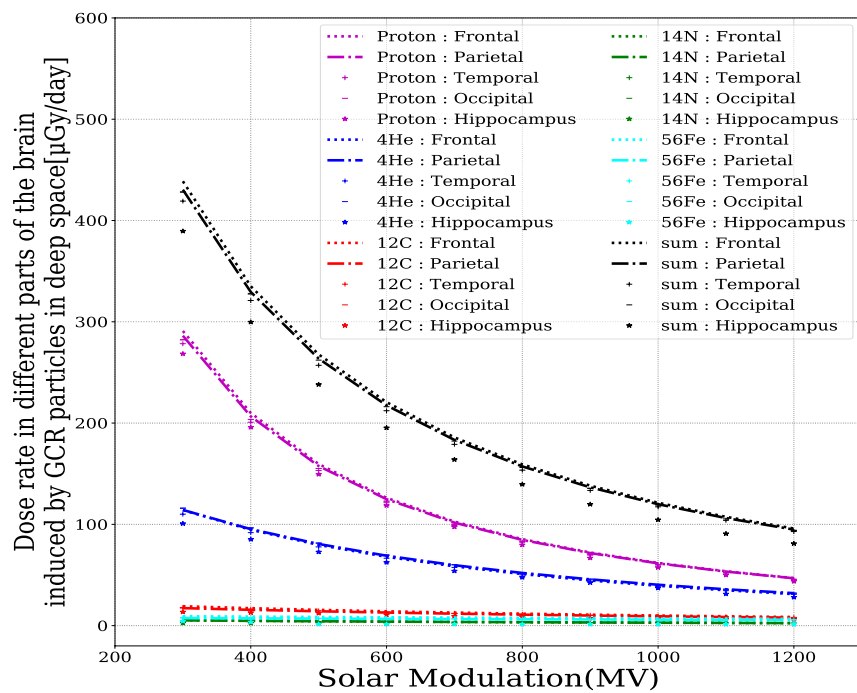
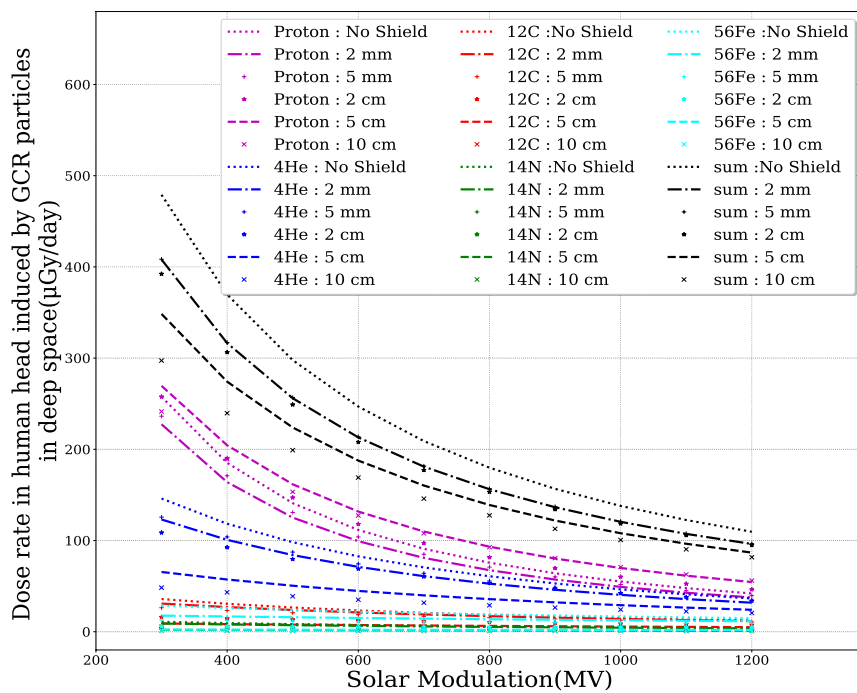


Figure 2. Folding the Brain Response Functions (BRFs) with primary GCR/SEP protons to calculate the dose rate inside different lobes, and in the hippocampus region of the brain as described in “[Application of the simulated results—the procedure to apply our ready functions for calculating the resulted radiation inside a brain](#)”. (a) BRFs as calculated in⁴¹ for protons. (b) Energy- and time-differential flux of GCRs under different solar modulation potential (MV) (dashed curves) and the energy-differential but event time-integrated fluence of SEP events (solid lines) in deep space. (c) Convolutions of the GCR/SEP particle spectra of panel (b) with the BRF for the frontal lobe.

Deep-space radiation from GCRs. We used the procedure discussed in “[Application of the simulated results—the procedure to apply our ready functions for calculating the resulted radiation inside a brain](#)” to calculate the dose rate in different parts of the brain for a range of GCR spectra at different solar activities throughout the solar cycle. The GCR spectra are obtained based on the Badwar O’Neil model⁵⁰, which depends on the parameter solar modulation potential, Φ . We made the calculations using different Φ values ranging from 300 MV (solar minimum) to 1200 MV (solar maximum). The results are shown in Fig. 3a for dose rate in different lobes without shielding. As expected, the differences between the dose rates in the different lobes are hardly discernible, but is smaller in the hippocampus region. This difference is mainly due to the contribution of low energy particles which can be more easily stopped before reaching hippocampus, which is located in the inner region of the temporal lobe and more shielded compared to different lobes. The dose rates, that concern all modeled GCR particles in deep space, vary between about 100 and 440 $\mu\text{Gy}/\text{day}$ for solar activity maximum and minimum. However, we note that our estimation of the GCR-induced dose rate might be slightly smaller than the expected values as we have cut off the particles above 10 GeV in our simulations since particle flux above this energy decreases versus the energy following a power-law.



(a) Dose rate in different lobes



(b) Dose rate in human head for different thickness of shielding around head

Figure 3. (a) The dose rates in different parts of the brain induced by GCR particles in deep space without shielding protection. (b) The dose rates in the human head under different thickness of shielding. The primary source GCRs include protons, helium and heavier ions such as carbon, nitrogen and iron under different solar modulation conditions. The summed dose rates from all these primary particles under different conditions (i.e., solar modulations, shielding depth and different lobes) are shown in black.

Figure 3b shows the dose rate for the entire human head given different solar modulation potentials, Φ , for different particle species considered here, and for different shielding, as explained in “Calculation method and setups”. Some subtle differences can be seen. For instance, the highest dose rate from protons is not for the unshielded scenario as for He-nuclei, but for a shielding thickness of 5 cm Al-equivalent. Nevertheless, the total dose rate from all primary GCR particle species shows a decrease when the shielding is increased. At solar minimum, a shielding of 2 mm of Al results in an overall reduction by approximately 14%. 27% reduction is reached with shielding by 5 cm of Al. A further increase in shielding thickness to 10 cm of Al results in a total reduction of 37%. These values are reduced somewhat during solar maximum conditions (12%, 20%, and 25%, respectively).

Exposure to 0.5 Gy of simulated GCR radiation, containing a mixture of different particle species may result in some long-term deficits in the recognition memory system of male mice⁵². Approximating this as an “upper limit” of the accumulated GCR radiation for brains in space despite of it being different from those of the mice, we can derive the appropriate shielding depth and the allowed duration of the space mission under different solar modulation conditions. In particular, during solar minimum when the GCR flux is around its maximum value, with 2 mm of shielding, the GCR radiation in the brain can be reduced to about 400 $\mu\text{Gy/day}$. On the other hand, during solar maximum, the GCR radiation in brains is already much lower, and extra shielding is not that necessary, but surely helpful.

Deep-space radiation from SEP events. Alternatively, the short-term sporadic solar energetic particles events generated during solar eruptions may result in some sudden and drastic enhancement of the radiation in the brains of astronauts in space. To assess the potential radiation effects associated with these SEP events, we evaluate the effect of 53 large SEP events⁵¹ without and with the various shielding thicknesses used in the previous section “Deep-space radiation from GCRs”. Table 1 lists dose deposits in the human head for 35 of these 53 SEP events. They were chosen as they deposit more than 10 cGy dose in the human head without shielding.

In the case of no shielding around the head, the dose in different lobes of the human brain is considerably less than the dose averaged in the entire human head because of the human cranium with an average of 6.5 mm thickness⁵³ protects the brain against low-energy ions. Moreover, the dose in the frontal lobe is slightly higher than other lobes, and the hippocampus experienced the lowest dose among the studied regions of the brain in our work. This is the same effect as already observed for low energy GCRs (below 100 MeV/nuc). The reason is that the frontal lobe has a larger portion at the outer edge of the brain and is more exposed to the radiation contribution from low-energy primary particles, but the hippocampus is located deep in the temporal lobe, and it is the most shielded part compared to the others. This effect is more obvious for SEP events because they have a larger contribution from low energy particles in comparison to GCRs.

The results reported in this table clearly show that even a modest shielding of only 2 mm of Al can reduce the dose in the head by more than 50% in the case of SEP events. Previous studies considered the Space-Permissible Exposure Limit (SPEL) for short-term radiation exposure of CNS to be about 50 cGy in 30-days⁵⁴. We mark the event doses that exceed 50 cGy in bold font in Table 1. As shown, even under 2 cm of Al shielding, some events exceed the 30-days SPEL in the human head. Besides, the enhanced solar activity during the maximum of a solar cycle often leads to multiple SEP events taking place within the course of days or weeks such as the few events associated with the famous Halloween storm in 2003 as shown in Table 1. It is therefore important to forecast SEP events and prepare with extra shielding during hazardous situations like this.

A statistical study of SEP-induced Martian surface radiation by events with different properties such as their energy range, intensity, and the power-law index has been performed by³⁹. They found a good correlation between the induced radiation on Mars and the fluence of the initial SEP spectra. In particular, they discovered a pivot energy (~ 300 MeV) at which the SEP flux alone can be used to determine the Martian surface dose rate for large SEP events. Based on the same idea, we try to correlate our calculated dose deposit in the human head under different scenarios (shielding and different lobes) versus the original SEP event fluence at selected energies, in particular at 40 MeV, where the Pearson correlation coefficient is nearly unity. This means that with a given fluence at this pivot energy, other information of the SEP spectra does not effectively influence the radiation deposit in the brain. This feature can be related to the balance of dose contribution by SEP events below and above the pivot energy³⁹. A SEP spectrum is often described as a power-law distribution. When the slope of the power-law changes from e.g., -4 to -2 , the reduction of the dose contribution from particles below the pivot energy is compensated by the increased dose from particles above this point.

Here we obtain the pivot point being 40 MeV in case of dose deposit in the head with a 2 mm Al shield. This pivot energy is lower than the case of Mars because of the thinner shielding considered compared to the Martian atmosphere. For a thicker shielding, we expect this pivot point to shift towards a higher energy. We also fit the correlation of dose deposit [cGy] versus the SEP events fluence [particles $\text{sr}^{-1} \text{cm}^{-2} \text{MeV}^{-1}$] at the pivot energy, for different events, with a linear function as shown in Fig. 4 and Eq. (2) as follows :

$$D_{\text{Brain}} = a \cdot I_{\text{Pivot Energy}} + b \quad (2)$$

where a has the unit of $\text{cGy sr cm}^2 \text{MeV}$ and b with unit of cGy. Their fitted values are represented in table 2 for different scenarios. The obtained function can be used to directly derive the dose deposit in the head (or different parts of the brain) using the SEP events fluence at the single energy and thus can significantly simplify the radiation forecast for future manned missions in space upon the onset of SEP events.

To better locate the pivot energy of the dose deposit in the brain under different cases studied, we calculate the Pearson correlation coefficient (Pcc) of the obtained dose versus the SEP fluence of each event at different energies. In Fig. 5a, we show the Pcc values versus energies of the original SEP spectra for various cases of shielding around the head. As expected, the best Pcc for each case has the peak value around 1 at a certain energy that is

Events	Dose(cGy) in a human head shielded by different thicknesses of Al						Dose(cGy) in different lobes of a human brain				
	Without shield	2 mm	5 mm	2 cm	5 cm	10 cm	Frontal	Parietal	Temporal	Occipital	Hippocampus
	(cGy)	Al (cGy)	Al (cGy)	Al (cGy)	Al (cGy)	Al (cGy)	(cGy)	(cGy)	(cGy)	(cGy)	(cGy)
6 Nov 1997	52	12	4	0.9	0.2	0	6	4.6	4.4	4.3	1.5
20 Apr 1998	123	39	13	2	0.4	0.1	13	9	9	8	5
24 Aug 1998	32	4	1.4	0.2	0	0	0.63	0.5	0.4	0.4	0.17
30 Sep 1998	31	5	2	0.4	0	0	1	0.8	0.7	0.7	0.3
14 Nov 1998	13	4	2	0	0	0	1.4	1.17	1.14	1.2	0.6
14 July 2000	2005	741	345	78	22	6	179	144	139	141	62
8 Nov 2000	1354	542	283	71	20	5	159	132	128	130	64
26 Nov 2000	26	4	1.5	0.3	0	0	0.69	0.53	0.5	0.5	0.19
2 Feb 2001	58	15	6	1.1	0.3	0	2.9	2.3	2.1	2.1	0.85
10 Feb 2001	10	2	0.7	0.1	0	0	0.36	0.28	0.26	0.25	0.1
12 Feb 2001	19	1	0.2	0	0	0	0.07	0.05	0.05	0.04	0
15 Feb 2001	79	39	28	14	7	3	21	19	18	17	12
18 Feb 2001	20	9	6	3	1.4	0.6	4.6	4.1	4.1	4	2.6
16 Aug 2001	28	13	8	3	1.4	0.6	5.7	4.8	4.8	4.3	2.8
24 Sep 2001	426	92	41	9	2	0.8	21	17	16	16	7
1 Oct 2001	70	8	1.7	0.1	0	0	0.6	0.4	0.35	0.3	0.07
4 Nov 2001	2255	736	256	34	7	1.7	110	82	77	76	26
22 Nov 2001	591	83	24	2	0.5	0.1	9	7	7	6	2
26 Dec 2001	48	18	10	3	1.3	0.5	6.3	5.7	5.3	5.5	2.9
21 Apr 2002	267	92	36	6	1.4	0.4	16.6	12.9	12.2	12	4.6
24 Aug 2002	29	9	4	1.3	0.5	0.2	2.8	2.5	2.3	2.3	1
26 Oct 2003	12	3	1.6	0.4	0.1	0	0.9	0.7	0.7	0.7	0.3
28 Oct 2003	1268	357	174	43	13	4	94	77	76	78	35
29 Oct 2003	244	68	36	10	3	1.2	21	18	17	18	9
2 Nov 2003	89	34	15	3	1	0.3	8	7	7	6	3
7 Nov 2004	12	1.5	0.5	0	0	0	0.27	0.21	0.2	0.2	0.07
10 Nov 2004	12	6	4	2	1.4	0.3	3.7	3.4	3.3	3.5	2.3
16 Jan 2005	27	4	2	0.4	0.1	0	1	0.78	0.74	0.7	0.3
17 Jan 2005	362	108	35	4	0.9	0.2	15	11	11	10	3
20 Jan 2005	158	90	69	37	20	10	53	49	48	50	34
13 May 2005	22	1.3	0.38	0	0	0	0.16	0.11	0.1	0.1	0.03
22 Aug 2005	19	2	0.6	0	0	0	0.24	0.18	0.16	0.15	0.05
7 Sep 2005	135	25	10	1.7	0.4	0.1	4.6	3.6	3.4	3	1.3
6 Dec 2006	174	44	21	5	1.5	0.4	11	8.9	8.6	8.4	3.9
13 Dec 2006	81	40	26	10	4	1.6	17	15	14.7	14.5	8.5

Table 1. Resulting dose (cGy) from 35 SEP events in a human head considering different thicknesses of Al as a shield around an astronaut's head/body. Dose deposits in different lobes of the human brain protected by 2 mm of shield are also shown. Those event doses that exceed 50 cGy are shown in bold font. These 35 events are chosen from the list as they would deposit more than 10 cGy of dose in the head without shielding (second column).

the pivot energy to be found. The pivot energy for a thicker shield shifts towards a larger value and equals about 300 MeV for 10 cm of Al shield. This is the same pivot energy found by³⁹ as the accumulated shielding depth in this case (27 g/cm²) is comparable to the Martian atmospheric depth studied by⁴¹ (the vertical column mass is about 22 g/cm² of CO₂ and the average shielding depth is slightly larger). In Fig. 5b, the pivot energy is determined, for dose deposit in four lobes under 2 mm of Al shielding, to be 75 MeV for the frontal lobe and 90 MeV for the other three lobes and increases to 120 MeV for the hippocampus region as this part is embedded deep into temporal lobe and more shielded compared to other lobes. On the other hand, the slightly smaller pivot energy for the frontal lobe also reveals the fact that it is the least shielded lobe compared to the others. Fig. 5c,d plot the correlation of the dose deposit versus the SEP fluence at the determined pivot energy, which is obtained with the best Pcc values larger than 0.998. Different lobes have been considered and different thicknesses of shielding can approximate different situations such as helmet, spacesuit, and various possible shielding depths within a habitat. Such determined pivot energy, the Pcc of the fitting, and the fitted parameters of the linear function for each case are given in Table 2. These values can be used as a look-up table to forecast or nowcast the dose deposit inside a human head in space (under different shielding depths as well as in various parts of the brain) based solely on the SEP events fluence at these pivot energies.

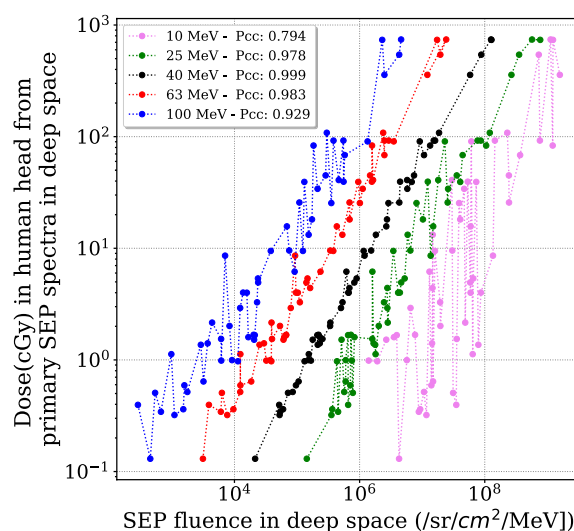


Figure 4. Dose (cGy) deposit in the human head, with 2 mm of shielding around, induced by each SEP event under study versus the original SEP fluence at a few specific energies as marked in different colors and labeled in the legend with the Pearson correlation coefficients (Pcc) for different cases.

Summary and conclusions

Among various effects that may cause health problems for astronauts on long-duration missions to outer space such as the Moon or Mars, space radiation deserves special attention because it has known long-term effects, but can also become critical in the course of short time periods. Effects on the CNS are important because they can lead to changes in motor function and behavior or neurological disorders, which can have devastating effects during a deep space mission.

The radiation induced by the background GCRs is omnipresent but mostly stable and easier to predict. However, the radiation associated with SEP events is sporadic, highly variable from events to events, and may cause severe acute syndromes to astronauts if no sufficient protection is prepared, such as during extravehicular activities. This requires the most straightforward and easy-to-apply approach to forecast the SEP events induced radiation effect during the course of a manned mission.

In the previous work⁴¹, we have established a set of GEANT4 Monte Carlo simulations to describe the interactions of highly energetic particles with an actual human head structure and lobes inside the brain. The dose deposit in different lobes of the brain, in the hippocampus region and in the whole human head under different shielding scenarios, has been summarized as statistical functions, which depend on the primary particle energy of the SEP events/GCRs. In this paper, we apply these functions to the GCRs and SEP events environment that an astronaut may encounter in deep space.

First, we fold these BRFs with Badwhar O'Neil⁵⁰ input spectra for different GCR modulation parameters and derive the doses in different lobes, and in the hippocampus region. The overall dose rate is between 99 and 437 $\mu\text{Gy/day}$ for solar maximum and minimum conditions. Not unexpectedly, there is no substantial difference between the dose rate in different lobes for GCRs. Increased shielding thickness, however, shows a noticeable reduction in the dose rate experienced by the brain. Reductions are 12% and 25% for 2 mm and 10 cm of Al shielding during solar maximum, respectively, but reach to 14% and 37% during solar minimum conditions, respectively.

This sensitivity to shielding is even more pronounced for SEP events because they typically cover a lower energy range than GCRs. Shielding by 2 mm of Al can reduce the dose from SEP events by more than 65%, an increased shielding by 2 cm of Al reduces it by 90%. This reduction is sufficient to protect astronauts against acute radiation syndromes for all SEP events encountered during the space age.

Although the differences in dose experienced by the different lobes during SEP events are small, the frontal lobe sees the largest dose because it has the largest area close to the surface of the human brain. On the other hand, the hippocampus region, which is located deep inside the temporal lobe absorbed a lower dose than the outer parts. The low-energy part of SEP events deposits most of its energy in the outer surface of the brain, thus mostly affecting the frontal lobe. This could be mitigated by a clever helmet design.

The dose-fluence relationships are shown for proton in different energies for each scenario to determine the best correlation coefficient, and then, the pivot energy. Finally, we formulate the correlation between SEP events intensity and the brain dose for each scenario that have been reported in Table 2. Using this function and parameter for each scenario, one can quickly calculate the SEP events induced dose at a certain part of the brain or the human head considering the different thickness of shielding around, given the intensity of the SEP events at the pivot energy. These results show that the pivot energy in the a human head with 10 cm of Al as a shield is about 300 MeV, which is the same as the pivot energy on the surface of Mars with $\sim 22 \text{ g/cm}^2$ of vertical column depth of CO_2 ³⁹.

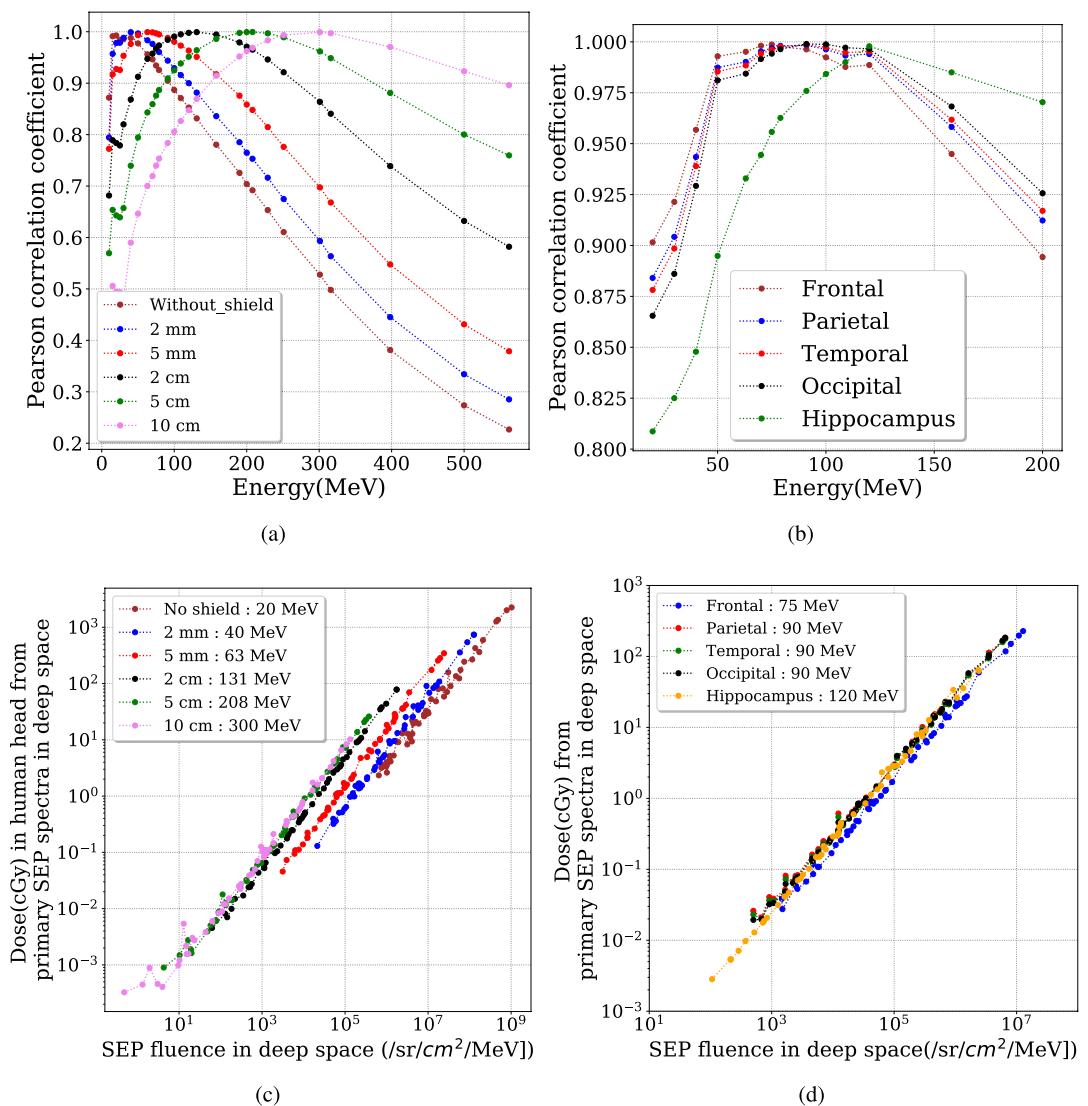


Figure 5. Upper panels: correlation coefficients between the event dose and SEP fluence of each event at different energies for (a) various thicknesses of Al around a human head and (b) different lobes of the human brain with 2 mm of Al shielding. Lower panels: The dose (cGy) deposit in a human head from primary SEP spectra in deep space versus SEP events fluence at the determined pivot energy for (c) a human head with different Al thickness and (d) different lobes of the brain under a 2 mm of Al shield.

The statistical analysis of the resulted dose versus the properties of the incoming SEP events spectra of 50+ historical events provides us some empirical correlations which can be directly applied to predict the dose in the brain from the initial SEP-event fluence, thus minimizing the complication of the forecast while keeping the accuracy as a full Monte Carlo simulation and saving the computational power. We note, however, that using only historical event data bears with it the risk that one is not prepared for an event which was not known in the past. Here we rely on our knowledge which has been accumulated in the space age and is hopefully short compared with the many generations of humans that will visit space in the future.

The pivot energies for the head, various lobes and the hippocampus region, range between about 20 and 300 MeV, mainly depending on different shielding depths. We suggest the importance of in-situ (outside the vessel or the base) measurement of particle fluences at these energies, which are an important parameter for a direct prediction of SEP radiation impacts on human brains.

The radiation effect on the hippocampus of mice, which is an important structure for the formation of long-term episodic memory has been studied in⁵⁵. Their results show that 1 Gy of proton radiation can produce long-term changes to neuronal electrophysiological states. With 0.1 Gy radiation from incident protons, object recognition memory is impaired three months following the irradiation experiment⁵⁶. As shown in Table 1, our statistical analysis includes multiple cases with the event radiation dose exceeding 0.1 Gy, even under 2 or 5 mm of shielding. Of course, the human head and brain structure is different from that of a mouse, and it is not certain

	Scenarios	Pivot energy (MeV)	$a \times 10^6$	b	R ²
Human head	No shield	20	2.42 ± 0.04	15.69 ± 8.60	0.985
	2 mm Al	40	5.89 ± 0.03	2.048 ± 1.05	0.998
	5 mm Al	63	14.5 ± 0.08	0.721 ± 0.44	0.998
	2 cm Al	131	45.3 ± 0.25	0.114 ± 0.10	0.998
	5 cm Al	208	70.6 ± 0.33	0.021 ± 0.03	0.999
	10 cm Al	300	77.6 ± 0.46	0.011 ± 0.01	0.998
Lobes of brain protected by 2 mm of shield	Frontal	75	18.0 ± 0.13	0.57 ± 0.36	0.997
	Parietal	90	28.4 ± 0.23	0.40 ± 0.33	0.996
	Temporal	90	27.4 ± 0.20	0.38 ± 0.27	0.997
	Occipital	90	28.3 ± 0.18	0.38 ± 0.26	0.997
	Hippocampus	120	26.8 ± 0.35	0.18 ± 0.11	0.990

Table 2. The fitted parameters of Eq. (2) for deriving the SEP events induced dose D_{Brain} at a certain part of the brain or the head under different thickness of Al shielding. The determined pivot energy $I_{\text{Pivot energy}}$ of the SEP events for different cases is also given. The fitted parameter a has the unit of $\text{cGy} \cdot \text{sr} \cdot \text{cm}^2 \cdot \text{MeV}$ and b with unit of cGy .

that the same neurological impact can be expected. However, together with these biological experiments, our statistical study suggests that the drastically-enhanced dose induced by SEP events may pose long-term effects to the CNS of brains in space and even lead to their malfunction in a long term. This should be taken into consideration for long-duration space missions, such as future missions to Mars.

Received: 17 November 2020; Accepted: 6 May 2021

Published online: 03 June 2021

References

- Maalouf, M., Durante, M. & Foray, N. Biological effects of space radiation on human cells: History, advances and outcomes. *J. Radiat. Res.* **52**(2), 126–146. <https://doi.org/10.1269/jrr.10128> (2011).
- Simonsen, L. C., Wilson, J. W., Kim, M. H. & Cucinotta, F. A. Radiation exposure for human mars exploration. *Health Phys.* **79**(5), 515–525. <https://doi.org/10.1097/00004032-200011000-00008> (2000).
- Chancellor, J. C., Scott, G. B. & Sutton, J. P. Space radiation: The number one risk to astronaut health beyond low earth orbit. *Life (Basel)* **4**, 491–510. <https://doi.org/10.3390/life4030491> (2014).
- Wu, H., Huff, J., Casey, R., Kim, M., & Cucinotta, F. Risk of acute radiation syndromes due to solar particle events, National Aeronautical and Space Agency. *The Human Health and Performance Risks for Space Explorations*. Houston, Texas: NASA Human Research Program, **171**, <https://humanresearchroadmap.nasa.gov/Evidence/reports/ars.pdf> (2009).
- Cucinotta, F. A., Alp, M., Sulzman, F. M. & Wang, M. Space radiation risks to the central nervous system. *Life Sci. Space Res.* **2**, 54–69. <https://doi.org/10.1016/j.lssr.2014.06.003> (2014).
- Kennedy, A. R. Biological effects of space radiation and development of effective countermeasures. *Life Sci. Space Res. (Amst)* **1**, 10–43. <https://doi.org/10.1016/j.lssr.2014.02.004> (2014).
- Boerma, M. *et al.* Space radiation and cardiovascular disease risk. *World J. Cardiol.* **7**, 882–888. <https://doi.org/10.4330/wjc.v7.i12.882> (2015).
- Delp, M. D., Charvat, J. M., Limoli, C. L., Globus, R. K. & Ghosh, P. Apollo lunar astronauts show higher cardiovascular disease mortality: Possible deep space radiation effects on the vascular endothelium. *Sci. Rep.* **6**, 29901. <https://doi.org/10.1038/srep29901> (2016).
- Cucinotta, F. A. *et al.* Space radiation cancer risks and uncertainties for mars missions. *Radiat. Res.* **156**(5), 682–688. [https://doi.org/10.1667/0033-7587\(2001\)156\[0682:SRCRAU\]2.0.CO;2](https://doi.org/10.1667/0033-7587(2001)156[0682:SRCRAU]2.0.CO;2) (2001).
- Cucinotta, F. A. & Durante, M. Cancer risk from exposure to galactic cosmic rays: Implications for space exploration by human beings. *Lancet Oncol.* **7**(431–436), 682–688. [https://doi.org/10.1016/S1470-2045\(06\)70695-7](https://doi.org/10.1016/S1470-2045(06)70695-7) (2006).
- Barcellos-Hoff, M. H. *et al.* Concepts and challenges in cancer risk prediction for the space radiation environment. *Life Sci. Space Res.* **6**, 92–103. <https://doi.org/10.1016/j.lssr.2015.07.006> (2015).
- Cucinotta, F. A. & Durante, M. Risk of radiation carcinogenesis. Human health and performance risks of space exploration missions. *NASA SP-2009-3405*. Houston: National Aeronautics and Space Administration, 119–170. <https://humanresearchroadmap.nasa.gov/evidence/reports/carcinogenesis.pdf> (2009).
- Hellweg, C. E. & Baumstark-Khan, C. Getting ready for the manned mission to mars: The astronauts' risk from space radiation. *Naturwissenschaften* **94**(7), 517–526. <https://doi.org/10.1007/s00114-006-0204-0> (2007).
- Hu, S., Kim, M.-H. Y., McClellan, G. E., & Cucinotta, F. A. Modeling the acute health effects of astronauts from exposure to large solar particle events. *Health Phys.* **96**(4), 465–476. <https://ntrs.nasa.gov/citations/20070023912> (2009).
- Belli, M., Saporita, O. & Tabocchini, M. A. Molecular targets in cellular response to ionizing radiation and implications in space radiation protection. *J. Radiat. Res.* **43**(Suppl), S13–S19. <https://doi.org/10.1269/jrr.43.S139> (2002).
- Simpson, J. Elemental and isotopic composition of the galactic cosmic rays. *Annu. Rev. Nucl. Part. Sci.* **33**(1), 323–382. <https://doi.org/10.1146/annurev.ns.33.120183.001543> (1983).
- Parker, E. N. The passage of energetic charged particles through interplanetary space. *Planet. Space Sci.* **13**, 9–49. [https://doi.org/10.1016/0032-0633\(65\)90131-5](https://doi.org/10.1016/0032-0633(65)90131-5) (1965).
- Curtis, S. B. *et al.* Cosmic ray hit frequencies in critical sites in the central nervous system. *Adv. Space Res.* **22**(2), 197–207. [https://doi.org/10.1016/S0273-1177\(98\)80011-2](https://doi.org/10.1016/S0273-1177(98)80011-2) (1998).
- Lario, D. Advances in modeling gradual solar energetic particle events. *Adv. Space Res.* **36**(12), 2279–2288. <https://doi.org/10.1016/j.asr.2005.07.081> (2005).
- Hu, S., Kim, M.-H. Y., McClellan, G. E. & Cucinotta, F. A. Modeling the acute health effects of astronauts from exposure to large solar particle events. *Health Phys.* **96**(4), 465–476. <https://doi.org/10.1097/01.HP.0000339020.92837.61> (2009).

21. Moscovitch, M. and Winocur, G., Frontal Lobes, Memory, and Aging. *Annals of the New York Academy of Sciences*, **769**: 119–150. <https://doi.org/10.1111/j.1749-6632.1995.tb38135.x> (1995).
22. Strange, B., Fletcher, P., Henson, R., Friston, K. & Dolan, R. J. Segregating the functions of human hippocampus. *Proc. Natl. Acad. Sci.* **96**(7), 4034–4039. <https://doi.org/10.1073/pnas.96.7.4034> (1999).
23. Lowery, L. A. & Sive, H. Totally tubular: the mystery behind function and origin of the brain ventricular system. *Bioessays* **31**(4), 446–458. <https://doi.org/10.1002/bies.200800207> (2009).
24. Van Ombergen, A. *et al.* Brain ventricular volume changes induced by long-duration spaceflight. *Proc. Natl. Acad. Sci.* **116**(21), 10531–10536. <https://doi.org/10.1073/pnas.1820354116> (2019).
25. Jillings, S. *et al.* Macro- and microstructural changes in cosmonauts' brains after long-duration spaceflight. *Sci. Adv.* **6**(36), eaaz9488. <https://doi.org/10.1126/sciadv.aaz9488> (2020).
26. Roberts, D. R. *et al.* Effects of spaceflight on astronaut brain structure as indicated on mri. *N. Engl. J. Med.* **377**(18), 1746–1753. <https://doi.org/10.1056/NEJMoa1705129> (2017).
27. Webber C., The Heart of the Brain, <http://colinwebber.com/1404/insights/executive-function-insights/the-heart-of-the-brain/> (2010)
28. Andersen, B. L. & Tewfik, H. H. Psychological reactions to radiation therapy: Reconsideration of the adaptive aspects of anxiety. *J. Pers. Soc. Psychol.* **48**, 1024–1032. <https://doi.org/10.1037/0022-3514.48.4.1024> (1985).
29. Parihar, V. K. *et al.* Cosmic radiation exposure and persistent cognitive dysfunction. *Sci. Rep.* **6**, 34774. <https://doi.org/10.1038/srep34774> (2016).
30. Parihar, V. K. *et al.* What happens to your brain on the way to Mars. *Sci. Adv.* **1**(4), e1400256–e1400256. <https://doi.org/10.1126/sciadv.1400256> (2015).
31. Tang, Y., Luo, D., Rong, X., Shi, X. & Peng, Y. Psychological disorders, cognitive dysfunction and quality of life in nasopharyngeal carcinoma patients with radiation-induced brain injury. *PLoS One* **7**(6), e36529. <https://doi.org/10.1371/journal.pone.0036529> (2012).
32. Tofilon, P. J. & Fike, J. R. The radioresponse of the central nervous system: A dynamic process. *Radiat. Res.* **153**(4), 357–370. [https://doi.org/10.1667/0033-7587\(2000\)153\[0357:TROTCN\]2.0.CO;2](https://doi.org/10.1667/0033-7587(2000)153[0357:TROTCN]2.0.CO;2) (2000).
33. Grill, J. *et al.* Long-term intellectual outcome in children with posterior fossa tumors according to radiation doses and volumes. *Int. J. Radiat. Oncol. Biol. Phys.* **45**(1), 137–145. [https://doi.org/10.1016/S0360-3016\(99\)00177-7](https://doi.org/10.1016/S0360-3016(99)00177-7) (1999).
34. Spiegler, B. J., Bouffet, E., Greenberg, M. L., Rutka, J. T. & Mabbott, D. J. Change in neurocognitive functioning after treatment with cranial radiation in childhood. *J. Clin. Oncol.* **22**(4), 706–713. <https://doi.org/10.1200/JCO.2004.05.186> (2004).
35. Williams, N. L. *et al.* Late effects after radiotherapy for childhood low-grade glioma. *Am. J. Clin. Oncol.* **41**(3), 307–312. <https://doi.org/10.1097/COC.0000000000000267> (2018).
36. Zeitlin, C. *et al.* Measurements of energetic particle radiation in transit to Mars on the Mars Science Laboratory. *Science* **340**(6136), 1080–1084. <https://doi.org/10.1126/science.1235989> (2013).
37. Acharya, Munjal M *et al.* New Concerns for Neurocognitive Function during Deep Space Exposures to Chronic, Low Dose-Rate, Neutron Radiation. *eNeuro* **6**(4), ENEURO.0094-19. <https://doi.org/10.1523/ENEURO.0094-19> (2019)
38. Cherry, J. D. *et al.* Galactic cosmic radiation leads to cognitive impairment and increased $\alpha\beta$ plaque accumulation in a mouse model of alzheimer's disease. *PLoS One* **7**(12), e53275. <https://doi.org/10.1371/journal.pone.0053275> (2012).
39. Guo, J. *et al.* The pivot energy of solar energetic particles affecting the martian surface radiation environment. *Astrophys. J. Lett.* **883**(1), L12. <https://doi.org/10.3847/2041-8213/ab3ec2> (2019).
40. Cucinotta, F. A. & Cacao, E. Risks of cognitive detriments after low dose heavy ion and proton exposures. *Int. J. Radiat. Biol.* **95**(7), 985–998. <https://doi.org/10.1080/09553002.2019.1623427> (2019).
41. Khaksarighiri, S., Guo, J., Wimmer-Schweingruber, R., Narici, L., & Lohf, H. Calculation of dose distribution in a realistic brain structure and the indication of space radiation influence on human brains. *Life Sci. Space Res.* **27**, 33–48, <https://doi.org/10.1016/j.lssr.2020.07.003> (2020).
42. Agostinelli, S. *et al.* GEANT4: A Simulation toolkit. *Nucl. Instrum. Meth. A* **506**, 250–303. [https://doi.org/10.1016/S0168-9002\(03\)01368-8](https://doi.org/10.1016/S0168-9002(03)01368-8) (2003).
43. Allison, J. *et al.* Recent developments in Geant4. *Nucl. Instrum. Meth. A* **835**, 186–225. <https://doi.org/10.1016/j.nima.2016.06.125> (2016).
44. Guo, J. *et al.* A generalized approach to model the spectra and radiation dose rate of solar particle events on the surface of mars. *Astron. J.* **155**(1), 49. <https://doi.org/10.3847/1538-3881/aaa085> (2018) [arXiv:1705.06763](https://arxiv.org/abs/1705.06763).
45. Guo, J. *et al.* Implementation and validation of the GEANT4/ATrIS code to model the radiation environment at Mars, *J. Space Weather Space Clim.*, **9**(A2). <https://doi.org/10.1051/swsc/2018051> (2019).
46. Guo, J., Wimmer-Schweingruber, R. F., Grande, M., Lee-Payne, Z. H., & Matthiä, D. Ready functions for calculating the martian radiation environment. *J. Space Weather Space Clim.* **9**(A7). <https://doi.org/10.1051/swsc/2019004> (2019).
47. Zeitlin C. Space Radiation Shielding. In: Young L., Sutton J. (eds) *Encyclopedia of Bioastronautics*. Springer, Cham. https://doi.org/10.1007/978-3-319-10152-1_28-1 (2019).
48. Norman, R. B. *et al.* Early results from the advanced radiation protection thick GCR shielding project. <https://core.ac.uk/download/pdf/84914147.pdf> (2017).
49. Wilson, J. W. *et al.* Shielding from solar particle event exposures in deep space. *Radiat. Meas.* **30**(3), 361–382. [https://doi.org/10.1016/S1350-4487\(99\)00063-3](https://doi.org/10.1016/S1350-4487(99)00063-3) (1999).
50. O'Neill, P. M. Badwar-o'Neill 2010 galactic cosmic ray flux model-revised. *IEEE Transactions on Nuclear Sci.*, **6**, 3148 <https://doi.org/10.1109/TNS.2010.2083688> (2010).
51. Skobel'syn Institute Of Nuclear Physics. Database of solar energetic particles (SEP) fluences measured from august 1997 till 2006, <http://dec1.sinp.msu.ru/~chapai/projects/database/> (2015).
52. Krukowski, K. *et al.* Female mice are protected from space radiation-induced maladaptive responses. *Brain Behav. Immun.* **74**, 106–120. <https://doi.org/10.1016/j.bbi.2018.08.008> (2018).
53. De Boer, H. H., Van der Merwe, A. L. & Soerdjbalie-Maikoe, V. V. Human cranial vault thickness in a contemporary sample of 1097 autopsy cases: Relation to body weight, stature, age, sex and ancestry. *Int. J. Legal Med.* **130**(5), 1371–1377. <https://doi.org/10.1007/s00414-016-1324-5> (2016).
54. Cucinotta, F.A. Radiation risk acceptability and limitations, *Space Radiation Program Element*, NASA Johnson Space Center. <https://three.jsc.nasa.gov/articles/AstronautRadLimitsFC.pdf> (2010).
55. Sokolova, I. V. *et al.* Proton radiation alters intrinsic and synaptic properties of ca1 pyramidal neurons of the mouse hippocampus. *Radiat. Res.* **183**(2), 208–218. <https://doi.org/10.1667/RR13785.1> (2015).
56. Raber, J. *et al.* Effects of proton and combined proton and ^{56}Fe radiation on the hippocampus. *Radiat. Res.* **185**(1), 20–30. <https://doi.org/10.1667/RR14222.1> (2016).

Acknowledgements

J. G. is supported by the Strategic Priority Program of the Chinese Academy of Sciences (Grant No. XDB41000000 and XDA15017300), the National Natural Science Foundation of China (Grant No. 42074222) and the CNSA pre-research Project on Civil Aerospace Technologies (Grant No. D020104). S.K. and R.F.W.S. are supported by

DLR and DLR's Space Administration grant numbers 50QM0501, 50QM1201, and 50QM1701 to the Christian Albrechts University, Kiel. L.N. acknowledges ASI support under agreement ALTEA-BrainRad, 2016-28-H.O. We thank Mikhail I. Dobynde (from University of Science and Technology of China) for sharing the SEP event database.

Author contributions

S.K did the calculations of the radiation propagation in the brain structure. J.G developed the idea of the analysing and correlating the SEP spectral property with the radiation in the brain. All have contributed to the discussions throughout the study and to the writing and reviewing of the manuscript.

Funding

Open Access funding enabled and organized by Projekt DEAL.

Competing interests

The authors declare no competing interests.

Additional information

Correspondence and requests for materials should be addressed to J.G.

Reprints and permissions information is available at www.nature.com/reprints.

Publisher's note Springer Nature remains neutral with regard to jurisdictional claims in published maps and institutional affiliations.



Open Access This article is licensed under a Creative Commons Attribution 4.0 International License, which permits use, sharing, adaptation, distribution and reproduction in any medium or format, as long as you give appropriate credit to the original author(s) and the source, provide a link to the Creative Commons licence, and indicate if changes were made. The images or other third party material in this article are included in the article's Creative Commons licence, unless indicated otherwise in a credit line to the material. If material is not included in the article's Creative Commons licence and your intended use is not permitted by statutory regulation or exceeds the permitted use, you will need to obtain permission directly from the copyright holder. To view a copy of this licence, visit <http://creativecommons.org/licenses/by/4.0/>.

© The Author(s) 2021

Characterizing Radiation Environment on the Martian Surface: Zenith-Angle Dependence of Downward Dose Rate and Directionality of Surface Radiation

4.3 Paper III: Zenith-Angle Dependence of Downward Radiation Dose Rate on the Martian Surface

Placing humans on the surface of Mars presents significant challenges due to the harsh radiation environment prevailing there. **GCRs**, which can penetrate the Martian surface, largely determine space radiation on the surface of Mars. In a study conducted by Wimmer-Schweingruber et al. (2015), it was revealed that the radiation field's directionality is not entirely isotropic within the limited field of view of the **RAD** onboard the **MSL** Curiosity rover. To gain a more comprehensive understanding of the surface radiation's directionality across a wide range of zenith angles (θ), we conducted a three-dimensional Geant4 Monte Carlo simulation. This simulation allowed us to investigate and analyze the dependence of the surface dose rate on θ . By examining the θ -dependence of the surface dose rate, we aimed to enhance our understanding of the directional characteristics of radiation on the Martian surface. Through the Geant4 Monte Carlo simulation, we generated realistic radiation scenarios and accurately estimated the dose rates that reach the **RAD** at various zenith angles. This approach enabled us to capture the complex interplay between the incoming radiation and the Martian surface, taking into account factors such as atmospheric pressure or the atmosphere's column density, the heliospheric modulation which determines the input at the top of the Martian atmosphere, and local and large-scale topography, that may provide shielding. By considering a wide range of zenith angles, we ensured that our analysis covered different orientations of the Martian surface relative to the incident radiation.

The following article, which is reproduced from Khaksarighiri et al. (2023) with permission from the Journal of Geophysical Research: Planets, presents the study that used a Geant4 model to investigate the zenith-angle dependence of the downward radiation field on the surface of Mars and compared it with the measurements obtained with the **RAD** instrument on the **MSL** Curiosity rover. The study focused on two types of energetic particles, namely, protons and helium nuclei, which contribute significantly to the surface dose. Our findings show that there is a linear relationship between the dose rate on the surface of Mars and the solar modulation parameter. The results also suggest that the downward radiation dose on the surface of Mars only depends weakly on the zenith angle θ . The surface dose rate also depends on solar modulation, and weaker modulation results in a higher dose rate for each θ . The study highlights the importance of extra shielding against radiation towards the zenith than towards the horizon, particularly for deep space missions to Mars. These findings have implications for the design of radiation protection measures for astronauts during future missions to Mars.

The zenith-angle dependence of the downward radiation dose rate on the Martian surface: modeling versus MSL/RAD measurement

Khaksarighiri, S., Guo, J., Wimmer-Schweingruber, R. F., Löffler, S., Ehresmann, B., Matthä, D., Donald M.Hassler, Cary Zeitlin, Berger, T. (2023). Journal of Geophysical Research: Planets, e2022JE007644.

My contribution to this paper is 80% of the overall content and research efforts.

JGR Planets

RESEARCH ARTICLE

10.1029/2022JE007644

Key Points:

- We model the downward radiation dose on the surface of Mars and find that it only depends weakly on the zenith angle θ
- The surface dose rate depends on solar modulation, and weaker modulation results in higher dose rate for each θ
- The local topographical features influence the Martian surface radiation

Correspondence to:

S. Khaksarighiri, J. Guo, and R. F. Wimmer-Schweingruber,
khaksari@physik.uni-kiel.de;
jnguo@ustc.edu.cn;
wimmer@physik.uni-kiel.de

Citation:

Khaksarighiri, S., Guo, J., Wimmer-Schweingruber, R. F., Löffler, S., Ehresmann, B., Matthäi, D., et al. (2023). The zenith-angle dependence of the downward radiation dose rate on the Martian surface: Modeling versus MSL/RAD measurement. *Journal of Geophysical Research: Planets*, 128, e2022JE007644. <https://doi.org/10.1029/2022JE007644>









Received 27 OCT 2022

Accepted 6 APR 2023

© 2023. The Authors.

This is an open access article under the terms of the [Creative Commons Attribution License](#), which permits use, distribution and reproduction in any medium, provided the original work is properly cited.

The Zenith-Angle Dependence of the Downward Radiation Dose Rate on the Martian Surface: Modeling Versus MSL/RAD Measurement

Salman Khaksarighiri¹ , Jingnan Guo^{2,3} , Robert F. Wimmer-Schweingruber¹ , Sven Löffler¹, Bent Ehresmann⁴ , Daniel Matthäi⁵ , Donald M. Hassler⁴ , Cary Zeitlin⁶ , and Thomas Berger⁵ 

¹Institute of Experimental and Applied Physics, Christian-Albrechts-University, Kiel, Germany, ²Deep Space Exploration Laboratory/School of Earth and Space Sciences, University of Science and Technology of China, Hefei, PR China, ³CAS Center for Excellence in Comparative Planetology, USTC, Hefei, PR China, ⁴Solar System Science and Exploration Division, Southwest Research Institute, Boulder, CO, USA, ⁵German Aerospace Center (DLR), Institute of Aerospace Medicine, Cologne, Germany, ⁶Leidos Corporation, Houston, TX, USA

Abstract The Radiation Assessment Detector (RAD) on board the Mars Science Laboratory's Curiosity rover has been monitoring the surface radiation environment on Mars for just over 10 years. It has been found by Wimmer-Schweingruber et al. (2015, <https://doi.org/10.1002/2015gl066664>) that within the narrow view cone of RAD, the directionality of the radiation field is close to but not completely isotropic. In order to better understand the directionality of the surface radiation over a wide range of zenith angles (θ), we perform a three-dimensional Geant4 Monte Carlo simulation to derive the θ -dependence of the surface dose rate. The results show that galactic cosmic ray protons, coming in at $\theta \sim 74^\circ$ make the greatest contribution to the surface dose. For helium ions, this angle is at around 46° . This is a consequence of the increasing column depth at larger zenith angles and the complex interplay of the destruction of primary and the creation of secondary particles as the primary cosmic ray interacts with the Martian atmosphere. We also compared the simulated results with the RAD measurements and found a reasonable agreement. Our results are important for future human exploration of Mars, for instance, to estimate the effectiveness of radiation shielding of a given geometry or for optimizing the radiation shielding design of a Martian habitat.

Plain Language Summary Space agencies and private companies are working to place humans on the surface of Mars. Astronauts would be exposed to a different and considerably harsher radiation environment on Mars than humans are on Earth. Space radiation is largely determined by galactic cosmic rays, which have sufficient energy to reach the Martian surface. Thus, a better understanding of the radiation on the surface of Mars is needed. The shielding provided by the atmosphere increases with the zenith angle, and it also causes an increase in the creation of secondary particles. To better understand this, we perform a Geant4 Monte Carlo simulation to derive the dependence of the surface dose rate on the zenith angle θ . The results show that the radiation dose on the surface of Mars depends on the incoming angle of the primary radiation. Moreover, the radiation dose rate is significantly modulated by solar activity, and the Mars surface dose rate differs by about 50% between solar maximum and minimum periods. We validate our simulation by comparing the dose measured by the Mars Science Laboratory Radiation Assessment Detector and find good agreement.

1. Motivation and Introduction

Future expeditions into interplanetary space, and in particular to the Moon and Mars, will expose astronauts to much higher levels of cosmic radiation compared to the current low-Earth orbit (LEO) missions due to the strong shielding against interplanetary radiation provided by the Earth's magnetic field that attenuates the major effects of space radiation exposures for current LEO missions. Deep space is dominated by two major sources of energetic particle radiation: background Galactic Cosmic Rays (GCRs) and sporadic, but highly variable in intensity Solar Energetic Particles (SEPs). Protons and helium ions comprise about 87% and 12% of GCR nuclei with traces of heavier nuclei such as carbon, nitrogen, oxygen, and iron (Simpson, 1983). SEPs are dominated by protons and electrons, which are accelerated during sporadic solar eruptions and released into interplanetary space.

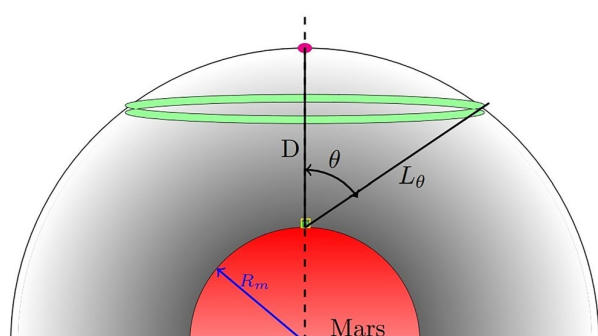


Figure 1. Schematic view of a full-size spherical Mars as a substrate; and is a representation of the real-world system. The red hemisphere represents a hemisphere of Mars. The position of the Radiation Assessment Detector is indicated by a green square with a yellow border. The green ring is an example of ring sources, and the magenta point represents the source with θ equal to 0° . More information can be found in the text.

Exposure to deep space radiation can lead to health risks such as acute and long-term effects for astronauts (Barcellos-Hoff et al., 2015; Cucinotta & Durante, 2006). SEPs can deliver a very high level of radiation over a short time to the human body and may cause acute radiation effects, such as nausea and vomiting or death in the worst case. Long-term exposure to GCRs does not cause immediate health effects but can increase the risk of cancer over a lifetime and also cataracts and central nervous system decrements (Cucinotta et al., 2014; Kennedy, 2014; Khaksarighiri et al., 2021). Thus, a better understanding of the radiation environment for space missions is necessary and fundamental for the safety of astronauts.

When GCRs and SEPs arrive at Mars, they can interact with the Martian atmosphere and lose energy via ionization processes, and they can also create secondary particles via spallation and fragmentation processes. With sufficient energy, they can arrive at the Martian surface and further penetrate the subsurface and produce secondary particles in both the atmosphere and soil. As a result, the radiation environment on the Martian surface is different from that in deep space (Guo, Zeitlin, et al., 2021; Wilson et al., 2004). The Radiation Assessment Detector (RAD, Hassler et al., 2012) on board the Mars Science Laboratory's (MSL) Curiosity rover has been monitoring

the surface radiation environment on Mars for just over 10 years since its landing in 2012 August. The shielding effect of Mars's atmosphere has been shown to be more important than the creation of secondary radiation (Guo et al., 2017; Raffin et al., 2014).

Radiation in deep space is nearly isotropic most of the time, that is, it comes from the full 4π solid angle. On the Martian surface, the planet itself provides excellent shielding against energetic particle radiation that would come from the bottom half of the full solid angle. There is, however, a small portion of the radiation that is directed upward. These secondary, upward-directed “albedo” particles are generated in the soil as by-products of the interaction of the GCR with the soil. Guo, Khaksarighiri, et al. (2021) estimated that the albedo radiation, measured as an absorbed dose by RAD, on flat terrain is about 19% of the total surface dose, that is, most of the radiation detected on the Martian surface is due to downward-directed particles.

While the primary GCRs are nearly isotropic in deep space, their angular distribution is modified as they travel through the Martian atmosphere to reach the surface. Particles coming through the atmosphere from the horizon need to pass through a much larger atmospheric column depth than particles coming from the vertical direction. The atmospheric column depth that a particle must traverse to reach the surface increases with zenith angle θ , which represents the angle from the surface normal as shown in Figure 1.

At $\theta = 0^\circ$, the atmospheric column depth is about $\sim 21 \text{ g/cm}^2$ at Curiosity's location in the Gale Crater. For comparison, at a zenith angle of $\sim 90^\circ$ the corresponding column depth is $\sim 400 \text{ g/cm}^2$.

As Curiosity moves across the surface, its inclination with respect to the surface of an idealized, spherical Mars changes due to local topography. Wimmer-Schweingruber et al. (2015) used these variations to study the radiation shielding effect of the atmosphere and found that the radiation field is close to isotropic with a slight increase of shielding toward larger zenith angles. That study was limited to a maximum rover tilt angle of $\sim 15^\circ$.

In order to better understand the directionality of the surface radiation over a wider range of zenith angles (θ), we perform a three-dimensional Geant4 (GEometry And Tracking, Agostinelli et al., 2003, 2006, 2016) Monte Carlo simulation to derive the θ -dependence of the surface dose rate. Specifically, we model the interaction of the incoming GCRs with the Martian atmosphere and also with the RAD detector to derive the surface radiation field across a large range of zenith angles. We thus investigate the zenith-angle dependence of dose (energy per mass) deposited in RAD.

In this paper, we first explain our model, especially the setup of the Martian environment and the input particle sources in Section 2. The modeled results and their zenith angle-dependence are presented in Section 3, including also the model prediction of RAD measurements. Finally, we validate our model in Section 3.3, using the dose measured by RAD within two telescope view cones to compare with our modeled results.

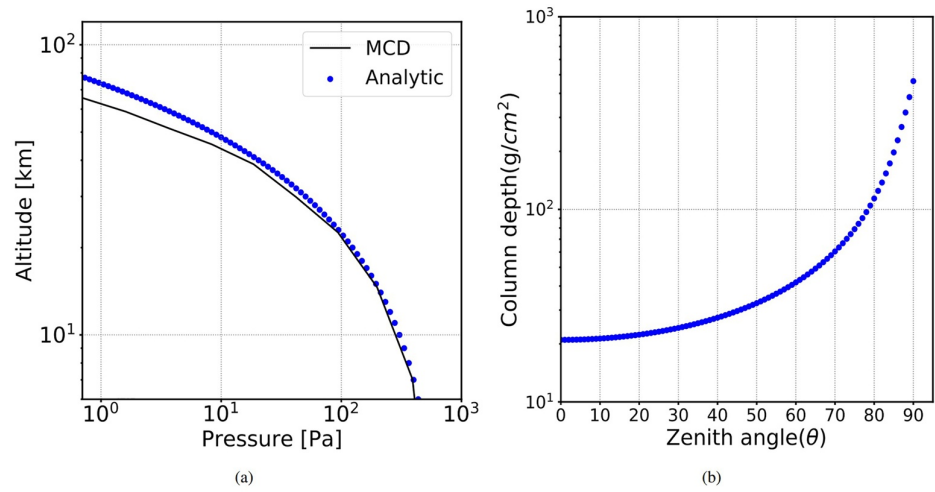


Figure 2. (a): Comparison of the pressure on the surface of Mars versus altitude based on the analytical model and the data obtained from the Mars Climate Database (b): CO₂ column depth for different zenith angles on the surface of Mars.

2. Model Description and Implementation

In order to build our geometry in Geant4, we first need to calculate the atmospheric column depth as a function of the zenith angle on the surface of Mars. Figure 1 has been used for this purpose, which illustrates a full-size spherical Mars as a substrate; and is a representation of the real-world system.

Considering Figure 1 we can derive the following equation:

$$(R_m + D)^2 = R_m^2 + L_\theta^2 + 2R_m L_\theta \cos(\theta). \quad (1)$$

Here R_m is Mars's radius, L_θ is the effective scale height which depends on the zenith angle θ , and D is the distance between RAD and the magenta point. The atmospheric column depth (σ) and its dependency on the zenith angle (θ) for each ring can be derived as follows:

$$L_\theta = -R_m \cos(\theta) + \sqrt{R_m^2 \cos^2(\theta) + D^2 + 2R_m D}. \quad (2)$$

We approximate the atmospheric density with the well-known barometric expression and find

$$\sigma = \int \rho_0 e^{-h/H} dh \quad (3)$$

where H is the scale height, ρ_0 is the atmospheric density on the surface of Mars, h represents the atmospheric height, and σ is the integrated atmospheric column depth in the vertical direction $\theta = 0^\circ$, which is set to 21 g/cm² in this model and calculate the D , which is the distance between the RAD and magenta point. As the pathlength through each thin spherical shell of roughly constant density along the two paths at θ and 0° is in the same ratio as L_θ and D , we can modify Equation 3 as follows:

$$\sigma = \rho_0 \times L_\theta. \quad (4)$$

where σ represents the CO₂ column depth (g/cm²) in different zenith angles.

With this model, we calculate the CO₂ column depth in different zenith angles on the surface of Mars shown in Figure 2b and used these data to build the Mars surface geometry in our model as different hemispheres in Figure 3, each hemisphere belong to a specific column depth correspond to the zenith angle.

Mars Climate Database (MCD, Millour et al., 2015, <http://www-mars.lmd.jussieu.fr/>) is a database containing Martian meteorological variables developed using various Martian atmospheric models and validated against available observational data (Millour et al., 2015). We compared the pressure at a certain height versus

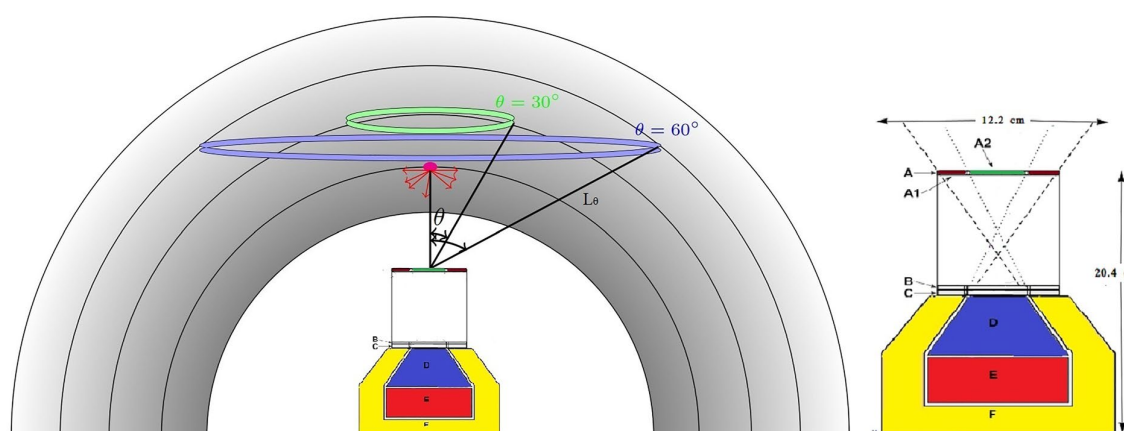


Figure 3. Schematic views of the zenith-angle (θ) dependence of the Mars atmospheric setup (left) and the Radiation Assessment Detector sensor head (right, adapted from Hassler et al. (2012)). The green and blue rings are example ring sources with θ being 30° and 60° , respectively, and the magenta point represents the source with θ equal to 0° . More information can be found in the text.

atmospheric altitude (between 0 and 95 km) based on the above analytical model with the data obtained from the MCD, as shown in Figure 2a. The vertical atmospheric distribution based on our model agrees well with MCD with less than 1% difference for altitudes lower than 35 km on the Martian surface, but the difference reaches 13% at higher altitudes because of the complexity of the MCD model compared to our simple model of the Martian surface. The right panel of Figure 2 shows the atmospheric column depth σ as a function of zenith angle θ as obtained from our model (Equation 4).

We include the RAD detector in our model, as shown in Figure 3 to allow the comparison of simulations with measurements as presented in Section 3.3. The Martian atmosphere is modeled as pure CO_2 because it makes up about 95% of the Martian atmosphere. The vertical ($\theta = 0^\circ$) atmospheric column depth is about 21 g/cm^2 when the surface pressure is about 800 Pa, which is the average value measured by MSL at Gale Crater (REMS, Gómez-Elvira et al., 2012), and column depth increases with increasing θ toward the horizon as shown in the right-hand panel of Figure 2.

2.1. Geant4 Toolkit

We used version 10.4 of the Geant4 (GEometry And Tracking, Agostinelli et al., 2003, 2006, 2016) three-dimensional Monte Carlo particle transport tool with the QGSP BERT physics list. The QGSP BERT physics list applies the quark-gluon string model for high energy particles ($\geq 20 \text{ GeV}$) and the Bertini cascade model in the middle and low energy range. In the model, the excited nuclei that are generated by high energy interactions are passed to the Precompound model which is used to describe the de-excitation process. In terms of modeling the Martian radiation environment, it has been found that different physics lists can affect the generation of secondary particles, especially those produced via spallation processes (Guo et al., 2019). However, the surface absorbed dose normally agrees within $\sim 5\%$ for different physics lists (Matthiä et al., 2016).

2.2. Model Description

As discussed above, the interaction of GCRs with a planetary atmosphere leads to a change in the isotropic nature of the radiation field, which results in a higher directional flux of primary particles from the zenith than from the horizon. This can be understood due to the interaction of primary particles with the atmosphere, which has a much smaller column depth in the zenith direction than toward the horizon. Our model is set up in order to quantify the above effect and to determine the surface dose rate arriving from different zenith angles.

The RAD sensor head shown in the right panel of Figure 3 is placed on the Martian surface in our model and consists of three silicon detectors (A, B, and C), a cesium iodide scintillator D, and a plastic scintillator E (Hassler et al., 2012). Absorbed dose values are simultaneously recorded and also modeled in detectors B and E with the

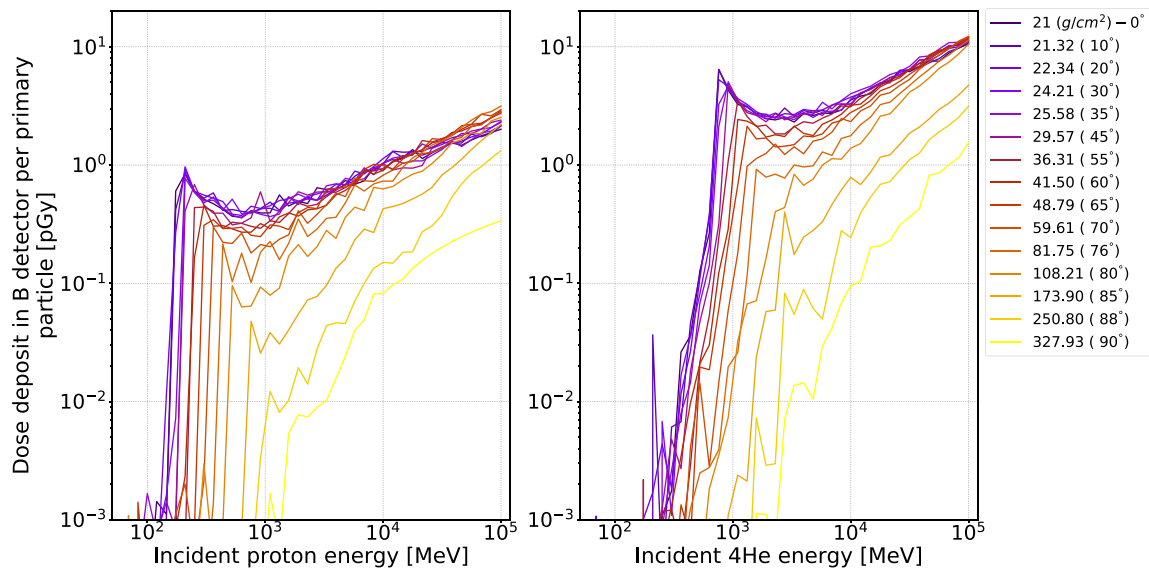


Figure 4. Simulated dose deposit in the Radiation Assessment Detector B detector as a function of the primary particle energy at various zenith angles with different column depths (represented by different line colors) for protons (left) and ^4He ions (right).

masses of 1.3×10^{-4} kg and 34.9×10^{-3} kg, respectively. Both scintillators are surrounded by a plastic antineutrino scintillator (F). The modeled geometry corresponds exactly to the RAD geometry, which is a small packed instrument with a total mass of 1.5 kg. As simulating dose to RAD embedded in a planet-scale illuminated volume of atmosphere would take forever to build up statistics, we have compressed the atmospheric representation starting from 25 cm on top of the RAD and more layers with different densities of CO_2 will be added for larger zenith angles and reach to 125 cm for the last layer in 400 g/cm^2 of CO_2 . σ calculated in Equation 4 represents the column depth of the atmosphere, which increases with the zenith angle from vertical to horizontal directions, as shown in Figure 2b. The gray scale represents the Mars atmosphere which is set to be 100% CO_2 in this model. The green and blue rings are example ring sources with θ being 30° and 60° placed in various layers with corresponding column depth of atmosphere, respectively. The magenta point represents the source with θ equal to 0° corresponding to 21 g/cm^2 of CO_2 , placed on top of the first layer of CO_2 with 30 cm of radius. The RAD itself has been placed in a high vacuum hemisphere, which means all the primary and secondary particles will follow their direction, after passing through the CO_2 layers.

High-energy particles at the top of Mars' atmosphere do not necessarily follow the black line labeled L_θ in Figure 3, but are scattered, they lose energy, and—if energetic enough—may create secondary particles or even a shower of secondary particles. To account for this, we placed our primary particle sources along spherical segments of constant zenith angle, as indicated by the green and blue rings at $30^\circ \pm 1^\circ$ and $60^\circ \pm 1^\circ$ in Figure 3. From the inner surface of each ring, particles were launched with an inward cosine directional distribution with a power-law index of -1 to result in an isotropic homogeneous field inside the hemisphere as shown with red arrows for the magenta source. The modeled energies of primary protons and ^4He ions were distributed from 1 MeV to 100 GeV in 62 logarithmically spaced bins to simplify the rebinning and convolutions with different primary GCR spectra, as explained later. For each such spherical segment, a total of 6.2×10^7 particles of the two-particle types were simulated, that is, 10^6 particles per energy bin.

3. Simulation Results and Comparison With Measurements

The results of the total dose (absorbed by the RAD B 300- μm silicon detector) per particle versus the incoming energy of particles from 1 MeV to 100 GeV for different zenith angles (or column depths) are shown in Figure 4 with left and right panels for protons and ^4He ions, respectively. The simulations are performed for detector B without regard to coincidence or anticoincidence, and then the dose rates are restricted to the A1B and A2B acceptance cones for comparison with observations that will be explained in more detail in Section 3.3.

As shown in Figure 4, there is a sharp increase in the surface dose contribution from protons at 164 MeV/nuc for 0° zenith angle. This “cutoff” energy is equivalent to the energy required for particles to penetrate 21 g/cm² of carbon dioxide, which is 164 MeV for protons and 630 MeV for ⁴He ions and defined as 10% of the peak dose at 0° zenith angle. The small contributions to the surface dose below this primary energy are mainly from proton-generated secondaries such as electrons, gammas, and neutrons. Figure 4 also shows that this cutoff energy depends on the zenith angle (which is color-coded in this figure), and that larger zenith angles have a larger cutoff energy because of the larger column depth that particles need to penetrate. As expected, the dose from the lowest energy particles is seen for the thinnest column depth whereas the thickest column depth results in a lower energy deposit.

The simulation results also show that at energies lower than ~1 GeV/nuc, the dose decreases as the primary energy increases as is to be expected from the Bethe-Bloch approximation (Bethe, 1930; Bloch, 1933). But, at energies above the relativistic minimum of around 1 GeV/nucleon, the electromagnetic ionization dose per unit pathlength departs from the Bethe-Bloch approximation and starts to increase with energy; this, together with the generation of secondary particles, particle fragmentation, and spallation interactions in the atmosphere lead to a rise in dose per primary particle toward high energies.

Note that the total dose in our model comprises all primary particles and secondary particles generated by primaries interacting with the atmosphere which are detected by the RAD within a small zenith angle range (from $\theta - 1^\circ$ to $\theta + 1^\circ$) of the primaries.

This assumption is more reliable when the atmosphere is thin, as in the case of Mars, and a small number of secondaries are generated.

3.1. Procedure of the Model Application

Figure 4 shows the dose deposited in the RAD B detector by an individual primary particle versus its primary energy. In this section, we show how to weight this result with various GCR input spectra to compute the dose rate measured by the RAD B detector. Figure 5 gives a visual summary of the procedure and shows the results for the example of primary GCR protons. The procedure for ⁴He ions (right-hand panel of Figure 4) is the same, but not shown here. The proton dose distributions for different zenith angles in the B detector, that is, Figure 4a shows the dose deposit in the B detector per primary particles and is multiplied by the area and solid angle of primary rings in each zenith angle and gives us the dose deposit per primary fluence [$\mu\text{Gy}/[\text{particles}/\text{cm}^2 \text{ sr}]$] shown in Figure 5a.

Various input spectra of the GCR proton flux in deep space are shown in Figure 5b. These primary GCR spectra are predicted by the Badhwar O'Neill 2014 model (BON, O'Neill et al., 2015) for different solar modulation potentials as indicated in the legend.

We then multiplied a dose-deposit function of a certain θ value in Figure 5a with a GCR input spectrum from Figure 5b by first multiplying the functions in Figure 5a by the widths of the energy bins used in the simulation to have units of [$\mu\text{Gy}/[\text{particles}/\text{cm}^2 \text{ sr MeV}]$] and then multiplying the values of this normalized function with the differential flux in each corresponding energy-bin. Taking the GCR spectrum with Φ of 400 MV as an example, we obtain the dose rate as a function of energy as shown in panel (c) for different inclination angles, θ . For each θ , the total dose summed over all energy bins would be the expected radiation in RAD B from that zenith angle. Note that the total dose is induced by primary GCR protons and also the secondaries generated by primary protons in the atmosphere. The same procedure is used to derive GCR ⁴He induced dose for each θ angle and also for different solar modulation conditions.

Mathematically, the procedure described above can be summarized as given in Equation 5:

$$\dot{D} = \left\{ \frac{D}{f} \right\} \times F, \quad (5)$$

where D (μGy) is the dose-deposit function of a certain θ value from the Geant4 simulation, f is the fluence of the source used in the simulation given as the number of particles per $\text{cm}^2 \text{ sr MeV}$, and F represents the differential flux of GCRs given as the number of particles per $\text{cm}^2 \text{ sr MeV}$ and sec, which finally gives us \dot{D} , that is the dose rate per energy bin in the B detector of RAD for the surface of Mars in each zenith angle.

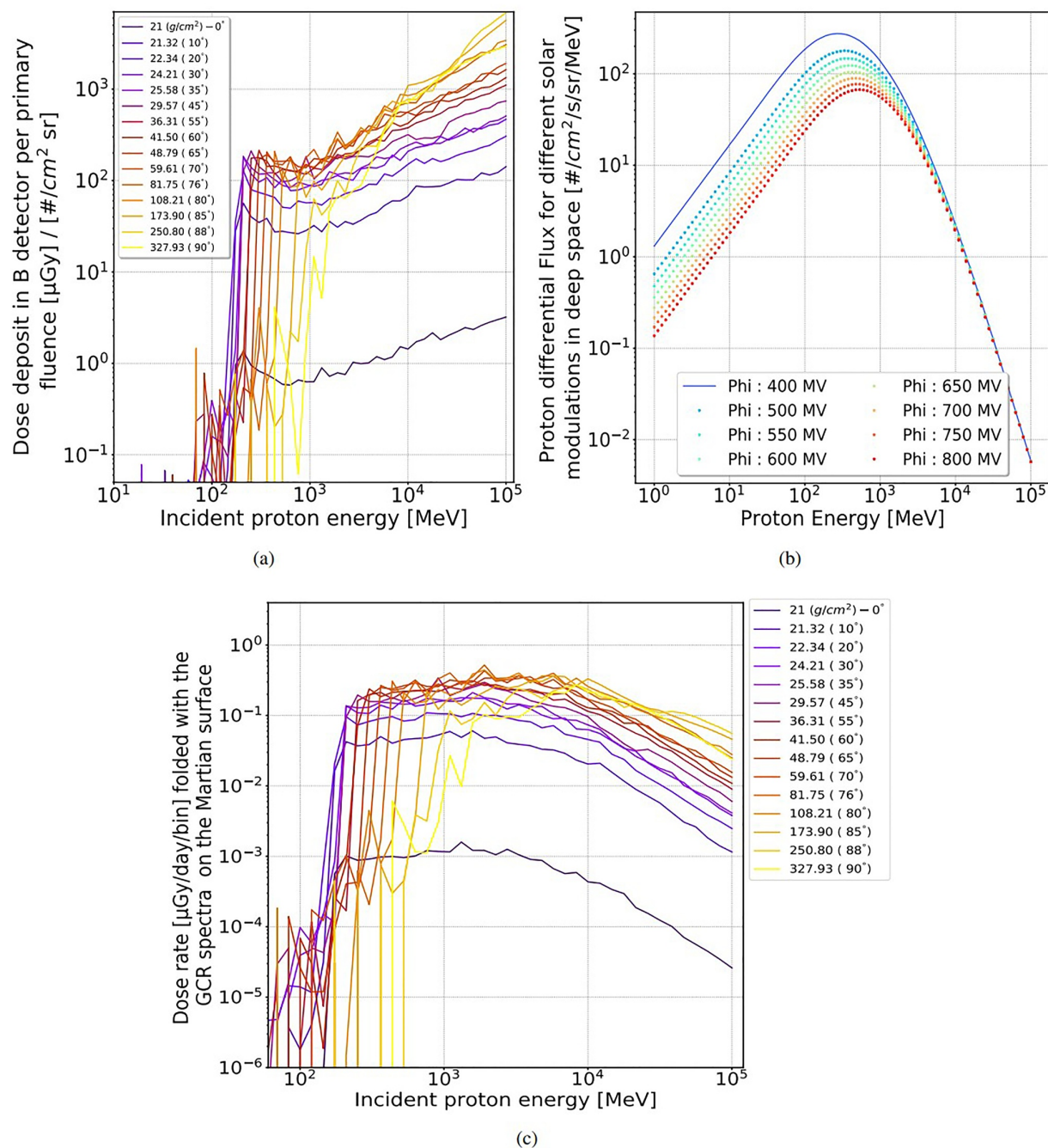


Figure 5. Multiplying the precalculated dose functions in Figure 4 with input galactic cosmic ray (GCR) spectra to calculate the Martian surface dose rate as measured in the Radiation Assessment Detector (RAD) B detector. (a): Proton dose functions in the RAD B detector for different zenith angles (normalized to the [$\text{particles}/\text{cm}^2 \text{ sr}$]). (b): Energy- and time-differential flux of GCR protons for different solar modulation potentials Φ (MV). (c): Multiplication results of the dose-response functions of the panel (a) with the 400 MV primary GCR spectrum in panel (b) in each corresponding energy bin. More details can be found in Section 3.1.

3.2. Modeled Zenith-Angle Dependence of Dose in RAD-B on Mars

After integrating the dose rate in Figure 5c over energy, we obtain the expected RAD-B dose rate from each θ direction. Results for different solar modulation potentials are easily derived with the same procedure but using a different input spectrum from panel b in Figure 5. Figure 6 shows the thus predicted dose rate in the RAD-B

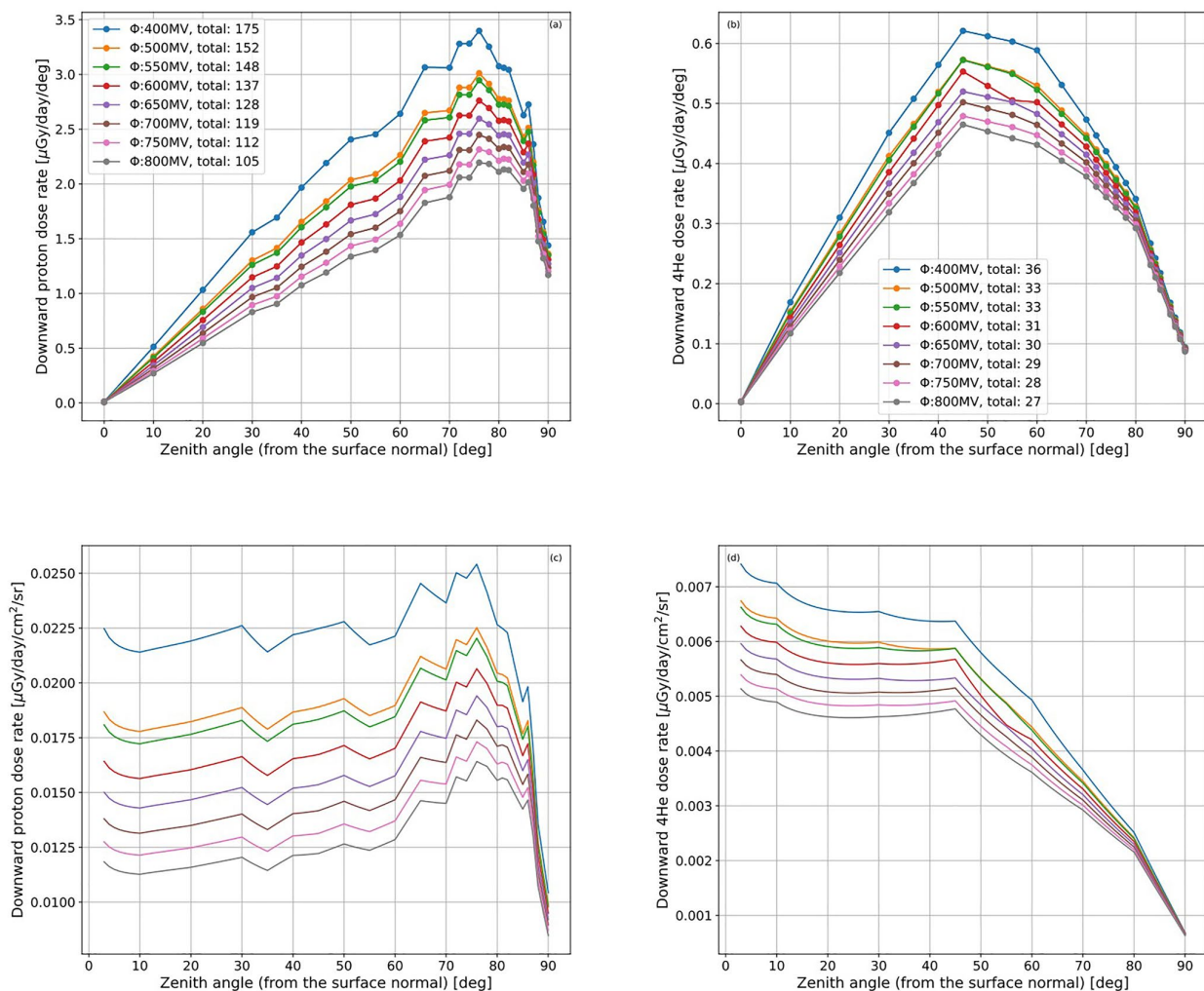


Figure 6. Dependence of modeled dose rate in the Radiation Assessment Detector B detector on zenith angle (θ) for (a)/(c) primary galactic cosmic ray (GCR) protons and (b)/(d) ^4He ions. Different primary GCR spectra are considered under different solar modulation potentials Φ shown in different colors. (a, b) show the dose rate per degree of θ ; (c, d) show the dose rate scaled to per solid angle. Total dose rate [$\mu\text{Gy/day}$] integrated over θ is also given for each case in the legend in (a, b).

detector versus zenith angle θ for different GCR spectra under different solar modulations. The results of dose rate per θ angle from GCR protons and ^4He ions are shown in panels (a) and (b), respectively.

Figures 6a and 6b show that the surface downward radiation dose of particles depends on the zenith angle, θ . For instance, protons coming in at an angle of about 75° contribute more to the RAD-B dose distribution than protons coming in at other angles. For helium ions, this angle is smaller, about 45° . As described by Guo, Khaksarighiri, et al. (2021), two factors play a role here: (a) the atmospheric column depth increases from about 21 g/cm^2 at $\theta = 0^\circ$ to more than 400 g/cm^2 at the horizon; a thicker traverse path would result in primaries losing more energy and becoming more ionizing or more easily stopped before reaching the surface; moreover, more secondaries are generated along a thicker path and can contribute to the total dose; (b) the area of the source particles incident at each degree of zenith angle is different (distributed as rings on the spherical shell), and it increases with θ . These two concurrent reasons result in the directionality of the dose rate on the surface of Mars as shown in (a) and (b). Scaling the dose by the geometric factor of the ring source using Equation 6, removes the influence of the second factor and one obtains the dose rate in units of [$\mu\text{Gy/day/cm}^2/\text{sr}$] as a function of θ as shown in Figures 6c and 6d for protons and helium ions, respectively.

$$\dot{D}(\mu\text{Gy/day/cm}^2/\text{sr}) = \left\{ \frac{\dot{D}}{\sin(\theta) \times 2\pi \times r^2} \right\}, \quad (6)$$

This normalization accounts for the variation in the area exposed to the radiation and enables comparison of the dose at different points on the surface of the hemisphere. The proton functions in (c) show an almost isotropic profile before gradually increasing to the major peak at $\theta \sim 75^\circ$. This peak arises from the combination of primary protons slowing down and the efficient generation of secondary particles. On the other hand, the induced dose deposit from helium ions decreases monotonically with θ (or the traverse depths) since they have a smaller mean free path and are more likely to fragment in the atmosphere. But at θ between $\sim 10^\circ$ and $\sim 45^\circ$, Helium functions also show an approximately isotropic distribution.

Figure 6 also clearly shows that the surface dose rate depends on solar modulation with smaller modulation potential resulting in a larger dose rate for each θ . With the modulation parameter varying between 800 and 400 MV, the total dose rate in the B detector of RAD varies between 106 and 175 $\mu\text{Gy/day}$ for protons, which is about 3.9–4.8 times larger than that induced by helium ions (27–36 $\mu\text{Gy/day}$). The summed proton and helium dose with Φ of 400 MV (solar minimum) is 211 $\mu\text{Gy/day}$ in silicon or 281 $\mu\text{Gy/day}$ in water. During the deep solar minimum in 2019, the dose rate measured in RAD's silicon detector B is about 230 $\mu\text{Gy/day}$ and about 310 $\mu\text{Gy/day}$ in its tissue-equivalent detector E (Ehresmann et al., 2022; Guo, Zeitlin, et al., 2021). Our model estimation is about 10% lower than the RAD measurements. Considering that the current model does not include ions heavier than helium ions and also does not include albedo particles (both will be explained in more details later in Section 3.3), the model values reported here are in reasonable agreement with RAD measurements.

3.3. Model Validation: Predictions of the Acceptance Cone Dose Compared With RAD Measurements

The telescope geometry for charged-particle detection in RAD is defined using the A and B detectors as shown in Figure 3. Charged particles entering RAD from the top are measured in a view-cone with an opening half-angle of about 32° . Two view cones are defined by a coincidence of hits in the A and B detectors, which both are 300 μm thick (Hassler et al., 2012). The first cone uses the inner segment, that is, A2 detector, which spans a half angle of 18° , and the other one uses the outer segment, A1 detector, so that the larger cone has a half angle of 32° . As the angular dependence calculated from our model is for each zenith angle shaped as a ring, but the RAD A and B detectors are hexagonal, we assumed that the hexagonal shape can be well approximated by a circular shape and the opening angles reported here are averaged angles, which are $<18^\circ$ half angle and 18° – 32° half angle for the A2B and A1B, respectively.

Linear Energy Transfer (LET, dE/dx) is measured in RAD B for an incoming charged particle that satisfies either the A1B coincidence or the A2B coincidence. LET is the amount of ionizing energy that an ionizing particle transfers to the material traversed per unit distance. The unit usually used for this quantity is $(\text{keV}/\mu\text{m})$. LET is an average quantity because, at the microscopic level, the energy per unit length of the track varies over a wide range. The LET of charged particles is a function of particle velocity, β , or kinetic energy, and its charge, Z , and is approximately proportional to Z^2/β^2 (Bethe, 1930; Bloch, 1933; Grimes et al., 2017). This measured quantity is referred to hereinafter as the “LET dose,” since we use that term below. RAD records the energy deposited in B within the LET view cone for every particle without determining Z and β of each particle. As a result, the energy distribution contributed by all particles entering the cone and penetrating through B is recorded as an onboard histogram and sent back to Earth (Hassler et al., 2012). This histogram of energy deposits can be used to derive the LET or dE/dx histogram using the mean path length, dx , of particles inside the A1B or A2B cone.

We sum over all the onboard dE histograms to derive the total absorbed energy in silicon detector B from particles coming through the acceptance cone.

RAD is mounted in the Curiosity rover with its central axis perpendicular to the rover deck, and its fields of view are centered vertically when the rover is on flat ground, that is, the center of the acceptance cone would correspond to $\theta = 0^\circ$ when the rover is horizontal. However, along the traverse of Curiosity, the rover body was generally not exactly horizontal, as it would be on level ground. Guo, Zeitlin, et al. (2021, Figure 16) shows the zenith tilt angle of the rover body through the first 2800 sols after MSL landed on Mars. The rover is tilted at angles up to about 25° from the zenith, with an average value of 7.3° . If we expect the downward radiation to be nonisotropic within the tilt angles experienced by Curiosity, we would observe a change of the LET-dose as the rover changes its inclination, for example, when ascending a slope.

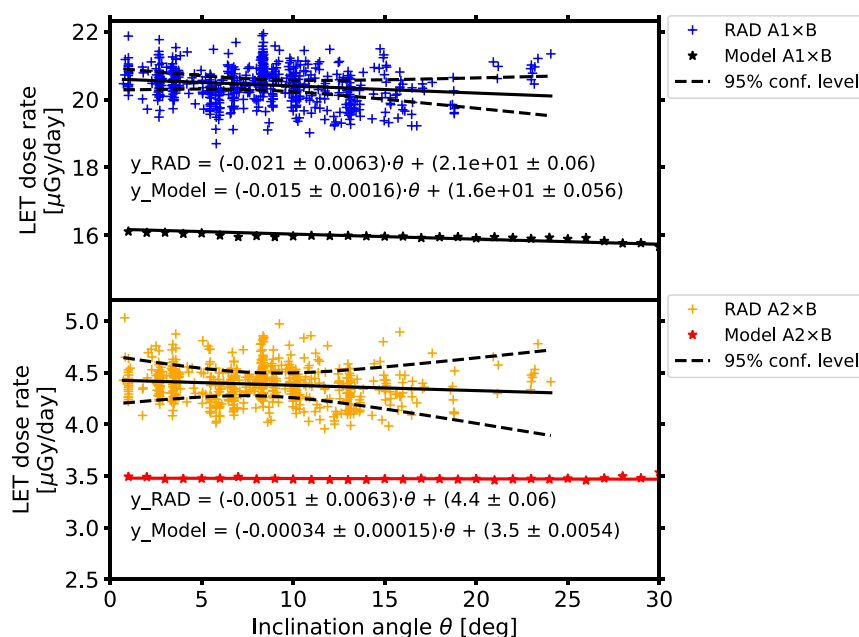


Figure 7. LET dose rate within the inner view cones (A2B) and outer cone (A1B) of Radiation Assessment Detector (RAD) derived from the measurements and model predictions versus inclination of RAD.

In the following, we will compare the dose rates integrated from the LET spectra with the model predictions presented in Section 3.2. As our model contains the θ -dependent dose, it is straightforward to derive the total dose integrated within the acceptance cone given the viewing angle of the cone and the inclination of the rover (the inclination angle equals the zenith angle of the central axis of the cone). Because of the hexagonal shape of the individual RAD detector segments, this calculation cannot be performed analytically but is best calculated numerically. To do so, we first calculate the function for the proportion of the source ring area inside the RAD's field of view cones (half opening angles of 18° (A2B) and 32° (A1B)) and then multiplied these functions with our dose functions shown in Figures 6a and 6b.

Next, we investigate whether the observed or modeled LET dose depends on the rover inclination angle. To do so, we need to minimize the influence of other factors on the Martian surface radiation (Guo, Zeitlin, et al., 2021). The most pronounced one is the solar modulation which drives the long-term variations of the GCR radiation on Mars. Here, we select the data with monthly Φ between 420 and 430 MV as derived by the Oulu Neutron Monitor (<https://cosmicrays.oulu.fi>) to minimize the impact of solar modulation. Note that modulation factors could be different between Earth and Mars (Guo et al., 2015). However, as a statistical study integrated through a long time period, we do not expect this difference to significantly impact our results because the modulation is equal *on average*—except for a very weak radial dependence (Saganti, 2005).

Figure 7 shows LET-derived dose rates for the view cones spanned by RAD's A1-B and A2-B detectors. The acceptance cone dose from the RAD measurement and the derived data from the model in different view cones, which were selected under a specific modulation for the inclination angle covered by RAD as shown in this figure. As one can see, the data are consistent with no slope at the 95% confidence level. The measurements cover inclination angles up to $\sim 24^\circ$ while the model prediction extends to larger values. It shows that the LET dose does not depend on the inclination angle within the range of 60° . This is related to the fact that both proton and helium doses are not far from isotropic for θ below $\sim 50^\circ$ and also that the acceptance cone is perhaps too large to detect the change of the fields. This result is consistent with that obtained by Wimmer-Schweingruber et al. (2015) over a narrower range of rover tilt angles. The variations in Figure 7 in RAD data are due to changes in pressure, the range in solar modulation that is included in the RAD data, and other small perturbations, which affect the measurements (Guo, Zeitlin, et al., 2021).

However, there is a difference of about 28% between the RAD measurement and our model for both A1B and A2B cones. There are two reasons for this difference. First, we only considered protons and ^4He ions as primary

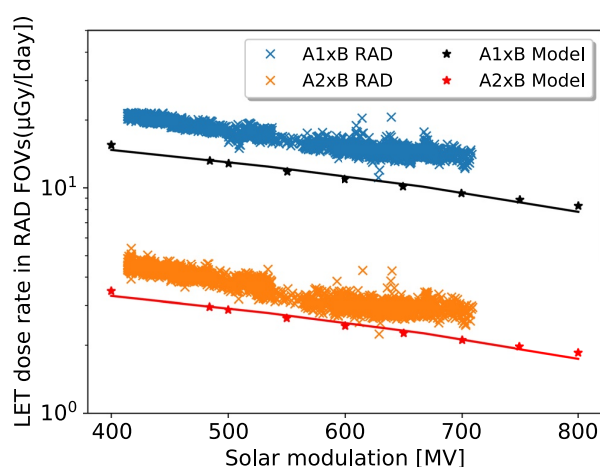


Figure 8. LET dose rate within the two view cones of Radiation Assessment Detector derived from the measurement and modeling data versus the solar modulation parameter Φ . The difference between the modeled results and the measurement is expected, as explained in the main text.

GCRs in our model, but other species of GCR ions with high (H) atomic number (Z) and energy (E) (HZE ions) also contribute to the dose deposit in RAD data. Primary GCRs heavier than protons and helium ions contribute around 10% to the total absorbed dose on the surface of Mars as suggested by results of simulations including both light and heavy ions (Zhang et al., 2022, Figure 7). But the 28% difference reported here is significantly larger than the expected 10% contribution by HZE particles. Moreover, it is also higher than the 10% difference when considering the modeled and measured dose integrated over all zenith angles as discussed in the previous section. The most likely explanation is that the contribution from HZEs is higher since the average path length through the Martian atmosphere is shorter, resulting in less fragmentation of heavy ions before reaching RAD than within the acceptance cone as compared to directions outside the cone.

Second, secondary particles created in the Martian soil (so-called albedo particles which move upward, away from Mars) also in principle contribute to the measured LET-cone dose rate. Guo, Khaksarighiri, et al. (2021) used the absorbed dose in the plastic detector “E” and estimated that the albedo radiation, measured as an absorbed dose by RAD, on flat terrain is about 19% of the total surface dose. Although these albedo particles need energy higher than about 110 MeV/nuc to reach the B detector, and the low-energy albedo particles traveling upward from the surface are likely to deposit energy in E

and stop in the detector stack before reaching B. But, they can contribute slightly to the dose in the B detector (Appel et al., 2018). Considering both the HZE and albedo contributions to the LET dose, the 28% difference between our model and the RAD measurement is rather reasonable.

Finally, we consider the influence of solar modulation on the Martian surface radiation. This has been quantified as the most important factor that affects the long-term dose rate recorded by MSL/RAD (Guo, Zeitlin, et al., 2021). As shown in Figure 8, both the RAD-measured LET dose and modeled LET-cone dose are anticorrelated with the solar modulation potential Φ as also shown in previous studies of the RAD GCR radiation dose (Guo, Zeitlin, et al., 2021; Zeitlin et al., 2019). The ~28% difference between the modeled results and measurements has the same origin as that in Figure 7, as discussed before.

4. Summary and Conclusion

We used a Geant4 model to investigate the zenith-angle dependence of the downward radiation field on the surface of Mars and have compared this with measurements obtained with the RAD instrument on the MSL Curiosity rover. We investigated the two largest contributions to the surface dose: energetic protons and helium nuclei. The latter can fragment as they interact with the Martian atmosphere. At sufficiently high energies, both types of particles can lead to cascades of secondary particles, at lower energies, their main interaction is by ionization. The model takes into account the increase in column depth with increasing zenith angle. The calculations were performed for a model spectrum with a power-law index of -1 and stored as Mars atmosphere “response functions.” These were subsequently folded with the Badhwar-O’Neill (O’Neill et al., 2015) GCR model spectra for a representative range of solar modulation potentials.

The model results suggest that the radiation dose is nonisotropic on the surface of Mars, especially at large zenith angles $>60^\circ$. We cannot exclude an isotropic behavior at the 95% confidence level within the $\sim 25^\circ$ range of inclination angles experienced by Curiosity in the course of its mission on Mars. This is consistent with and extends a previous study by Wimmer-Schweingruber et al. (2015), which, however, did not cover a wide range of inclination angles.

We found that the RAD measurements show an average dose rate that is about 28% higher than our model results. However, when considering the full sky view, that is, integrating over all zenith angles, this difference is only about 10% as explained in Section 3.2. Moreover, previous model results show that HZE ions contribute about 10% to the total dose on the surface of Mars (Röstel et al., 2020; Zhang et al., 2022) when considering particles arriving from the full sky view. We expect that this discrepancy between 28% and 10% is due to the fragmentation

of HZE particles at large zenith angles because such particles need to traverse a significantly larger column depth. Because the Geant4 calculations for such particles are extremely time consuming, we have not yet been able to perform them and will report them in a forthcoming publication.

As is well-known, HZE ions may contribute significantly to cell damage because the energy deposited in an individual cell is proportional to the square of the particle's charge. For deep space missions to Mars, GCR HZE ions induced radiation has been a major concern (Cucinotta & Durante, 2006). Our study suggests that the HZE contribution could be higher at smaller zenith angles for explorers on the surface of Mars. This indicates that extra shielding against radiation is particularly important toward the zenith than toward the horizon.

Data Availability Statement

The data used in this study are archived in the NASA Planetary Data System's Planetary Plasma Interactions Node at the University of California, Los Angeles. The archival volume includes the full binary raw data files, detailed descriptions of the structures, and higher level data products in human-readable form. The binary RAD EDR data are archived under (Peterson et al., 2013), while the human-readable RAD RDR data are archived under (Rafkin et al., 2013). The MSL/REMS data archived in the NASA planetary data systems' planetary plasma interactions node (Gomez Elvira, 2013). Data plotted in the figures are available via (Khaksarighiri, 2022). The data are available in txt format and contain the columns with the x - and y -values for the data points plotted in the figures. More information about the structure of the files is contained within the files themselves.

Acknowledgments

RAD is supported by NASA SMD/Heliophysics and HEOMD/AES under Jet Propulsion Laboratory (JPL) subcontract 1273039 to Southwest Research Institute and in Germany by the German Aerospace Center (DLR) and DLR's Space Administration Grants 50QM0501, 50QM1201, and 50QM1701 to the Christian Albrechts-Universität zu Kiel. Work at the NASA Johnson Space Center was performed under the Human Health and Performance Contract, NNJ15HK11B. J.G. is supported by the Strategic Priority Program of the Chinese Academy of Sciences (Grant XDB41000000), the National Natural Science Foundation of China (Grant 42074222) and the CNSA preresearch Project on Civil Aerospace Technologies (Grant D020104). Open Access funding enabled and organized by Projekt DEAL.

References

- Agostinelli, S., Allison, J., Amako, K., Apostolakis, J., Araujo, H., Arce, P., et al. (2003). GEANT4: A simulation toolkit. *Nuclear Instruments & Methods*, *A506*(3), 250–303. [https://doi.org/10.1016/S0168-9002\(03\)01368-8](https://doi.org/10.1016/S0168-9002(03)01368-8)
- Allison, J., Amako, K., Apostolakis, J., Araujo, H., Arce Dubois, P., Asai, M., et al. (2006). GEANT4 developments and applications. *IEEE Transactions on Nuclear Science*, *53*(1), 270–278. <https://doi.org/10.1109/TNS.2006.869826>
- Allison, J., Amako, K., Apostolakis, J., Arce, P., Asai, M., Aso, T., et al. (2016). Recent developments in GEANT4. *Nuclear Instruments & Methods A*, *835*, 186–225. <https://doi.org/10.1016/j.nima.2016.06.125>
- Appel, J., Köehler, J., Guo, J., Ehresmann, B., Zeitlin, C., Matthäi, D., et al. (2018). Detecting upward directed charged particle fluxes in the Mars Science Laboratory radiation assessment detector. *Earth and Space Science*, *5*(1), 2–18. <https://doi.org/10.1002/2016EA000240>
- Barcellos-Hoff, M. H., Blakely, E. A., Burma, S. E., Fornace, A. J., Gerson, S., Hlatky, L., et al. (2015). Concepts and challenges in cancer risk prediction for the space radiation environment. *Life Sciences and Space Research*, *6*, 92–103. <https://doi.org/10.1016/j.lssr.2015.07.006>
- Bethe, H. (1930). Zur Theorie des Durchgangs schneller Korpuskularstrahlen durch Materie. *Annalen der Physik*, *397*(3), 325–400. <https://doi.org/10.1002/andp.19303970303>
- Bloch, F. (1933). Bremsvermögen von Atomen mit mehreren Elektronen. *Zeitschrift für Physik*, *81*(5–6), 363–376. <https://doi.org/10.1007/BF01344553>
- Cucinotta, F. A., Alp, M., Sulzman, F. M., & Wang, M. (2014). Space radiation risks to the central nervous system. *Life Sciences and Space Research*, *2*, 54–69. <https://doi.org/10.1016/j.lssr.2014.06.003>
- Cucinotta, F. A., & Durante, M. (2006). Cancer risk from exposure to galactic cosmic rays: Implications for space exploration by human beings. *The Lancet Oncology*, *7*(431–436), 682–688. [https://doi.org/10.1016/S1470-2045\(06\)70695-7](https://doi.org/10.1016/S1470-2045(06)70695-7)
- Ehresmann, B., Zeitlin, C., Hassler, D., Guo, J., Wimmer-Schweingruber, R., Berger, T., et al. (2022). The Martian surface radiation environment at solar minimum measured with MSL/RAD. *Icarus*, *393*, 115035. <https://doi.org/10.1016/j.icarus.2022.115035>
- Gomez Elvira, J. (2013). MSL rover environmental monitoring station RDR data V1.0, MSL-M-REMS-4-ENVEDR-V1.0. *NASA Planetary Data System*. <https://doi.org/10.17189/1523028>
- Gómez-Elvira, J., Armiens, C., Castañer, L., Domínguez, M., Genzer, M., Gómez, F., et al. (2012). REMS: The environmental sensor suite for the Mars Science Laboratory rover. *Space Science Reviews*, *170*(1–4), 583–640. <https://doi.org/10.1007/s11214-012-9921-1>
- Grimes, D. R., Warren, D. R., & Partridge, M. (2017). An approximate analytical solution of the bethe equation for charged particles in the radiotherapeutic energy range. *Scientific Reports*, *7*(1), 1–12. <https://doi.org/10.1038/s41598-017-10554-0>
- Guo, J., Banjac, S., Röstel, L., Terasa, J. C., Herbst, K., Heber, B., & Wimmer-Schweingruber, R. F. (2019). Implementation and validation of the GEANT4/AtIRIS code to model the radiation environment at Mars. *Journal of Space Weather and Space Climate*, *9*(A2), A2. <https://doi.org/10.1051/swsc/2018051>
- Guo, J., Khaksarighiri, S., Wimmer-Schweingruber, R. F., Hassler, D. M., Ehresmann, B., Zeitlin, C., et al. (2021). Directionality of the Martian surface radiation and derivation of the upward albedo radiation. *Geophysical Research Letters*, *48*(15), e2021GL093912. <https://doi.org/10.1029/2021GL093912>
- Guo, J., Slaba, T. C., Zeitlin, C., Wimmer-Schweingruber, R. F., Badavi, F. F., Böhm, E., et al. (2017). Dependence of the Martian radiation environment on atmospheric depth: Modelling and measurement. *Journal of Geophysical Research: Planetary Science*, *122*(2), 329–341. <https://doi.org/10.1002/2016je005206>
- Guo, J., Zeitlin, C., Wimmer-Schweingruber, R. F., Rafkin, S., Hassler, D. M., Posner, A., et al. (2015). Modeling the variations of dose rate measured by RAD during the first MSL Martian year: 2012–2014. *The Astrophysical Journal*, *810*(1), 24. <https://doi.org/10.1088/0004-637X/810/1/24>
- Guo, J., Zeitlin, R. F., Wimmer-Schweingruber, C., Hassler, D. M., Ehresmann, B., Rafkin, S., et al. (2021). Radiation environment for future human exploration on the surface of Mars: The current understanding based on MSL/RAD dose measurements. *Astronomy and Astrophysics Review*, *29*(1), 1–81. <https://doi.org/10.1007/s00159-021-00136-5>
- Hassler, D. M., Zeitlin, C., Wimmer-Schweingruber, R., Böttcher, S., Martin, C., Andrews, J., et al. (2012). The radiation assessment detector (RAD) investigation. *Space Science Reviews*, *170*(1–4), 503–558. <https://doi.org/10.1007/s11214-012-9913-1>

- Kennedy, A. R. (2014). Biological effects of space radiation and development of effective countermeasures. *Life Sciences and Space Research*, 1, 10–43. <https://doi.org/10.1016/j.lssr.2014.02.004>
- Khaksarighiri, S. (2022). Data to reproduce figures in Khaksarighiri et al. (2023), JGR Planets. [Dataset]. Zenodo. <https://doi.org/10.5281/zenodo.7257306>
- Khaksarighiri, S., Guo, J., Wimmer-Schweingruber, R., & Narici, L. (2021). An easy-to-use function to assess deep space radiation in human brains. *Scientific Reports*, 11(1), 1–12. <https://doi.org/10.1038/s41598-021-90695-5>
- Matthiä, D., Ehresmann, B., Lohf, H., Köhler, J., Zeitlin, C., Appel, J., et al. (2016). The Martian surface radiation environment—a comparison of models and MSL/RAD measurements. *Journal of Space Weather and Space Climate*, 6(27), 1–17. <https://doi.org/10.1051/swsc/2016008>
- Millour, E., Forget, F., Spiga, A., Navarro, T., Madeleine, J.-B., Montabone, L., et al. (2015). The Mars climate database (MCD version 5.2). *European planetary science congress*, 10, 2015–2438.
- O'Neill, P., Golge, S., & Slaba, T. (2015). *Badhwar–O'Neill 2014 galactic cosmic ray flux model*. NASA/TP. Retrieved from <https://ntrs.nasa.gov/archive/nasa/casi.ntrs.nasa.gov/20150003026.pdf>
- Peterson, J., Rafkin, S., Zeitlin, C., Ehresmann, B., Weigle, E., Jeffers, S., & Hassler, D. M. o. (2013). MSL Mars radiation assessment detector RDR V1.0, MSL-M-RAD-3-RDR-V1.0. *NASA Planetary Data System*. <https://doi.org/10.17189/1519761>
- Rafkin, S., Peterson, J., Zeitlin, C., Ehresmann, B., Weigle, E., & Hassler, D. M. o. (2013). MSL Mars radiation assessment detector EDR V1.0, MSL-M-RAD-2-EDR-V1.0t. *NASA Planetary Data System*. <https://doi.org/10.17189/1519760>
- Rafkin, S. C., Zeitlin, C., Ehresmann, B., Hassler, D., Guo, J., Köhler, J., et al. (2014). Diurnal variations of energetic particle radiation at the surface of Mars as observed by the Mars Science Laboratory Radiation Assessment Detector. *Journal of Geophysical Research: Planets*, 119(6), 1345–1358. <https://doi.org/10.1002/2013je004525>
- Röstel, L., Guo, J., Banjac, S., Wimmer-Schweingruber, R. F., & Heber, B. (2020). Subsurface radiation environment of Mars and its implication for shielding protection of future habitats. *Journal of Geophysical Research: Planets*, 125(3), e2019JE006246. <https://doi.org/10.1029/2019JE006246>
- Saganti, P. (2005). Marie measurements and model predictions of solar modulation of galactic cosmic rays at Mars.
- Simpson, J. (1983). Elemental and isotopic composition of the galactic cosmic rays. *Annual Review of Nuclear and Particle Science*, 33(1), 323–382. <https://doi.org/10.1146/annurev.ns.33.120183.001543>
- Wilson, J., Cloudsley, M., Cucinotta, F., Tripathi, R., Nealy, J., & De Angelis, G. (2004). Deep space environments for human exploration. *Advances in Space Research*, 34(6), 1281–1287. <https://doi.org/10.1016/j.asr.2003.10.052>
- Wimmer-Schweingruber, R. F., Köhler, J., Hassler, D. M., Guo, J., Appel, J.-K., Zeitlin, C., et al. (2015). On determining the zenith angle dependence of the Martian radiation environment at gale crater altitudes. *Geophysical Research Letters*, 42(24), 10–557. <https://doi.org/10.1002/2015GL066664>
- Zeitlin, C., Hassler, D., Ehresmann, B., Rafkin, S., Guo, J., Wimmer-Schweingruber, R. F., et al. (2019). Measurements of radiation quality factor on Mars with the Mars Science Laboratory radiation assessment detector. *Life Sciences and Space Research*, 22, 89–97. <https://doi.org/10.1016/j.lssr.2019.07.010>
- Zhang, J., Guo, J., Dobynde, M. I., Wang, Y., & Wimmer-Schweingruber, R. F. (2022). From the top of Martian Olympus to deep craters and beneath: Mars radiation environment under different atmospheric and regolith depths. *Journal of Geophysical Research: Planets*, 127(3), e2021JE007157. <https://doi.org/10.1029/2021je007157>

4.4 *Paper IV: Modeling, Observations, and Albedo Radiation Analysis.*

The radiation environment on the Martian surface is influenced by the presence of local topographical features that vary as the rover traverses Gale Crater. During Curiosity's exploration near the Murray Butte area, an interesting observation was made regarding the impact of the butte structure on the surrounding radiation levels. It was found that the butte structure partially blocked approximately 19% of the sky, as compared to 10% during the preceding period. This obstruction resulted in a measurable decrease of $5 \pm 1\%$ in the background **GCR** dose. While this reduction may not provide full protection against cosmic radiation for future astronauts on Mars, it signifies the potential significance of natural structures such as buttes, cave skylights (Cushing et al., 2007), or lava tubes (Léveillé and Datta, 2010) as potential radiation shelters for future Martian habitats. These findings align with the broader strategy of in-situ resource utilization (Starr and Muscatello, 2020) and emphasize the importance of leveraging existing natural formations to enhance radiation shielding capabilities for long-term human habitation on Mars. In a previous study, paper 4.3, we investigated the relationship between zenith angles (θ) and surface downward radiation dose on Mars, considering the influence of varying atmospheric column depth for particles arriving from different zenith angles. To investigate this phenomenon, we developed a comprehensive model that encompasses different solar modulation conditions and particle types, enabling us to derive dose- θ functions. The Curiosity rover has been actively exploring the Gale crater, ascending the central peak of Mount Sharp located within the crater. In September 2016, Curiosity traversed through a geological formation named Murray Buttes, characterized by eroded sandstone mesas and buttes. On Sol (Martian day) 1455 (2016-09-08), the rover closely approached one of these buttes and was subsequently parked there for 13 sols, to perform drilling and contact science operations and drove away from the butte on Sol 1468. By combining our model with the panoramic sky visibility of **RAD** during and before the parking period, we quantified the obstructed and remaining radiation originating from the sky direction. Our analysis revealed that the ratio of the radiation from the sky during the parking compared to that before the parking is estimated to be about 88% assuming the same solar modulation condition. However, this reduction of 12% exceeds the measured decrease in dose of $5 \pm 1\%$. We attribute this discrepancy to the additional contribution of albedo radiation resulting from the obstructing butte. To determine the flat terrain albedo dose (i.e., without obstruction), we considered both the expected dose reduction due to sky blockage and the observed dose changes based on two independent scenarios. Through a comprehensive comparison of dose rates under various sky-obstruction conditions and an understanding of the zenith-angle dependence of radiation, we estimated that the flat-terrain albedo dose contributes to be about $19 \pm 1\%$ of the total surface dose. This knowledge is pivotal in improving our comprehension of the Martian radiation environment and developing effective strategies for radiation mitigation.

Directionality of the Martian surface radiation and derivation of the upward albedo radiation.

Guo, J., **Khaksarighiri, S.**, Wimmer-Schweingruber, R. F., et.al. (2021). Geophysical Research Letters, 48(15), e2021GL093912.

My contribution to this paper is 50% of the overall content and research efforts.

Geophysical Research Letters



RESEARCH LETTER

10.1029/2021GL093912

Key Points:

- The Martian surface radiation is influenced by topographical features
- The surface downward radiation dose of particles traversing through the atmosphere depends on the zenith angle
- The surface upward radiation dose is about 19% of the total dose

Correspondence to:

J. Guo and S. Khaksarighiri,
jnguo@ustc.edu.cn;
khaksari@physik.uni-kiel.de

Citation:

Guo, J., Khaksarighiri, S., Wimmer-Schweingruber, R. F., Hassler, D. M., Ehresmann, B., Zeitlin, C., et al. (2021). Directionality of the Martian surface radiation and derivation of the upward albedo radiation. *Geophysical Research Letters*, 48, e2021GL093912. <https://doi.org/10.1029/2021GL093912>

Received 19 APR 2021

Accepted 9 JUL 2021

Directionality of the Martian Surface Radiation and Derivation of the Upward Albedo Radiation

Jingnan Guo^{1,2,3} , Salman Khaksarighiri³ , Robert F. Wimmer-Schweingruber³ , Donald M. Hassler⁴ , Bent Ehresmann⁴ , Cary Zeitlin⁵ , Sven Löffler³, Daniel Matthiä⁶ , Thomas Berger⁶ , Günther Reitz⁶ , and Fred Calef⁷

¹School of Earth and Space Sciences, University of Science and Technology of China, Hefei, PR China, ²CAS Center for Excellence in Comparative Planetology, USTC, Hefei, PR China, ³Institute of Experimental and Applied Physics, Christian-Albrechts-University, Kiel, Germany, ⁴Planetary Science Division, Southwest Research Institute, Boulder, CO, USA, ⁵Leidos Corporation, Houston, TX, USA, ⁶German Aerospace Center (DLR), Institute of Aerospace Medicine, Cologne, Germany, ⁷Jet Propulsion Laboratory, California Institute of Technology, Pasadena, CA, USA

Abstract Since 2012 August, the Radiation Assessment Detector (RAD) on the Curiosity rover has been characterizing the Martian surface radiation field which is essential in preparation for future crewed Mars missions. RAD observed radiation dose is influenced by variable topographical features as the rover traverses through the terrain. In particular, while Curiosity was parked near a butte in the Murray Buttes area, we find a decrease of the dose rate by $(5 \pm 1)\%$ as 19% of the sky was obstructed, versus 10% in an average reference period. Combining a zenith-angle-dependent radiation model and the rover panoramic visibility map leads to a predicted reduction of the downward dose by $\sim 12\%$ due to the obstruction, larger than the observed decrease. With the hypothesis that this difference is attributable to albedo radiation coming from the butte, we estimate the (flat-terrain) albedo radiation to be about 19% of the total surface dose.

Plain Language Summary Interplanetary space is filled with energetic particles that can affect the health of astronauts, for example, by causing late-arising cancer and possibly hereditary diseases. Mars lacks a global magnetic field and its atmosphere is very thin compared to Earth's. Thus its surface is exposed to such space radiation which presents risks to future humans on Mars. Mitigation strategies could include using natural geological structures on Mars, for example, cave skylights and lava tubes and even simple buttes, for protection. The Radiation Assessment Detector (RAD) on the Curiosity rover has observed a decrease of the radiation absorbed dose rate by $(5 \pm 1)\%$ while Curiosity was parked near a butte. This provides the first direct illustration that Mars's surface features may serve as potential radiation shelters for future missions. However, when exploiting such shielding possibilities, the secondary radiation generated in the terrain of Mars that is, emitted backwards must also be considered. Combining the RAD observation with a radiation transport model, we derive such “reflected” radiation dose on a flat terrain to be about 19% of the total surface dose.

1. Introduction

Health risks induced by exposure to space radiation have been classified as one of the potential “show stoppers” for future human missions to Mars (e.g., Cucinotta et al., 2017; Walsh et al., 2019). To evaluate such radiation risks, the Radiation Assessment Detector (RAD, Hassler et al., 2012; Zeitlin et al., 2016) was designed to measure energetic particle radiation on the Martian surface (Hassler et al., 2014) as part of the Mars Science Laboratory (MSL, Grotzinger et al., 2012) mission, which landed the Curiosity rover in Gale crater in August 2012.

Space radiation near Mars is contributed by the continuous background Galactic Cosmic Ray (GCR) particles and, occasionally, Solar Energetic Particles (SEPs) resulting from solar eruptions. Mars lacks a global intrinsic magnetosphere but has a thin atmosphere. The primary space radiation can directly propagate through the atmosphere with no interactions or lose part of its energy and generate secondaries via ionization, fragmentation, spallation, etc. Secondary particles can also be generated in the terrain and escape the surface to be detected as upward-directed “albedo” particles. The Martian radiation environment can be studied via particle transport modeling through the Martian atmosphere and surface (De Angelis et al., 2006;

© 2021. The Authors.

This is an open access article under the terms of the [Creative Commons Attribution-NonCommercial](https://creativecommons.org/licenses/by-nc/4.0/) License, which permits use, distribution and reproduction in any medium, provided the original work is properly cited and is not used for commercial purposes.

Ehresmann et al., 2011; Gronoff et al., 2015; Keating et al., 2005; Kim et al., 2014; Saganti et al., 2004; etc). The successful operation of RAD on Mars also made it possible to benchmark these models against in-situ measurements (e.g., Matthiä et al., 2016, 2017; Guo et al., 2019).

The Radiation Assessment Detector consists of three silicon detectors (A, B, and C, each having a thickness of 300 μm), a thallium-doped cesium iodide scintillator (D with a thickness of 28 mm), and a plastic scintillator (Bicron BC432 m, E with a thickness of 18 mm and mass of 34.9 gram). In particular, the absorbed dose rate, defined as the energy deposited by radiation per unit mass ($\text{Gray} = \text{J/kg}$) and time, is measured concurrently in two active dosimeters, that is, detectors B and E. The latter has much better statistics due to a large geometric factor. It has a composition similar to that of human tissue and is more sensitive to neutrons. Additionally, low-energy albedo particles traveling upward from the surface are likely to deposit energy in E but may stop in the detector stack (or scatter out of the stack) before reaching B. Therefore, we use the absorbed dose in the plastic detector “E” in this study.

The Martian topographic structures may serve for radiation shielding for future human missions on Mars. They can be particularly helpful to provide shielding during highly intense SEP events and can also serve to achieve a steady reduction of exposure to the long-term GCR-induced radiation (Dartnell et al., 2007; Kim et al., 1998; Röstel et al., 2020). Locations with higher iron and/or hydrogen content can also be beneficial especially via moderating the neutron contribution to radiation as suggested by models (Da Pieve et al., 2021; Keating & Gonçalves, 2012; Masarik & Reedy, 1996; Röstel et al., 2020). In order to evaluate potential regolith shielding strategies, it is essential to correctly model particle interactions with the Martian surface material. The assessment of surface albedo radiation is therefore important as it is a direct result of radiation interaction in the Martian terrain.

Particles coming into RAD from all directions can contribute to the recorded dose. However, the directionality of the incoming particle is not registered in the dose-rate data, and it is not possible to directly assess the observed albedo radiation. In this study, we estimate the contribution of albedo dose using a Martian atmosphere radiation model anchored to the RAD measurements. The model provides the angular dependence of the downward-directed dose as it would be measured by RAD if it had this capability (Section 2). The measurements are taken before and during a period when the rover was parked close to a butte with a portion of the downward-directed dose blocked by the butte structure (Section 3). We then derive the first observation-based assessment of the Martian surface albedo dose (Section 4) and find that it is about 19% of the total surface dose on a flat terrain without obstructions.

2. The Zenith Angle Dependence of the Dose

Wimmer-Schweingruber et al. (2015) have studied the zenith angle (θ , the angle from the surface normal) dependence of the particle fluxes reaching RAD and found that the radiation field is nearly, but not entirely isotropic for $\theta \leq \sim 15^\circ$. In order to better understand the directionality of the dose on the surface of Mars over a wide range of zenith angles ($0^\circ \leq \theta \leq 90^\circ$), we construct a Monte Carlo model of GCRs propagating through the Martian atmosphere, which allows to derive the dose dependence on θ .

The input primary GCRs are obtained using the Badhwar-O'Neill (BON) 2014 prescription of solar modulation, which solves the Fokker-Planck equations to transport the local interstellar GCR spectrum to 1 AU (O'Neill et al., 2015). The intensity of GCRs is modulated by solar activity and heliospheric magnetic field, which evolve with the 22-year solar Hale cycle (Potgieter, 2013). The strength of the modulation is quantified by the so-called “modulation potential Φ ” in the BON model, which is normally determined monthly. We assume the monthly averaged GCR spectra to be the same at Mars since the radial gradient of GCR flux in the heliosphere is only about 1%–2% between 1 AU and 1.5 AU (within 10 AU) according to multi-spacecraft observations (Honig et al., 2019; Roussos et al., 2020).

We calculate the interaction of primary GCRs with the Martian atmosphere represented by a spherical shell of CO_2 gas using the GEANT4 particle transport code (Agostinelli et al., 2003). The vertical atmospheric mass ($\theta = 0^\circ$) is set as 21 g/cm^2 , which approximately corresponds to an average surface pressure of ~ 800 Pa as measured by MSL's Rover Environmental Monitoring Station (REMS, Gómez-Elvira et al., 2012). The thickness of the atmosphere increases with θ to account for a realistic 3D atmospheric structure. Only

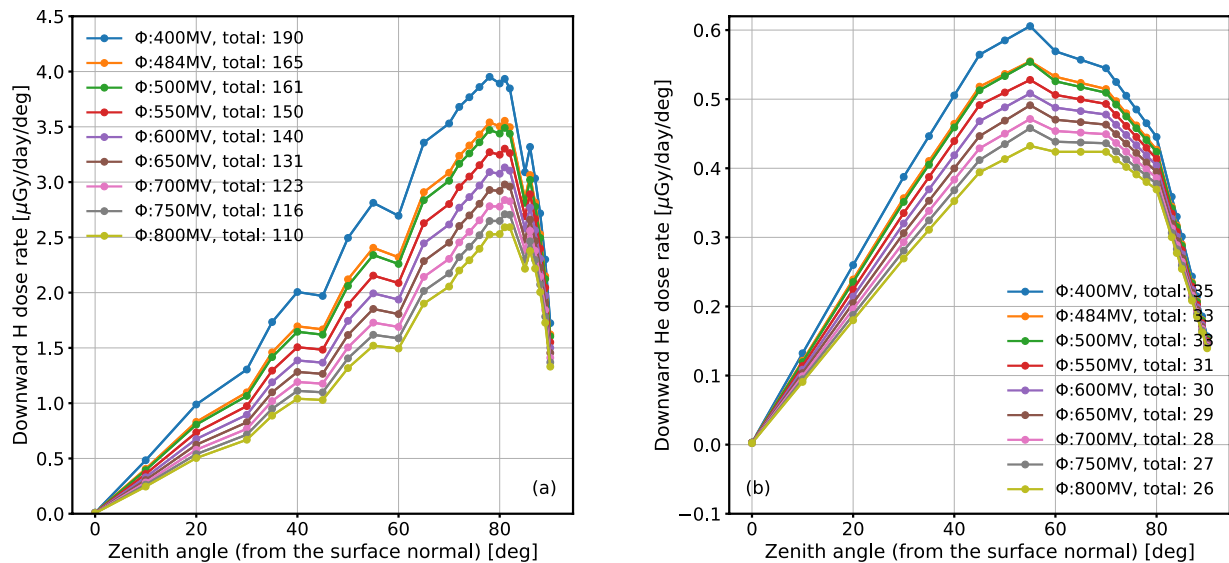


Figure 1. Simulation results for the dependence of dose rate on zenith angle, θ , of (a) incoming primary GCR protons and (b) helium ions. Different primary GCR spectra are considered under different solar modulation potentials Φ , as inputs to the BON model, as explained in Section 2. The total dose rates [$\mu\text{Gy/day}$] integrated over θ are also given in each case.

protons and helium ions are modeled as they make up about 99% of the GCR atomic nuclei (Simpson, 1983). Heavier ion contributions to the surface dose will be additionally considered in Section 4. All primary and secondary particles tracked in the model that reach RAD can also interact with the RAD detectors and contribute to absorbed dose. As the simulated particle direction is known, we can track the dose, as would be measured by the RAD E detector, contributed by particles arriving from specific zenith angles. The physics list QGSP_BERT has been used in the current model setup. Although the model selection in GEANT4 may affect the calculated secondary particle spectra, the surface absorbed dose agrees within $\sim 5\%$ for different physics lists (Matthiä et al., 2016).

The modeled zenith-angle dependence of the dose rate in RAD E detector is shown in Figure 1 for primary protons and helium ions under different solar modulation potential Φ . As shown, the surface dose rate depends on solar modulation, with a smaller Φ (weaker modulation) resulting in a larger dose rate for each θ . The dose rate summed over θ from 0 to 90° represents the total downward-directed dose rate on the surface for each Φ value. The dose induced by primary protons is 4.2–5.4 times (depending on Φ) larger than that induced by primary helium ions.

The modeled results show that radiation on Mars is dependent on θ . For example, protons coming in at $\theta \sim 80^\circ$ make the greatest contribution to the surface dose per angular bin. For helium ions, this angle is at around 55° . Two factors drive this result: (1) transport through larger depths of atmosphere at larger zenith angle θ and (2) simple geometry, since the solid angle subtended at large zenith angles is greater for each degree of θ than at smaller angles. The transport effects can be qualitatively understood by considering that the atmospheric column depth increases from about 21 g/cm^2 at $\theta = 0^\circ$ to more than 300 g/cm^2 at angles above 85° . These longer paths slow primaries substantially which become more ionizing or more easily stopped; meanwhile, the probability of the initial ion undergoing a nuclear interaction and fragmenting into lighter ions is higher with a thicker path.

One can scale the dose rate in Figure 1 by the geometric factor of each θ to remove the area effect (so that the y-axis has units of $\mu\text{Gy/day/cm}^2/\text{sr}$). The scaled proton functions (not plotted here) have a more gradual increase before the major peak at $\theta \sim 80^\circ$ (with a column depth of 110 g/cm^2) followed by a secondary peak at $\theta \sim 86^\circ$. As described above, the primary peak arises from the combination of primary protons slowing down and the efficient generation of secondary particles. The secondary peak is due to the fact that particles arriving from near-horizontal directions have longer paths in the hexagonal prism-shaped RAD E detector

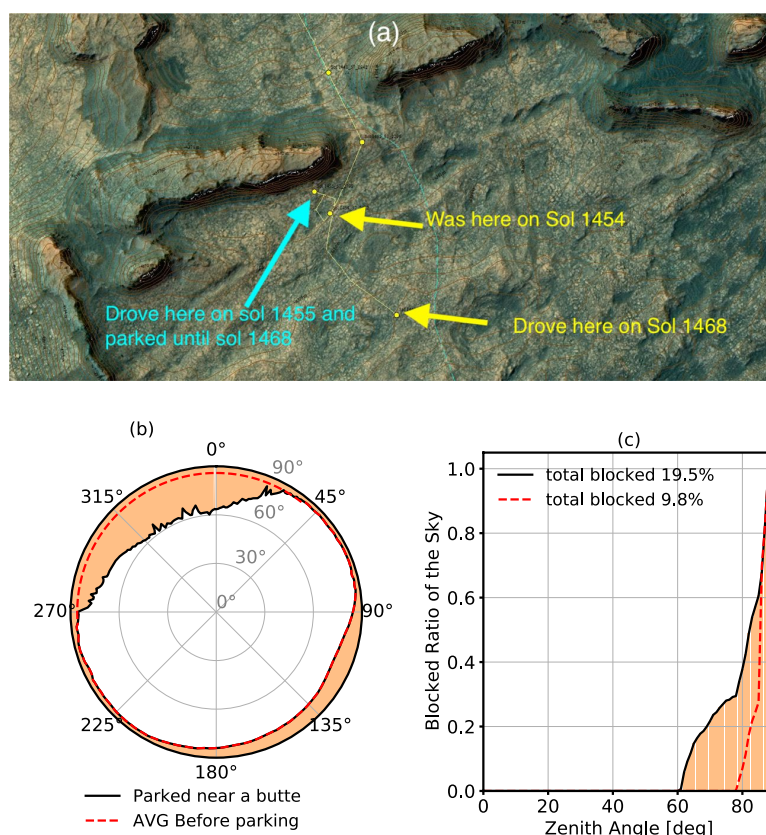


Figure 2. (a) The rover traverse map through the Murray Buttes area (North is up.). Each drive is marked as the path between the yellow dots where the rover stopped. The locations before, after, and during the 13-sol parking are marked. The base image is adapted from here <https://mars.nasa.gov/resources/38045/curiosity-rovers-location-for-sol-1468/>. (b) The panoramic sky visibility of RAD as a function of the 360° of azimuth angle (0° for North). The zenith angle of obstructed view during the 13-sol parking is shown in orange shaded area. Surface particles can directly reach RAD from the non-shaded area. The red dashed curve shows the sky view averaged for periods before the parking as described in Section 4. (c): The ratio of blocked sky as a function of the zenith angle for the two periods. The integrated value is shown for each period.

compared to those arriving from smaller zenith angles. On the other hand, the scaled helium dose (not plotted here) decreases monotonically with increased θ (so as column depth) since helium ions have smaller mean free paths and are more likely to fragment in a thicker atmosphere.

Figure 1a also shows some bumpy features from $\sim 30^\circ$ to 60° , which are due to a combination of uncertainties in the transport calculations and statistical variations. (Using smoothed functions without such features, we performed the analysis throughout this work and found the exact same result with a precision of $1 \mu\text{Gy/day}$.)

3. The Reduction of Radiation Due to Topographical Shielding at Murray Buttes

The Curiosity rover has been exploring Gale crater while gradually climbing up Mount Sharp, which forms the central peak within the crater. In September 2016, Curiosity traversed through a geological formation called “Murray Buttes” (MB), which contains mesas and buttes consisting of eroded sandstone (Byrne, 2020). The relevant rover traverse path is shown in Figure 2a. [A Martian day (sol) lasts 24 h and 39 min. Mission progress is measured in sols since landing.] On Sol 1455 (2016-09-08), the rover drove close to a butte as pointed out by the cyan arrow and was subsequently parked there for nearly 13 sols to perform

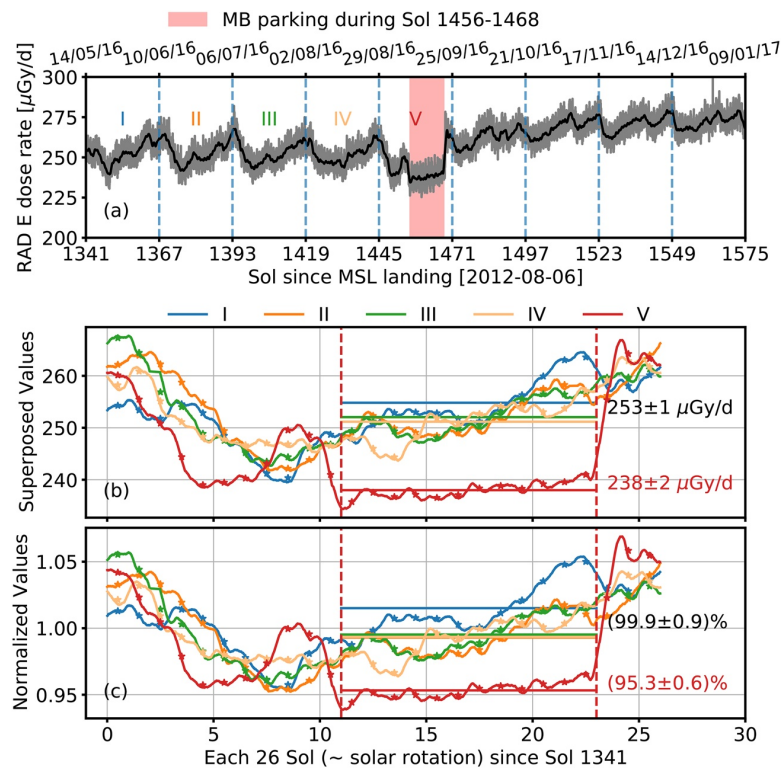


Figure 3. (a): The RAD E dose rate measurement from May 2016 until January 2017. Original data are in gray, and smoothed daily values are in black. Each solar rotation cycle of about 26 sols is separated by dashed lines. (b): Superposed daily dose rates for the five rotations which are marked from I to V in (a). The time of each rotation ranges from sol 1 until 26. The period, when Curiosity was parked, is shaded in red in (a) and marked between dashed vertical lines in (b). The average dose rate during the parking and the average dose rate for cycles I to IV between the dashed lines are marked. (c): The same as (b), but with the normalized dose rate. See Section 3 for more details.

drilling and contact science operations and drove away from the butte on Sol 1468. Figures 2b and 2c shows the obstructed fraction of the sky during the course and will be discussed in Section 4.

GCR flux in the heliosphere can be modulated by the recurrent heliospheric structures, called corotating interaction regions (CIRs), which often appear during the declining phase of a solar cycle (e.g., Crooker et al., 1999; Richardson, 2004). CIRs are formed when high speed solar wind streams arising from coronal holes (CHs) run into preceding slow solar wind in the interplanetary space. As CHs may exist stably for several solar rotations, the consequent GCR modulation occurs periodically. Geyer et al. (2021) have studied the evolution of CIRs at Mars and Earth using *in situ* solar wind and magnetic field data as well as remote-sensing solar images of the CHs. They found that there are multiple CHs and corresponding CIRs reappearing for at least five solar rotations from the end of May until the end of September 2016.

As shown in Figure 3a, the RAD measured dose rate repeats very similar evolutionary patterns throughout this period including four solar rotational cycles (marked as I–IV) followed by a cycle “V,” which contains the MB parking (shaded in red). The regularity of GCR variation in the subsequent cycles started to deteriorate as the CIRs became unstable due to the evolution of the solar CHs, which often experience growing and decaying phases (Heinemann et al., 2018). Therefore, if no topographical influence were present, dose rate throughout cycles I–V should repeat similar temporal evaluations. However, as shown, there is a sudden drop and a quick recovery of the RAD dose rate at the start and end of the parking period. The fundamental reason is that a portion of the sky is blocked by the butte where downward particles are stopped from reaching RAD directly. Nevertheless, because the dose rate varies with time, we need to derive this reduction excluding the background variation due to the above-discussed heliospheric influences.

We then superpose and analyze the RAD dose rate measured throughout solar rotational cycles I–V. The daily dose rate of each cycle is re-plotted with a time span of 26 sols in Figure 3b. The dose rate during ~13 sols of MB parking as marked between dashed vertical lines is substantially lower than that recorded in the same window of the previous four cycles. The average dose rate of the MB parking period is $238 \pm 2 \mu\text{Gy/d}$ and is $253 \pm 1 \mu\text{Gy/d}$ for cycles I–IV in this window with a difference of $15 \pm 2 \mu\text{Gy/d}$ due to the butte's obstruction.

Considering that there is a slight variation of the long-term GCR flux throughout the five cycles, for each cycle, we also normalized the data by the mean value of the data outside the dashed-line-delimited window and repeat the superpose analysis (see Figure 3c). The normalized data are averaged as $(99.9 \pm 0.9)\%$ during this window for cycles I–IV and are $(95.3 \pm 0.6)\%$ during the parking, resulting in a drop ratio of $5\% \pm 1\%$ between the two.

4. The Derivation of Regolith-Generated Albedo Radiation

The panoramic angle of obstructed view (AOV, angle from the horizon) of the sky seen by RAD during the MB parking of the rover is shown in Figure 2b. The AOV ranges from $\sim 3^\circ$ from the horizon ($\theta = 87^\circ$) upto about 30° ($\theta = 60^\circ$). The butte obstruction of the sky is mainly found at azimuth angle $\phi < 40^\circ$ and $\phi > 265^\circ$. Before the parking, the rover was driving through the MB area and did not have a full view of the sky either. Therefore, for this period, we approximate the AOV at $\phi < 40^\circ$ and $\phi > 265^\circ$ using the median value of AOV at other azimuth angles, which is 4.13° . Such derived AOV, averaged for months before the parking, is shown as the red-dashed curve. Considering that each zenith angle corresponds to a 1° -wide ring area of the 2π full-sky sphere, we calculate the ratio of the obstructed area (ROA) as shown in Figure 2c, for the two periods. At $\theta > 85^\circ$, the ROA is above 80% in both periods. The total blocked ratio of the sky integrated over θ is about 0.19 for the period of MB parking and about 0.10 averaged before the parking.

Previously, the model of zenith-angle dependence of the dose (Section 2 and Figure 1) gives the dose functions $d_H(\theta)$ and $d_{He}(\theta)$ for proton and helium ions, respectively. Combining the dose- θ functions and the RAD sky view, we can calculate the expected dose rate contributed by particles arriving from the sky direction as:

$$D_{\text{GCRH}} = \sum_{\theta=0^\circ}^{90^\circ} (1 - \text{ROA}(\theta)) \cdot d_H(\theta) \quad (1)$$

$$D_{\text{GCRHe}} = \sum_{\theta=0^\circ}^{90^\circ} (1 - \text{ROA}(\theta)) \cdot d_{He}(\theta). \quad (2)$$

The term $1 - \text{ROA}(\theta)$ is the unblocked ratio of the sky as also plotted in Figure 4a under three different topographical arrangements (as explained later). Additionally, primary GCRs heavier than protons and helium ions contribute nearly 10% to the total absorbed dose on the surface of Mars as suggested by results of simulations using the atmospheric condition at Gale crater (Röstel et al., 2020). Therefore, we approximate the total dose rate contributed by all GCRs arriving from the sky direction as:

$$D_{\text{sky}} = 1.10 \cdot (D_{\text{GCRH}} + D_{\text{GCRHe}}) \quad (3)$$

Now, we consider three topographical scenarios and the corresponding dose rate derived from the combination of the dose-zenith model (Figure 1) and ROA observation (Figure 2b) as following.

- For a completely flat terrain without any surface obstruction, $1 - \text{ROA}(\theta)$ is constantly unity as $\text{ROA}(\theta)$ is simply zero, shown as “a full sky-view” in Figure 4a. The solar modulation potential Φ during 2016 September is about 484 MV used for the BON model (the orange curves in Figure 1). Following Equation 1, we derive $D_{\text{GCRH}}^a = 165 \mu\text{Gy/d}$ induced by primary protons and their secondaries and $D_{\text{GCRHe}}^a = 33 \mu\text{Gy/d}$ from primary helium ions and their secondaries, which result in $D_{\text{sky}}^a = 218 \mu\text{Gy/d}$ (Equation 3). The corresponding calculations are also shown as azure curves in Figure 4b.
- Before the parking, folding the sky-view function b) in Figure 4a with the modeled $d_H(\theta)$ and $d_{He}(\theta)$ under the average modulation Φ of 500 MV from May–August 2016 (the green curves in Figure 1), we

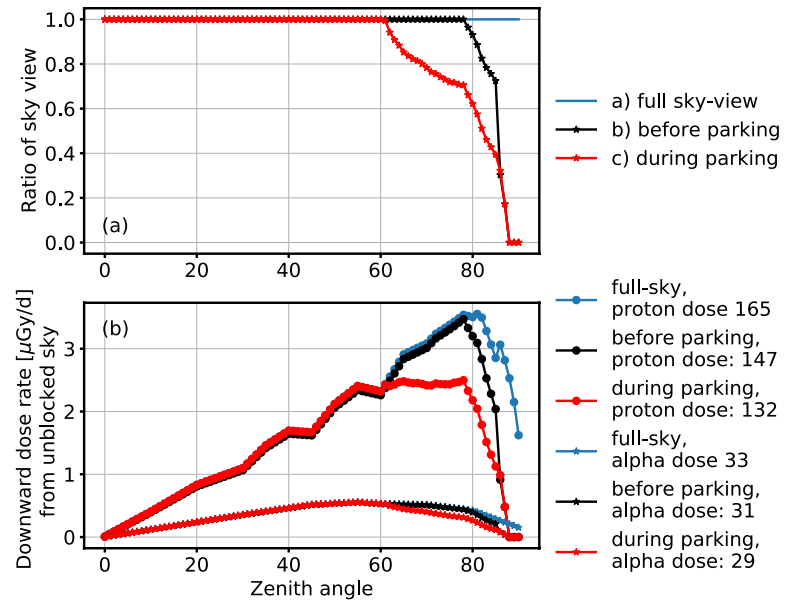


Figure 4. (a) The unblocked ratio of the sky as a function of the zenith angle θ for three geospatial scenarios: (a) full sky view, (b) before the MB parking, and (c) during the MB parking. (b): The dose rate resulting from particles arriving from the sky as a function of θ for primary GCR protons (filled circles) and helium ions (stars) under the three different scenarios. In each case, the dose rate integrated over θ is marked in the legend.

obtain $D_{\text{GCRH}}^b = 147 \mu\text{Gy/d}$ and $D_{\text{GCRHe}}^b = 31 \mu\text{Gy/d}$, which lead to $D_{\text{sky}}^b = 196 \mu\text{Gy/d}$, shown as black curves in Figure 4b. Note that Φ of 484 MV (for September 2016) would result in $201 \mu\text{Gy/d}$, which is about 92% of the full-sky dose D_{sky}^a under the same Φ .

(c) During the parking, with the sky-view function c) in Figure 4a, we obtain $D_{\text{GCRH}}^c = 132 \mu\text{Gy/d}$ and $D_{\text{GCRHe}}^c = 29 \mu\text{Gy/d}$, which result in $D_{\text{sky}}^c = 177 \mu\text{Gy/d}$, shown as red lines in Figure 4b. This is about 81% of the full sky-view dose D_{sky}^a and 90% of the dose rate D_{sky}^b before the parking or 88% of the dose rate in scenario (b) if the exact same solar modulation is present. In other words, radiation from the atmosphere reaching RAD decreased by about 12% during the parking caused by sky obstruction of the nearby butte.

Such estimated decrease is much larger than the observed 4%–6% (Section 3) because the butte blocked the radiation from the sky but meanwhile contributing to the albedo radiation. The interaction of particles with the Martian regolith happens mostly within the uppermost 2 m of the subsurface as modeled by Röstel et al. (2020, Figure 2). The model also suggests that the albedo radiation detected as dose changes little as the soil composition varies (Figure 4 of the article). We then assume that albedo radiation generated by the butte is similar to that from the ground regolith, and the total albedo dose only depends on the effective geometric area of the regolith source.

Defining the dose rate contributed by a completely flat terrain to be D_{albedo} , that is, when the sky or terrain contributes an exact half of the full 4π solid angle, we formulate the total dose rate on a terrain with obstructions as below:

$$\left(1 + \sum_{\theta=0^\circ}^{90^\circ} \text{ROA}(\theta)\right) D_{\text{albedo}} + D_{\text{sky}} = D_{\text{total}}, \quad (4)$$

where $\sum_{\theta=0^\circ}^{90^\circ} \text{ROA}(\theta)$ is the total blocked ratio of the sky that contributes alternatively to the albedo radiation and is about 0.19 during the MB parking and 0.10 averaged before the parking (Figure 2). D_{sky} is the remaining dose of particles propagating from the atmosphere and has been derived for above different scenarios. Scenario (a) is however unrealistic for the Curiosity rover inside Gale crater which almost always

provides some viewing obstructions. Applying scenario (b) with $D_{\text{sky}} = 196 \mu\text{Gy/d}$ and the estimated dose rate $D_{\text{total}} \approx 253 \mu\text{Gy/d}$ before the parking (Figure 3), we obtain $D_{\text{albedo}} \approx 52 \mu\text{Gy/d}$. Similarly, for scenario (c) during the parking, that is, $D_{\text{sky}} = D_{\text{sky}}^c = 177 \mu\text{Gy/d}$ and $D_{\text{total}} \approx 238 \mu\text{Gy/d}$, we obtain $D_{\text{albedo}} \approx 51 \mu\text{Gy/d}$. It is remarkable how well the two estimates agree.

This gives the first estimation of the Martian surface albedo radiation dose based on synergistic assessments of modeled results and *in situ* observations. The ratio of such estimated albedo radiation, $51\text{--}52 \mu\text{Gy/d}$, to the downward radiation on a flat terrain, D_{sky}^a , is about 23% and is about 19% to the total surface dose. The albedo contribution is slightly higher when there are surface obstructions as expected, for example, about 21% with 10% blockage of the sky. It is in good agreement with the 18%–20% upward dose ratio obtained from GEANT4 particle transport models (Guo et al., 2018; Matthiä & Berger, 2017) but larger than that modeled by Kim et al. (2014), which is only about 10%. More topographic information collected at other locations in combination with RAD measurements can further verify and improve our assessment and may also be able to provide a “radiation map” along the path of the Curiosity rover. Moreover, different solar activities, surface elevations or Martian seasons may also affect the albedo contribution and surface radiation. A low elevation and consequently a thicker atmosphere can also enhance the shielding effect as observed by RAD (Guo et al., 2017; Rafkin et al., 2014).

5. Discussion and Conclusion

The Martian surface radiation is influenced by surface topographical features. While Curiosity was parked near a butte in the Murray Butte area, we found the butte structure, blocking out about 19% of the sky (vs. 10% in the preceding period), induced a decrease of the background GCR dose by $(5 \pm 1)\%$. Although this reduction is not significant enough to fully protect future astronauts from cosmic radiation on Mars, it illustrates that existing natural structures such as buttes, cave skylights (Cushing et al., 2007), or lava tubes (Léveillé & Datta, 2010) may serve as a potential radiation shelter for future habitats on Mars, benefiting from the grander strategy of *in situ* resource utilization (Starr & Muscatello, 2020). For instance, the modeled radiation environment on and under the surface of Mars suggests that ~ 1 m of shielding depth may limit the annual absorbed dose in water within 20 mGy (Röstel et al., 2020).

Due to the varying atmospheric column depth for particles arriving from different zenith angles θ , the surface downward radiation dose of particles is θ dependent. We have modeled this process and provided the dose- θ functions for different solar modulation conditions and particle types. This model is then used in combination with the RAD panoramic visibility map to derive the obstructed and remaining radiation coming from the sky direction. The ratio of the radiation from the sky during the parking compared to that before the parking is estimated to be about 88% assuming the same solar modulation condition. This reduction of 12% is significantly higher than the observed $(5 \pm 1)\%$ of dose decrease. This is because the obstructing butte contributes to additional albedo radiation.

Accounting for the expected dose reduction due to the sky blockage and observed dose changes, we derive the flat-terrain (i.e., zero obstruction) albedo dose to be about 19% of total surface dose based on two independent scenarios. This result is consistent with previous modeled results (Guo et al., 2018; Matthiä et al., 2017). Appel et al. (2018) have studied the charged protons detected in RAD's vertical telescope cone (with a half angle of 18°) and found a 10% ratio of the upward to downward flux of 100–200 MeV protons. This ratio is different from what we obtain here mainly for two reasons: (1) dose is contributed by all particles over a wide energy range and cannot be represented solely by protons in this energy range and (2) downward particles within the semi-vertical cone used in Appel et al. (2018) traverse through a much thinner atmosphere than those coming from more horizontal directions so that the downward flux/dose ratio in this cone is different from the averaged downward value.

In summary, the Martian surface radiation is influenced by local topographical features which change as the rover traverses through Gale crater. Detailed comparison of dose rates measured under different sky-obstruction conditions combined with zenith-angle dependence of the radiation allow us to estimate the contribution of the albedo radiation on Mars, which is an important assessment for better understanding the Martian radiation environment and developing radiation mitigation strategies.

Data Availability Statement

MSL/RAD data are archived in the NASA planetary data systems (<https://pds.nasa.gov/ds-view/pds/view-Dataset.jsp?dsid=MSL-M-RAD-3-RDR-V1.0>). Data plotted in the figures are archived at Zenedo <https://doi.org/10.5281/zenodo.4701689>.

Acknowledgments

RAD is supported by NASA (HEOMD) under JPL subcontract 1273039 to SWRI, and in Germany by DLR (under German Space Agency grants 50QM0501, 50QM1201, and 50QM1701) to the CAU Kiel. J. G. is supported by the Strategic Priority Program of the Chinese Academy of Sciences (Grant No. XDB41000000), the National Natural Science Foundation of China (Grant No. 42074222) and the CNSA pre-research Project on Civil Aerospace Technologies (Grant No. D020104). Open access funding enabled and organized by Projekt DEAL.

References

- Agostinelli, S., Allison, J., Amako, K., Apostolakis, J., Araujo, H., Arce, P., et al. (2003). GEANT4: A simulation toolkit. *Nuclear Instruments & Methods in Physics Research, Section A*, 506(3), 250–303.
- Appel, J. K., Köhler, J., Guo, J., Ehresmann, B., Zeitlin, C., Matthiä, D., et al. (2018). Detecting upward directed charged particle fluxes in the Mars Science Laboratory Radiation Assessment Detector. *Earth and Space Science*, 5(1), 2–18. <https://doi.org/10.1002/2016EA000240>
- Byrne, C. J. (2020). Murray and Stimson Formations, Murray Buttes, and the Dune Campaign. In *Travels with curiosity* (pp. 69–94). Springer. https://doi.org/10.1007/978-3-030-53805-7_7
- Crooker, N. U., Gosling, J. T., Bothmer, V., Forsyth, R. J., Gazis, P. R., Hewish, A., et al. (1999). CIR morphology, turbulence, discontinuities, and energetic particles. *Space Science Reviews*, 89, 179–220. <https://doi.org/10.1023/A:1005253526438>
- Cucinotta, F. A., To, K., & Cacao, E. (2017). Predictions of space radiation fatality risk for exploration missions. *Life Sciences and Space Research*, 13, 1–11. <https://doi.org/10.1016/j.lssr.2017.01.005>
- Cushing, G. E., Titus, T. N., Wynne, J. J., & Christensen, P. R. (2007). THEMIS observes possible cave skylights on Mars. *Geophysical Research Letters*, 34, 17201. <https://doi.org/10.1029/2007GL030709>
- Da Pieve, F., Gronoff, G., Guo, J., Mertens, C., Neary, L., Gu, B., & Cleri, F. (2021). Radiation environment and doses on Mars at Oxia Planum and Mawrth Vallis: Support for exploration at sites with high biosignature preservation potential. *Journal of Geophysical Research: Planets*, 126(1), e2020JE006488. <https://doi.org/10.1029/2020je006488>
- Dartnell, L., Desorgher, L., Ward, J., & Coates, A. (2007). Modeling the surface and subsurface martian radiation environment: Implications for astrobiology. *Geophysical Research Letters*, 34, L02207. <https://doi.org/10.1029/2006gl027494>
- De Angelis, G., Wilson, J. W., Cloudsley, M. S., Qualls, G. D., & Singleterry, R. C. (2006). Modeling of the Martian environment for radiation analysis. *Radiation Measurements*, 41(9–10), 1097–1102. <https://doi.org/10.1016/j.radmeas.2006.04.032>
- Ehresmann, B., Burmeister, S., Wimmer-Schweingruber, R. F., & Reitz, G. (2011). Influence of higher atmospheric pressure on the martian radiation environment: Implications for possible habitability in the Noachian epoch. *Journal of Geophysical Research: Space Physics*, 116(A15), 10106. <https://doi.org/10.1029/2011ja016616>
- Geyer, P., Temmer, M., Guo, J., & Heinemann, S. G. (2021). Properties of stream interaction regions at Earth and Mars during the declining phase of sc 24. *Astronomy & Astrophysics*, 649, A80. <https://doi.org/10.1051/0004-6361/202040162>
- Gómez-Elvira, J., Armien, C., Castañer, L., Domínguez, M., Genzer, M., Gómez, F., et al. (2012). REMS: The environmental sensor suite for the Mars Science Laboratory rover. *Space Science Reviews*, 170(1–4), 583–640. <https://doi.org/10.1007/s11214-012-9921-1>
- Gronoff, G., Norman, R. B., & Mertens, C. J. (2015). Computation of cosmic ray ionization and dose at Mars. I: A comparison of HZETRN and planetocosmics for proton and alpha particles. *Advances in Space Research*, 55(7), 1799–1805. <https://doi.org/10.1016/j.asr.2015.01.028>
- Grotzinger, J. P., Crisp, J., Vasavada, A. R., Anderson, R. C., Baker, C. J., Barry, R., et al. (2012). Mars Science Laboratory mission and science investigation. *Space Science Reviews*, 170(1), 5–56. <https://doi.org/10.1007/s11214-012-9892-2>
- Guo, J., Banjac, S., Röstel, L., Terasa, J. C., Herbst, K., Heber, B., & Wimmer-Schweingruber, R. F. (2019). Implementation and validation of the GEANT4/ATrIS code to model the radiation environment at Mars. *Journal of Space Weather and Space Climate*, 9(A2), A7. <https://doi.org/10.1051/swsc/2019004>
- Guo, J., Slaba, C., Tony, C., Zeitlin Wimmer-Schweingruber, R. F., Badavi, F. F., Böhm, E., et al. (2017). Dependence of the martian radiation environment on atmospheric depth: Modeling and measurement. *Journal of Geophysical Research: Planets*, 122(2), 329–341. <https://doi.org/10.1002/2016JE005206>
- Guo, J., Zeitlin, C., Wimmer-Schweingruber, R. F., McDole, T., Kühl, P., Appel, J. C., et al. (2018). A generalized approach to model the spectra and radiation dose rate of solar particle events on the surface of Mars. *The Astronomical Journal*, 155(1), 49. <https://doi.org/10.3847/1538-3881/aaa085>
- Hassler, D. M., Zeitlin, C., Wimmer-Schweingruber, R. F., Böttcher, S. I., Martin, C., Andrews, J., et al. (2012). The Radiation Assessment Detector (RAD) investigation. *Space Science Reviews*, 170(1), 503–558. <https://doi.org/10.1007/s11214-012-9913-1>
- Hassler, D. M., Zeitlin, C., Wimmer-Schweingruber, R. F., Ehresmann, B., Rafkin, S., Eigenbrode, J. L., et al. (2014). Mars's surface radiation environment measured with the Mars Science Laboratory's curiosity rover. *Science*, 343(6169), 1244797.
- Heinemann, S. G., Temmer, M., Hofmeister, S. J., Veronig, A. M., & Vennerström, S. (2018). Three-phase Evolution of a Coronal Hole. I. 360° Remote Sensing and In Situ Observations. *The Astrophysical Journal*, 861, 151. <https://doi.org/10.3847/1538-4357/aac897>
- Honig, T., Witasse, O. G., Evans, H., Nieminen, P., Kuulkers, E., Taylor, M. G. T., et al. (2019). Multi-point galactic cosmic ray measurements between 1 and 4.5 AU over a full solar cycle. *Annales Geophysicae*, 37(5), 903–918. <https://doi.org/10.5194/angeo-37-903-2019>
- Keating, A., & Gonçalves, P. (2012). The impact of Mars geological evolution in high energy ionizing radiation environment through time. *Planetary and Space Science*, 72(1), 70–77. <https://doi.org/10.1016/j.pss.2012.04.009>
- Keating, A., Mohammadzadeh, A., Nieminen, P., Maia, D., Coutinho, S., Evans, H., et al. (2005). A model for Mars radiation environment characterization. *IEEE Transactions on Nuclear Science*, 52(6), 2287–2293. <https://doi.org/10.1109/tns.2005.860748>
- Kim, M.-H. Y., Cucinotta, F. A., Nounu, H. N., Zeitlin, C., Hassler, D. M., Rafkin, S. C. R., et al. (2014). The MSL Science Team Comparison of martian surface ionizing radiation measurements from MSL-RAD with Badhwar-O'Neill 2011/HZETRN model calculations. *Journal of Geophysical Research: Planets*, 119(6), 1311–1321. <https://doi.org/10.1002/2013JE004549>
- Kim, M.-H. Y., Thibeault, S. A., Simonsen, L. C., & Wilson, J. W. (1998). Comparison of Martian meteorites and Martian regolith as shield materials for galactic cosmic rays (NASA Langley technical report).
- Léveillé, R. J., & Datta, S. (2010). Lava tubes and basaltic caves as astrobiological targets on Earth and Mars: A review. *Planetary and Space Science*, 58(4), 592–598. <https://doi.org/10.1016/j.pss.2009.06.004>
- Masarik, J., & Reedy, R. C. (1996). Gamma ray production and transport in Mars. *Journal of Geophysical Research: Planets*, 101(E8), 18891–18912. <https://doi.org/10.1029/96je01563>
- Matthiä, D., & Berger, T. (2017). The radiation environment on the surface of Mars—numerical calculations of the galactic component with GEANT4/planetocosmics. *Life Sciences and Space Research*, 14, 57–63. <https://doi.org/10.1016/j.lssr.2017.03.005>

- Matthiä, D., Ehresmann, B., Lohf, H., Köhler, J., Zeitlin, C., Appel, J., et al. (2016). The martian surface radiation environment—a comparison of models and MSL/RAD measurements. *Journal of Space Weather and Space Climate*, 6(27), 1–17. <https://doi.org/10.1051/swsc/2016008>
- Matthiä, D., Hassler, D. M., de Wet, W., Ehresmann, B., Firan, A., Flores-McLaughlin, J., et al. (2017). The radiation environment on the surface of Mars - Summary of model calculations and comparison to RAD data. *Life Sciences and Space Research*, 14, 18–28. <https://doi.org/10.1016/j.lssr.2017.06.003>
- O'Neill, P., Golge, S., & Slaba, T. (2015). *Badhwar–O'Neill 2014 galactic cosmic ray flux model*. (Technical report no. NASA/TP-2015.218569). Retrieved from <https://ntrs.nasa.gov/archive/nasa/casi.ntrs.nasa.gov/20150003026.pdf>
- Potgieter, M. S. (2013). Solar modulation of cosmic rays. *Living Reviews in Solar Physics*, 10(1), 1–66. <https://doi.org/10.12942/lrsp-2013-3>
- Rafkin, S. C., Zeitlin, C., Ehresmann, B., Hassler, D., Guo, J., Köhler, J., et al. (2014). Diurnal variations of energetic particle radiation at the surface of Mars as observed by the Mars Science Laboratory Radiation Assessment Detector. *Journal of Geophysical Research: Planets*, 119, 1345–1358. <https://doi.org/10.1002/2013je004525>
- Richardson, I. G. (2004). Energetic Particles and Corotating Interaction Regions in the Solar Wind. *Space Science Reviews*, 111, 267–376. <https://doi.org/10.1023/B:SPAC.0000032689.52830.3e>
- Röstel, L., Guo, J., Banjac, S., Wimmer-Schweingruber, R. F., & Heber, B. (2020). Subsurface radiation environment of Mars and its implication for shielding protection of future habitats. *Journal of Geophysical Research: Planets*, 125(3), e2019JE006246. <https://doi.org/10.1029/2019JE006246>
- Roussos, E., Dialynas, K., Krupp, N., Kollmann, P., Paranicas, C., Roelof, E. C., et al. (2020). Long- and short-term variability of galactic cosmic-ray radial intensity gradients between 1 and 9.5 au: Observations by cassini, BESS, BESS-polar, PAMELA, and AMS-02. *The Astrophysical Journal*, 904(2), 165. <https://doi.org/10.3847/1538-4357/abc346>
- Saganti, P. B., Cucinotta, F. A., Wilson, J. W., Simonsen, L. C., & Zeitlin, C. (2004). Radiation climate map for analyzing risks to astronauts on the Mars surface from galactic cosmic rays. *Space Science Reviews*, 110(1–2), 143–156. <https://doi.org/10.1023/b:spac.0000021010.20082.1a>
- Simpson, J. (1983). Elemental and isotopic composition of the galactic cosmic rays. *Annual Review of Nuclear and Particle Science*, 33(1), 323–382. <https://doi.org/10.1146/annurev.ns.33.120183.001543>
- Starr, S. O., & Muscatello, A. C. (2020). Mars in situ resource utilization: A review. *Planetary and Space Science*, 182, 104824. <https://doi.org/10.1016/j.pss.2019.104824>
- Walsh, L., Schneider, U., Fogtman, A., Kausch, C., McKenna-Lawlor, S., Narici, L., et al. (2019). Research plans in Europe for radiation health hazard assessment in exploratory space missions. *Life Sciences and Space Research*, 21, 73–82. <https://doi.org/10.1016/j.lssr.2019.04.002>
- Wimmer-Schweingruber, R. F., Köhler, J., Hassler, D. M., Guo, J., Appel, J.-K., Zeitlin, C., et al. (2015). On determining the zenith angle dependence of the martian radiation environment at gale crater altitudes. *Geophysical Research Letters*, 42(24), 10557–10564. <https://doi.org/10.1002/2015gl066664>
- Zeitlin, C., Hassler, D. M., Wimmer-Schweingruber, R. F., Ehresmann, B., Appel, J., Berger, T., et al. (2016). Calibration and characterization of the Radiation Assessment Detector (RAD) on Curiosity. *Space Science Reviews*, 201(1–4), 201–233. <https://doi.org/10.1007/s11214-016-0303-y>

Chapter 5

Summary and Conclusions

The present study comprises two distinct yet interconnected parts aiming to estimate the radiation risk for the human's **CNS** and characterize the Martian radiation environment, including the directional behavior of radiation on the Martian surface. The objective is to evaluate the risk of radiation exposure for astronauts during deep space missions, particularly focusing on a mission to Mars, and develop effective strategies for radiation mitigation.

Prolonged exposure to ionizing radiation in outer space can lead to various health issues, including cancer, cataracts, and radiation sickness. Furthermore, radiation exposure may have a significant impact on the **CNS**, leading to cognitive impairment, memory loss, and other neurobehavioral changes. In the first two publications, paper 4.1 and 4.2 we evaluate the potential risks of radiation exposure to astronauts during a human mission to Mars. Specifically, we examine the effects of radiation on the human brain in deep space. The study employs various models and simulations to evaluate the effects of **GCRs** and **SEPs** on the human brain. In addition, it aims to devise proactive strategies for minimizing potential hazards.

The **CNS**, encompassing the brain and spinal cord, is characterized by its intricate components. Notably, the cerebrum, the largest division of the brain, comprises both the cerebral cortex and sub-cortical structures. The cerebral cortex consists of two hemispheres connected by the corpus callosum, which are further divided into frontal, parietal, temporal, and occipital lobes. While different brain regions work together for cognitive functions, each lobe has specific responsibilities. Therefore, it is crucial to assess the energy deposition in each lobe within the radiation environment during space missions. To address this issue, we used Geant4 Monte Carlo simulations to model an actual human head based on **CT** images and calculated **BRFs** that represent the ready-to-use functions of energy/dose deposit induced by primary particles of protons, helium, neutrons, and heavier ions such as carbon and nitrogen and iron impinging isotropically towards the head to evaluate the impact these particles have on the brain structure. We take into account the most probable interactions of the primary particles with the brain and the generation of secondary particles that can contribute to the extra absorbed dose. Our simulations revealed that the deposited energy and dose for charged particles in the brain increase with incoming

particle energy in the range below 100-150 MeV/nuc, after which they decrease slightly at higher energies. Alternatively, for primary neutrons, the contribution to the dose/energy increases with energy. We derived **BRFs** for dose deposition in different lobes, and these values only show slight differences at low energies (below ~ 100 MeV/nuc) due to the position and geometry of the lobes. Notably, the frontal lobe, with its larger area and less external shielding from the cranium and other lobes, is more exposed to radiation from low-energy primary particles.

The evaluation of shielding effects against charged particles around the human head revealed that thicker shielding materials resulted in a noticeable reduction in the dose rate to the brain, particularly in the case of **SEPs**, where most particles have energies below a few hundred MeV. A 2 cm aluminum shield can provide up to a 90% reduction in SEP dose, offering sufficient protection against acute radiation syndromes for astronauts. However, it is important to consider that the dose from higher-energy particles, particularly those above approximately 500 MeV/nucleon, show a slight increase with thicker shielding, as higher-energy particles are more likely to interact with the shielding material, producing lower-energy secondary particles that can deposit additional energy in the brain.

The shielding approach for mitigating neutron-induced radiation presents challenges. This is because, with enhanced shielding depth, the generation of secondary particles by neutrons with energies higher than 200 MeV becomes more effective. Consequently, this leads to an amplified dose of radiation deposited by neutrons in the brain. This complexity arises in radiation fields where neutrons may be abundant, particularly as they are generated by primary **GCRs** interacting with the local environment, such as on the surface of Mars or within a spacecraft. To accurately assess the appropriate shielding depth, it becomes crucial to properly evaluate both the flux of charged particles and neutrons across the entire energy spectrum. Studies (Köhler et al., 2014; Guo et al., 2017) highlight the significance of accurately assessing the charged and neutron flux for determining the optimal shielding depth in environments where neutrons are prevalent.

The contrasting effects of shielding on charged particles and high-energy neutrons emphasize the significance of comprehensively understanding the energy-dependent radiation field before implementing suitable shielding measures. The appropriateness of shielding requirements varies depending on the specific scenario. For example, during extravehicular activities where charged particles are the primary source of radiation, shielding plays a critical role in ensuring adequate protection. However, in environments with an atmosphere, such as the surface of a planet, i.e., Mars, the radiation field may be rich in neutrons generated by interactions between high-energy particles and the planetary atmosphere and soil. In such cases, the presence of neutrons with energies exceeding approximately 100 MeV introduces a different consideration, where additional shielding might even have counterproductive effects. Therefore, a careful assessment of the radiation field's characteristics is essential for determining the most appropriate shielding strategies in different scenarios.

The results of the dose rate from **GCR**s in deep space under different solar modulations in various lobes of the brain indicate that the difference in dose rates among the lobes is barely noticeable, although it is slightly smaller in the hippocampus region. This is due to the impact of low-energy particles, which can be effectively stopped before reaching the hippocampus. The hippocampus is located in the inner region of the temporal lobe and is relatively more shielded compared to other lobes. The dose rates considered encompass all modeled **GCR** particles in deep space, ranging from approximately 100 to 440 $\mu\text{Gy}/\text{day}$ for solar activity levels between 300 MV (solar minimum) to 1200 MV (solar maximum).

The findings reported in this thesis reveal that the total dose rate from all primary **GCR** particle species decreases as the shielding thickness increases. During a solar minimum, a shielding of 2 mm of Al leads to an overall reduction of approximately 14%. With a shielding of 5 cm of Al, a reduction of 27% is achieved. Further increasing the shielding thickness to 10 cm of Al results in a total reduction of 37%.

Exposure to 0.5 Gy of simulated **GCR** radiation, which consists of a mixture of various particle species, results in long-term defects in the recognition memory system of male mice (Krukowski et al., 2018). Although this does not directly correspond to the brains of humans in space, it can be considered an upper limit of the accumulated **GCR** radiation. From this, we can determine the required shielding depth and permissible duration of a space mission under different solar modulation conditions. Specifically, during solar minimum when the **GCR** flux is at its maximum value, using 2 mm of shielding can reduce **GCR** radiation in the brain to approximately 400 $\mu\text{Gy}/\text{day}$. On the other hand, during solar maximum, the **GCR** radiation in brains is already significantly lower, and while additional shielding is not crucial, it can still be beneficial.

In the case of **SEP** events in deep space, the findings indicate that even a 2 mm thickness of aluminum shielding can reduce the radiation dose to the head by over 50%. Previous studies have considered the **SPeL** for short-term radiation exposure to the **CNS** to be approximately 50 cGy within 30 days. Our results demonstrate that even with 2 cm of aluminum shielding, some events surpass the 30-day **SPeL** in the human head. Thus, it is crucial to forecast **SEP** events and be prepared with additional shielding during such hazardous circumstances (Cucinotta, 2010). Although the differences in dose experienced by the various lobes during **SEP** events are minor, the frontal lobe receives the highest dose due to its larger surface area near the surface of the human brain. In contrast, the hippocampus region, situated deep within the temporal lobe, absorbs a lower dose. The low-energy component of **SEP** events primarily deposits its energy in the outer surface of the brain, predominantly impacting the frontal lobe. However, this issue could be alleviated through a clever helmet design.

We also performed a statistical analysis of the resulting dose versus the properties of the incoming **SEP** events spectra of 50+ historical events. This analysis provides empirical correlations between the radiation dose deposited in different parts of the brain or the human head protected by different thicknesses of shielding and the intensity of the **SEP**

events at the pivot energy of the original SEP spectra. The pivot energy represents the energy at which the dose deposit in the head has the best correlation with the original SEP fluence. That means with a given fluence at this pivot energy, other information of the SEP spectra does not effectively influence the radiation deposit in the brain. These empirical correlations can be directly applied to predict the dose in the brain from the initial SPE-event fluence and minimize the complexity of the forecast while maintaining accuracy as a full Monte Carlo simulation and saving computational power.

The second part of the study published in papers 4.3 and 4.4 also investigates the safety constraints for future human missions to space, specifically on the surface of Mars. The local topographical features on the Martian surface can play a crucial role in surface radiation (Ehresmann et al., 2021; Guo et al., 2021a). Depending on the characteristics of these features, they can either pose health risks to astronauts or provide potential shelter during their missions. To evaluate these effects and gain a deeper understanding of the directionality of radiation on the Martian surface, we employed a Monte Carlo method and compared the resulting data with observations obtained from the RAD measurements. Our objective was to develop a comprehensive model that accurately describes the process of radiation exposure on the Martian surface from different zenith angles, taking into account various solar modulation conditions and particle types.

We specifically focused on establishing dose- θ functions to quantify the radiation exposure as a function of the incident angle. The model's findings suggest that radiation dose on the surface of Mars is nonisotropic, particularly at large zenith angles $\geq 60^\circ$. Within the $\sim 25^\circ$ range of inclination angles experienced by Curiosity, isotropic behavior cannot be excluded at a 95% confidence level. This finding aligns with a previous study by Wimmer-Schweingruber et al. (2015), although their research did not cover such a wide range of inclination angles. The results demonstrate that the surface dose rate depends primarily on solar modulation. A smaller modulation potential leads to a higher dose rate for each θ . With the modulation parameter ranging from 800 to 400 MV, the total dose rate recorded in the B detector of RAD spans from 106 to 175 $\mu\text{Gy}/\text{day}$ for protons, and 27 to 36 $\mu\text{Gy}/\text{day}$ for helium ions.

The summed proton and helium dose is 211 $\mu\text{Gy}/\text{day}$ in the B detector at ϕ of 400 MV (solar minimum). During the deep solar minimum in 2019, the dose rate measured in RAD's silicon detector B was approximately 230 $\mu\text{Gy}/\text{day}$ (Ehresmann et al., 2023; Guo et al., 2021b). The results from our model are slightly lower by about 10% compared to the RAD measurements. Considering that the current model does not account for ions heavier than helium and albedo particles, the model's reported values demonstrate reasonable agreement with the RAD measurements.

We also compare the integrated dose rates obtained from the LET spectra in RAD with the predictions of our model. Since our model includes the θ -dependent dose, it is straightforward to calculate the total dose integrated within the two acceptance cones based on the cone's viewing angle and the rover's inclination. The comparison reveals a difference of

approximately 28% between the **RAD** measurement and our model for both view cones. However, this difference of 28% is significantly higher than the 10% difference observed when considering the modeled and measured dose integrated over all zenith angles, as discussed in the previous section. The most likely explanation for this notable difference is that the contribution from **HZE**s is higher within the acceptance cone. This is due to the shorter average path length through the Martian atmosphere, which results in less fragmentation of heavy ions before they reach **RAD**, compared to directions outside the cone. In addition, secondary albedo particles generated in the Martian soil may also in principle contribute to the measured **LET**-cone dose rate.

As **HZE** ions can have a substantial impact on cellular damage since the energy transferred to a single cell is directly proportional to the square of the particle's charge, concerns regarding radiation induced by **HZE** ions have been prominent in the context of deep space missions to Mars (Cucinotta and Durante, 2006). Our study proposes that the contribution of **HZE** ions could be greater at lower zenith angles for individuals exploring the Martian surface. This implies that additional shielding against radiation is especially crucial when facing the zenith as opposed to the horizon.

By combining the outcomes of our model with the panoramic visibility map obtained from **RAD**, we were able to estimate the obstructed and remaining radiation originating from the sky direction. The analysis revealed that during the parking period that Curiosity was parked close to Butte M12 in the Murray Buttes formation, the ratio of radiation from the sky decreased by approximately 12% due to the obstructing topographical features on the Martian surface, which led to additional albedo radiation. However, this reduction was notably higher than the measured decrease in dose, which was found to be $5 \pm 1\%$ (Ehresmann et al., 2021; Guo et al., 2021a). To accurately determine the flat-terrain albedo dose without any obstruction, we considered the expected dose reduction due to sky blockage and observed dose changes based on two independent scenarios. By comparing the dose rates measured under different sky-obstruction conditions and considering the zenith-angle dependence of radiation, we were able to estimate the contribution of albedo radiation on Mars. Our analysis indicated that the flat-terrain albedo dose accounted for approximately 19% of the total surface dose, which is consistent with previous modeled results (Matthiä et al., 2017; Guo et al., 2018).

This information is crucial for enhancing our understanding of the Martian radiation environment and developing effective strategies to mitigate radiation risks. The methods employed in this study provide a comprehensive understanding of the directionality of Martian surface radiation and its potential implications for astronauts during future human missions to Mars. It emphasizes the importance of taking into account local topographical features on the Martian surface and their impact on radiation exposure when designing and selecting a landing site for astronauts to promptly establish habitats and implement strategies to mitigate radiation. The results emphasize the necessity for additional research and development of efficient radiation shielding and protection measures to guarantee the safety and well-being of astronauts throughout their missions to Mars.

Chapter 6

Outlook

We have analyzed the characteristics of more than 50 historical [SEP](#) event spectra in order to derive easy-to-use functions for calculating the dose deposited in various brain regions and differing aluminum shielding thicknesses. Moving forward, our investigation holds the potential for extension through the utilization of the Solar Energetic Particle Environment Modelling ([SEP-EM](#)) application server provided by the European Space Agency ([ESA](#)). By utilizing this tool, we can do statistical modeling of the cumulative and the worst-case proton fluences at, for example a 90% confidence level for a mission to Mars. Combining modeled [SEP](#) events with historical [SEP](#) data allows us to develop new easy-to-use functions. While we do not anticipate significant deviations from our existing functions, it is still worth to conduct a thorough investigation in this regard. By comparing the modeled and historical data, we can validate the consistency and accuracy of our functions and identify any potential variations or refinements. So, the analysis would benefit from including the probability of astronaut exposure, for example, during a standard 3-year Mars trip (9 months of travel in each direction + 18 months on the surface).

This approach of calculating the radiation doses deposited inside the brain based on the particle type, energy, and shielding is novel and well-defined. This model holds the potential for broader accessibility, possibly in the form of an online tool. This can be done by creating a user interface where different shielding thicknesses, lobes, and radiation qualities, could be used as an input to receive the average dose deposited inside the human brain as an output.

In our zenith-angle dependence radiation model, we did not consider the influence of soil and surface ground. The estimation of albedo radiation was derived by comparing dose rates measured under various sky-obstruction conditions, while also accounting for the zenith-angle dependence of radiation as predicted by our model. To enhance the robustness of our model, we can undertake several improvements. First, we can develop an advanced representation of the Martian surface by accounting for various soil materials and calculating the albedo of upward particles originating from the surface. This would allow us to compare our calculations with existing results and refine our predictions. In addition, we can incorporate the presence of different buttes or surface features into the

model to assess their impact on reducing the radiation dose reaching the **RAD**. Furthermore, we can extend the scope of our simulations to include **HZE** particles, expanding beyond our current focus on protons and ^4He . This broader inclusion would provide a more comprehensive understanding of the radiation environment and its effects on space missions, enhancing the reliability and applicability of our model.

6.1 Space Radiation Environment and Ground-based Experiment Discrepancies

As previously discussed, space radiation poses a significant challenge for human space exploration due to the potential health risks it poses for astronauts, including cancer, cataracts, and cardiovascular disease. Despite numerous years of research, our understanding of the space radiation environment and its potential risks to astronauts during long-duration space missions remains inadequate. The discrepancy between research results and the effects of space radiation on human astronaut crews may be attributed to the complexity of the space radiation environment. This complexity poses a challenge in simulating the environment on Earth and accurately predicting the health risks associated with radiation exposure in space. Moreover, it is challenging to extrapolate clinical outcomes from animal models. A major issue in this regard is the lack of experimental ground-based data on space radiation, mainly due to the difficulty in replicating the full spectrum of space radiation on Earth.

As human space exploration continues to advance, there is an urgent need to improve our understanding of space radiation risk, predict clinical outcomes, and develop effective mitigation strategies. To achieve this, researchers have conducted various initiatives to simulate space radiation exposure on Earth, including the use of ground-based facilities such as particle accelerators and cosmic ray simulators, as well as experiments on high-altitude balloons and aircraft. However, it is important to note that these simulations have limitations and cannot fully replicate the complex radiation environment of space. To gather more data on radiation exposure in space, space agencies such as **NASA** have conducted several studies using radiation detectors on board spacecraft and the **ISS**. These studies have provided valuable data on the radiation environment in space and its effects on human health. In addition, computer models have been developed to simulate radiation exposure in space and its effects on the human body. In our current research, we have developed a model of the human head to calculate the total dose from **GCRs** and **SEPs** in different brain regions, taking into account the effect of aluminum shielding using simulations. These models can help to predict the risks associated with long-duration space missions and guide the development of radiation protection strategies for astronauts. However, a big question remains: how reliable are these data, and how can we validate them based on ground-based experiments, given the limited information available on human exposure to space radiation?

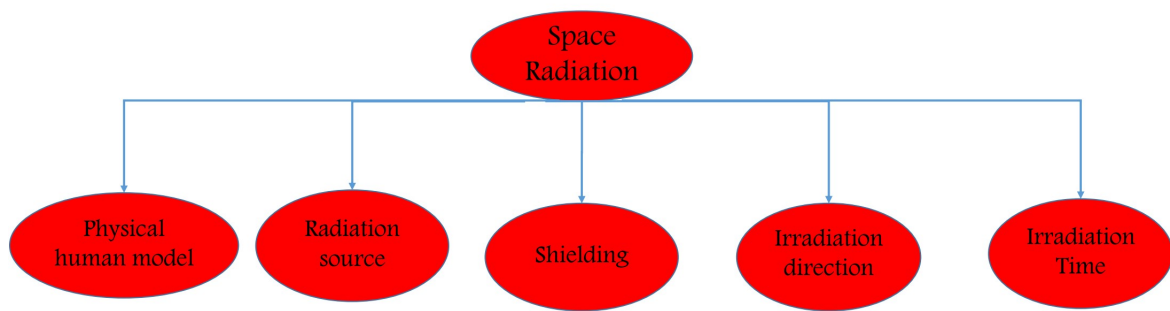


FIGURE 6.1: Factors that can lead to discrepancies between ground-based experiments and actual space radiation exposure

The lack of experimental ground-based data poses a challenge in space exploration, and further research and data collection are needed to fully understand the effects of radiation exposure in space and develop effective radiation protection strategies for astronauts on long-duration missions.

Figure 6.1 represents factors that can lead to discrepancies between ground-based experiments and actual space radiation exposure. Our aim here is to assess the limitations of previous ground-based experiments on the effects of radiation on the human body and identify the various factors that hinder our understanding of the risks of space radiation for human crews. Moreover, we propose feasible solutions to improve our understanding of the impact of radiation on the human body by leveraging innovative technologies in ground-based experiments.

6.1.1 Radiation Environment Types

The radiation environment in space is composed of a complex mixture of ionizing radiation, which includes **SEPs** and **GCRs**. Simulating the effects of this radiation on human phantoms in ground-based experiments is a significant challenge. **SEPs** are mainly high-energy protons emitted from the Sun during solar flares or **CMEs**, while **GCRs** are a form of ionizing radiation comprising a complex mixture of high-energy charged particles that originate beyond the solar system. To accurately simulate the effects of these radiation types, researchers must consider factors such as energy spread, diverse particle types, shielding materials, exposure times, and secondary particles (Axford, 1994; Parizot, 2014; Wijzen et al., 2019; Reames, 2013). Regarding the energy spread, ground-based experiments can utilize particle beams to produce high-energy particle beams with a diverse range of energies by adjusting parameters such as magnetic field strength and acceleration voltage (Davidson and Hong, 2001; Edwards and Syphers, 2008). A passive scattering system is another method to distribute the energy of a high-energy particle beam, which involves placing a moderator block with various thicknesses in front of the particle beam

that scatters the particles, and generates a range of energies (Chen, 2011). By adjusting the thickness and composition of the scattering material, the desired energy spread can be achieved. This system can create secondaries that further simulate the space radiation environment, as space particles also interact with spacecraft and generate secondaries before contributing to the dose in astronauts.

6.1.2 Irradiation Direction and Time

Considering the required irradiation time to replicate the complex mixture of ionizing radiation in ground-based experiments can be challenging. For example, GCRs have a low flux density in space, which means that experiments that aim to replicate the GCR environment on Earth may require long exposure times and large detector surfaces to achieve sufficient statistics. One approach to overcome this challenge is to increase the dose rate of the radiation beam. However, this can be limited by the available accelerator technology and the risk of damage to the sample. Another approach is to use an active beam delivery system that can optimize the dose rate, beam position, and beam angle to reduce the irradiation time while still achieving an accurate simulation of the space radiation environment.

Ground-based experiments aiming to replicate the effects of space radiation must strive to closely replicate the directionality of irradiation encountered in space environments. This fidelity is essential to ensure that the results obtained from such experiments accurately represent the radiation conditions experienced during space missions. One solution is to use gantries in accelerators, which allow the accelerator beam to be directed at a sample from any angle. Gantries provide flexibility to mimic the complex geometries of the GCR and SEP environments in space and can replicate the directional and angular distribution of incident particles with some approximation. The isocentric type of gantry is the most commonly used, in which a patient is placed in a fixed position, and the gantry rotates around them (Weinrich, 2006; Reimoser, 2000). Using an incident beam that can rotate 180° around the patient and a patient table that rotates by 360° in the horizontal plane can deliver a full 4π coverage of irradiation angles. However, many gantries opt for a full 360° of gantry rotation to reduce positioning errors and the need to rotate the patient (Weinrich, 2006; Reimoser, 2000; Lante et al., 2012). Although gantries are complex and expensive equipment that requires careful maintenance and operation, the benefits of using gantries for space radiation studies make them a valuable tool for advancing our understanding of the effects of space radiation on biological tissues and spacecraft materials (Alonso and Antaya, 2012; Lante et al., 2012).

6.1.3 Human Phantoms

A variety of models have been employed to investigate the consequences of radiation exposure on humans during space travel. These models encompass the use of human phantoms, modeling outcomes, and animal models. Computational human phantoms play a

crucial role in accurately modeling patient anatomy and physiology, considering factors like tissue properties, organ geometry, and compatibility with simulation codes (Kainz et al., 2018; Kim, Jeong, and Yeom, 2012). These phantoms are categorized into stylized, voxel, and hybrid models. Stylized phantoms use primitive shapes, voxel phantoms assign labels to 3D voxels based on anatomy and tissue characteristics, and hybrid phantoms combine voxel data with stylized modeling (Griffin et al., 2020; Bolch et al., 2010; Lee et al., 2006). Boundary REPresentation (**BREP**) techniques are valuable for creating realistic computational phantoms that can model anatomical deformations (Kainz et al., 2018; Xu, 2014). While BREP phantoms are not directly compatible with Monte Carlo particle transport codes, Non-Uniform Rational B-Splines (**NURBS**) phantoms (a **BREP** subcategory) can be used after voxelization, which can result in the loss of small tissue structures (Anderson, Kelley, and Goorley, 2012). The **ICRP** has converted voxel phantoms into the tetrahedral mesh geometry format to improve compatibility with Monte Carlo codes, enabling more accurate dosimetry calculations while preserving fine tissue details (Yeom et al., 2014). Furthermore, the use of physical human phantoms has emerged as a promising research avenue for understanding the radiation environment inside the human body and evaluating radiation risks for space travelers in the short and long term. Various anthropomorphic phantoms, such as the USSR Torso, a water-filled spherical, and the Fred phantom, have been employed in different spacecraft studies. A notable illustration of this is the ESA's MATROSHKA project (Reitz and Berger, 2006; Reitz et al., 2009; Semkova et al., 2012), which employs an anthropomorphic phantom, and the MATROSHKA-R spherical phantom experiment (Kartsev et al., 2005; Semkova et al., 2012) initiated in 2004. This innovative endeavor employs tissue-equivalent materials to gauge radiation absorption, dose equivalent, **LET** spectra, and quality factor at various points on the **ISS**. While physical phantoms offer intricate details, yet they fall short in depicting repair mechanisms and biological processes.

Animal models are also frequently utilized in space radiation studies discussed in the section (2.3.1). These models serve as ethical alternatives to human studies and provide data that would be otherwise difficult to obtain. However, it's important to note that animal models have limitations, including anatomical and physiological differences compared to humans, which can restrict their applicability and relevance to human scenarios.

These discrepancies, along with environmental factors contribute to uncertainties in space radiobiology studies, making it challenging to predict clinical outcomes for spaceflight crews. Recognizing these limitations and developing comprehensive physical models that capture the complexity of human response is also essential for accurate predictions and advancing our knowledge in this field.

Advanced manufacturing technologies, such as 3D printing, hold great potential for enhancing the development of physical human phantoms. They enable the creation of highly detailed and precise structures that closely mimic human anatomy. This technology empowers researchers to construct physical phantoms with specific regions or structures that

can be precisely targeted, such as distinct brain lobes. Furthermore, improving the materials used to replicate the body's various tissues and organs can result in more accurate simulations of the body's response to radiation. The utilization of advanced polymers or gels with physical properties akin to human tissue, along with the incorporation of microfluidic channels and sensors, could facilitate more realistic simulations of biological reactions to radiation exposure. Advancements in imaging technologies offer the potential to generate high-resolution images of human anatomy and function, which, in turn, can be employed to create more precise physical human phantoms.

In addition, advanced dosimetry techniques, including gel dosimetry and radiochromic films (Schreiner, 2015; Oldham et al., 2003), provide the capability to measure the dose delivered to specific regions of a phantom with greater precision. Gel dosimetry, a notable technique in this field, utilizes specialized gel materials that undergo changes in optical properties upon exposure to radiation. By analyzing these changes, researchers can determine the distribution of radiation dose within the gel. Similarly, radiochromic films consist of radiation-sensitive materials that change color in response to radiation exposure. By analyzing the color changes on the film, researchers can map out the dose distribution within the phantom, allowing for a detailed evaluation of radiation effects on different regions (Schreiner, 2015; Oldham et al., 2003).

These technologies offer a robust avenue for precisely assessing the dose distribution within the phantom, enabling a comprehensive evaluation of the accuracy and precision of the studied radiation therapy techniques. Utilizing these techniques in ground-based experiments and phantom models holds the potential to explore the implications of space radiation on astronauts, offering valuable insights into radiation exposure during space missions.

6.1.4 Shielding

Ideal shielding scenarios are not practical in space due to the penetration of very high energy primary **GCRs** and the increased biological effectiveness of secondary radiation. However, conventional shielding methods are effective for **SEPs** with limited energies and ranges. Assessing space radiation exposures requires understanding the radiation environment, shielding physics, and a framework for dose and dose equivalent calculations. Space radiation transport codes like OLTARIS can evaluate passive shielding in different environments (Singletary Jr et al., 2011; Gohel and Makwana, 2022). Various methods are used for shielding against space radiation, including active, passive, bulk, water-based, hydrogen-based, composite, and biological shielding. Active shielding employs magnetic or electrostatic fields or plasma bubbles but is not viable for protecting against **GCRs**. Passive shielding uses high-density and low atomic number materials such as aluminum or polyethylene. Water-based shielding surrounds crew and equipment with water tanks.

Hydrogen-based shielding uses hydrogen-rich materials like polyethylene or liquid hydrogen. Composite shielding combines different materials for optimized radiation attenuation (Singleterry Jr et al., 2011; Warden and Bayazitoglu, 2021; Zeitlin, 2021).

Shielding against ionizing radiation necessitates different approaches for charged particles and neutrons. Charged particles, like protons and heavy ions, primarily interact through electromagnetic forces. The effectiveness of shielding against charged particles depends on factors such as the material's atomic number (Z), density, and particle energy. Materials with higher Z values and greater densities, such as lead or tungsten, are particularly adept at mitigating the impact of charged particles by amplifying ionization and dissipating energy. Enhancing protection often involves the use of multi-layer shielding incorporating a variety of Z values and densities to bolster overall defense.

Shielding against neutrons necessitates separate considerations. Neutrons primarily engage via strong nuclear forces and weak interactions. The efficiency of neutron shielding hinges on material composition, density, and hydrogen content. Materials rich in hydrogen, like water or polyethylene, adeptly decelerate and absorb neutrons due to abundant hydrogen nuclei. Neutrons scatter off hydrogen nuclei, lowering their energy and minimizing harm. Effective materials combine heavy elements for inelastic scattering with fast neutrons, light elements as moderators for thermal neutrons via elastic scattering, and high-neutron-absorption boron elements. Neutron shielding relies on substances with mass similar to neutrons, like hydrogen, found in hydrogenous materials such as water, paraffin, and hydrocarbon polymers (Dees, 2017; Fu et al., 2021). Polymer-based composites, due to high hydrogen content, small atomic diameter, and structural adaptability with particles and fibers, are promising for effective neutron attenuation while maintaining mechanical properties (Jumpee, Rattanaplome, and Kumwang, 2020; Dees, 2017; Fu et al., 2021).

Moreover, multi-layered shields combining diverse materials provide potent protection. Recent research underscores the success of combinations like Al + LiH and Al + Liquid Methane in diminishing dose equivalents, with Al + LiH proving most efficient. Hydrogen-rich materials manifest superior unit thickness efficiency in multi-layered shields. Material selection weighs radiation exposure expectations, spacecraft mass, and cost concerns. To ensure adequate protection for astronauts, it may be necessary to combine various materials and configurations (Gohel and Makwana, 2022).

In ground-based experiments, researchers can emulate space shielding effects by employing spacecraft shielding data or modeling simulations to assess astronaut radiation exposure post-shielding implementation. Such experiments yield crucial insights into potential space radiation effects on the human body and enable the evaluation of diverse shielding strategies to alleviate these effects. The insights garnered aid in refining shielding materials and designs for forthcoming space missions, ensuring astronauts' safety during extended space travel (Gohel and Makwana, 2022).

Bibliography

- Abelson, PH and PG Kruger (1949). "Cyclotron-induced radiation cataracts". In: *Science* 110.2868, pp. 655–657. URL: https://www.science.org/doi/pdf/10.1126/science.110.2868.655?casa_token=coJ-S5o8TNMAAAA:nMShIy5d185_escU5cvgICv3bj-UsMJJgMzl89XvstpDnCQF9JwA3L13JDjCNDZrTD-zSW6x4bhNQEO.
- AbuHasan, Qais et al. (2019). "Neuroanatomy, amygdala". In: URL: <https://pubmed.ncbi.nlm.nih.gov/30725787/>.
- Acharya, Munjal M et al. (2019). "New concerns for neurocognitive function during deep space exposures to chronic, low dose-rate, neutron radiation". In: *Eneuro* 6.4. DOI: [10.1523/ENEURO.0094-19.2019](https://doi.org/10.1523/ENEURO.0094-19.2019).
- Adloff, C et al. (2014). "Shower development of particles with momenta from 1 to 10 GeV in the CALICE Scintillator-Tungsten HCAL". In: *Journal of instrumentation* 9.01, P01004. DOI: [10.1088/1748-0221/9/01/P01004](https://doi.org/10.1088/1748-0221/9/01/P01004).
- Afshinnekoo, Ebrahim et al. (2020). "Fundamental biological features of space-flight: advancing the field to enable deep-space exploration". In: *Cell* 183.5, pp. 1162–1184. DOI: <https://doi.org/10.1016/j.cell.2020.10.050>.
- Agostinelli, S. et al. (2003). "GEANT4: A Simulation toolkit". In: *Nucl. Instrum. Meth.* A506, pp. 250–303. DOI: [10.1016/S0168-9002\(03\)01368-8](https://doi.org/10.1016/S0168-9002(03)01368-8).
- Ahlen, SP and K Kinoshita (1982). "Calculation of the stopping power of very-low-velocity magnetic monopoles". In: *Physical Review D* 26.9, p. 2347. DOI: <https://doi.org/10.1103/PhysRevD.26.2347>.
- Ahlen, Steven P (1980). "Theoretical and experimental aspects of the energy loss of relativistic heavily ionizing particles". In: *Reviews of Modern Physics* 52.1, p. 121. DOI: <https://doi.org/10.1103/RevModPhys.52.121>.
- Ahn, HS et al. (2010). "Measurements of the relative abundances of high-energy cosmic-ray nuclei in the TeV/nucleon region". In: *The Astrophysical Journal* 715.2, p. 1400. DOI: [10.1088/0004-637X/715/2/1400](https://doi.org/10.1088/0004-637X/715/2/1400).
- Akhavanallaf, Azadeh et al. (2022). "An update on computational anthropomorphic anatomical models". In: *Digital health* 8, p. 20552076221111941. DOI: <https://doi.org/10.1177/20552076221111941>.
- Aleksandrovskiy, Yuri A and Mikhail A Novikov (1996). "Psychological prophylaxis and treatments for space crews". In: *Space biology and medicine*. 3, pp. 433–443. DOI: <https://doi.org/10.2514/5.9781624104671.0433.0444>.

- Allen, Antiño R et al. (2015). "56Fe irradiation alters spine density and dendritic complexity in the mouse hippocampus". In: *Radiation research* 184.6, pp. 586–594. DOI: <https://doi.org/10.1667/RR14103.1>.
- Allison, J. et al. (2016). "Recent developments in Geant4". In: *Nucl. Instrum. Meth. A* 835, pp. 186–225. DOI: [10.1016/j.nima.2016.06.125](https://doi.org/10.1016/j.nima.2016.06.125).
- Alonso, Jose R and Timothy A Antaya (2012). "Superconductivity in medicine". In: *Reviews of Accelerator Science and Technology* 5, pp. 227–263. DOI: <https://doi.org/10.1142/S1793626812300095>.
- Amato, Elena (2014). "The origin of galactic cosmic rays". In: *International Journal of Modern Physics D* 23.07, p. 1430013. DOI: <https://doi.org/10.1142/S0218271814300134>.
- Andersen, Barbara L. and Hamed H. Tewfik (Apr. 1985). "Psychological Reactions to Radiation Therapy: Reconsideration of the Adaptive Aspects of Anxiety". In: *J Pers Soc Psychol* 48, 1024–1032. DOI: [10.1037//0022-3514.48.4.1024](https://doi.org/10.1037//0022-3514.48.4.1024).
- Anderson, Casey A, Karen C Kelley, and John T Goorley (2012). "Mesh human phantoms with MCNP". In: *LA-UR-12-00139*, (Los Alamos, NM, US: Los Alamos National Laboratory). URL: <https://api.semanticscholar.org/CorpusID:49488500>.
- Androjna, C et al. (2012). "Effects of spaceflight and skeletal unloading on bone fracture healing". In: *Clinical Reviews in Bone and Mineral Metabolism* 10.2, pp. 61–70. DOI: <https://doi.org/10.1007/s12018-011-9080-z>.
- Antonutto, G et al. (2003). "Cardiovascular deconditioning in microgravity: some possible countermeasures". In: *European journal of applied physiology* 90.3-4, pp. 283–291. DOI: <https://doi.org/10.1007/s00421-003-0884-5>.
- Apostolakis, John et al. (2009). "Progress in hadronic physics modelling in Geant4". In: *Journal of Physics: Conference Series*. Vol. 160. 1. IOP Publishing, p. 012073. DOI: [10.1088/1742-6596/160/1/012073](https://doi.org/10.1088/1742-6596/160/1/012073).
- Appel, JK et al. (2018). "Detecting upward directed charged particle fluxes in the Mars Science Laboratory Radiation Assessment Detector". In: *Earth and Space Science* 5.1, pp. 2–18. DOI: <https://doi.org/10.1002/2016EA000240>.
- Arnould, Marcel and Stéphane Goriely (2020). "Astronuclear Physics: A tale of the atomic nuclei in the skies". In: *Progress in Particle and Nuclear Physics* 112, p. 103766. DOI: <https://doi.org/10.1016/j.ppnp.2020.103766>.
- Avdeev, S et al. (2002). "Eye light flashes on the Mir space station". In: *Acta Astronautica* 50.8, pp. 511–525. DOI: [https://doi.org/10.1016/S0094-5765\(01\)00190-4](https://doi.org/10.1016/S0094-5765(01)00190-4).
- Axford, WI (1994). "The origins of high-energy cosmic rays". In: *International Astronomical Union Colloquium*. Vol. 142. Cambridge University Press, pp. 937–944. DOI: <https://doi.org/10.1017/S0252921100078349>.

- Badhwar, Gautam D (2004). "Martian radiation environment experiment (MARIE)". In: *2001 Mars Odyssey*, pp. 131–142. URL: https://link.springer.com/chapter/10.1007/978-0-306-48600-5_4.
- Badhwar, GAUTAM D and PM O'Neill (1996). "Galactic cosmic radiation model and its applications". In: *Advances in Space Research* 17.2, pp. 7–17. DOI: [https://doi.org/10.1016/0273-1177\(95\)00507-B](https://doi.org/10.1016/0273-1177(95)00507-B).
- Badhwar, Gautam D et al. (1994). "An analysis of interplanetary space radiation exposure for various solar cycles". In: *Radiation research* 138.2, pp. 201–208. DOI: <https://doi.org/10.2307/3578590>.
- Badhwar, GD and PM O'Neill (1994). "Long-term modulation of galactic cosmic radiation and its model for space exploration". In: *Advances in Space Research* 14.10, pp. 749–757. DOI: [https://doi.org/10.1016/0273-1177\(94\)90537-1](https://doi.org/10.1016/0273-1177(94)90537-1).
- Barger, Laura K et al. (2014). "Prevalence of sleep deficiency and use of hypnotic drugs in astronauts before, during, and after spaceflight: an observational study". In: *The Lancet Neurology* 13.9, pp. 904–912. DOI: [https://doi.org/10.1016/S1474-4422\(14\)70122-X](https://doi.org/10.1016/S1474-4422(14)70122-X).
- Barratt, Michael R (2019). "Physical and bioenvironmental aspects of human space flight". In: *Principles of clinical medicine for space flight*, pp. 3–37. DOI: [10.1007/978-1-4939-9889-0_1](https://doi.org/10.1007/978-1-4939-9889-0_1).
- Bartsch, Thorsten et al. (2011). "CA1 neurons in the human hippocampus are critical for autobiographical memory, mental time travel, and autonoetic consciousness". In: *Proceedings of the National Academy of Sciences* 108.42, pp. 17562–17567. DOI: <https://doi.org/10.1073/pnas.1110266108>.
- Batmunkh, Munkhbaatar et al. (2019). "Optimized neuron models for estimation of charged particle energy deposition in hippocampus". In: *Physica Medica* 57, pp. 88–94. DOI: <https://doi.org/10.1016/j.ejmp.2019.01.002>.
- Battistoni, G (2016). "NUCLEUS-NUCLEUS INTERACTIONS AND THEIR APPLICATION IN MEDICINE". In: *Frascati Physics Series* 64.2016. URL: <https://inspirehep.net/files/f4956abd2054c55c16810bbefea86436>.
- Bazilevskaya, Galina A et al. (2014). "Solar cycle in the heliosphere and cosmic rays". In: *Space Science Reviews* 186, pp. 409–435. DOI: <https://doi.org/10.1007/s11214-014-0084-0>.
- Beatty, J Kelly et al. (1999). *The new solar system*. Cambridge University Press. URL: <https://www.cambridge.org/de/universitypress/subjects/physics/planetary-systems-and-astrobiology/new-solar-system-4th-edition?format=PB&isbn=9780521645874>.
- Beckman, John Etienne (2021). "Cosmic Rays? Cosmic Particles". In: *Multimes-senger Astronomy*. Springer, pp. 259–283. URL: https://link.springer.com/chapter/10.1007/978-3-030-68372-6_9.

- Bellone, John A et al. (2015). "A single low dose of proton radiation induces long-term behavioral and electrophysiological changes in mice". In: *Radiation research* 184.2, pp. 193–202. DOI: <https://doi.org/10.1667/RR13903.1>.
- Benton, Eric R and EV Benton (2001). "Space radiation dosimetry in low-Earth orbit and beyond". In: *Nuclear Instruments and Methods in Physics Research Section B: Beam Interactions with Materials and Atoms* 184.1-2, pp. 255–294. DOI: [https://doi.org/10.1016/S0168-583X\(01\)00748-0](https://doi.org/10.1016/S0168-583X(01)00748-0).
- Berger, Martin J (1998). "XCOM: photon cross sections database". In: <http://physics.nist.gov/PhysRefData/Xcom/Text/XCOM.html> 8, p. 3587. DOI: <https://dx.doi.org/10.18434/T48G6X>.
- Bhaskaran, Santosh et al. (2009). "Life and gravity". In: *Biophysical Reviews and Letters* 4.04, pp. 299–318. DOI: <https://doi.org/10.1142/S179304800900106X>.
- Biermann, Peter L and Günter Sigl (2001). "Introduction to cosmic rays". In: *Physics and astrophysics of ultra-high-energy cosmic rays*, pp. 1–26. DOI: https://doi.org/10.1007/3-540-45615-5_1.
- Boerma, Marjan et al. (2015). "Space radiation and cardiovascular disease risk". In: *World journal of cardiology* 7.12, p. 882. DOI: [10.4330/wjc.v7.i12.882](https://doi.org/10.4330/wjc.v7.i12.882).
- Boice Jr, John D (2017). "The linear nonthreshold (LNT) model as used in radiation protection: an NCRP update". In: *International journal of radiation biology* 93.10, pp. 1079–1092. DOI: <https://doi.org/10.1080/09553002.2017.1328750>.
- Bolch, Wesley et al. (2010). "Hybrid computational phantoms for medical dose reconstruction". In: *Radiation and environmental biophysics* 49, pp. 155–168. DOI: <https://doi.org/10.1007/s00411-009-0260-x>.
- Braibant, Sylvie, Giorgio Giacomelli, et al. (2011). *Particles and fundamental interactions: an introduction to particle physics*. Springer Science & Business Media. URL: <https://link.springer.com/book/10.1007/978-94-007-4135-5>.
- Braver, Todd S et al. (1997). "A parametric study of prefrontal cortex involvement in human working memory". In: *Neuroimage* 5.1, pp. 49–62. DOI: <https://doi.org/10.1006/nimg.1996.0247>.
- Breckow, Joachim (1993). "Concepts of microdosimetry and their applicability to radiation protection problems in manned space missions". In: *Biological Effects and Physics of Solar and Galactic Cosmic Radiation: Part A*. Springer, pp. 269–281. DOI: [10.1007/978-1-4615-2918-7_24](https://doi.org/10.1007/978-1-4615-2918-7_24).
- Brenner, Alina V et al. (2020). "Radiation risk of central nervous system tumors in the Life Span Study of atomic bomb survivors, 1958–2009". In: *European journal of epidemiology* 35, pp. 591–600. DOI: <https://doi.org/10.1007/s10654-019-00599-y>.

- Britten, Richard A, Laurie L Wellman, and Larry D Sanford (2021). "Progressive increase in the complexity and translatability of rodent testing to assess space-radiation induced cognitive impairment". In: *Neuroscience & Biobehavioral Reviews* 126, pp. 159–174. DOI: <https://doi.org/10.1016/j.neubiorev.2021.01.027>.
- Britten, Richard A et al. (2012). "Low (20 cGy) doses of 1 GeV/u ⁵⁶Fe-particle radiation lead to a persistent reduction in the spatial learning ability of rats". In: *Radiation research* 177.2, pp. 146–151. DOI: <https://doi.org/10.1667/RR2637.1>.
- Britten, Richard A et al. (2016). "Impaired spatial memory performance in adult Wistar rats exposed to low (5–20 cGy) doses of 1 GeV/n ⁵⁶Fe particles". In: *Radiation Research* 185.3, pp. 332–337. DOI: <https://doi.org/10.1667/RR14120.1>.
- Britten, Richard A et al. (2017a). "Changes in the hippocampal proteome associated with spatial memory impairment after exposure to low (20 cGy) doses of 1 GeV/n ⁵⁶Fe radiation". In: *Radiation research* 187.3, pp. 287–297. DOI: <https://doi.org/10.1667/RR14067.1>.
- (2017b). "Spatial memory performance of socially mature wistar rats is impaired after exposure to low (5 cGy) doses of 1 GeV/n ⁴⁸Ti particles". In: *Radiation research* 187.1, pp. 60–65. DOI: <https://doi.org/10.1667/RR14550.1>.
- Buckey, Jay C (2006). *Space physiology*. Oxford University Press, USA. URL: https://books.google.de/books/about/Space_Physiology.html?id=RYnxmAEACAAJ&redir_esc=y.
- Budinger, Thomas F et al. (1971). "Visual phenomena noted by human subjects on exposure to neutrons of energies less than 25 million electron volts". In: *Science* 172.3985, pp. 868–870. DOI: [10.1126/science.172.3985.868](https://doi.org/10.1126/science.172.3985.868).
- (1972). "Visual perception of accelerated nitrogen nuclei interacting with the human retina". In: *Nature* 239.5369, pp. 209–211. DOI: <https://doi.org/10.1038/239209a0>.
- Budinger, Thomas F.others (Sept. 1972). "Visual Perception of Accelerated Nitrogen Nuclei interacting with the Human Retina". In: *Nature* 239.5369, pp. 209–211. DOI: [10.1038/239209a0](https://doi.org/10.1038/239209a0). URL: <https://ui.adsabs.harvard.edu/abs/1972Natur.239..209B>.
- Busza, Wit and Alfred S Goldhaber (1984). "Nuclear stopping power". In: *Physics Letters B* 139.4, pp. 235–238. DOI: [https://doi.org/10.1016/0370-2693\(84\)91070-0](https://doi.org/10.1016/0370-2693(84)91070-0).
- Butt, Yousaf (2009). "Beyond the myth of the supernova-remnant origin of cosmic rays". In: *Nature* 460.7256, pp. 701–704. DOI: <https://doi.org/10.1038/nature08127>.

- Byun, Hwa Kyung et al. (2021). "Physical and biological characteristics of particle therapy for oncologists". In: *Cancer Research and Treatment: Official Journal of Korean Cancer Association* 53.3, pp. 611–620. DOI: <https://doi.org/10.4143/crt.2021.066>.
- Cacao, Eliedonna and Francis A Cucinotta (2019). "Meta-analysis of cognitive performance by novel object recognition after proton and heavy ion exposures". In: *Radiation research* 192.5, pp. 463–472. DOI: <https://doi.org/10.1667/RR15419.1>.
- Cacao, Eliedonna et al. (2016). "Modeling heavy-ion impairment of hippocampal neurogenesis after acute and fractionated irradiation". In: *Radiation research* 186.6, pp. 624–637. DOI: <https://doi.org/10.1667/RR14569.1>.
- Caddy, Becca (2018). *The tech that could keep astronauts happy on their missions to the stars*. URL: <https://www.techradar.com/news/the-tech-that-could-keep-astronauts-happy-on-their-missions-to-the-stars>.
- Cane, HV et al. (1999). "Cosmic ray modulation and the solar magnetic field". In: *Geophysical Research Letters* 26.5, pp. 565–568. DOI: <https://doi.org/10.1029/1999GL900032>.
- Carlsson, Gudrun Alm (1981). "Absorbed dose equations. On the derivation of a general absorbed dose equation and equations valid for different kinds of radiation equilibrium". In: *Radiation research* 85.2, pp. 219–237. DOI: <https://doi.org/10.2307/3575556>.
- Carr, Hannah et al. (2018). "Early effects of ^{16}O radiation on neuronal morphology and cognition in a murine model". In: *Life Sciences in Space Research* 17, pp. 63–73. DOI: <https://doi.org/10.1016/j.lssr.2018.03.001>.
- Carrihill-Knoll, KL et al. (2007). "Amphetamine-induced taste aversion learning in young and old F-344 rats following exposure to ^{56}Fe particles". In: *Age* 29, pp. 69–76. DOI: <https://doi.org/10.1007/s11357-007-9032-1>.
- Catling, David C and James F Kasting (2017). *Atmospheric evolution on inhabited and lifeless worlds*. Cambridge University Press. URL: <https://www.cambridge.org/us/universitypress/subjects/physics/planetary-systems-and-astrobiology/atmospheric-evolution-inhabited-and-lifeless-worlds?format=HB&isbn=9780521844123>.
- Chalupecky, H (1897). "Ueber die Wirkung der Rontgenstrahlen auf das Auge und die Haut". In: *Zentralbl F Prakt Augenh* 21, p. 886. URL: <https://cir.nii.ac.jp/crid/1572261550444335872>.
- Chancellor, Jeffery C. et al. (Sept. 2014). "Space Radiation: The Number One Risk to Astronaut Health beyond Low Earth Orbit ". In: *Life (Basel)* 4, pp. 491–510. DOI: [10.3390/life4030491](https://doi.org/10.3390/life4030491).

- Chancellor, Jeffery C et al. (2014). "Space radiation: the number one risk to astronaut health beyond low earth orbit". In: *Life* 4.3, pp. 491–510. DOI: <https://doi.org/10.3390/life4030491>.
- Chen, Gary (2011). "Designing a Complex Fragmentation Block for Simulating the Galactic Environment by Using a Single Accelerator Beam in PHITS (Practicle and Heavy Ion Transport Code System)". PhD thesis. Texas A & M University. URL: <https://core.ac.uk/download/pdf/147194908.pdf>.
- Cherry, Jonathan D et al. (2012). "Galactic cosmic radiation leads to cognitive impairment and increased $\alpha\beta$ plaque accumulation in a mouse model of Alzheimer's disease". In: *PloS one* 7.12, e53275. DOI: <https://doi.org/10.1371/journal.pone.0053275>.
- Cholis, Ilias et al. (2016). "A predictive analytic model for the solar modulation of cosmic rays". In: *Physical Review D* 93.4, p. 043016. DOI: <https://doi.org/10.1103/PhysRevD.93.043016>.
- Chylack Jr, Leo T et al. (2009). "NASA study of cataract in astronauts (NASCA). Report 1: Cross-sectional study of the relationship of exposure to space radiation and risk of lens opacity". In: *Radiation research* 172.1, pp. 10–20. DOI: <https://doi.org/10.1667/RR1580.1>.
- Chylack Jr, Leo T et al. (2012). "NASCA report 2: Longitudinal study of relationship of exposure to space radiation and risk of lens opacity". In: *Radiation research* 178.1, pp. 25–32. DOI: <https://doi.org/10.1667/RR2876.1>.
- Clément, Gilles (2011). *Fundamentals of space medicine*. Vol. 23. Springer Science & Business Media. URL: <https://link.springer.com/book/10.1007/978-1-4419-9905-4>.
- Clément, Gilles R et al. (2020). "Challenges to the central nervous system during human spaceflight missions to Mars". In: *Journal of neurophysiology* 123.5, pp. 2037–2063. DOI: <https://doi.org/10.1152/jn.00476.2019>.
- Cloutier, Roger J (1981). *Radiation Quantities and Units*. ICRU Report 33: Washington, DC, International Commission on Radiation Units and Measurements, 1980, 25 pp, 8.50. URL: <https://jnm.snmjournals.org/content/22/6/566.3>.
- Cogan, David G et al. (1949). "Atom bomb cataracts". In: *Science* 110.2868, pp. 654–655. DOI: [10.1126/science.110.2868.654](https://doi.org/10.1126/science.110.2868.654).
- Collaboration, Geant (2020). *Guide For Physics Lists*. URL: <https://gentoo.osuosl.org/distfiles/PhysicsListGuide-4.10.7.pdf>.
- Correa, Alfredo A (2018). "Calculating electronic stopping power in materials from first principles". In: *Computational Materials Science* 150, pp. 291–303. DOI: <https://doi.org/10.1016/j.commatsci.2018.03.064>.

- Cousins, Claire et al. (2011). "International commission on radiological protection". In: *ICRP publication 120*, pp. 1–125. URL: [https://www.icrp.org/docs/P111\(Special%20Free%20Release\).pdf](https://www.icrp.org/docs/P111(Special%20Free%20Release).pdf).
- Cucinotta, FA et al. (2001). "Space radiation and cataracts in astronauts". In: *Radiation research* 156.5, pp. 460–466. DOI: [https://doi.org/10.1667/0033-7587\(2001\)156\[0460:SRACIA\]2.0.CO;2](https://doi.org/10.1667/0033-7587(2001)156[0460:SRACIA]2.0.CO;2).
- Cucinotta, Francis A (2002). *Space radiation cancer risk projections for exploration missions: uncertainty reduction and mitigation*. DIANE Publishing. URL: <https://ntrs.nasa.gov/api/citations/20020073167/downloads/20020073167.pdf>.
- (2010). "Radiation risk acceptability and limitations". In: *Space Radiation Program Element*, NASA Johnson Space Center, Houston, TX. URL: <https://three.jsc.nasa.gov/articles/astronautradlimitsfc.pdf>.
- (2015). "Review of NASA approach to space radiation risk assessments for Mars exploration". In: *Health physics* 108.2, pp. 131–142. DOI: [10.1097/HP.0000000000000255](https://doi.org/10.1097/HP.0000000000000255).
- Cucinotta, Francis A and Marco Durante (2006). "Cancer risk from exposure to galactic cosmic rays: implications for space exploration by human beings". In: *The lancet oncology* 7.5, pp. 431–435. DOI: [10.1016/S1470-2045\(06\)70695-7](https://doi.org/10.1016/S1470-2045(06)70695-7).
- (2009). "Risk of radiation carcinogenesis". In: *Human health and performance risks of space exploration missions*. NASA SP-2009-3405. Houston: National Aeronautics and Space Administration, pp. 119–170. URL: https://www.researchgate.net/profile/Francis-Cucinotta-2/publication/266469707_Risk_of_Radiation_Carcinogenesis/links/54b3a8c00cf26833efce9f79/Risk-of-Radiation-Carcinogenesis.pdf.
- Cucinotta, Francis A et al. (2003). "Radiation dosimetry and biophysical models of space radiation effects". In: *Gravitational and Space Biology* 16.2, pp. 11–19. URL: https://www.researchgate.net/publication/10580019_Radiation_dosimetry_and_biophysical_models_of_space_radiation_effects.
- Cucinotta, Francis A et al. (2009). "Risk of acute or late central nervous system effects from radiation exposure". In: *Human health and performance risks of space exploration missions: evidence reviewed by the NASA Human Research Program* 191, p. 212. URL: <https://humanresearchroadmap.nasa.gov/Evidence/reports/CNS.pdf>.
- Cucinotta, Francis A et al. (2013). "How safe is safe enough? Radiation risk for a human mission to Mars". In: *PloS one* 8.10, e74988. DOI: <https://doi.org/10.1371/journal.pone.0074988>.
- Cucinotta, Francis A et al. (2014). "Space radiation risks to the central nervous system". In: *Life sciences in space research* 2, pp. 54–69. DOI: <https://doi.org/10.1016/j.lssr.2014.06.003>.

- Cucinotta, Francis A. et al. (July 2014). "Space radiation risks to the central nervous system". In: *Life Sciences and Space Research* 2, pp. 54–69. DOI: [10.1016/j.lssr.2014.06.003](https://doi.org/10.1016/j.lssr.2014.06.003).
- Cucinotta, Francis A et al. (2015). "Safe days in space with acceptable uncertainty from space radiation exposure". In: *Life sciences in space research* 5, pp. 31–38. DOI: <https://doi.org/10.1016/j.lssr.2015.04.002>.
- Cucinotta, Francis A et al. (2021). "A proposed change to astronaut exposures limits is a giant leap backwards for radiation protection". In: *Life Sciences in Space Research* 31, pp. 59–70. DOI: <https://doi.org/10.1016/j.lssr.2021.07.005>.
- Cushing, G. E. et al. (2007). "THEMIS observes possible cave skylights on Mars". In: *Geophysical Research Letters* 34, p. 17201. DOI: [10.1029/2007GL030709](https://doi.org/10.1029/2007GL030709).
- Czechowski, A et al. (2001). "Anomalous cosmic rays and the generation of energetic neutrals in the region beyond the termination shock". In: *Astronomy & Astrophysics* 368.2, pp. 622–634. DOI: <https://doi.org/10.1051/0004-6361:20010028>.
- Czeisler, Charles A et al. (2009). *Sleep-Wake Actigraphy and Light Exposure During Spaceflight-Long*. Tech. rep. URL: <https://ntrs.nasa.gov/api/citations/20090014819/downloads/20090014819.pdf>.
- Dalla, S et al. (2003). "Properties of high heliolatitude solar energetic particle events and constraints on models of acceleration and propagation". In: *Geophysical Research Letters* 30.19. DOI: <https://doi.org/10.1029/2003GL017139>.
- Davidson, Ronald C and Qin Hong (2001). *Physics of intense charged particle beams in high energy accelerators*. World Scientific. URL: <https://readlink.com/front-book.html?id=11145213>.
- Davies, DM (1993). "Cosmic radiation in Concorde operations and the impact of new ICRP recommendations on commercial aviation". In: *Radiation Protection Dosimetry* 48.1, pp. 121–124. DOI: <https://doi.org/10.1093/oxfordjournals.rpd.a081854>.
- De Angelis, Alessandro (2013). "Spontaneous ionization to subatomic physics: Victor Hess to Peter Higgs". In: *Nuclear Physics B-Proceedings Supplements* 243, pp. 3–11. DOI: <https://doi.org/10.1016/j.nuclphysbps.2013.09.008>.
- Dees, C (2017). *Neutron Radiation Shielding Strategies for Glovebox Applications*. Tech. rep. Idaho National Lab.(INL), Idaho Falls, ID (United States). URL: <https://www.osti.gov/servlets/purl/1401982>.
- Denisova, NA et al. (2002). "Brain signaling and behavioral responses induced by exposure to ⁵⁶Fe-particle radiation". In: *Radiation research* 158.6, pp. 725–734. DOI: [https://doi.org/10.1667/0033-7587\(2002\)158\[0725:BSABRI\]2.0.CO;2](https://doi.org/10.1667/0033-7587(2002)158[0725:BSABRI]2.0.CO;2).
- DenOtter, Tami D. and Johanna Schubert (2022). *Hounsfield Unit*. StatPearls Publishing, Treasure Island (FL). URL: <http://europepmc.org/books/NBK547721>.

- Desai, Prasun N and Philip C Knocke (2007). "Mars exploration rovers entry, descent, and landing trajectory analysis". In: *The Journal of the Astronautical Sciences* 55.3, pp. 311–323. DOI: <https://doi.org/10.1007/BF03256527>.
- Deuker, Lorena et al. (2014). "Human neuroimaging studies on the hippocampal CA3 region—integrating evidence for pattern separation and completion". In: *Frontiers in cellular neuroscience* 8, p. 64. DOI: <https://doi.org/10.3389/fncel.2014.00064>.
- Dietze, G and H-G Menzel (2004). "Dose quantities in radiation protection and their limitations". In: *Radiation protection dosimetry* 112.4, pp. 457–463. DOI: <https://doi.org/10.1093/rpd/nch097>.
- Domingo, V et al. (1995). "The SOHO mission: an overview". In: *Solar Physics* 162, pp. 1–37. DOI: <https://doi.org/10.1007/BF00733425>.
- Donnelly, Elizabeth H et al. (2010). "Acute radiation syndrome: assessment and management". In: *Southern medical journal* 103.6, p. 541. DOI: [10.1097/SMJ.0b013e3181ddd571](https://doi.org/10.1097/SMJ.0b013e3181ddd571).
- Dornhoffer, John et al. (2004). "Stimulation of the semicircular canals via the rotary chair as a means to test pharmacologic countermeasures for space motion sickness". In: *Otology & Neurotology* 25.5, pp. 740–745. URL: https://journals.lww.com/otology-neurotology/Fulltext/2004/09000/Stimulation_of_the_Semicircular_Canals_Via_the.16.aspx.
- Duda, Kevin R et al. (2021). "HUMAN SIDE OF SPACE EXPLORATION AND HABITATION". In: *Handbook of Human Factors and Ergonomics*, pp. 1480–1511. DOI: <https://doi.org/10.1002/9781119636113.ch56>.
- Durante, Marco and Francis A Cucinotta (2011). "Physical basis of radiation protection in space travel". In: *Reviews of modern physics* 83.4, p. 1245. DOI: <https://doi.org/10.1103/RevModPhys.83.1245>.
- Durrani, Saeed A and Richard K Bull (2013). *Solid state nuclear track detection: principles, methods and applications*. Vol. 111. Elsevier. URL: https://books.google.de/books?hl=de&lr=&id=pZY3BQAAQBAJ&oi=fnd&pg=PP1&ots=0Yts7Ll6L6&sig=qzZgsG4b7phAZyDfFa9ynrDx3Rk&redir_esc=y#v=onepage&q&f=false.
- Edwards, Donald A and Michael J Syphers (2008). *An introduction to the physics of high energy accelerators*. John Wiley & Sons. URL: <https://onlinelibrary.wiley.com/doi/book/10.1002/9783527617272>.
- Egami, Takeshi and Simon JL Billinge (2012). *Underneath the Bragg peaks: structural analysis of complex materials*. Newnes. URL: <https://lib.ugent.be/en/catalog/ebk01:1000000000384085>.
- Ehresmann, B et al. (2021). "Natural radiation shielding on Mars measured with the MSL/RAD instrument". In: *Journal of Geophysical Research: Planets* 126.8, e2021JE006851. DOI: <https://doi.org/10.1029/2021JE006851>.

- Ehresmann, B et al. (2023). "The Martian surface radiation environment at solar minimum measured with MSL/RAD". In: *Icarus* 393, p. 115035. DOI: <https://doi.org/10.1016/j.icarus.2022.115035>.
- Ehresmann, Bent et al. (2014). "Charged particle spectra obtained with the Mars Science Laboratory Radiation Assessment Detector (MSL/RAD) on the surface of Mars". In: *Journal of Geophysical Research: Planets* 119.3, pp. 468–479. DOI: <https://doi.org/10.1002/2013JE004547>.
- Eidelman, Simon I and Boris A Shwartz (2021). "Interactions of particles and radiation with matter". In: *Handbook of Particle Detection and Imaging*. Springer, pp. 3–27. DOI: [10.1007/978-3-319-93785-4_1](https://doi.org/10.1007/978-3-319-93785-4_1).
- Ellis, Stephen R (2000). "Collision in space". In: *Ergonomics in Design* 8.1, pp. 4–9. URL: https://journals.sagepub.com/doi/pdf/10.1177/106480460000800102?casa_token=CJ1AZsNkJqQAAAAA:rw_7W4SaDfph-mWOXMOXkHn_H0n3W8utEHJe0FVPXFu7Ews1fgG1D
- Fazio, GG et al. (1970). "Generation of Cherenkov light flashes by cosmic radiation within the eyes of the Apollo astronauts". In: *Nature* 228.5268, pp. 260–264. DOI: <https://doi.org/10.1038/228260a0>.
- Fleck, Bernhard (2005). "The SOHO mission". In: *Coronal Magnetic Energy Releases: Proceedings of the CESRA Workshop Held in Caputh/Potsdam, Germany 16–20 May 1994*. Springer, pp. 233–244. URL: <https://link.springer.com/book/10.1007/978-94-009-0191-9>.
- Folger, Gunter, VN Ivanchenko, and Johannes Peter Wellisch (2004). "The binary cascade: nucleon nuclear reactions". In: *The European Physical Journal A-Hadrons and Nuclei* 21, pp. 407–417. DOI: <https://doi.org/10.1140/epja/i2003-10219-7>.
- Forstner, Johan Freiherr von et al. (2020). "Multipoint observations of ICMEs in the inner heliosphere: Forbush decreases and remote sensing". PhD thesis. URL: https://macau.uni-kiel.de/servlets/MCRFileNodeServlet/macau_derivate_00002202/Johan_Lauritz_Freiherr_von_Forstner.pdf.
- Fremlin, JH (1970). "Cosmic ray flashes". In: *New Scientist* 47, p. 42.
- Friedlander, Michael (2012). "A century of cosmic rays". In: *Nature* 483.7390, pp. 400–401. DOI: <https://doi.org/10.1038/483400a>.
- Fu, Xuelong et al. (2021). "The advancement of neutron shielding materials for the storage of spent nuclear fuel". In: *Science and Technology of Nuclear Installations* 2021, pp. 1–13. DOI: <https://doi.org/10.1155/2021/5541047>.
- Geant4_Collaboration (2017). "Geant4 Physics Reference manual 10.4". In: *Accessible from the GEANT4 web page*. URL: <http://geant4-userdoc.web.cern.ch/geant4-userdoc/UsersGuides/PhysicsListGuide/html/index.html>.

- Geiss, Johannes, G Gloeckler, and R Von Steiger (1995). "Origin of the solar wind from composition data". In: *Space Science Reviews* 72, pp. 49–60. DOI: <https://doi.org/10.1007/BF00768753>.
- Giacalone, Joe et al. (2022). "Anomalous cosmic rays and heliospheric energetic particles". In: *Space Science Reviews* 218.4, p. 22. DOI: <https://doi.org/10.1007/s11214-022-00890-7>.
- Giacometti, Valentina et al. (2017). "Development of a high resolution voxelised head phantom for medical physics applications". In: *Physica Medica* 33, pp. 182–188. DOI: <https://doi.org/10.1016/j.ejmp.2017.01.007>.
- Gieseler, Jan (2018). "Understanding Galactic Cosmic Ray Modulation: Observations and Theory". PhD thesis. URL: https://macau.uni-kiel.de/receive/diss_mods_00022749?lang=en.
- Gleeson, LJ and WI Axford (1968). "Solar modulation of galactic cosmic rays". In: *Astrophysical Journal*, vol. 154, p. 1011. URL: <https://adsabs.harvard.edu/full/1968ApJ...154.1011G>.
- Globus, Noémie and Roger Blandford (2023). "Ultra High Energy Cosmic Ray Source Models: Successes, Challenges and General Predictions". In: *arXiv preprint arXiv:2302.06791*. DOI: <https://doi.org/10.48550/arXiv.2302.06791>.
- Gohel, Ankit and Rajnikant Makwana (2022). "Multi-layered shielding materials for high energy space radiation". In: *Radiation Physics and Chemistry* 197, p. 110131. DOI: <https://doi.org/10.1016/j.radphyschem.2022.110131>.
- Goldhaber, Alfred S and Harry H Heckman (1978). "High energy interactions of nuclei". In: *Annual Review of Nuclear and Particle Science* 28.1, pp. 161–205. URL: <https://www.annualreviews.org/doi/pdf/10.1146/annurev.ns.28.120178.001113>.
- Goodhead, Dudley T (2018). *Track structure and the quality factor for space radiation cancer risk (REID)*. URL: https://three.jsc.nasa.gov/articles/Track_QF_Goodhead.pdf.
- Gopalswamy, N et al. (2020). "Effect of the weakened heliosphere in solar cycle 24 on the properties of coronal mass ejections". In: *Journal of Physics: Conference Series*. Vol. 1620. 1. IOP Publishing, p. 012005. DOI: [10.1088/1742-6596/1620/1/012005](https://doi.org/10.1088/1742-6596/1620/1/012005).
- Gosling, John T (1993). "The solar flare myth". In: *Journal of Geophysical Research: Space Physics* 98.A11, pp. 18937–18949. DOI: <https://doi.org/10.1029/93JA01896>.
- (2014). "The solar wind". In: *Encyclopedia of the solar system*. Elsevier, pp. 261–279. DOI: <https://doi.org/10.1016/B978-0-12-415845-0.00012-8>.

- Grande, PL and G Schiwietz (2004). "Ionization and energy loss beyond perturbation theory". In: *Advances in quantum chemistry* 45, pp. 7–46. DOI: [https://doi.org/10.1016/S0065-3276\(04\)45002-3](https://doi.org/10.1016/S0065-3276(04)45002-3).
- gravity (2022). *How strong is gravity on Mars?* URL: <https://curiokids.net/en/how-strong-is-gravity-on-mars/>.
- Griffin, Keith T et al. (2020). "Stylized versus voxel phantoms: a juxtaposition of organ depth distributions". In: *Physics in Medicine & Biology* 65.6, p. 065007. DOI: [10.1088/1361-6560/ab7686](https://doi.org/10.1088/1361-6560/ab7686).
- Grotzinger, John P et al. (2012). "Mars Science Laboratory mission and science investigation". In: *Space science reviews* 170, pp. 5–56. DOI: <https://doi.org/10.1007/s11214-012-9892-2>.
- Gruppen, Claus (2021). "Historical Introduction to Astroparticle Physics". In: *Neutrinos, Dark Matter and Co. From the Discovery of Cosmic Radiation to the Latest Results in Astroparticle Physics*. Springer, pp. 1–10. URL: https://inis.iaea.org/search/search.aspx?orig_q=RN:51004730.
- Guo, Jingnan, Salman Khaksarighiri, et al. (2021). "Directionality of the Martian Surface Radiation and Derivation of the Upward Albedo Radiation". In: *Geophysical Research Letters* 48.15, e2021GL093912. DOI: <https://doi.org/10.1029/2021GL093912>.
- Guo, Jingnan et al. (2017). "Measurements of the neutral particle spectra on Mars by MSL/RAD from 2015-11-15 to 2016-01-15". In: *Life sciences in space research* 14, pp. 12–17. DOI: <https://doi.org/10.1016/j.lssr.2017.06.001>.
- Guo, Jingnan et al. (2018). "A generalized approach to model the spectra and radiation dose rate of solar particle events on the surface of Mars". In: *The Astronomical Journal* 155.1, p. 49. DOI: [10.3847/1538-3881/aaa085](https://doi.org/10.3847/1538-3881/aaa085).
- Guo, Jingnan et al. (2019). "Implementation and validation of the GEANT4/AtRIS code to model the radiation environment at Mars". In: *Journal of Space Weather and Space Climate* 9.A2. DOI: [10.1051/swsc/2018051](https://doi.org/10.1051/swsc/2018051).
- Guo, Jingnan et al. (2021a). "Directionality of the Martian surface radiation and derivation of the upward albedo radiation". In: *Geophysical Research Letters* 48.15, e2021GL093912. DOI: <https://doi.org/10.1029/2021GL093912>.
- Guo, Jingnan. et al. (2021b). "Radiation environment for future human exploration on the surface of Mars: the current understanding based on MSL/RAD dose measurements". In: *The Astronomy and Astrophysics Review* 29, pp. 1–81. DOI: <https://doi.org/10.1007/s00159-021-00136-5>.
- Gushin, Vadim I et al. (1993). "Soviet psychophysiological investigations of simulated isolation: some results and prospects". In: *Advances in space biology and medicine*. Vol. 3. Elsevier, pp. 5–14. DOI: [https://doi.org/10.1016/S1569-2574\(08\)60093-3](https://doi.org/10.1016/S1569-2574(08)60093-3).

- Hadley, Melissa M et al. (2016). "Exposure to mission-relevant doses of 1 GeV/n ^{48}Ti particles impairs attentional set-shifting performance in retired breeder rats". In: *Radiation Research* 185.1, pp. 13–19. DOI: <https://doi.org/10.1667/RR14086.1>.
- Hale, George E et al. (1919). "The magnetic polarity of sun-spots". In: *Astrophysical Journal*, vol. 49, p. 153. URL: <https://adsabs.harvard.edu/full/1919ApJ...49..153H>.
- Haley, Gwendolen E et al. (2013). "Early effects of whole-body ^{56}Fe irradiation on hippocampal function in C57BL/6J mice". In: *Radiation research* 179.5, pp. 590–596. DOI: <https://doi.org/10.1667/RR2946.1>.
- Hamada, Nobuyuki and Tatsuhiko Sato (2016). "Cataractogenesis following high-LET radiation exposure". In: *Mutation Research/Reviews in Mutation Research* 770, pp. 262–291. DOI: <https://doi.org/10.1016/j.mrrev.2016.08.005>.
- Harrison, JD et al. (2021). "ICRP publication 147: use of dose quantities in radiological protection". In: *Annals of the ICRP* 50.1, pp. 9–82. DOI: <https://doi.org/10.1177/0146645320911864>.
- Hassler, Donald M et al. (2012). "The radiation assessment detector (RAD) investigation". In: *Space science reviews* 170, pp. 503–558. DOI: <https://doi.org/10.1007/s11214-012-9913-1>.
- Heber, B, TR Sanderson, and M Zhang (1999). "Corotating interaction regions". In: *Advances in Space Research* 23.3, pp. 567–579. DOI: [https://doi.org/10.1016/S0273-1177\(99\)80013-1](https://doi.org/10.1016/S0273-1177(99)80013-1).
- Heikkinen, Aatos, Nikita Stepanov, and Johannes Peter Wellisch (2003). "Bertini intra-nuclear cascade implementation in Geant4". In: *arXiv preprint nucl-th/0306008*. DOI: <https://doi.org/10.48550/arXiv.nucl-th/0306008>.
- Hellweg, Christine E et al. (2007). "Getting ready for the manned mission to Mars: the astronauts' risk from space radiation". In: *Naturwissenschaften* 94, pp. 517–526. DOI: <https://doi.org/10.1007/s00114-006-0204-0>.
- Hendee, William R (1993). "History, current status, and trends of radiation protection standards". In: *Medical physics* 20.5, pp. 1303–1314. DOI: <https://doi.org/10.1118/1.597153>.
- Heslet, Lars et al. (2012). "Acute radiation syndrome (ARS)–treatment of the reduced host defense". In: *International journal of general medicine*, pp. 105–115. URL: <https://www.tandfonline.com/doi/abs/10.2147/IJGM.S22177>.
- Hess, Viktor F (1912). "Über Beobachtungen der durchdringenden Strahlung bei sieben Freiballonfahrten". In: *Phys. Zeits.* 13, pp. 1084–1091. URL: <https://cds.cern.ch/record/262750>.

- Hidajat, N et al. (1999). "Relationships between physical dose quantities and patient dose in CT." In: *The British journal of radiology* 72.858, pp. 556–561. DOI: <https://doi.org/10.1259/bjr.72.858.10560337>.
- Hienz, Robert et al. (2010). "Neurobehavioral Effects of Space Radiation on Psychomotor Vigilance Tests". In: *38th COSPAR Scientific Assembly* 38, p. 8. URL: <https://ui.adsabs.harvard.edu/abs/2010cosp...38.3174H/abstract>.
- Higuchi, Yoshinori et al. (2002). "Apolipoprotein E expression and behavioral toxicity of high charge, high energy (HZE) particle radiation". In: *Journal of radiation research* 43.Suppl, S219–S224. DOI: [10.1269/jrr.43.S219](https://doi.org/10.1269/jrr.43.S219).
- Hodgson, Peter Edward (1971). *Nuclear reactions and nuclear structure*. Vol. 426. Clarendon Press Oxford. URL: <https://pdfs.semanticscholar.org/11d9/949b7de78f4b69c5ad5c4e62e4e64e347a68.pdf>.
- Hörandel, Jörg R (2008). "The origin of galactic cosmic rays". In: *Nuclear Instruments and Methods in Physics Research Section A: Accelerators, Spectrometers, Detectors and Associated Equipment* 588.1-2, pp. 181–188. DOI: <https://doi.org/10.1016/j.nima.2008.01.036>.
- Horneck, Gerda et al. (2003). "HUMEX, a study on the survivability and adaptation of humans to long-duration exploratory missions, part I: lunar missions". In: *Advances in space Research* 31.11, pp. 2389–2401. DOI: [https://doi.org/10.1016/S0273-1177\(03\)00568-4](https://doi.org/10.1016/S0273-1177(03)00568-4).
- Horneck, Gerda et al. (2006). "Radiation biology". In: *Fundamentals of Space Biology: Research on Cells, Animals, and Plants in Space*, pp. 291–336. DOI: [10.1007/0-387-37940-1_7](https://doi.org/10.1007/0-387-37940-1_7).
- Hu, S, JE Barzilla, et al. (2020). "Acute radiation risk assessment and mitigation strategies in near future exploration spaceflights". In: *Life Sciences in Space Research* 24, pp. 25–33. DOI: <https://doi.org/10.1016/j.lssr.2019.10.006>.
- Hu, Shaowen et al. (2009). "Modeling the acute health effects of astronauts from exposure to large solar particle events". In: *Health physics* 96.4, pp. 465–476. DOI: [10.1097/01.HP.0000339020.92837.61](https://doi.org/10.1097/01.HP.0000339020.92837.61).
- Hüfner, Jörg (1985). "Heavy fragments produced in proton-nucleus and nucleus-nucleus collisions at relativistic energies". In: *Physics Reports* 125.4, pp. 129–185. DOI: [https://doi.org/10.1016/0370-1573\(85\)90124-3](https://doi.org/10.1016/0370-1573(85)90124-3).
- ICRP (1991). *ICRP publication 60: 1990 recommendations of the international commission on radiological protection*. 60. Elsevier Health Sciences. URL: <https://www.icrp.org/publication.asp?id=icrp%20publication%2060>.
- ICRU (1962). *Radiation quantities and units*. Vol. 84. US Government Printing Office. URL: <https://nvlpubs.nist.gov/nistpubs/Legacy/hb/nbshandbook84.pdf>.

- Ilardo, Melissa and Rasmus Nielsen (2018). "Human adaptation to extreme environmental conditions". In: *Current opinion in genetics & development* 53, pp. 77–82. DOI: <https://doi.org/10.1016/j.gde.2018.07.003>.
- Impey, Soren et al. (2016). "Short-and long-term effects of 56 Fe irradiation on cognition and hippocampal DNA methylation and gene expression". In: *BMC genomics* 17, pp. 1–18. DOI: <https://doi.org/10.1186/s12864-016-3110-7>.
- (2017). "Bi-directional and shared epigenomic signatures following proton and 56Fe irradiation". In: *Scientific reports* 7.1, p. 10227. DOI: <https://doi.org/10.1038/s41598-017-09191-4>.
- Iwase, Satoshi et al. (2020). "Effects of microgravity on human physiology". In: *Beyond LEO-Human Health Issues for Deep Space Exploration*. IntechOpen. URL: <https://www.intechopen.com/chapters/70679>.
- Jaffee, Michael S (2005). "The neurology of aviation, underwater, and space environments". In: *Neurologic clinics* 23.2, pp. 541–552. DOI: <https://doi.org/10.1016/j.ncl.2004.12.009>.
- Jewell, Jessica S et al. (2018). "Exposure to ≤ 15 cGy of 600 MeV/n 56Fe particles impairs rule acquisition but not long-term memory in the attentional set-shifting assay". In: *Radiation Research* 190.6, pp. 565–575. DOI: <https://doi.org/10.1667/RR15085.1>.
- Ji, Wu et al. (2021). "International cooperation: A brief history We've experienced". In: *Journal of Space Weather and Space Climate* 11, p. 27. DOI: <https://doi.org/10.1051/swsc/2021008>.
- Joseph, J. A. et al. (Apr. 1992). "Possible Accelerated Striatal Aging" Induced by 56 Fe Heavy-Particle Irradiation: Implications for Manned Space Flights". In: *Radiation Research* 130.1, p. 88. DOI: [10.2307/3578484](https://doi.org/10.2307/3578484).
- Joseph, JA et al. (1993). "Deficits in the Sensitivity of Striatal Muscarinic Receptors Induced by Heavy-Particle Irradiation: Further" Age-Radiation" Parallels". In: *Radiation research* 135.2, pp. 257–261. DOI: <https://doi.org/10.2307/3578303>.
- Joseph, JA et al. (1998). "CNS effects of heavy particle irradiation in space: behavioral implications". In: *Advances in Space Research* 22.2, pp. 209–216. DOI: [https://doi.org/10.1016/S0273-1177\(98\)80012-4](https://doi.org/10.1016/S0273-1177(98)80012-4).
- Jumpee, Chayanit, Tithinun Rattanaplome, and Natthaporn Kumwang (2020). "A wide energy range neutron shielding material based on natural rubber and boron". In: *IOP Conference Series: Materials Science and Engineering*. Vol. 773. 1. IOP Publishing, p. 012036. DOI: [10.1088/1757-899X/773/1/012036](https://doi.org/10.1088/1757-899X/773/1/012036).
- Kahler, SW (1992). "Solar flares and coronal mass ejections". In: *Annual review of astronomy and astrophysics* 30.1, pp. 113–141. DOI: <https://doi.org/10.1146/annurev.aa.30.090192.000553>.

- Kainz, Wolfgang et al. (2018). "Advances in computational human phantoms and their applications in biomedical engineering—a topical review". In: *IEEE transactions on radiation and plasma medical sciences* 3.1, pp. 1–23. DOI: <https://doi.org/10.1109/TRPMS.2018.2883437>.
- Kallenrode, May-Britt (2004). *Space physics: an introduction to plasmas and particles in the heliosphere and magnetospheres*. Springer Science & Business Media. URL: <https://link.springer.com/book/10.1007/978-3-662-04443-8>.
- Kamal, Anwar (2014). "Passage of Charged Particles Through Matter". In: *Nuclear Physics*, pp. 1–81. URL: https://link.springer.com/chapter/10.1007/978-3-642-38655-8_1.
- Kamiya, Kenji et al. (2015). "Long-term effects of radiation exposure on health". In: *The lancet* 386.9992, pp. 469–478. DOI: [https://doi.org/10.1016/S0140-6736\(15\)61167-9](https://doi.org/10.1016/S0140-6736(15)61167-9).
- Kanas, N (1998). "Psychiatric issues affecting long duration space missions." In: *Aviation, space, and environmental medicine* 69.12, pp. 1211–1216. URL: <https://europepmc.org/article/med/9856550>.
- Kanas, Nick (1990). "Psychological, psychiatric, and interpersonal aspects of long-duration space missions". In: *Journal of spacecraft and rockets* 27.5, pp. 457–463. DOI: [10.2514/3.26165](https://doi.org/10.2514/3.26165).
- (2015). "Humans in space". In: *New York*. URL: <https://link.springer.com/book/10.1007/978-3-319-18869-0>.
- Kanas, Nick and Dietrich Manzey (2008). *Space psychology and psychiatry*. Vol. 16. Springer. URL: <https://link.springer.com/book/10.1007/978-1-4020-6770-9>.
- Kandasamy, Sathasiva B et al. (1994). "Exposure to heavy charged particles affects thermoregulation in rats". In: *Radiation research* 139.3, pp. 352–356. DOI: <https://doi.org/10.2307/3578833>.
- Kartsev, IS et al. (2005). "Spherical phantom for research of radiation situation in outer space. Design-structural special features". In: *Yadernye Izmeritel'no-Informatsionnye Tekhnologii*, pp. 36–45. URL: https://inis.iaea.org/search/search.aspx?orig_q=RN:37070175.
- Kasaboski, D and H Hill (2014). "Galactic Cosmic Radiation Risk in Human Space Missions". In: *65th International Astronautical Congress. Toronto, Canada: International Astronautical Federation*. URL: https://www.researchgate.net/profile/Dallas-Kasaboski/publication/273988604_Galactic_cosmic_radiation_risk_in_human_space_missions/links/5511a2c90cf268a4aae84a48/Galactic-cosmic-radiation-risk-in-human-space-missions.pdf.
- Kase, Kenneth R (2004). "Radiation protection principles of NCRP". In: *Health physics* 87.3, pp. 251–257. DOI: [10.1097/00004032-200409000-00005](https://doi.org/10.1097/00004032-200409000-00005).

- Kennedy, Ann R (2014). "Biological effects of space radiation and development of effective countermeasures". In: *Life sciences in space research* 1, pp. 10–43. DOI: <https://doi.org/10.1016/j.lssr.2014.02.004>.
- Kerr, George D (1988). "Quality factors". In: *Health Physics* 55.2, pp. 241–249. DOI: [10.1097/00004032-198808000-00016](https://doi.org/10.1097/00004032-198808000-00016).
- Khaksarighiri, Salman et al. (2020). "Calculation of dose distribution in a realistic brain structure and the indication of space radiation influence on human brains". In: *Life Sciences in Space Research* 27, pp. 33–48. DOI: <https://doi.org/10.1016/j.lssr.2020.07.003>.
- Khaksarighiri, Salman et al. (2021). "An easy-to-use function to assess deep space radiation in human brains". In: *Scientific reports* 11.1, p. 11687. DOI: <https://doi.org/10.1038/s41598-021-90695-5>.
- Khaksarighiri, Salman et al. (2023). "The zenith-angle dependence of the downward radiation dose rate on the Martian surface: Modeling versus MSL/RAD measurement". In: *Journal of Geophysical Research: Planets*, e2022JE007644. DOI: <https://doi.org/10.1029/2022JE007644>.
- Kiffer, Frederico et al. (2018). "Late effects of 1H irradiation on hippocampal physiology". In: *Life sciences in space research* 17, pp. 51–62. DOI: <https://doi.org/10.1016/j.lssr.2018.03.004>.
- Kiffer, Frederico et al. (2019a). "Behavioral effects of space radiation: A comprehensive review of animal studies". In: *Life sciences in space research* 21, pp. 1–21. DOI: <https://doi.org/10.1016/j.lssr.2019.02.004>.
- (2019b). "Late effects of 16O-particle radiation on female social and cognitive behavior and hippocampal physiology". In: *Radiation research* 191.3, pp. 278–294. DOI: <https://doi.org/10.1667/RR15092.1>.
- Kikinis, Ron et al. (2013). "3D Slicer: a platform for subject-specific image analysis, visualization, and clinical support". In: *Intraoperative imaging and image-guided therapy*. Springer, pp. 277–289. DOI: [10.1007/978-1-4614-7657-3_19](https://doi.org/10.1007/978-1-4614-7657-3_19).
- Kim, Chan Hyeong, Jong Hwi Jeong, and Yeon Soo Yeom (2012). "Recent advances in computational human phantom for Monte Carlo dose calculation". In: *Progress in nuclear science and technology* 3, pp. 7–10. DOI: [http://dx.doi.org/10.15669/pnst.3.7](https://doi.org/10.15669/pnst.3.7).
- Kim, Myung-Hee Y et al. (2015). "Issues for simulation of galactic cosmic ray exposures for radiobiological research at ground-based accelerators". In: *Frontiers in oncology* 5, p. 122. DOI: <https://doi.org/10.3389/fonc.2015.00122>.
- Kim, Sang-Tae (2012). "Geant4-DICOM Interface-based Monte Carlo Simulation to Assess Dose Distributions inside the Human Body during X-Ray Irradiation". In: *International Journal of Contents* 8.2, pp. 52–59. URL: <https://citeseerx.ist.psu.edu/document?repid=rep1&type=pdf&doi=b3c10760445fce42fa89c8dabb091d9204aec3b7>

- Kimura, A et al. (2004). "DICOM data handling for Geant4-based medical physics application". In: *IEEE Symposium Conference Record Nuclear Science 2004*. Vol. 4. IEEE, pp. 2124–2127. DOI: [10.1109/NSSMIC.2004.1462682](https://doi.org/10.1109/NSSMIC.2004.1462682).
- Kimura, A et al. (2005). "DICOM interface and visualization tool for Geant4-based dose calculation". In: *IEEE Nuclear Science Symposium Conference Record, 2005*. Vol. 2. IEEE, pp. 981–984. DOI: [10.1109/NSSMIC.2005.1596418](https://doi.org/10.1109/NSSMIC.2005.1596418).
- Kleiman, Norman J (2012). "Radiation cataract". In: *Annals of the ICRP* 41.3-4, pp. 80–97. DOI: <https://doi.org/10.1016/j.icrp.2012.06.018>.
- Köhler, J et al. (2011). "Inversion of neutron/gamma spectra from scintillator measurements". In: *Nuclear Instruments and Methods in Physics Research Section B: Beam Interactions with Materials and Atoms* 269.22, pp. 2641–2648. DOI: <https://doi.org/10.1016/j.nimb.2011.07.021>.
- Köhler, Jan et al. (2014). "Measurements of the neutron spectrum on the Martian surface with MSL/RAD". In: *Journal of Geophysical Research: Planets* 119.3, pp. 594–603. DOI: <https://doi.org/10.1002/2013JE004539>.
- Koizuka, Izumi and Isao Kato (1999). "Space motion sickness and spatial orientation of vestibulo-ocular reflex". In: *Equilibrium Research* 58.1, pp. 9–20. DOI: <https://doi.org/10.3757/jser.58.9>.
- Kouloumvakos, A et al. (2023). "The effect of shock wave properties on the release timings of solar energetic particles". In: *Astronomy & Astrophysics* 669, A58. DOI: <https://doi.org/10.1051/0004-6361/202244363>.
- Krukowski, Karen et al. (2018). "Female mice are protected from space radiation-induced maladaptive responses". In: *Brain, behavior, and immunity* 74, pp. 106–120. DOI: <https://doi.org/10.1016/j.bbi.2018.08.008>.
- Kudlak, Megan et al. (2022). "Physiology, muscarinic receptor". In: *StatPearls [Internet]*. StatPearls Publishing. URL: <https://www.ncbi.nlm.nih.gov/books/NBK555909/>.
- Kuznetsov, VD et al. (2015). "Yakov Alpert: Sputnik-1 and the first satellite ionospheric experiment". In: *Advances in Space Research* 55.12, pp. 2833–2839. DOI: <https://doi.org/10.1016/j.asr.2015.02.033>.
- Lante, V et al. (2012). "Conceptual design for a carbon ion gantry–ULICE". In: *D. JRA6* 3. DOI: [10.13140/2.1.1930.1445](https://doi.org/10.13140/2.1.1930.1445).
- Launius, Roger D (1994). "NASA: A history of the US civil space program". In: *NASA: a history of the US civil space program/Roger D. Launius*. Malabar. URL: <https://doi.org/10.2307/3377902>.
- Lechner, Anton (2018). "CERN: Particle interactions with matter". In: *CERN Yellow Rep. School Proc.* 5, p. 47. DOI: [10.23730/CYRSP-2018-005.47](https://doi.org/10.23730/CYRSP-2018-005.47).

- Lee, Andrew G et al. (2018). "Space flight-associated neuro-ocular syndrome (SANS)". In: *Eye* 32.7, pp. 1164–1167. DOI: <https://doi.org/10.1038/s41433-018-0070-y>.
- Lee, Choonik et al. (2006). "Whole-body voxel phantoms of paediatric patients—UF Series B". In: *Physics in Medicine & Biology* 51.18, p. 4649. DOI: [10.1088/0031-9155/51/18/013](https://doi.org/10.1088/0031-9155/51/18/013).
- Lee, Sang-Hun et al. (2017). "Neurophysiology of space travel: energetic solar particles cause cell type-specific plasticity of neurotransmission". In: *Brain Structure and Function* 222, pp. 2345–2357. DOI: <https://doi.org/10.1007/s00429-016-1345-3>.
- Leo, William R (1988). "Techniques for nuclear and particle physics experiments". In: *Nucl Instrum Methods Phys Res* 834, p. 290. URL: https://inis.iaea.org/search/search.aspx?orig_q=RN:19033249.
- (2012). *Techniques for nuclear and particle physics experiments: a how-to approach*. Springer Science & Business Media. URL: <https://link.springer.com/book/10.1007/978-3-642-57920-2>.
- Leroy, Claude and Pier-Giorgio Rancoita (2011). *Principles of radiation interaction in matter and detection*. World Scientific. URL: https://cds.cern.ch/record/813695/files/9812389091_T0C.pdf.
- Léveillé, Richard J. and Saugata Datta (Mar. 2010). "Lava tubes and basaltic caves as astrobiological targets on Earth and Mars: A review". In: *Planetary and Space Science* 58.4, pp. 592–598. DOI: [10.1016/j.pss.2009.06.004](https://doi.org/10.1016/j.pss.2009.06.004).
- Liu, Zhexing et al. (2010). "Quality control of diffusion weighted images". In: *Medical Imaging 2010: Advanced PACS-based Imaging Informatics and Therapeutic Applications*. Vol. 7628. SPIE, pp. 137–145. DOI: <https://doi.org/10.1117/12.844748>.
- Lobascio, Cesare et al. (2018). "PERSEO: personal radiation shielding in space, a multifunctional approach". In: 48th International Conference on Environmental Systems. URL: <https://ttu-ir.tdl.org/handle/2346/74180>.
- Lonart, György et al. (2012). "Executive function in rats is impaired by low (20 cGy) doses of 1 GeV/u 56Fe particles". In: *Radiation research* 178.4, pp. 289–294. DOI: <https://doi.org/10.1667/RR2862.1>.
- Luo, Jing and Kazuhisa Niki (2003). "Function of hippocampus in "insight" of problem solving". In: *Hippocampus* 13.3, pp. 316–323. DOI: <https://doi.org/10.1002/hipo.10069>.
- Malandraki, Olga E and Norma B Crosby (2018). "Solar energetic particles and space weather: Science and applications". In: *Solar particle radiation storms forecasting and analysis: the HESPERIA HORIZON 2020 project and beyond*, pp. 1–26. URL: <https://library.oapen.org/bitstream/handle/20.500.12657/27952/1/1002047.pdf#page=15>.

- Manda, Kailash, Megumi Ueno, and Kazunori Anzai (2007). "AFMK, a melatonin metabolite, attenuates X-ray-induced oxidative damage to DNA, proteins and lipids in mice". In: *Journal of pineal research* 42.4, pp. 386–393. DOI: <https://doi.org/10.1111/j.1600-079X.2007.00432.x>.
- Marov, Mikhail Ya (2015). "The Sun and Heliosphere". In: *The Fundamentals of Modern Astrophysics: A Survey of the Cosmos from the Home Planet to Space Frontiers*, pp. 157–175. URL: https://link.springer.com/chapter/10.1007/978-1-4614-8730-2_5.
- Mase, Robert A (2005). "Introduction: 2001 Mars Odyssey Mission". In: *Journal of Spacecraft and Rockets* 42.3, pp. 385–385. DOI: <https://doi.org/10.2514/1.17749>.
- Matthiä, Daniel et al. (2016). "The Martian surface radiation environment—a comparison of models and MSL/RAD measurements". In: *Journal of Space Weather and Space Climate* 6.27, pp. 1–17. DOI: <https://doi.org/10.1051/swsc/2016008>.
- Matthiä, Daniel et al. (2017). "The radiation environment on the surface of Mars—Summary of model calculations and comparison to RAD data". In: *Life sciences in space research* 14, pp. 18–28. DOI: <https://doi.org/10.1016/j.lssr.2017.06.003>.
- McAulay, IR (1971). "Cosmic ray flashes in the eye". In: *Nature* 232.5310, pp. 421–422. DOI: <https://doi.org/10.1038/232421a0>.
- McDonald, Frank Bethune and George H Ludwig (1964). "Measurement of low-energy primary cosmic-ray protons on IMP-1 satellite". In: *Physical Review Letters* 13.26, p. 783. DOI: <https://doi.org/10.1103/PhysRevLett.13.783>.
- McGill, Natalie et al. (2016). "Crew Radiation Exposure Estimates from GCR and SPE Environments During a Hypothetical Mars Mission". In: 46th International Conference on Environmental Systems. URL: <https://ttu-ir.tdl.org/handle/2346/67500>.
- McKenna-Lawlor, Susan et al. (2014). "Feasibility study of astronaut standardized career dose limits in LEO and the outlook for BLEO". In: *Acta Astronautica* 104.2, pp. 565–573. DOI: <https://doi.org/10.1016/j.actaastro.2014.07.011>.
- Meier, Matthias M et al. (2020). "Radiation in the atmosphere—A hazard to aviation safety?" In: *Atmosphere* 11.12, p. 1358. DOI: <https://doi.org/10.3390/atmos11121358>.
- Menzel, Hans-Georg (2014). "International commission on radiation units and measurements". In: *Journal of the ICRU* 14.2, pp. 1–2. DOI: [10.1093/jicru/ndx006](https://doi.org/10.1093/jicru/ndx006).
- Messina, G et al. (1988). "Radiation-matter interaction in the space translation method". In: *Il Nuovo Cimento D* 10, pp. 901–914. DOI: <https://doi.org/10.1007/BF02450193>.

- Mewaldt, RA (1994). "Galactic cosmic ray composition and energy spectra". In: *Advances in Space Research* 14.10, pp. 737–747. DOI: [https://doi.org/10.1016/0273-1177\(94\)90536-3](https://doi.org/10.1016/0273-1177(94)90536-3).
- Mewaldt, RA et al. (2001). "Long-term fluences of energetic particles in the heliosphere". In: *AIP Conference proceedings*. Vol. 598. 1. American Institute of Physics, pp. 165–170. DOI: <https://doi.org/10.1063/1.1433995>.
- Mildenberger, Peter et al. (2002). "Introduction to the DICOM standard". In: *European radiology* 12, pp. 920–927. DOI: <https://doi.org/10.1007/s003300101100>.
- Moore, Steven T et al. (2019). "Long-duration spaceflight adversely affects post-landing operator proficiency". In: *Scientific reports* 9.1, pp. 1–14. DOI: <https://doi.org/10.1038/s41598-019-39058-9>.
- Morgan Jr, SH and PB Eby (1973). "Corrections to the Bethe-Bloch formula for average ionization energy loss of relativistic heavy nuclei Close collisions". In: *Nuclear Instruments and Methods* 106.3, pp. 429–435. DOI: [https://doi.org/10.1016/0029-554X\(73\)90303-0](https://doi.org/10.1016/0029-554X(73)90303-0).
- Morphew, Ephimia (2001). "Psychological and human factors in long duration spaceflight". In: *McGill Journal of Medicine* 6.1. DOI: <https://doi.org/10.26443/mjmm.v6i1.555>.
- Morris, Nathaniel P (2014). "Mental health in outer space". In: *Scientific American*. <https://blogs.scientificamerican.com/guest-blog/mental-health-in-outer-space>. URL: <https://blogs.scientificamerican.com/guest-blog/mental-health-in-outer-space/>.
- Mrigakshi, Alankrita Isha (2013). "Galactic Cosmic Ray Exposure of Humans in Space". PhD thesis. Kiel University Kiel. URL: https://macau.uni-kiel.de/receive/diss_mods_00014489?lang=en.
- Mullan, DJ (1984). "Corotating interaction regions in stellar winds". In: *Astrophysical Journal, Part 1 (ISSN 0004-637X)*, vol. 283, Aug. 1, 1984, p. 303–312. 283, pp. 303–312. DOI: [10.1086/162307](https://doi.org/10.1086/162307).
- Nahum, Alan (2021). "Interactions of charged particles with matter". In: *Handbook of Radiotherapy Physics*. CRC Press, Vol1–25. URL: <https://www.taylorfrancis.com/chapters/edit/10.1201/9780429201493-4/interactions-charged-particles-matter-alan-nahum>.
- Narici, L. (July 2008). "Heavy ions light flashes and brain functions: recent observations at accelerators and in spaceflight". In: *New Journal of Physics* 10.7, 075010, p. 075010. DOI: [10.1088/1367-2630/10/7/075010](https://doi.org/10.1088/1367-2630/10/7/075010).
- Nelson, Gregory A, Lisa Simonsen, and Janice L Huff (2016). *Evidence report: risk of acute and late central nervous system effects from radiation exposure*. Tech. rep. URL: <https://ntrs.nasa.gov/citations/20160004368>.

- Ness, Norman F (1996). "Pioneering the swinging 1960s into the 1970s and 1980s". In: *Journal of Geophysical Research: Space Physics* 101.A5, pp. 10497–10509. DOI: <https://doi.org/10.1029/96JA00138>.
- Neufeld, Esra et al. (2018). "Functionalized anatomical models for computational life sciences". In: *Frontiers in physiology* 9, p. 1594. DOI: <https://doi.org/10.3389/fphys.2018.01594>.
- Nikjoo, Hooshang et al. (2012). *Interaction of radiation with matter*. CRC press. DOI: <https://doi.org/10.1201/b12109>.
- Nymmik, R (2015). "Database of Solar Energetic Particles (SEP) fluences, measured from August 1997 till 2006". In: URL: <http://smdc.sinp.msu.ru/index.py?nav=model-sep>.
- Oldham, Mark et al. (2003). "Optical-CT gel-dosimetry I: Basic investigations". In: *Medical physics* 30.4, pp. 623–634. DOI: <https://doi.org/10.1118/1.1559835>.
- O'Neill, Patrick M (2010). "Badhwar–O'Neill 2010 galactic cosmic ray flux model—Revised". In: *IEEE Transactions on Nuclear Science* 57.6, pp. 3148–3153. DOI: [10.1109/TNS.2010.2083688](https://doi.org/10.1109/TNS.2010.2083688).
- O'Neill, PM et al. (2015). *Badhwar–O'Neill 2014 galactic cosmic ray flux model description*. Tech. rep. URL: <https://ntrs.nasa.gov/citations/20150003026>.
- Opitz, Bertram (2014). "Memory function and the hippocampus". In: *The hippocampus in clinical neuroscience* 34, pp. 51–59. DOI: <https://doi.org/10.1159/000356422>.
- Osborne, W Zachary et al. (1975). "Apollo light flash investigations". In: *Biomedical results of Apollo 368*, p. 355. URL: <https://ntrs.nasa.gov/citations/19760005597>.
- OTAKE, M. (1998). "Review: Radiation-related brain damage and growth retardation among the prenatally exposed atomic bomb survivors". In: *International Journal of Radiation Biology* 74.2, pp. 159–171. DOI: [10.1080/095530098141555](https://doi.org/10.1080/095530098141555).
- Pacheco Mateo, Daniel (2019). "Analysis and modelling of the solar energetic particle radiation environment in the inner heliosphere in preparation for solar orbiter". In: *Universitat de Barcelona*. URL: <https://diposit.ub.edu/dspace/handle/2445/134743>.
- Page, Lou Williams et al. (1977). *Apollo-Soyuz Pamphlet [s]: General science*. 9. National Aeronautics and Space Administration. URL: <https://ntrs.nasa.gov/api/citations/19780019211/downloads/19780019211.pdf>.
- Palinkas, Lawrence A (2007). "Psychosocial issues in long-term space flight: overview". In: *Gravitational and Space Research* 14.2. DOI: <https://citeseerx.ist.psu.edu/document?repid=rep1&type=pdf&doi=4a051c73f4e1282c94906e25c95e3b6528abd2ef>.

- Papadopoulos, Alexis et al. (2023). "Space radiation quality factor for Galactic Cosmic Rays and typical space mission scenarios using a microdosimetric approach". In: *Radiation and Environmental Biophysics*, pp. 1–14. DOI: <https://doi.org/10.1007/s00411-023-01023-6>.
- Parihar, V. K. et al. (May 2015). "What happens to your brain on the way to Mars". In: *Science Advances* 1.4, e1400256–e1400256. DOI: [10.1126/sciadv.1400256](https://doi.org/10.1126/sciadv.1400256).
- Parihar, Vipin K et al. (2015a). "Targeted overexpression of mitochondrial catalase prevents radiation-induced cognitive dysfunction". In: *Antioxidants & redox signaling* 22.1, pp. 78–91. DOI: <https://doi.org/10.1089/ars.2014.5929>.
- (2015b). "What happens to your brain on the way to Mars". In: *Science advances* 1.4, e1400256. DOI: [10.1126/sciadv.1400256](https://doi.org/10.1126/sciadv.1400256).
- Parihar, Vipin K. et al. (Oct. 2016). "Cosmic radiation exposure and persistent cognitive dysfunction". In: *Scientific Reports* 6, 34774, p. 34774. DOI: [10.1038/srep34774](https://doi.org/10.1038/srep34774).
- Parihar, Vipin K et al. (2016). "Cosmic radiation exposure and persistent cognitive dysfunction". In: *Scientific reports* 6.1, pp. 1–14. DOI: [10.1038/srep34774](https://doi.org/10.1038/srep34774).
- Paris, Antonio (2014). "Physiological and psychological aspects of sending humans to Mars: Challenges and recommendations". In: *Journal of the Washington Academy of Sciences* 100.4, pp. 3–20. URL: <https://www.jstor.org/stable/10.2307/jwashacadscie.100.4.0003>.
- Parizot, Etienne (2014). "Cosmic ray origin: lessons from ultra-high-energy cosmic rays and the Galactic/extragalactic transition". In: *Nuclear Physics B-Proceedings Supplements* 256, pp. 197–212. DOI: <https://doi.org/10.1016/j.nuclphysbps.2014.10.023>.
- Park, Seo Hyun and Jin Oh Kang (2011). "Basics of particle therapy I: physics". In: *Radiation oncology journal* 29.3, p. 135. DOI: [10.3857/roj.2011.29.3.135](https://doi.org/10.3857/roj.2011.29.3.135).
- Paterson, Laura C et al. (2022). "High-accuracy relative biological effectiveness values following low-dose thermal neutron exposures support bimodal quality factor response with neutron energy". In: *International Journal of Molecular Sciences* 23.2, p. 878. DOI: [10.3390/ijms23020878](https://doi.org/10.3390/ijms23020878).
- Paule, Merle G et al. (2004). "Effects of drug countermeasures for space motion sickness on working memory in humans". In: *Neurotoxicology and teratology* 26.6, pp. 825–837. DOI: <https://doi.org/10.1016/j.ntt.2004.07.002>.
- Paulus, Martin P et al. (2009). "A neuroscience approach to optimizing brain resources for human performance in extreme environments". In: *Neuroscience & Biobehavioral Reviews* 33.7, pp. 1080–1088. DOI: <https://doi.org/10.1016/j.neubiorev.2009.05.003>.

- Pavy-Le Traon, A et al. (1997). "Pharmacology in space: pharmacotherapy". In: *Advances in space biology and medicine*. Vol. 6. Elsevier, pp. 93–105. DOI: <https://doi.org/10.5664/jcsm.7230>.
- Petoussi-Henss, N et al. (2020). "ICRP Publication 144: Dose Coefficients for External Exposures to Environmental Sources". In: *Annals of the ICRP* 49.2, pp. 11–145. DOI: <https://doi.org/10.1177/0146645320906277>.
- Physicisphun (2022). *Cosmic Rays*. URL: https://bigbangtheory.fandom.com/wiki/Cosmic_Ray.
- Pieper, Steve et al. (2004). "3D Slicer". In: *2004 2nd IEEE international symposium on biomedical imaging: nano to macro (IEEE Cat No. 04EX821)*. IEEE, pp. 632–635. DOI: [10.1109/ISBI.2004.1398617](https://doi.org/10.1109/ISBI.2004.1398617).
- Pietri, S et al. (2005). "Coincidence Measurement of Residue, Neutrons, and Light Charged Particles in a Spallation Experiment". In: *AIP Conference Proceedings*. Vol. 769. 1. American Institute of Physics, pp. 784–787. DOI: <https://doi.org/10.1063/1.1945124>.
- Pinsky, L. S. et al. (Mar. 1974). "Light Flashes Observed by Astronauts on Apollo 11 through Apollo 17". In: *Science* 183.4128, pp. 957–959. DOI: [10.1126/science.183.4128.957](https://doi.org/10.1126/science.183.4128.957).
- Pinsky, LS et al. (1975). "Light flashes observed by astronauts on Skylab 4". In: *Science* 188.4191, pp. 928–930. DOI: [10.1126/science.188.4191.928](https://doi.org/10.1126/science.188.4191.928).
- Podgorsak, Ervin B et al. (2003). "Review of radiation oncology physics: a handbook for teachers and students". In: *Vienna, Austria: IAE Agency* 19, p. 133. URL: https://edisciplinas.usp.br/pluginfile.php/5618241/mod_resource/content/1/Syllabus-iaea.pdf.
- Potgieter, Marius S (2013). "Solar modulation of cosmic rays". In: *Living Reviews in Solar Physics* 10, pp. 1–66. DOI: <https://doi.org/10.12942/lrsp-2013-3>.
- Powers, Darden (1989). "An overview of current stopping power phenomena, measurements, and related topics". In: *Nuclear Instruments and Methods in Physics Research Section B: Beam Interactions with Materials and Atoms* 40, pp. 324–328. DOI: [https://doi.org/10.1016/0168-583X\(89\)90990-7](https://doi.org/10.1016/0168-583X(89)90990-7).
- Preuss, Todd M and Steven P Wise (2022). "Evolution of prefrontal cortex". In: *Neuropsychopharmacology* 47.1, pp. 3–19. DOI: <https://doi.org/10.1038/s41386-021-01076-5>.
- Pxhere (2017). *Title of the Webpage*. URL: <https://pxhere.com/de/photo/1172921>.
- Raber, Jacob et al. (2015). "16Oxygen irradiation enhances cued fear memory in B6D2F1 mice". In: *Life sciences in space research* 7, pp. 61–65. DOI: <https://doi.org/10.1016/j.lssr.2015.10.004>.

- Rabin, B. M. et al. (Jan. 2000). "Effects of Exposure to Heavy Particles on a Behavior Mediated by the Dopaminergic System". In: *Advances in Space Research* 25.10, pp. 2065–2074. DOI: [10.1016/S0273-1177\(99\)01014-5](https://doi.org/10.1016/S0273-1177(99)01014-5).
- Rabin, Bernard M et al. (2002). "Effects of heavy particle irradiation and diet on amphetamine-and lithium chloride-induced taste avoidance learning in rats". In: *Brain research* 953.1-2, pp. 31–36. DOI: [https://doi.org/10.1016/S0006-8993\(02\)03263-8](https://doi.org/10.1016/S0006-8993(02)03263-8).
- Rabin, Bernard M et al. (2014). "Comparison of the effects of partial-or whole-body exposures to ^{16}O particles on cognitive performance in rats". In: *Radiation research* 181.3, pp. 251–257. DOI: <https://doi.org/10.1667/RR13469.1>.
- Rabin, Bernard M et al. (2015). "Acute effects of exposure to ^{56}Fe and ^{16}O particles on learning and memory". In: *Radiation research* 184.2, pp. 143–150. DOI: <https://doi.org/10.1667/RR13935.1>.
- Rabin, Bernard M et al. (2018). "Age as a factor in the responsiveness of the organism to the disruption of cognitive performance by exposure to HZE particles differing in linear energy transfer". In: *Life sciences in space research* 16, pp. 84–92. DOI: <https://doi.org/10.1016/j.lssr.2017.12.001>.
- Rabin, Bernard M et al. (2019). "Effects of head-only or whole-body exposure to very low doses of ^4He (1000 MeV/n) particles on neuronal function and cognitive performance". In: *Life Sciences in Space Research* 20, pp. 85–92. DOI: <https://doi.org/10.1016/j.lssr.2019.02.001>.
- Ragheb, M (2011). "Gamma Rays interaction with matter". In: *Nuclear, Plasma and Radiation Science. Inventing the Future*, <https://netfiles.uiuc.edu/mragheb/www>. URL: <https://mragheb.com/NPRE%20402%20ME%20405%20Nuclear%20Power%20Engineering/Gamma%20Rays%20Interactions%20with%20Matter.pdf>.
- Rao, UR (1972). "Solar modulation of galactic cosmic radiation". In: *Space Science Reviews* 12.6, pp. 719–809. DOI: <https://doi.org/10.1007/BF00173071>.
- Raphael, RNS et al. (2018). "Overview about radiation–matter interaction mechanisms and mitigation techniques". In: *Proceedings of the 3rd Brazilian Technology Symposium: Emerging Trends and Challenges in Technology*. Springer, pp. 223–238. DOI: [10.1007/978-3-319-93112-8_23](https://doi.org/10.1007/978-3-319-93112-8_23).
- Reames, Donald V (1995). "Solar energetic particles: A paradigm shift". In: *Reviews of Geophysics* 33.S1, pp. 585–589. DOI: <https://doi.org/10.1029/95RG00188>.
- (2013). "The two sources of solar energetic particles". In: *Space Science Reviews* 175, pp. 53–92. DOI: <https://doi.org/10.1007/s11214-013-9958-9>.
- Reedy, R_C and JR Arnold (1972). "Interaction of solar and galactic cosmic-ray particles with the Moon". In: *Journal of Geophysical Research* 77.4, pp. 537–555. DOI: <https://doi.org/10.1029/JA077i004p00537>.

- Rees, David (1995). "Observations and modelling of ionospheric and thermospheric disturbances during major geomagnetic storms: A review". In: *Journal of Atmospheric and Terrestrial Physics* 57.12, pp. 1433–1457. DOI: [https://doi.org/10.1016/0021-9169\(94\)00142-B](https://doi.org/10.1016/0021-9169(94)00142-B).
- Rehani, Madan M et al. (2011). "Radiation and cataract". In: *Radiation protection dosimetry* 147.1-2, pp. 300–304. DOI: <https://doi.org/10.1093/rpd/ncr299>.
- Reimoser, Stefan (2000). "Development and Engineering Design of a Novel Exocentric Carbon-Ion Gantry for Cancer Therapy: The "Riesenrad" Gantry". PhD thesis. CERN. URL: <https://cds.cern.ch/record/440482>.
- Reitz, Guenther (2008). "Characteristic of the radiation field in low Earth orbit and in deep space". In: *Zeitschrift für Medizinische Physik* 18.4, pp. 233–243. DOI: <https://doi.org/10.1016/j.zemedi.2008.06.015>.
- Reitz, Guenther and Thomas Berger (2006). "The MATROSHKA facility—Dose determination during an EVA". In: *Radiation protection dosimetry* 120.1-4, pp. 442–445. DOI: <https://doi.org/10.1093/rpd/nci558>.
- Reitz, Guenther et al. (2009). "Astronaut's organ doses inferred from measurements in a human phantom outside the International Space Station". In: *Radiation research* 171.2, pp. 225–235. DOI: <https://doi.org/10.1667/RR1559.1>.
- Ribba, Benjamin et al. (2006). "A multiscale mathematical model of cancer, and its use in analyzing irradiation therapies". In: *Theoretical Biology and Medical Modelling* 3, pp. 1–19. DOI: <https://doi.org/10.1186/1742-4682-3-7>.
- Richmond, AD and G Lu (2000). "Upper-atmospheric effects of magnetic storms: a brief tutorial". In: *Journal of Atmospheric and Solar-Terrestrial Physics* 62.12, pp. 1115–1127. DOI: [https://doi.org/10.1016/S1364-6826\(00\)00094-8](https://doi.org/10.1016/S1364-6826(00)00094-8).
- Rodriguez-Garcia, Laura et al. (2021). "The unusual widespread solar energetic particle event on 2013 August 19-Solar origin and particle longitudinal distribution". In: *Astronomy & Astrophysics* 653, A137. DOI: <https://doi.org/10.1051/0004-6361/202039960>.
- Rojdev, Kristina et al. (2015). "Comparison and validation of fluka and hzetrn as tools for investigating the secondary neutron production in large space vehicles". In: *AIAA SPACE 2015 Conference and Exposition*, p. 4601. DOI: <https://doi.org/10.2514/6.2015-4601>.
- Rola, Radoslaw et al. (2005). "High-LET radiation induces inflammation and persistent changes in markers of hippocampal neurogenesis". In: *Radiation research* 164.4, pp. 556–560. DOI: <https://doi.org/10.1667/RR3412.1>.
- Romero, Elkin and David Francisco (2020). "The NASA human system risk mitigation process for space exploration". In: *Acta Astronautica* 175, pp. 606–615. DOI: <https://doi.org/10.1016/j.actaastro.2020.04.046>.

- Romero-Weaver, AL et al. (2013). "Effect of SPE-like proton or photon radiation on the kinetics of mouse peripheral blood cells and radiation biological effectiveness determinations". In: *Astrobiology* 13.6, pp. 570–577. DOI: <https://doi.org/10.1089/ast.2012.0916>.
- Ross, Eddie and William J Chaplin (2019). "The behaviour of galactic cosmic-ray intensity during solar activity cycle 24". In: *Solar physics* 294, pp. 1–17. DOI: <https://doi.org/10.1007/s11207-019-1397-7>.
- Rouillard, Alexis P et al. (2021). "The solar wind". In: *Solar Physics and Solar Wind*, pp. 1–33. DOI: <https://doi.org/10.1002/9781119815600.ch1>.
- Rudbeck, Emil et al. (2017). "Low-dose proton radiation effects in a transgenic mouse model of Alzheimer's disease—Implications for space travel". In: *PloS one* 12.11, e0186168. DOI: <https://doi.org/10.1371/journal.pone.0186168>.
- Saadi, M Kheradmand and R Machrafi (2020). "Development of a new code for stopping power and CSDA range calculation of incident charged particles, part A: Electron and positron". In: *Applied Radiation and Isotopes* 161, p. 109145. DOI: <https://doi.org/10.1016/j.apradiso.2020.109145>.
- Sabol, Jozef and Pao-shan Weng (1995). *Introduction to radiation protection dosimetry*. World scientific. URL: https://inis.iaea.org/search/search.aspx?orig_q=RN:28028050.
- Santy, Patricia A et al. (1988). "Analysis of sleep on Shuttle missions." In: *Aviation, space, and environmental medicine* 59.11 Pt 1, pp. 1094–1097. URL: <https://europepmc.org/article/med/3202794>.
- Santy, Patricia A et al. (1993). "Multicultural factors in the space environment: results of an international shuttle crew debrief." In: *Aviation, space, and environmental medicine*. URL: <https://europepmc.org/article/med/8447799>.
- Sauer, Jonas-Frederic et al. (2020). "The role of the dentate gyrus in mnemonic functions". In: *Neuroforum* 26.4, pp. 247–254. DOI: <https://doi.org/10.1515/nf-2020-0021>.
- Saunders, RS et al. (2004). "2001 Mars Odyssey mission summary". In: *Space Science Reviews* 110, pp. 1–36. DOI: <https://doi.org/10.1023/B:SPAC.0000021006.84299.18>.
- Scandale, W et al. (2010). "Probability of inelastic nuclear interactions of high-energy protons in a bent crystal". In: *Nuclear Instruments and Methods in Physics Research Section B: Beam Interactions with Materials and Atoms* 268.17-18, pp. 2655–2659. DOI: <https://doi.org/10.1016/j.nimb.2010.07.002>.
- Scherer, Hans et al. (2001). "Motion sickness and otolith asymmetry". In: *Biological Sciences in Space* 15.4, pp. 401–404. DOI: <https://doi.org/10.2187/bss.15.401>.

- Schorn, Julia M and Peter G Roma (2020). "Physical hazards of space exploration and the biological bases of behavioral health and performance in extreme environments". In: *Psychology and Human Performance in Space Programs*. CRC Press, pp. 1–22. URL: <https://www.taylorfrancis.com/chapters/edit/10.1201/9780429440878-1/physical-hazards-space-exploration-biological-bases-behavioral-health-performance-extreme-environments-julia-schorn-peter-roma>.
- Schreiner, LJ (2015). "True 3D chemical dosimetry (gels, plastics): Development and clinical role". In: *Journal of Physics: Conference Series*. Vol. 573. 1. IOP Publishing, p. 012003. DOI: [10.1088/1742-6596/573/1/012003](https://doi.org/10.1088/1742-6596/573/1/012003).
- Schwenn, R (2007). "Solar wind sources and their variations over the solar cycle". In: *Solar dynamics and its effects on the heliosphere and Earth*, pp. 51–76. DOI: [10.1007/978-0-387-69532-7_5](https://doi.org/10.1007/978-0-387-69532-7_5).
- Schwenn, Rainer (2006). "Space weather: The solar perspective". In: *Living reviews in solar physics* 3.1, pp. 1–72. DOI: <https://doi.org/10.12942/lrsp-2006-2>.
- Seltzer, Stephen M and Martin J Berger (1982). "Procedure for calculating the radiation stopping power for electrons". In: *The International Journal of Applied Radiation and Isotopes* 33.11, pp. 1219–1226. DOI: [https://doi.org/10.1016/0020-708X\(82\)90245-9](https://doi.org/10.1016/0020-708X(82)90245-9).
- Semkova, J et al. (2012). "Depth dose measurements with the Liulin-5 experiment inside the spherical phantom of the Matroshka-R project onboard the International Space Station". In: *Advances in space research* 49.3, pp. 471–478. DOI: <https://doi.org/10.1016/j.asr.2011.10.005>.
- Setlow, Richard B (1999). "The US National Research Council's views of the radiation hazards in space". In: *Mutation Research/Fundamental and Molecular Mechanisms of Mutagenesis* 430.2, pp. 169–175. DOI: [https://doi.org/10.1016/S0027-5107\(99\)00127-X](https://doi.org/10.1016/S0027-5107(99)00127-X).
- Shen, Z-N et al. (2019). "Modulation of galactic cosmic rays from helium to nickel in the inner heliosphere". In: *The Astrophysical Journal* 887.2, p. 132. DOI: [10.3847/1538-4357/ab5520](https://doi.org/10.3847/1538-4357/ab5520).
- Shibamoto, Yuta et al. (2012). "Radiobiological evaluation of the radiation dose as used in high-precision radiotherapy: effect of prolonged delivery time and applicability of the linear-quadratic model". In: *Journal of radiation research* 53.1, pp. 1–9. DOI: <https://doi.org/10.1269/jrr.11095>.
- Shukitt-Hale, Barbara et al. (2000). "Spatial learning and memory deficits induced by exposure to iron-56-particle radiation". In: *Radiation research* 154.1, pp. 28–33. DOI: [https://doi.org/10.1667/0033-7587\(2000\)154\[0028:SLAMDI\]2.0.CO;2](https://doi.org/10.1667/0033-7587(2000)154[0028:SLAMDI]2.0.CO;2).
- Sigmund, Peter (1998). "Stopping power in perspective". In: *Nuclear Instruments and Methods in Physics Research Section B: Beam Interactions with Materials and*

- Atoms* 135.1-4, pp. 1–15. DOI: [https://doi.org/10.1016/S0168-583X\(97\)00638-1](https://doi.org/10.1016/S0168-583X(97)00638-1).
- Sihver, Lembit et al. (2015). “Radiation environment at aviation altitudes and in space”. In: *Radiation protection dosimetry* 164.4, pp. 477–483. DOI: <https://doi.org/10.1093/rpd/ncv330>.
- Simpson, JA (1983). “Elemental and isotopic composition of the galactic cosmic rays”. In: *Annual Review of Nuclear and Particle Science* 33.1, pp. 323–382. DOI: <https://doi.org/10.1146/annurev.ns.33.120183.001543>.
- Sinclair, WARREN K (1981). “Radiation protection: the NCRP guidelines and some considerations for the future.” In: *The Yale Journal of Biology and Medicine* 54.6, p. 471. URL: <https://www.ncbi.nlm.nih.gov/pmc/articles/PMC2596042/>.
- Singleterry Jr, Robert C et al. (2011). “OLTARIS: On-line tool for the assessment of radiation in space”. In: *Acta Astronautica* 68.7-8, pp. 1086–1097. DOI: <https://doi.org/10.1016/j.actaastro.2010.09.022>.
- Smith, Michael T et al. (2018). “Use of actigraphy for the evaluation of sleep disorders and circadian rhythm sleep-wake disorders: an American Academy of Sleep Medicine clinical practice guideline”. In: *Journal of Clinical Sleep Medicine* 14.7, pp. 1231–1237. DOI: <https://doi.org/10.5664/jcsm.7230>.
- Smith, PF (1988). “Terrestrial searches for new stable particles”. In: *Contemporary physics* 29.2, pp. 159–186. DOI: <https://doi.org/10.1080/00107518808213759>.
- Sofocleous, Angelos (2019). *Human Mars landing: so much more than a ‘small step’*. URL: <https://nouse.co.uk/2019/10/29/human-mars-landing-so-much-more-than-a-small-step>.
- Song, Da et al. (2020). “The lateralization of left hippocampal CA3 during the retrieval of spatial working memory”. In: *Nature Communications* 11.1, p. 2901. DOI: <https://doi.org/10.1038/s41467-020-16698-4>.
- Soppera, N et al. (2014). “JANIS 4: an improved version of the NEA java-based nuclear data information system”. In: *Nuclear Data Sheets* 120, pp. 294–296. DOI: <https://doi.org/10.1016/j.nds.2014.07.071>.
- Stanev, Todor (2004). *High energy cosmic rays*. Vol. 2. Springer. URL: <https://link.springer.com/book/10.1007/978-3-540-85148-6>.
- Starr, Stanley O and Anthony C Muscatello (2020). “Mars in situ resource utilization: a review”. In: *Planetary and Space Science* 182, p. 104824. DOI: <https://doi.org/10.1016/j.pss.2019.104824>.
- Stavnychuk, Mariya et al. (2020). “A systematic review and meta-analysis of bone loss in space travelers”. In: *npj Microgravity* 6.1, pp. 1–9. DOI: <https://doi.org/10.1038/s41526-020-0103-2>.

- Stenger, Michael B et al. (2019). "Focus on the optic nerve head in spaceflight-associated neuro-ocular syndrome". In: *Ophthalmology* 126.12, pp. 1604–1606. DOI: <https://doi.org/10.1016/j.ophtha.2019.09.009>.
- Stone, EC et al. (1998). "The advanced composition explorer". In: *Space Science Reviews* 86.1-4, p. 1. DOI: [10.1023/A:1005082526237](https://doi.org/10.1023/A:1005082526237).
- Strigari, Lidia et al. (2021). "Dose-effects models for space radiobiology: an overview on dose-effect relationships". In: *Frontiers in Public Health* 9, p. 733337. DOI: <https://doi.org/10.3389/fpubh.2021.733337>.
- Stuhlinger, Ernst (1999). "Sputnik 1957-Memories of an Oldtimer". In: *Huntsville Historical Review* 26.1, p. 6. URL: <https://louis.uah.edu/huntsville-historical-review/vol26/iss1/6>.
- Stuster, Jack W (2011). *Bold endeavors: Lessons from polar and space exploration*. Naval Institute Press. URL: <https://pubmed.ncbi.nlm.nih.gov/11543280/>.
- Swift, Damian C and James M McNaney (2009). "Approximate, analytic solutions of the Bethe equation for charged particle range". In: *arXiv preprint arXiv:0901.4145*. DOI: <https://doi.org/10.48550/arXiv.0901.4145>.
- Tafforin, Carole et al. (2015). "Correlation of etho-social and psycho-social data from "Mars-500" interplanetary simulation". In: *Acta Astronautica* 111, pp. 19–28. DOI: <https://doi.org/10.1016/j.actaastro.2015.02.005>.
- Tang, Henry HK (1996). "Nuclear physics of cosmic ray interaction with semiconductor materials: Particle-induced soft errors from a physicist's perspective". In: *IBM journal of research and development* 40.1, pp. 91–108. DOI: [10.1147/rd.401.0091](https://doi.org/10.1147/rd.401.0091).
- Tang, Yamei et al. (June 2012). "Psychological Disorders, Cognitive Dysfunction and Quality of Life in Nasopharyngeal Carcinoma Patients with Radiation-Induced Brain Injury". In: *PLoS ONE* 7.6, e36529. DOI: [10.1371/journal.pone.0036529](https://doi.org/10.1371/journal.pone.0036529).
- Taylor, Lauriston S (1958). "Brief history of the National Committee on Radiation Protection and Measurements (NCRP) covering the period 1929–1946". In: *Health Physics* 1.1, pp. 3–10. URL: https://journals.lww.com/health-physics/Abstract/1958/01000/Brief_History_of_the_National_Committee_on.1.aspx.
- Taylor, Lauriston S and Harold O Wyckoff (1972). "Radiation protection standards". In: *Critical Reviews in Environmental Science and Technology* 2.1-4, pp. 81–124. DOI: <https://doi.org/10.1080/10643387109381579>.
- Thomas, Simon R et al. (2014). "The 22-year hale cycle in cosmic ray flux—evidence for direct heliospheric modulation". In: *Solar Physics* 289, pp. 407–421. DOI: <https://doi.org/10.1007/s11207-013-0341-5>.

- Tofilon, Philip J. and John R. Fike (Apr. 2000). "The Radioresponse of the Central Nervous System: A Dynamic Process". In: *Radiation Research* 153.4, pp. 357–370. DOI: [10.1667/0033-7587\(2000\)153\[0357:TR0TCN\]2.0.CO;2](https://doi.org/10.1667/0033-7587(2000)153[0357:TR0TCN]2.0.CO;2).
- Usoskin, Ilya G et al. (2011). "Solar modulation parameter for cosmic rays since 1936 reconstructed from ground-based neutron monitors and ionization chambers". In: *Journal of Geophysical Research: Space Physics* 116.A2. DOI: <https://doi.org/10.1029/2010JA016105>.
- Valentin, Jack (2003). "Relative biological effectiveness (RBE), quality factor (Q), and radiation weighting factor (w R) ICRP Publication 92: Approved by the Commission in January 2003". In: *Annals of the ICRP* 33.4, pp. 1–121. DOI: [https://doi.org/10.1016/S0146-6453\(03\)00024-1](https://doi.org/10.1016/S0146-6453(03)00024-1).
- Valentin, Jack et al. (2007). *The 2007 recommendations of the international commission on radiological protection*. Vol. 37. 2-4. Elsevier Oxford. URL: <https://www.maff.go.jp/e/policies/market/reference/attach/pdf/reference-25.pdf>.
- Velazquez, Emmanuel Rios et al. (2013). "Volumetric CT-based segmentation of NSCLC using 3D-Slicer". In: *Scientific reports* 3.1, p. 3529. DOI: <https://doi.org/10.1038/srep03529>.
- Vlahos, Loukas et al. (2019). "Sources of solar energetic particles". In: *Philosophical Transactions of the Royal Society A* 377.2148, p. 20180095. DOI: <https://doi.org/10.1098/rsta.2018.0095>.
- Walsh, L et al. (2019). "Research plans in Europe for radiation health hazard assessment in exploratory space missions". In: *Life sciences in space research* 21, pp. 73–82. DOI: <https://doi.org/10.1016/j.lssr.2019.04.002>.
- Warden, David and Yildiz Bayazitoglu (2021). "Consideration of backscatter radiation from galactic cosmic rays in spacecraft shielding design". In: *Journal of Thermophysics and Heat Transfer* 35.3, pp. 650–656. DOI: <https://doi.org/10.2514/1.T6223>.
- Weinrich, Udo (2006). "Gantry design for proton and carbon hadrontherapy facilities". In: *Proceedings of EPAC*, p. 89. URL: <https://accelconf.web.cern.ch/e06/PAPERS/TUYFI01.PDF>.
- Wijzen, Nicolas et al. (2019). "Modelling three-dimensional transport of solar energetic protons in a corotating interaction region generated with EUHFORIA". In: *Astronomy & Astrophysics* 622, A28. DOI: <https://doi.org/10.1051/0004-6361/201833958>.
- Williams, David R (2003). "The biomedical challenges of space flight". In: *Annual review of medicine* 54.1, pp. 245–256. DOI: <https://doi.org/10.1146/annurev.med.54.101601.152215>.

- Wilson, JW et al. (2004). "Emerging Radiation Health-Risk Mitigation Technologies". In: *AIP Conference Proceedings*. Vol. 699. 1. American Institute of Physics, pp. 913–924. DOI: <https://doi.org/10.1063/1.1649656>.
- Wimmer-Schweingruber, Robert F et al. (2015). "On determining the zenith angle dependence of the Martian radiation environment at Gale Crater altitudes". In: *Geophysical Research Letters* 42.24, pp. 10–557. DOI: <https://doi.org/10.1002/2015GL066664>.
- Wotring, Virginia E and Virginia E Wotring (2012). "Multiple Systems Spaceflight Effects". In: *Space Pharmacology*, pp. 71–82. DOI: [10.1007/978-1-4614-3396-5_9](https://doi.org/10.1007/978-1-4614-3396-5_9).
- Wright, Dennis and Sébastien Incerti (2012). "A short guide to choosing a physics list". In: *Geant4 Tutorial, Marshall Space Flight Center*. URL: http://geant4.in2p3.fr/IMG/pdf_PhysicsLists.pdf.
- Wright Jr, JM et al. (2010). "The National Space Weather Program: The Strategic Plan". In: *Rep. FCM-P30-1995*. URL: <https://www.spaceweathercenter.org/research/05/NSWPStratPlan.pdf>.
- Wrixon, Anthony D (2008). "New ICRP recommendations". In: *Journal of radiological protection* 28.2, p. 161. DOI: [10.1088/0952-4746/28/2/R02](https://doi.org/10.1088/0952-4746/28/2/R02).
- Wu, Honglu et al. (2009). "Risk of acute radiation syndromes due to solar particle events". In: *The Human Health and Performance Risks for Space Explorations*. Houston, Texas: NASA Human Research Program, pp. 171–90. URL: <https://humanresearchroadmap.nasa.gov/Evidence/reports/ars.pdf>.
- Xu, X George (2014). "An exponential growth of computational phantom research in radiation protection, imaging, and radiotherapy: a review of the fifty-year history". In: *Physics in Medicine & Biology* 59.18, R233. DOI: [10.1088/0031-9155/59/18/R233](https://doi.org/10.1088/0031-9155/59/18/R233).
- Yarba, Julia (2012). "Recent developments and validation of Geant4 hadronic physics". In: *Journal of Physics: Conference Series*. Vol. 396. 2. IOP Publishing, p. 022060. DOI: [10.1088/1742-6596/396/2/022060](https://doi.org/10.1088/1742-6596/396/2/022060).
- Yazici, Ayşe Meriç et al. (2021). "Space tourism: An initiative pushing limits". In: *Journal of Tourism Leisure and Hospitality* 3.1, pp. 38–46. DOI: <https://doi.org/10.48119/toleho.862636>.
- Yeom, Yeon Soo et al. (2014). "Tetrahedral-mesh-based computational human phantom for fast Monte Carlo dose calculations". In: *Physics in Medicine & Biology* 59.12, p. 3173. DOI: [10.1088/0031-9155/59/12/3173](https://doi.org/10.1088/0031-9155/59/12/3173).
- Young, Robert W (1987). "Acute radiation syndrome". In: *Military radiobiology* 9, pp. 165–186. URL: https://books.google.de/books?hl=de&lr=&id=q_JEJrG-Gq8C&oi=fnd&pg=PA165&dq=Acute+radiation+syndrome,+Young&ots=EjeZFfz3Mc&sig=PZlvvpj2dYx1HNYIFL00vlbvbUo&redir_esc=y#v=onepage&q=Acute%20radiation%20syndrome%2C%20Young&f=false.

- Zanni, Giulia et al. (2018). "Whole-body ^{12}C irradiation transiently decreases mouse hippocampal dentate gyrus proliferation and immature neuron number, but does not change new neuron survival rate". In: *International journal of molecular sciences* 19.10, p. 3078. DOI: <https://doi.org/10.3390/ijms19103078>.
- Zayzafoon, Majd et al. (2005). "Microgravity: the immune response and bone". In: *Immunological reviews* 208.1, pp. 267–280. DOI: <https://doi.org/10.1111/j.0105-2896.2005.00330.x>.
- Zeitlin, C. et al. (May 2013). "Measurements of Energetic Particle Radiation in Transit to Mars on the Mars Science Laboratory". In: *Science* 340.6136, pp. 1080–1084. DOI: [10.1126/science.1235989](https://doi.org/10.1126/science.1235989).
- Zeitlin, Cary (2021). "Space radiation shielding". In: *Handbook of Bioastronautics*, pp. 353–375. DOI: [10.1007/978-3-319-12191-8_28](https://doi.org/10.1007/978-3-319-12191-8_28).
- Zeitlin, Cary et al. (2016). "Calibration and characterization of the Radiation Assessment Detector (RAD) on Curiosity". In: *Space Science Reviews* 201, pp. 201–233. DOI: <https://doi.org/10.1007/s11214-016-0303-y>.
- Zeitlin, Cary et al. (2019). "Comparisons of high-linear energy transfer spectra on the ISS and in deep space". In: *Space Weather* 17.3, pp. 396–418. DOI: <https://doi.org/10.1029/2018SW002103>.
- Zhang, Jian et al. (2022). "From the top of martian olympus to deep craters and beneath: Mars radiation environment under different atmospheric and regolith depths". In: *Journal of Geophysical Research: Planets* 127.3, e2021JE007157. DOI: <https://doi.org/10.1029/2021JE007157>.
- Zhang, Qiuning et al. (2021). "Ion therapy guideline (Version 2020)". In: *Precision Radiation Oncology* 5.2, pp. 73–83. DOI: [10.1002/pro6.1120](https://doi.org/10.1002/pro6.1120).
- Zhang, Shenyi et al. (2020). "First measurements of the radiation dose on the lunar surface". In: *Science Advances* 6.39, eaaz1334. DOI: [10.1126/sciadv.aaz1334](https://doi.org/10.1126/sciadv.aaz1334).
- Ziegler, James F (1999). "Stopping of energetic light ions in elemental matter". In: *Journal of applied physics* 85.3, pp. 1249–1272. DOI: <https://doi.org/10.1063/1.369844>.

Appendix A

Convert NRRD files to PNG

```
%\begin{lstlisting}[language=Python, caption=Python example]
class nrrd:
    class NRRDError(Exception):
        pass
    def __init__(self, fn):
        self.fn = fn
        self.f = open(fn, 'rb')
        self.extract_header()
        self.extract_data()
    def __str__(self):
        s = "NRRD file (version: {:d}):\n".format(self.version)
        for k, v in self.properties.items():
            s += "\t"+k+": "+str(v)+"\n"
        return s
    def __repr__(self):
        return str(self)
    def extract_properties(self, lines):
        import numpy
        self.version = int(lines[0][4:])
        self.properties = {}
        for line in lines[1:]:
            ls = line.split(": ")
            self.properties.update({ls[0]: ls[1]})
        self.dim = int(self.properties['dimension'])
        self.shape = tuple([int(x) for x in self.properties['sizes']
                             .split()])

        if self.dim != len(self.shape):
            raise nrrd.NRRDError("Inconsistent NRRD file, dimension
                                   != sizeof(sizes)")

        dirs = self.properties['space directions'].split(" ")
        self.directions = tuple([tuple(map(float, dirs[0][1:].split(
            ', '))), tuple(map(float,
            dirs[1].split(', '))),
            tuple(map(float, dirs[2][:
            -1].split(', ')))]])

```

```

self.encoding = self.properties['encoding']
self.origin = tuple([float(x) for x in self.properties['
                        space origin'][1:-1].split
                        ('',)])

self.space = self.properties['space']
self.endian = self.properties['endian']
self.dtype = numpy.dtype(self.properties['type']).
                newbyteorder(self.endian[0
                ].upper())

def extract_header(self):
    lines = []
    buf = []
    while True:
        buf.append(self.f.read(1))
        if buf[-1] == b'\n':
            lines.append(b"".join(buf[:]).decode('utf8'))
            buf = []
            if len(lines[-1]) == 1:
                break
    lines = [l.strip() for l in lines if not l[0] in ('#', '\n')]

    self.extract_properties(lines)
def extract_data(self):
    import numpy
    import gzip
    if self.encoding == 'raw':
        self.data = numpy.fromfile(self.f, dtype=self.dtype,
                                    count=numpy.prod(self.
                                    shape))

    elif self.encoding == 'gzip':
        gz = gzip.GzipFile(fileobj=self.f, mode='rb')
        data = gz.read()
        self.data = numpy.frombuffer(data, dtype=self.dtype,
                                    count=numpy.prod(self.
                                    shape))

    self.data = self.data.reshape(self.shape, order='F')
def export_image(self, layer=0, outpath=None):
    from PIL import Image
    import os
    idata = self.data - self.data.min()
    i = Image.fromarray(idata[:, :, layer])
    outname = os.path.splitext(os.path.basename(self.fn))[0]
    outname = outname + "_layer_{:03d}.png".format(layer)
    i.save(os.path.join(outpath, outname), format='PNG')
def export_images(self, outpath=None):
    for l in range(self.shape[-1]):
        self.export_image(l, outpath=outpath)
if __name__ == '__main__':

```

```
import sys
import os
if len(sys.argv) < 2:
    sys.stderr.write("synopsis: {} <in.nrrd> [<outdir>]\n".
                     format(sys.argv[0]))
    sys.exit(0)
outpath = os.path.dirname(sys.argv[1])
if len(sys.argv) == 3:
    try:
        os.makedirs(sys.argv[2])
    except OSError:
        pass
    outpath = sys.argv[2]
n = nrrd(sys.argv[1])
n.export_images(outpath)
print(py.stdout.getvalue())
%\end{lstlisting}
```

Appendix B

Dose Resulting from GCRs and SEP Events

In the paper 4.1 and paper 4.2, we have extensively described the procedure for folding our **BRFs** with various **GCR** and **SEP** spectra. These papers provide valuable insights into the utilization of pre-determined **BRFs** for accurately calculating the radiation dose rate within different lobes of the brain in deep space environments. To illustrate the practical application of our approach, figure B.1 showcases the results of the dose rate specifically in the frontal lobes, considering **GCR** spectra on the surface of Mars for proton, neutron, and ^4He particles under different solar modulations. These findings shed light on the radiation exposure levels in this critical region of the brain across varying solar conditions. Furthermore, figure B.2 presents the comprehensive dose rate analysis for the entire human head, encompassing different solar modulation potentials (Φ), particle species, and varying shielding scenarios. It is important to note that the **GCR** spectra utilized in our calculations are derived from the Badwhar O'Neil model (O'Neill, 2010), which takes into account the solar modulation potential (Φ). To capture a wide range of solar conditions, we have performed calculations using different Φ values ranging from 300 MV to 1200 MV. These investigations can provide valuable insights into the dose rates experienced in deep space environments, allowing for a better understanding of the radiation risks faced by astronauts and facilitating the development of appropriate shielding strategies.

In paper 4.2, we have studied over 50 **SEP** events and the resulting dose (cGy) from just 35 events in a human head considering different thicknesses of Al as a shield around an astronaut's head/body as well as in different lobes of the human brain protected by 2 mm of the shield are shown. These 35 events are chosen from the list as they would deposit more than 10 cGy of dose in the head without shielding (second column). In tables B.1 and B.2, we have included the results of all the **SEP** events that were studied, providing a comprehensive representation of the data.

TABLE B.1: Resulted dose (cGy) from 51 SEP events in human head considering the different thicknesses of Aluminium as a shield around an astronaut's head/body.

Events	Dose (cGy) for each evant					
	Without shield	2mm Al	5mm Al	2cm Al	5cm Al	10 cm Al
4 Nov 1997	4	1.6	0.9	0.3	0.1	0
6 Nov 1997	52	12	4	0.9	0.2	0
20 Apr 1998	123	39	13	2	0.4	0.1
6 May 1998	4	1.7	1	0.4	0.2	0
24 Aug 1998	32	4	1.4	0.2	0	0
30 Sep 1998	31	5	2	0.4	0	0
14 Nov 1998	13	4	2	0	0	0
14 July 2000	2005	741	345	78	22	6
8 Nov 2000	1354	542	283	71	20	5
24 Nov 2000	3	1	0.5	0.2	0	0
26 Nov 2000	26	4	1.5	0.3	0	0
28 Jan 2001	4	0.5	0.2	0	0	0
2 Feb 2001	58	15	6	1.1	0.3	0
10 Feb 2001	10	2	0.7	0.1	0	0
12 Feb 2001	19	1	0.2	0	0	0
15 Feb 2001	79	39	28	14	7	3
18 Feb 2001	20	9	6	3	1.4	0.6
16 Aug 2001	28	13	8	3	1.4	0.6
24 Sep 2001	426	92	41	9	2	0.8
1 Oct 2001	70	8	1.7	0.1	0	0
4 Nov 2001	2255	736	256	34	7	1.7
22 Nov 2001	591	83	24	2	0.5	0.1
26 Dec 2001	48	18	10	3	1.3	0.5
21 Apr 2002	267	92	36	6	1.4	0.4
22 May 2002	9	0.5	0.1	0	0	0
22 Aug 2002	2	0.9	0.6	0.2	0.1	0
24 Aug 2002	29	9	4	1.3	0.5	0.2
5 Sep 2002	1.4	0.1	0	0	0	0
9 Nov 2002	5	0.6	0.2	0	0	0
26 Oct 2003	12	3	1.6	0.4	0.1	0
28 Oct 2003	1268	357	174	43	13	4
29 Oct 2003	244	68	36	10	3	1.2
2 Nov 2003	89	34	15	3	1	0.3
4 Nov 2003	9	3	1.1	0.2	0	0
25 July 2004	5	0.6	0.3	0	0	0
12 Sep 2004	9	0.4	0	0	0	0
1 Nov 2004	2	0.9	0.4	0.1	0	0
7 Nov 2004	12	1.5	0.5	0	0	0
8 Nov 2004	3	0.3	0.1	0	0	0
10 Nov 2004	12	6	4	2	1.4	0.7
16 Jan 2005	27	4	2	0.4	0.1	0
17 Jan 2005	362	108	35	4	0.9	0.2
20 Jan 2005	158	90	69	37	20	10
13 May 2005	22	1.3	0.38	0	0	0
17 June 2005	3	1.5	1	0.5	0.2	0.1
14 July 2005	8	1.4	0.4	0	0	0
22 Aug 2005	19	2	0.6	0	0	0
7 Sep 2005	135	25	10	1.7	0.4	0.1
13 Sep 2005	4	1.6	1	0.4	0.2	0
6 Dec 2006	174	44	21	5	1.5	0.4
13 Dec 2006	81	40	26	10	4	1.6

TABLE B.2: Dose (cGy) from 51 SEP events in different lobes of the human brain protected by 2mm of shield

Events	Dose (cGy) for each evant				
	Frontal	Parietal	Temporal	Occipital	Hippocampus
4 Nov 1997	1	0.8	0.7	0.7	0.3
6 Nov 1997	6	4.6	4.4	4.3	1.5
20 Apr 1998	13	9	9	8	5
6 May 1998	1.2	1	0.9	0.9	0.34
24 Aug 1998	0.6	0.5	0.4	0.4	0.4
30 Sep 1998	1	0.8	0.7	0.7	0.3
14 Nov 1998	1.4	1.17	1.14	1.2	0.6
14 July 2000	179	144	139	141	62
8 Nov 2000	159	132	128	130	64
24 Nov 2000	0.6	0.5	0.4	0.4	0.15
26 Nov 2000	0.69	0.53	0.5	0.5	0.19
28 Jan 2001	0.2	0.15	0.1	0.1	0.04
2 Feb 2001	2.9	2.3	2.1	2.1	0.85
10 Feb 2001	0.36	0.28	0.26	0.25	0.1
12 Feb 2001	0.07	0.05	0.05	0.04	0.01
15 Feb 2001	21	19	18	17	12
18 Feb 2001	4.6	4.1	4.1	4	2.6
16 Aug 2001	5.7	4.8	4.8	4.3	2.8
24 Sep 2001	21	17	16	16	7
1 Oct 2001	0.6	0.4	0.35	0.3	0.07
4 Nov 2001	110	82	77	76	26
22 Nov 2001	9	7	7	6	2
26 Dec 2001	6.3	5.7	5.3	5.5	2.9
21 Apr 2002	16.6	12.9	12.2	12	4.6
22 May 2002	0.16	0.1	0.07	0.05	0.02
22 Aug 2002	0.6	0.5	0.4	0.5	0.23
24 Aug 2002	2.8	2.5	2.3	2.3	1
5 Sep 2002	0.05	0.038	0.029	0.02	0.008
9 Nov 2002	0.2	0.14	0.12	0.1	0.03
26 Oct 2003	0.9	0.7	0.7	0.7	0.3
28 Oct 2003	94	77	76	78	35
29 Oct 2003	21	18	17	18	9
2 Nov 2003	8	7	7	6	3
4 Nov 2003	1.2	0.9	0.7	0.6	0.2
25 July 2004	0.3	0.2	0.18	0.16	0.08
12 Sep 2004	0.07	0.05	0.03	0.03	0.009
1 Nov 2004	0.4	0.3	0.3	0.3	0.14
7 Nov 2004	0.27	0.21	0.2	0.2	0.07
8 Nov 2004	0.09	0.07	0.06	0.06	0.01
10 Nov 2004	3.7	3.4	3.3	3.5	2.3
16 Jan 2005	1	0.78	0.74	0.7	0.3
17 Jan 2005	15	11	11	10	3
20 Jan 2005	53	49	48	50	34
13 May 2005	0.16	0.11	0.1	0.1	0.03
17 June 2005	1.14	0.98	0.93	0.95	0.31
14 July 2005	0.5	0.4	0.3	0.26	0.12
22 Aug 2005	0.24	0.18	0.16	0.15	0.05
7 Sep 2005	4.6	3.6	3.4	3	1.3
13 Sep 2005	1.15	0.98	0.9	0.9	0.28
6 Dec 2006	11	8.9	8.6	8.4	3.9
13 Dec 2006	17	15	14.7	14.5	8.5

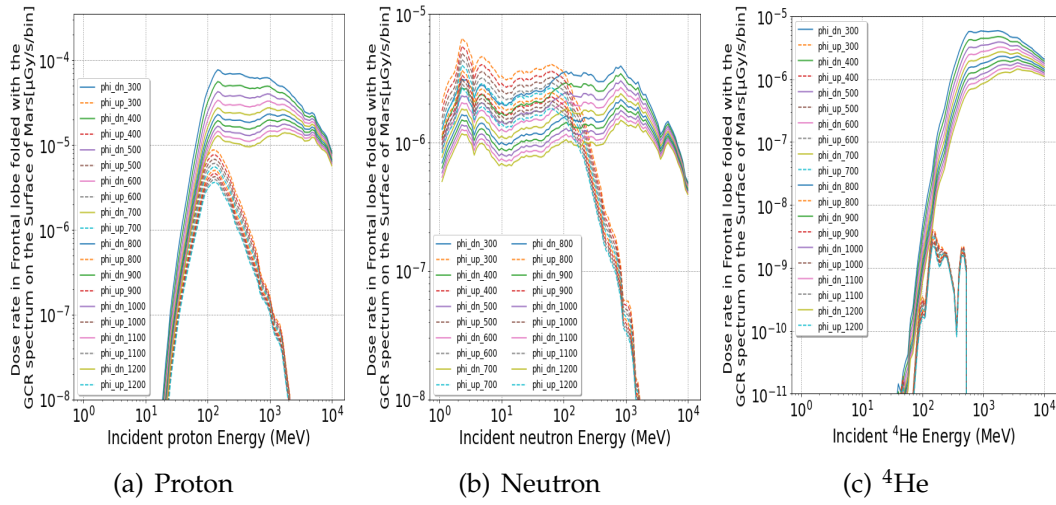


FIGURE B.1: Dose functions folded to downward and upward **GCR** spectra for the Frontal lobe, separately for: a) Protons, b) Neutrons, and c) ⁴He.

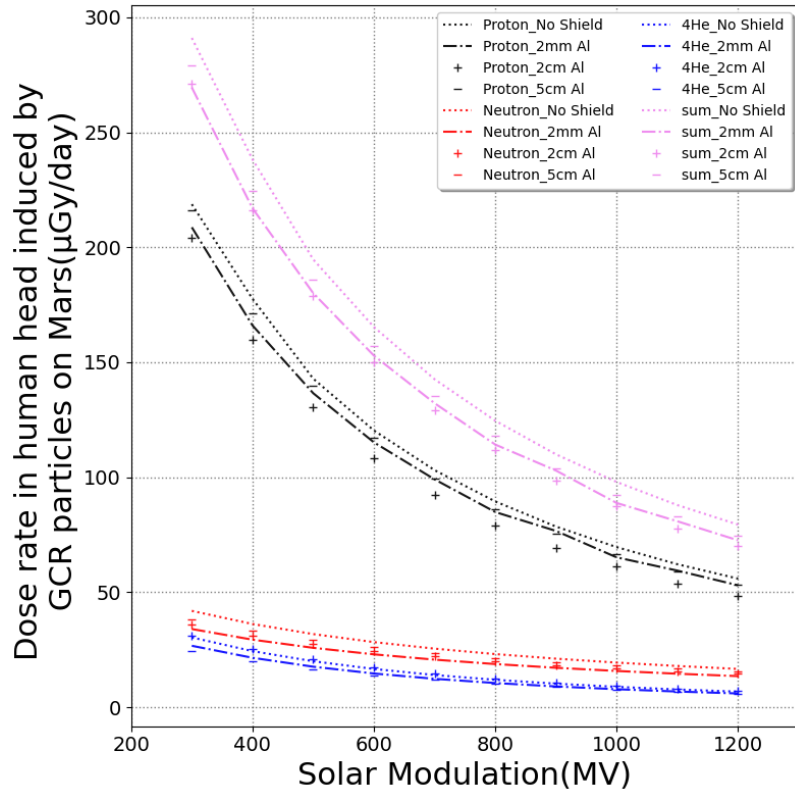


FIGURE B.2: The dose rates in the human head under different thicknesses of shielding induced by protons, neutrons, and helium ions on the Martian's surface in different solar modulation conditions. The summed dose rates from all these primary particles under different conditions (solar modulations, shielding depth) are also shown.

Appendix C

Calibration Curve

To generate a voxel-based phantom, the **HU**s obtained from **CT** images in the human body are categorized into various groups, spanning a range from -1000 to +3000, and are converted into different materials such as air, lung, soft tissue, and bone, along with their corresponding mass densities. The conversion process, represented by a curve, is illustrated in figure C.1. The **HU** values were utilized as a measure of radio-density to differentiate between various tissues within the human body. By associating specific **HU** ranges with different materials and mass densities, it became possible to accurately simulate the composition and characteristics of different anatomical structures. Geant4-DICOM package utilizes such a curve to convert **HU**s to the mass density and build the geometry based on that. We can define different intervals of converting **HU**s into the densities of materials to create different geometries. For example, in the paper 4.1, to evaluate the difference and possible advantage of using a realistic head structure in comparison to using a water-filled head structure concerning the dose distribution inside the brain, we consider three different head structures, a head filled with only water by setting all **HU** values into zero within the head of the **CT** images, a human head structure containing water, a hollow part (the nose), and all other hard tissues with a fixed density of bones, and finally the actual complex head, where **HU** values between -1000 to 3000 are divided into several intervals representing different parts of the brain (e.g., water, soft tissue, bone, etc.) with different densities.

Figure C.1 provides a visual representation of such a calibration curve, showcasing how the **HU** values were transformed into their respective materials and mass densities. This calibration curve serves as a crucial reference for accurately mapping the radiodensity of tissues in the voxel-based phantom, enabling the simulation of realistic and anatomically accurate models for further analysis and research purposes.

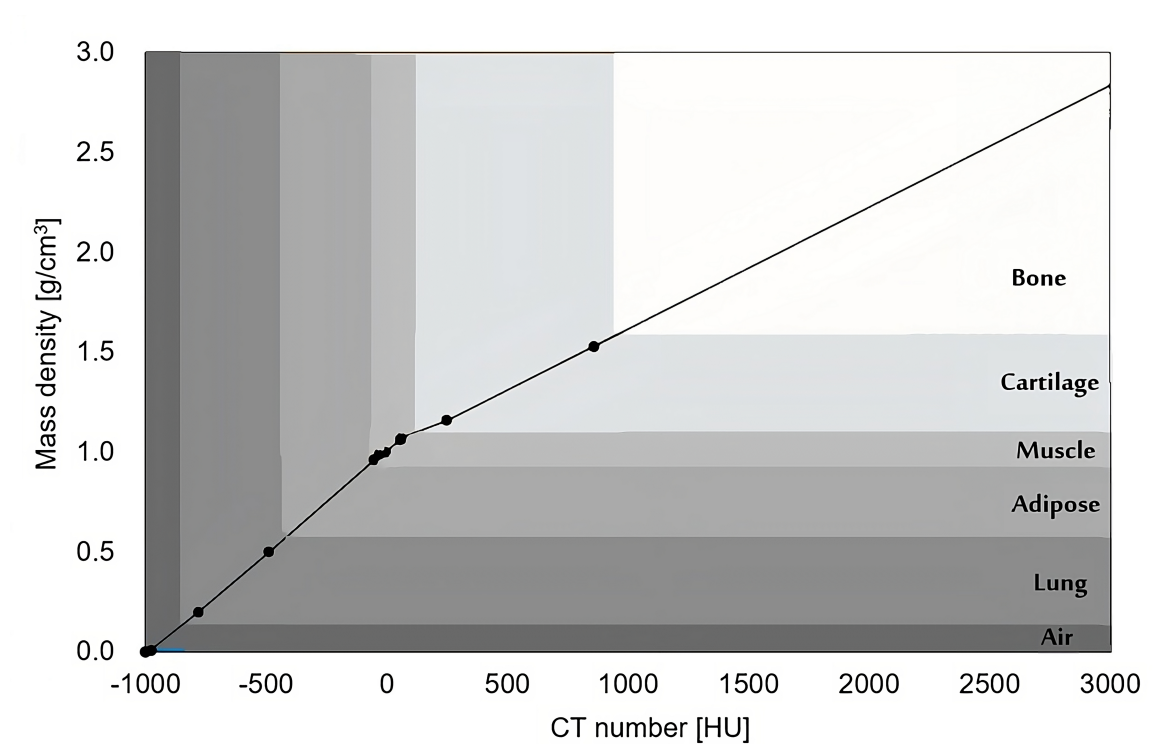


FIGURE C.1: The CT calibration curve for the **HU** to mass density conversion

Appendix D

List of Peer-Reviewed Publications

This list shows all peer-reviewed publications that I have contributed to. Not all of these publications were included in this thesis, as they do not all fit into the logical flow of this thesis

1. Publication 1: *Calculation of dose distribution in a realistic brain structure and the indication of space radiation influence on human brains*

Khaksarighiri, S., Guo, J., Wimmer-Schweingruber, R., Narici, L., Lohf, H. (2020). Life Sciences in Space Research, 27, 33-48. DOI:10.1016/j.lssr.2020.07.003

Own contribution: 80%

2. Publication 2: *An easy-to-use function to assess deep space radiation in human brains*

Khaksarighiri, S., Guo, J., Wimmer-Schweingruber, R., Narici, L. (2021). Scientific reports, 11(1), 11687. DOI:10.1038/s41598-021-90695-5

Own contribution: 80%

3. Publication 3: *The Zenith-Angle Dependence of the Downward Radiation Dose Rate on the Martian Surface: Modeling Versus MSL/RAD Measurement*

Khaksarighiri, S., Guo, J., Wimmer-Schweingruber, R. F., Löffler, S., Ehresmann, B., Matthiä, D., Donald M.Hassler, Cary Zeitlin, Berger, T. (2023). Journal of Geophysical Research: Planets, e2022JE007644. DOI:10.1029/2022JE007644

Own contribution: 80%

4. Publication 4: *Directionality of the Martian Surface Radiation and Derivation of the Upward Albedo Radiation*

Guo, J., **Khaksarighiri, S.**, Wimmer-Schweingruber, R. F., et.al (2021). Geophysical Research Letters, 48(15), e2021GL093912. DOI:10.1029/2021GL093912

Own contribution: 50%

5. Publication 5: *Radiation environment for future human exploration on the surface of Mars: the current understanding based on MSL/RAD dose measurements*

Guo, J., R. F. Wimmer-Schweingruber, C. Zeitlin, D. M. Hassler, B. Ehresmann, J. L. Freiherr von Forstner, **S. Khaksarighiri**, S. Rafkin, W. Liu, and Y. Wang, The Astronomy and Astrophysics Review (2021), 29. Jg., S. 1-81. DOI:10.1007/s00159-021-00136-5

Own contribution: 10%

6. Publication 6: *Natural Radiation Shielding on Mars measured with the MSL/RAD Instrument*

Ehresmann, B., Hassler, D. M., Zeitlin, C., Guo, J., Wimmer-Schweingruber, R. F., **Khaksarighiri, S.**, and Loeffler, S. (2021). Journal of Geophysical Research: Planets, 126(8), e2021JE006851. <https://doi.org/10.1029/2021JE006851>

Own contribution: 10%

7. Publication 7: *Primary and albedo protons detected by the Lunar Lander Neutron and Dosimetry experiment on the lunar farside*

Xu, Z., Guo, J., Wimmer-Schweingruber, R. F., Dobynde, M. I., Kühl, P., **Khaksarighiri, S.**, and Zhang, S. (2022). Front. Astron. Space Sci., 26 September 2022 Sec. Space Physics Volume 9 - 2022. DOI:10.3389/fspas.2022.974946

Own contribution: 10%

8. Publication 8: *The impact of space radiation on brains of future Martian and lunar explorers*

Li, Y., Guo, J., **Khaksarighiri, S.**, Dobynde, I., M., Zhang, J., Liu, B., Wimmer-Schweingruber, R. F.. Space Weather(2023), <http://dx.doi.org/10.1029/2023SW003470>.

Own contribution: 30%

Acknowledgements

I would like to express my heartfelt gratitude to the MSL/RAD group and everyone who supported me during my Ph.D. studies.

First and foremost, I am immensely grateful to my supervisor, Prof. Robert Wimmer-Schweingruber, for granting me the opportunity to work on these exciting projects and for his invaluable guidance. His support has not only shaped my research but has also facilitated the publication of our results in esteemed scientific journals and their presentation at international conferences.

I am sincerely grateful to Prof. Jingnan Guo for her unwavering support throughout my work, even after her relocation to China. Despite the distance, Prof. Guo has provided invaluable guidance, encouragement, and insights that greatly influenced my research. Her dedication and commitment to my academic journey have been remarkable, and I am deeply grateful for her ongoing support.

I am also grateful to Prof. Livio Narici for his invaluable help, support, and insightful input in medical physics and the study of space radiation effects on the human head. His expertise and guidance have greatly contributed to my understanding and research in these areas.

I am deeply grateful to all my colleagues for their continuous support and insightful discussions. Special thanks to Christoph Terasa for coding assistance, as well as to Henning Lohf, Daniel Pacheco, Zigong Xu, and the rest of the Extraterrestrial Physics group at Kiel University. I would like to acknowledge and express my gratitude to Dr. Verena Heidrich-Meisner for her meticulous proofreading and valuable suggestions. I would also like to thank Dr. Patrick Kühl, Dr. Johannes Marquardt, Dr. Sönke Burmeister, Alexander Kollhoff, Maximilian Brüdern and Jan Leo Löwe for their significant support in improving the quality of this thesis.

Finally, my heartfelt appreciation goes to my parents, siblings, and family for their unwavering support, encouragement, and love throughout my academic journey. Their sacrifices, guidance, and unwavering belief in me have been invaluable in making this thesis possible. I am forever grateful for their constant motivation, understanding, and words of wisdom, which have been a continuous source of strength and inspiration to me.

Declaration of Authorship

I, Salman Khaksarighiri, declare that this thesis titled, “Quantification of the Impact of Space Radiation on the Human Brain in Preparation of a Human Exploration of Mars” and the work presented in it are my own. I confirm that:

- Apart from the supervisor’s guidance the content and design of the paper are all the candidate’s work;
- This work was done wholly or mainly while in candidature for a research degree at this University;
- The thesis has been prepared with regard to the Rules of Good Scientific Practice of the German Research Foundation;
- Where any part of this thesis has previously been submitted for a degree or any other qualification at this University or any other institution, this has been clearly stated;
- Where I have quoted from the work of others, the source is always given. With the exception of such quotations, this thesis is entirely my work;
- Whether an academic degree has ever been withdrawn;
- I have acknowledged all main sources of help;
- Where the thesis is based on work done by myself jointly with others, I have made clear exactly what was done by others and what I have contributed myself;

As mentioned in Appendix C, and referenced in the text, the thesis contain works that have already been published in scientific journals.

Signed:

Date:
